

Sheffield Hallam University

The thermal performance of water cooled panels in electric arc steelmaking furnaces.

SIMON, M. J.

Available from the Sheffield Hallam University Research Archive (SHURA) at:

<http://shura.shu.ac.uk/20363/>

A Sheffield Hallam University thesis

This thesis is protected by copyright which belongs to the author.

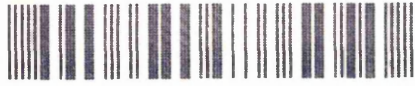
The content must not be changed in any way or sold commercially in any format or medium without the formal permission of the author.

When referring to this work, full bibliographic details including the author, title, awarding institution and date of the thesis must be given.

Please visit <http://shura.shu.ac.uk/20363/> and <http://shura.shu.ac.uk/information.html> for further details about copyright and re-use permissions.

100255230 3

TELEPEN



Sheffield City Polytechnic Library

REFERENCE ONLY

ProQuest Number: 10701009

All rights reserved

INFORMATION TO ALL USERS

The quality of this reproduction is dependent upon the quality of the copy submitted.

In the unlikely event that the author did not send a complete manuscript and there are missing pages, these will be noted. Also, if material had to be removed, a note will indicate the deletion.



ProQuest 10701009

Published by ProQuest LLC (2017). Copyright of the Dissertation is held by the Author.

All rights reserved.

This work is protected against unauthorized copying under Title 17, United States Code
Microform Edition © ProQuest LLC.

ProQuest LLC.
789 East Eisenhower Parkway
P.O. Box 1346
Ann Arbor, MI 48106 – 1346

THE THERMAL PERFORMANCE OF WATER
COOLED PANELS IN ELECTRIC ARC
STEELMAKING FURNACES

BY

M.J.SIMON

A THESIS SUBMITTED TO THE COUNCIL FOR NATIONAL
ACADEMIC AWARDS IN PARTIAL FULFILLMENT FOR THE
DEGREE OF DOCTOR OF PHILOSOPHY

SEPTEMBER 1989

COLLABORATING ESTABLISHMENT :-

British Steel Corporation,
Stocksbridge Works.
(Now United Engineering Steels)

SPONSORING ESTABLISHMENT :-

Department Of Metallurgy,
(Now Metals And Materials Engineering)
Sheffield City Polytechnic

DEDICATION.

This thesis is dedicated to all those who have helped during the course of the work, especially the following:

V. Gibson

G. Briggs

D. Simmonds

D. Latimer and the T2 Team

"B" Furnace Melters

PREFACE.

All the work reported in this thesis was carried out during the period for which the candidate was registered for a higher degree.

In accordance with the regulations for PhD, a full course in Metallurgical Process Management was successfully completed. The details of the course are given below : -

Module 1

Process Metallurgy

Mechanical Metallurgy

Advanced Thermodynamics

Module 2

Accountancy

Micro-Economics And Financial Control

Computational Methods And Operational Research

Module 3

Automatic And Computer Control

Metals And Competitive Materials

Refractories

Arc Furnace Steelmaking

Quality Control

Solidification Of Metals

Module 4

Industrial Case Studies

One of the case studies, which is related to this work, is attached with the thesis, as Appendix VIII.

ABSTRACT.

The Thermal Performance Of Water Cooled Panels In Electric Arc Steelmaking Furnaces.

M. J. Simon

The initial stage of the work was a study of an 80 tonne industrial furnace, taking observations, panel water temperature data and samples of slag layers from the sidewalls. This resulted in a simple model of layer formation which explained the observed structures, and also the effect of slag layer thickness on heat losses was examined.

However, the complexity and variety of structures found were such that a full series of direct thermal conductivity measurements was deemed impractical, and so a theoretical model to calculate the thermal conductivity of complex structures from the thermal conductivities of its components was developed. Other aspects of heat transfer both within the furnace and from the furnace interior to the water cooling were also explored.

In order to obtain a reliable value of thermal conductivity for the slag component of layer structures, a technique was developed to measure the thermal conductivity of the slag. This consisted of firstly determining a viable route for the production of homogenous samples, followed by the design, construction and refinement of an experimental measuring rig. After a large number of preliminary measurements, a series of thermal conductivity values at temperatures between 300 and 800 C were measured using operating conditions calibrated against a heat storage brick sample of known thermal conductivity. These results were used to provide the data for the theoretical thermal conductivity model, which was then applied to real structures for which thermal data was available. Comparison of the results showed good correlation.

Finally, in the appended case study, the heat loss calculation was applied for various furnace situations to identify the potential heat loss savings that could be achieved by controlling the slag layer thickness and structure, and the financial implications.

LIST OF CONTENTS.

	page no.
Title Page	i
Dedication	ii
Preface	iii
Abstract	iv
List Of Contents	v
List Of Symbols	x
1. Literature Review	
1.1. Arc Furnace Technology	
1.1.1. A Brief History	1
1.1.2. The Modern Electric Arc Furnace	3
1.1.3. Water Cooled Panels	6
1.2. Arc Furnace Studies	
1.2.1. Heat Transfer Within The EAF	12
1.2.2. Material Transfer Within The EAF	18
1.3. Slag Structures And Properties	
1.3.1. The Physical Configuration Of WCP Slag Layers	20
1.3.2. General Slag Microstructures And Chemistry	21
1.3.3. Thermal Properties Of Slags	22
1.4. Thermal Conductivity	
1.4.1. Theoretical Models Of Thermal Conductivity	24
1.4.2. Thermal Conductivity Measurement	28

2. Industry Based Studies	
2.1. Data And Sample Collection	31
2.2. Data And Sample Analysis	32
3. Theoretical Heat Transfer Studies	
3.1. The Development Of A Model For Heat Losses To Water Cooled Sidewalls	34
3.2. Heat Transfer Within The Furnace	
3.2.1. Heat transfer Characteristics Of Arcs	39
3.2.2. Radiation Networks	41
3.3. The Thermal Conductivity Of WCP Slag Coatings	
3.3.1. Assumptions And Objectives	44
3.3.2. The Computer Program	45
3.3.3. Derivation Of Data	46
4. Experimental Work	
4.1. Introduction	48
4.2. Sample Development	
4.2.1. Fused Samples	50
4.2.2. Sintered Samples	53
4.3. Development Of The Apparatus	
4.3.1. The Initial Design	57
4.3.2. The Refined Design	60
4.4. Experimental Technique	
4.4.1. General Operating Procedure	62
4.4.2. Sequence Of Experiments	63

5. Results	
5.1. Results Of Industry Based Studies	
5.1.1. Results Of Furnace Observations	68
5.1.2. Results Of Sample Examination	69
5.1.3. Results Of Water Temperature Measurements	72
5.2. Results Of Theoretical Heat Transfer Studies	73
5.3 Experimental Results	
5.3.1. Peripheral Work	74
5.3.2. The Initial Thermal Conductivity Apparatus	74
5.3.3. The Refined Apparatus	76
6. Discussion	
6.1. Experimental Work	
6.1.1. An Appraisal Of Experimental Technique	
6.1.1.1. Thermal Conductivity Measurement	80
6.1.1.2. Other Techniques	82
6.1.2. Discussion Of Results	
6.1.2.1. Thermal Conductivity Measurement	83
6.1.2.2. Other Results	84
6.1.3. Errors And Accuracy	
6.1.3.1. Thermal Conductivity Measurements	84

6.1.3.2.	Specific Density	87
6.1.3.3.	Specific Heat Capacity	88
6.2.	Water Cooled Panel Slag Layers	
6.2.1.	Formation Of Slag Layers	90
6.2.2.	Chemistry Of Slag Layers	95
6.2.3.	The Effect Of Slag Layers On Heat Losses	96
6.2.4.	Errors And Accuracy	
6.2.4.1.	Slag Cover Assessment	99
6.2.4.2.	Slag Layer Examination	100
6.2.4.3.	Heat Flux Calculations	101
6.3.	A Heat Transfer Model	
6.3.1.	Theories Of Thermal Conductivity	103
6.3.2.	Thermal Conductivities Of Complex Structures	105
6.3.3.	Heat Flux Within The Arc Furnace	106
6.3.4.	Heat Flow To The Water Cooling	
6.3.4.1.	Conditions For Testing The Model	107
6.3.4.2.	Samples Used In Testing The Model	108
6.3.4.3.	Data Used For Testing The Model	111
6.3.4.4.	Results Of Testing The Model	112
6.3.4.5.	Errors And Accuracy	114

7. Conclusions	
7.1. The Formation And Structure Of Slag Layers	115
7.2. Heat Transfer Through The Slag Layer	116
7.3. Properties Of Slags	117
7.4. Experimental Technique	118
8. Further Work	
8.1. Slag Layer Control	119
8.2. Heat Transfer Models	120
8.3. Thermal Conductivity Measurements	121
Figures	122
Tables	220
References	228
Appendices	236

LIST OF SYMBOLS

a = dimension	(m)
A = area	(m ²)
A ₁₂ = combined emissivity and view factor	(m)
b = dimension	(m)
c = dimension	(m)
C _p = specific heat capacity	(J/kg K)
F ₁₋₂ = view factor	(m ²)
h = convective heat transfer coefficient	(W/m ² K)
I = mean arc current	(A _{rms})
k = thermal conductivity	(W/m K)
\dot{m} = mass flowrate	(kg/s)
M = weight	(g)
P = pressure	(Pa)
\dot{q} = heat flow	(W)
\dot{q}^* = heat flux	(W/m ²)
R = resistance to flow	(kg/m ⁴ s)
R _{arc} = radiative power	(MW)
t = thickness	(mm)
T _m = absolute temperature	(K)
V = mean arc voltage	(V _{rms})
V = volume fraction	(m ³)
\dot{V} = volume flow rate	(m ³ /s)
x = pore diameter	(m)

x = distance from arc	(m)
x = number of surfaces	
γ = geometric pore factor	
ϵ = emissivity	
ρ = density	(kg/m ³)
σ = Boltzmann constant	(W/m ² K ⁴)
θ = temperature	(C or K)
Ω = thermal resistance	(m ² K/W)

1. LITERATURE REVIEW.

1.1 Arc Furnace Technology.

1.1.1. A Brief History.

The Heroult direct electric arc furnace was developed at the beginning of this century, and it has survived through adaptation to become a major tool of the modern steelmaker. Although it has been used outside the ferrous industry, today it is primarily a steel furnace, with some application in cast iron foundries in the United States.

The early success of the arc furnace was due to the ability to use it for melting and refining special alloy steels by providing the higher temperatures which could not be achieved by contemporary processes. Some furnaces were used as melting units only, others for the treatment of hot metal from another process. As alloy steel development continued after the Second World War, practices became centred on two types of product, namely ingot production for re-rolling coming primarily from basic-lined furnaces, and castings from acid furnaces. Electric arc steelmaking increased during the 1950s due to its advantages over the open hearth process, which included high temperatures with controlled heat input, superior quality from better mixing and slag control, greater speed, and a range of steels of any alloy content. As oxygen steelmaking replaced the open hearth, the arc furnace retained certain of the advantages, such as better temperature and slag control, but only

remained viable because the high running costs, it's main disadvantage, were reduced by the advent of the Ultra High Power furnace.

Prior to the early sixties, medium and large electric arc furnaces had power levels below 200 kVA/tonne¹ with tap-to-tap times between 4 and 6 hours, and refractory life limited by uneven and rapid sidewall erosion. In 1962 however, Schwabe² introduced the concept of a refractory erosion index, related to the electrical properties of the arc and it's distance from the sidewall. It was found that productivity could be substantially improved by increasing power input levels and implementing better arc control³ and scrap charging programs. Consequently, transformer power was increased⁴ and to cope with this water cooling replaced air cooling on the secondary circuit cables, and larger electrodes with superior properties were developed. The time utilisation principle^{1,5} led to the re-organisation of plant and practices, and tap-to-tap times were reduced to about two and a half hours. Other improvements were the triangulation of the secondary circuit⁵ to improve electrical balance, and more widespread use of direct extraction of furnace fume. The result of this progress was the retention of the special and alloy steel market and the expansion of the EAF into competition with other processes for carbon steel production.

During the 70s and 80s the growth of world steel output

has slowed considerably, with production in the West decreasing under competition from cheaper "Third World" material. Arc furnace production has continued to increase however, albeit at a modest rate, and this has been due to the evolution of the modern or third generation arc furnace.

1.1.2. The Modern Electric Arc Furnace.

The productivity of the UHP furnace of 15 years ago was still limited by the refractory life of the sidewall, and attempts to reduce erosion by the use of high currents with short arcs caused high electrode consumption. This problem was tackled by the Japanese steelmakers in the early 70s and the techniques introduced have been developed, along with other methods, to achieve better efficiency. The most successful and widely adopted of these is the use of water cooling for the sidewalls and roof of the furnace. This is discussed in more detail in the next section, but firstly the other major developments will be reviewed.

Scrap preparation has been improved to give faster meltdown with a more predictable bath analysis. Preheating of scrap using offgas or fuel burners⁶ has been used to reduce electrical energy cost and shorten melting times. Alternatives to conventional scrap have appeared, notably direct reduced iron which is being used in "Third World" countries who lack appreciable

quantities of scrap, and also in the production of low residual steels. Further increases in productivity have been achieved by continuous charging of DRI or scrap briquettes^{7,8} using thick foamy slags to protect the sidewalls from arc radiation.

The volume of oxygen blown has increased, with lancing during the meltdown period to accelerate melting and promote an early carbon boil. Melting time can also be reduced by using oxy-fuel burners to supplement the electrical input^{7,9} if it is economically viable.

New methods of regulating the arc have been tried¹⁰ and power programs have been improved to optimise refractory and electrode costs.^{11,12,13,14}

With the introduction of water cooling,⁷ more powerful arcs can be used and, with changes in power programming^{15,16}, transformer power levels have increased up to a maximum of 1 MVA/tonne.

General improvements in electrical engineering¹⁷ have also contributed to greater efficiency, and maximum demand control has improved.⁹

An alternative interpretation of the refractory erosion formula has led to new furnace designs¹⁴ incorporating such features as smaller electrode pitch diameter, inwardly inclined electrodes, and conical furnace shells.¹⁸ Such efforts have become less justifiable as the tendency towards secondary steelmaking has eliminated the refining period, restricting furnace operation to the more efficient melting mode where the

sidewalls are protected for much of the time.

Computers are increasingly becoming used in electric melting shops for direct control of the arcs,¹⁹ melting control using heat balance and refractory/electrode erosion equations,^{9,19,20} maximum demand control,¹⁹ feedback power control,^{21,22} temperature and analysis predictions and corrections,²³ and for data logging and other information tasks.

Electrode consumption has been reduced by the use of coatings, and more recently by the use of combination water cooled electrodes.^{24,25,26}

Another recent development is a sliding gate tapping system, either in the normal taphole position or at the bottom of the furnace,²⁷ which enables slag-free tapping. Bottom tapping has the added advantage of allowing greater areas of sidewall cooling.

D.C. power has been considered as an alternative to three phase A.C. throughout the history of the arc furnace, but has not been successful in large scale furnaces. However, the inherent advantages of the D.C. furnace: low electrode consumption, even refractory wear and less noise problem, have given the incentive for development,²⁸ and recent electrical engineering improvements have resulted in furnaces up to 50 tonnes capacity.²⁹

Worldwide, many furnaces have only a few of these improvements, and the range in performance has led to power classification being updated in a publication³⁰

which reviews recent developments. A more basic background to all aspects of the electric arc furnace is given by D.J.Swinden,⁸ and operating practices of a typical modern EAF plant are provided by Strohmeier.³¹

1.1.3. Water Cooled Panels.

Water cooling has been applied to the arc furnace for some years at isolated points such as the extraction elbow but, apart from a few smaller furnaces, widespread cooling of the sidewall and roof has only evolved over the last 10 to 15 years. Japan started the trend with panels set behind the refractories at the hotspots, but by 1974 one system replaced 50% of the sidewall,³² and today 75% of the sidewall and 85% of the roof may be water cooled.³³ Various designs for sidewall cooling have been developed,^{31,34,35,36,37} and with few exceptions³⁸ they can be divided into five types.

1) The box type, which consists of a welded steel box with inlet and outlet, usually having internal baffles and external studs or slag-catchers on the hot face. Systems have emerged from the U.S.S.R.,³⁹ Japan,⁴⁰ Italy⁴¹ and West Germany,⁴² the most successful being the Japanese DAIDO system^{32,34,37} and the German Korf/Fuchs type.^{33,34,35,36,43,44,45,46}

2) Tubular type panels, which consist of steel tubes arranged in either horizontal or vertical rows and connected at the ends by U pieces, through which the

water flows to present a cooling face to the furnace
35,37,47,48
interior.

3) The sandwich system, which uses smaller areas of
water cooling integrated with high thermal conductivity
refractory, but which has proved relatively
34,35,36
unpopular.

4) Water cooled blocks, which are usually cast iron with
30,34,35
internal steel cooling tubes, and are more
49,50,51
common in the U.S.A. than in Europe.

5) Copper panels, which have a higher thermal
conductivity, suffer less thermal loading and conduct
heat away more rapidly than steel panels. Most copper
panels are cast, but fabricated panels have been used
30,37
successfully.

Water cooled roofs have followed on from water cooled
sidewalls, and similar advantages, as detailed below,
have been recognised. Additionally, the structure of the
roof is stable, removing the danger of collapse present
with refractory. The roofs are normally of the box or
tube type, and they retain a refractory centre to
prevent arcing between the electrodes and the steel
30,33,34,36,44,52,53,54
panels.

One factor which has slowed the progress of all water
cooling systems is safety as, traditionally, the
combination of water and molten steel has been regarded
with apprehension. However, the safety precautions
33,34,55
recommended by WCP manufacturers (Appendix IX)
are readily implemented and there have been no major
problems recorded by users of water cooling systems.

Refractory practice for the lower sidewall has changed

since the introduction of WCPs, with high thermal conductivity bricks being used to allow conductive cooling of the sidewall down to the slagline (usually 500 mm below the panels). Magnesite-carbon bricks have been adopted by many steelmakers with carbon levels from 5 to 20% and sometimes as high as 35%. The optimum carbon level depends upon operating practice, particularly on the volume of oxygen blown.

The cost benefits of operating water cooled panels are consistently large enough to endorse their use on furnaces of all sizes and product types. The initial impetus for their use was the considerable savings possible on the refractories which were replaced, combined with reduced downtime from quicker and less frequent relines. Other benefits were recognised as more experience of WCP operation was gained.

The refractory savings are immediately apparent, although they vary with furnace size and practice for a medium or large UHP furnace, 60% brick and 50% gunning material savings are reported. A hard driven furnace may achieve an 80% brick reduction, but conversely, a less intense gunning practice could show only 20% materials savings.

Increases in steel output of between 5 and 19% have been recorded, due primarily to the increase in the number of heats per campaign, from 100/200 to

250/500. ^{36,42,43} Actual savings in downtime vary widely
^{32,36,43} from 25 to 75%. Productivity is also increased
by the ability, when water cooling is fitted, to use
^{15,32,42} higher powered arcs during melting, thus
reducing the overall tap-to-tap time. These shorter
melting times and the use of longer arcs have resulted
^{35,42} in reduced electrode consumption.

The effect of WCPs on the energy consumption of arc
³² furnaces is not clear, as some users claim a saving
while others report increases up to 20 kWh/tonne.
^{34,42,48,52}

It appears that, provided furnace practice
is modified to fully utilise the WCPs, then energy
^{30,40} consumption usually remains constant, although the
²⁸ type of system used can have a major effect.

Heat losses to the water cooled lining account for 16%
⁵⁷ of the total input, and furnace practice may be
adapted to try and reduce this, for example using foamy
slags to minimise arc radiation to the wall. An
alternative strategy is to recover the heat, either by
providing hot water or more recently by hot cooling to
produce wet steam. ⁵⁷ The latter requires some redesign
of the water supply system and improved panel quality
because of the higher temperatures and pressures
involved.

The Korf/Fuchs type panels were originally used with a
^{33,34,36} sprayed on refractory coating which was intended
to insulate the panel from electrical arcing and reduce
heat losses, although it was found in practice that the

gunning material was soon replaced with splashed-on slag and metal. Most plants now fit the panels bare, relying on the slag build-up, but unlike the gunning material the slag layer has an unknown thermal conductivity and a variable thickness.

Arc furnaces using part or whole charges of direct reduced iron have suffered more severely from sidewall refractory wear due to the longer periods without shielding from the arcs, and using WCPs has increased wall lives considerably.⁴⁶

The water cooled panels themselves have a lifespan dependent on their design, material of construction, position in the furnace and the mode of failure. Most panels fail by cracking,³⁷ the suggested causes being hot face shrinkage³⁰ and cyclic thermal shock,³⁷ and hence copper panels have longer lives as their higher thermal conductivity reduces the thermal stresses.^{30,37}

Panels may be scrapped when the slag-catchers have eroded away, but many users make minor repairs to prolong panel life.^{30,43} Failure can also occur from arcing onto the panel, careless oxygen blowing, or partial immersion in liquid steel,^{30,37,43} but these failures can be reduced or prevented by careful scrap loading and oxygen practice, and the use of a safety hole set above the tapping spout. When failure does occur, the resultant water leak may damage refractories and so water supply to the failed panel is cut off and

55

the panel is replaced at the end of the cast, or even
after several casts.³⁴

Some manufacturers have guaranteed a minimum life of
1500 casts for their panels^{43,51} and for the Korf/Fuchs
type panels this is generally exceeded by at least
1000.^{34,43} Other box panels are not as durable,^{40,47}
although this may be due to their position in the
furnace.³⁷ Cast cooling blocks have shown similar lives,
but there is considerable range from 250⁵⁰ to 5000
casts.⁵¹ Copper panels have lasted over 10,000 casts,
but this drops to 3300 for lower wall hot spot
positions.³⁷

In summary, the use of water cooling for large areas of
the furnace shell has resulted in considerable advances
in the productivity, cost-effectiveness and operating
practices of electric arc furnaces.

1.2. Arc Furnace Studies.

1.2.1. Heat Transfer Within The EAF.

The major heat source in the electric arc furnace is the arc itself, and most work concerned with heat transfer within the furnace has been based on investigating the properties of high powered arcs. Secondary heat sources consist of the chemical heat of oxidation and, when in use, oxy-fuel burners and continuously charged preheated scrap.

During the 1950s, some investigations into high powered arcs were undertaken in laboratory conditions, but it was not until the early 60s that Schwabe made the first study of industrial furnace arcs. Using high speed² photography, Schwabe examined the behaviour of the arc column during the electrical cycle and found that an arc flare existed which was directed from the arc toward the sidewall. He also considered how heat was transferred from the arc to it's surroundings, and consequently discussed the basic concepts behind power programming, including scrap shielding, sidewall hot spots (including phase imbalance) and he introduced the Refractory Erosion Index. The latter was used, with electrical characteristics, to demonstrate the advantages of using shorter arcs during flat bath periods and this represented the birth of the UHP philosophy. Also of interest was the monitoring of sidewall hot spot refractory temperature using thermocouples set in a graphite body which gave an indication of heat transfer

to the sidewall.

The hot spot phenomena was further investigated at the Swinden Laboratories of the British Steel Corporation (BSC) in the early 70s by Bowman and Fitzgerald⁵⁸ and more advanced aspects of power programming were^{11,13} developed subsequently by Bowman at Union Carbide.

The BSC work aimed to reduce hot spot wear by controlling the furnace atmosphere using various pressures, fume conditions and steam injection, but more importantly they examined the arc flame in detail. Bowman and Fitzgerald observed, as Schwabe had previously, that the arc column was not vertical but inclined toward the sidewall (supposedly due to magnetic repulsion), and together with the arc flame created the hot spot. At that time measurements indicated that 15% of the total dissipated power was from arc radiation, and between 10 and 40% from arc flame radiation. Using thermocouples embedded in the sidewall, they compared temperature profiles and heat flux variation with time at the hot and cold spots, concluding that heat flux at hot spots is approximately twice that at cold spots during melting, due to the arc flames filtering through the scrap, although once melt-out had occurred the temperature profile around the furnace became more even. In the flat bath condition, they noted the effect of slag depth on the force and directionality of the arc flame, and they confirmed the relationship between arc

voltage (i.e. arc length) and refractory wear at the sidewall. In his later papers, Bowman refined the refractory erosion index equation to allow the calculation of refractory wear, depending on the power program and type of refractory, and then included electrode wear equations to give an overall model by which to compare the effect on costs of various power programs.

An alternative application of the refractory index, based on a computer simulation,¹⁰ demonstrated how hot spots could be balanced by adjusting the electrode regulators. Also illustrated was the trade-off between refractory wear and longer melt times, with the concept of a cost optimum tap setting during refining.

The refractory index equations are only indirectly related to actual heat flux from the arc, and they represent the combined effect of radiation, convection, erosion and chemical attack. Actual heat flux measurements have been made by Sapiro et al⁵⁹ in the USSR and Montgomery⁶⁰ in Britain.

Sapiro et al inserted thermal probes into a production furnace and adjusted their readings to allow for effects such as dust screening and background radiation. Their findings were unclear, but they did show the variation of heat flux with height above the slag line and radial position, and suggested a typical heat flux level for a refractory lined furnace.

Montgomery's work, although mostly based on small

experimental furnaces, is more substantial, with the behaviour of the arc flame and the heat fluxes from the arc column and arc flame being investigated. Photographic observations on a small industrial furnace yielded some tentative relationships between the arc flame length and electrical parameters, and also clearly showed how the angle of the arc changed from inwards for short arcs to outwards for longer arcs. Experimental generation of arc flames in the laboratory led to the discovery that the directionality of the arc flame was not due, as previously thought, to the magnetic repulsion, but was effected by the electrode tip geometry and primarily by the current path in the bath. ⁶¹ Current distribution in the bath, as shown by Bowman, varies with time during the current cycle, and Montgomery has derived a locus of the arc vector over the cycle, which indicates the directionality of the arc flame. Directed arc flames were studied using photographic techniques and moveable calorimeters, from which were measured arc flame width and height and power density (heat flux) variation with distance. The results were related to the electrical parameters and empirical equations formulated. Montgomery also measured the radiation from the arc alone, and established further empirical equations to describe graphite arc (both electrodes graphite) and steel arc (graphite electrode on steel bath) radiation. He then measured the radiation

from the arc flame at various distances from the arc and at various arc powers and voltages. All the results are discussed critically with respect to industrial furnaces, as there have been no published measurements from suitable production units to confirm the conclusions, and the equations derived may be limited in application to the lower range of arc powers. However, a comparison was made between refractory wear index equations and the analysis of heat loading on the sidewall, and an energy balance for a 7 kA, 143 V a.c. arc was established.

With the introduction of water cooled panels the heat transfer to the sidewalls and roof can be measured by considering the panels as calorimeters. Some users have realised this,⁴⁸ but apart from some simple heat loss measurements,⁵² only Nanjo et al⁶² have attempted arc and arc flame heat transfer studies. They considered a theoretical heat balance for an arc and also for a water cooled sidewall block, and compared the calculated heat loss value with the actual value.

Heat transfer from the furnace interior to the water in the panels has been considered by a BSC Working Party⁶³ which investigated various aspects of different types of water cooling with the objective of recommending a system for use by BSC. A model for linear heat flow from the furnace atmosphere to the cooling water was applied to cast and fabricated panels in exposed, refractory coated and slag coated conditions. The model assumed a

furnace temperature of 1500 C and a cooling water temperature of 100 C with suitable thicknesses and thermal conductivities between, although the source of the latter values was not given. No allowance was made for the thermal barrier between the slag or refractory and the panel hot face due to a lack of data, but the heat transfer through the water boundary layer was considered, including the effect of pressure in the panel upon the required water velocity. The final conclusion of the report was that fabricated box panels using a slag coating for protection would prove to be the most economic choice. The subsequent success of the panels in operation has vindicated this choice.

64

Previous work by the author tried to relate theoretical heat transfer through the slag layer and panel wall to actual heat flows determined from water inlet and outlet temperatures. A simple linear model was used to calculate the response time from a change in steady state heat flux to outlet water temperature fluctuation, and also either thermal conductivity of the slag layer or heat loss for various conditions. It was found that over 90% of the thermal resistance between the furnace and the cooling water was due to the slag layer, and a sample of slag was obtained and its density, porosity and specific heat capacity were measured. Records of the sidewall cooling water temperatures were replotted and an average heat flux variation for the sidewall analysed, with reservations

about the validity of the results because of unknown process variables.

1.2.2. Material Transfer Within The EAF.

In the previous section the importance of the slag layer formed on the water cooled sidewall was noted and, although many EAF operators have observed slag and metal splashing,^{40,43,47,49,51} there has been little theoretical or experimental work to try and quantify this effect.

² Schwabe noted from high speed film that particles of metal and slag were projected horizontally from the arc at a velocity of approximately 13 m/s, with the bulk hitting the sidewall.⁶⁵ Piroznikov also observed the slag/metal splashing, and suggested that it was caused by slag being entrained in the arc flame at its root, a theory with which Montgomery was in agreement.⁶⁰ Bowman and Fitzgerald⁵⁸ examined the trajectory, speed, size and composition of particles ejected through the oxygen port of a 120 tonne furnace, and estimated a total material transfer to the sidewall of one third of a tonne per hour. Average particle velocity was found to be between 3 and 10 m/s, with the bulk of the particles in two size bands - less than 0.8 mm and 1.5 to 2.5 mm. The composition of the particles ranged from 100% slag to pure iron, depending on the bath conditions.

Quantitative relationships between particle characteristics and slag, bath and arc parameters have

1.3. Slag Structures And Properties.

1.3.1. The Physical Configuration Of WCP Slag Layers.

The build-up of slag on water cooled sidewalls has been observed by most electric steel producers, but there are differing reports over the thickness, integrity and benefits of this slag layer. Early total sidewall cooling systems were designed to be operated with a gunned refractory on the hot face, ^{33,34,47} which had a ³⁶ low thermal conductivity to minimise heat losses. Slag build-up occurred on top of this refractory, and although WCP manufacturers claimed that the refractory ⁴⁵ layer with the slag remained intact after 4000 casts, many users, especially those using systems without slag-catchers, have experienced peeling or breaking off of ^{49,51} the slag/gunning layer. Modern practice for steel panels is tending toward abandoning the refractory gunning application, and relying on the slag to cover the panel.

The benefits of having a slag layer on the panel hot ^{47,51} face are thought to be "protection" of the panel, ^{35,40,42} insulation against heat losses, and electrical insulation reducing the risk of arcing onto the ^{35,46} panel. Whether these are realised depends upon the nature of the slag layer, which has been variously ⁴³ described from a "hard coating" to a "filmy ³⁷ deposition", ^{40,54} built up by "splashing", ⁵¹ "meltdown ^{34,36,49} spatter", or simply the "self-coating effect".

The metallic content of the slag layer has been ³⁴ considered by very few WCP users, although it became

more prominent with the development of water cooled roofs, when electrical arcing occurred through the slag/metal accretion.^{33,36}

The thickness of the slag layer has been recorded by some authors, but the ranges quoted vary from 0.5 - 1.5 cm,³⁹ through 1 - 5 cm,⁴⁷ up to 3 - 12 cm,⁵¹ or a combined refractory and slag thickness of 2 - 4 cm.^{34,54}

This suggests that the thickness of the slag varies immensely, and may depend on particular furnace or practice parameters.

1.3.2. General Slag Microstructures And Chemistry.

Many types of steel are made in the basic arc furnace (acid furnaces are now rare), and the slag practices used can be categorised as either single or double slag practice. The former uses one basic oxidising slag, and the melt is usually either a high tonnage non-special steel or destined for a secondary steelmaking process. Double slag practice is used for quality steels which are refined in the arc furnace, with the first slag being removed and replaced with a highly basic deoxidising slag.⁸

The desired slag composition is determined using thermodynamic methods, and the chemical behaviour at high temperatures is described in terms of basicity ratios and ionic theory. The phases which actually exist in the slag during the oxidation period have been

investigated, but the only work concerned with actual microstructures appears to be limited to BF and LD slags, with respect to their use as a secondary product. The microstructure of a slag can contain many different phases due to its complex chemical nature. EAF slags will often contain appreciable amounts of CaO , SiO_2 , FeO_x , Al_2O_3 , MnO , MgO , and Cr_2O_3 , and this makes it difficult to relate them to phase diagrams. Some slags may approximate to a four or five oxide quasiternary system, but even then the equilibrium data is of little use when the oxygen activity and the slag composition are constantly changing, as they do during the furnace cycle.

Hence it can be seen that the slag adhering to WCPs can have a range of compositions, even within the same furnace, and the microstructure will differ from bath samples and can only be determined by direct sampling from the panel face. Identifying the phases present in the microstructure can be done optically, spectroscopically, by x-ray diffraction, or from the composition determined by electron microprobe.

1.3.3. Thermal Properties Of Slags.

There is little published thermal data for slags, probably because they are not constructional or scientific materials. The variation of specific heat capacity with temperature for a slag of given chemical analysis is included in Chester's data, and a value of

specific heat capacity was obtained for an arc furnace slag by the author in earlier work.⁶⁴ Detailed measurement of thermal conductivity has been limited to CaF₂-based electroslag refining (ESR) slags⁷³ and ironmaking slags,⁷⁴ although an unsubstantiated value⁶³ for an EAF slag has been quoted in a BSC report.⁶³ Nagata et al⁷⁴ used the hot wire method for measuring the thermal conductivities of a range of synthetic slags with a single industrial BF slag for comparison, the measurements being made at 50 degree intervals between 100 and 1500 C on both heating and cooling cycles. None of the compositions used correlate closely with the highly basic EAF slags, but nevertheless the range of conductivities and their behaviour with respect to temperature are of interest. Generally, the values obtained for synthetic CaO/SiO₂/Al₂O₃ slags increased from approximately 1 W/mK at room temperature up to 2 W/mK before dropping rapidly at the fusion temperature. A synthetic slag containing 19% CaO, 40% SiO₂, 27% FeO and 12% Al₂O₃ gave a constant value of approximately 1.8 W/mK at all temperatures between 100 and 1000 C, and the compositionally more complex industrial slag increased from approximately 2 to 2.5 W/mK between 500 and 1200 C. This gradual increase may not be a real effect, considering the accuracy of the measurement technique.

1.4. Thermal Conductivity.

1.4.1. Theoretical Models Of Thermal Conductivity.

The conduction of heat in solids can occur by two processes of energy transfer - coupling between lattice vibrations or electron movement and collisions with atoms. In non-metals, electrons are not free to move through the structure and heat is transferred by lattice vibrations alone. The quanta of lattice vibrational energy are called phonons by analogy with photons, the quanta of electromagnetic radiation. Thermal conductivity of non-metals is therefore related to the rate of phonon transfer through the lattice, which is affected by scattering due to interaction or barriers such as point defects, dislocations and grain boundaries. A mean free path concept can be applied, and by analogy with the kinetic theory of gases, thermal conductivity is directly related to the phonon velocity, specific heat capacity and the mean free path. ^{75,76}

⁷⁷ Hence thermal conductivity is lowered by impurities or mixed isotopes and other lattice imperfections, and in some circumstances is limited by the crystallite size. Glassy materials have a random lattice with a very small mean free path, and tend to have a low thermal conductivity proportional to specific heat capacity, although radiative heat transfer occurs through translucent glasses at high temperatures. ⁷⁶

Most materials contain porosity or consist of more than one phase, and their thermal conductivity must be

evaluated on a microstructural scale , rather than on an atomic lattice scale. Early work in this field was concerned with ceramic refractories and insulators and was based on Maxwell's relation for conductors and resistors. Eucken proposed the following equation for a continuous primary phase containing randomly distributed spherical inclusions/pores -

$$k_s = k_c \frac{1 + (2 V_d A)}{1 - (V_d A)} \quad (1)$$

$$\text{where } A = \frac{1 - Q}{2Q + 1} \quad Q = \frac{k_c}{k_d}$$

- k_s = thermal conductivity of the composite structure
- k_c = thermal conductivity of the continuous phase
- k_d = thermal conductivity of the disperse phase
- V_d = volume fraction of the disperse phase

Note that the value of k_s is sensitive to which phase is continuous and which is dispersed. Russell's equation was derived for porous insulators, again assuming random unisize porosity -

$$k_s = k_c \frac{V_d^{2/3} + Q (1 - V_d^{2/3})}{V_d^{2/3} - V_d + Q (1 - V_d^{2/3} + V_d)} \quad (2)$$

Russell attempted to include the effect of radiation across the pores by defining the conductivity of the pore in terms of the gas conductivity and a radiation component -

$$k_p = k_d + k_r \quad (3)$$

where k_p = effective pore conductivity

$$k_r = 4 \sigma A_{12} T_m^3 x$$

σ = Boltzmann constant

A_{12} = combined emissivity and view factor

T_m = absolute temperature

x = pore diameter

The resultant value of k_p then replaces k_d in equation (2). Loeb⁸⁰ tried to allow for the anisotropic nature of porosity by including more parameters of the porosity distribution, giving the following equation -

$$k_s = k_c (1 - V_{dC}) + \frac{V_{dC}}{\frac{V_{dL} k_c + (1 - V_{dL})}{4 \epsilon \gamma x T_m^3}} \quad (4)$$

where V_{dC} = cross sectional pore fraction
 V_{dL} = longitudinal pore fraction
 ϵ = emissivity
 δ = geometrical pore factor

This equation assumes a large differential between the thermal conductivities of the solid and the gaseous phases, and at temperatures below 500 C when radiation is negligible, it simplifies to -

$$k_s = k_c (1 - V_{dC}) \quad (5)$$

Experimental work by Franci and Kingery⁸¹ showed that the Loeb equation was superior to both Russell's and Eucken's for anisotropic porosity measured in two dimensions, although for isotropic pores the advantage was less marked. Later work by Kingery⁷⁷ examined multiphase systems and confirmed Eucken's equation for a series of ceramics, correcting for porosity using equation (5). The importance of pore size regarding radiation heat transfer was noted by Kingery,⁶⁶ but was more clearly demonstrated by Cooper⁸² with respect to insulating powders and fibres where the low conductivity phase is continuous. At lower temperatures however, the validity of equation (5) was questioned by Rhee,⁸³ who⁸⁴ concluded that the equation of Aivazov and Domashnev was the best of those examined in correlating variable

porosity with thermal conductivity. Their equation is of the form -

$$k_s = k_c \frac{1 - V_d}{1 + n \frac{V_d^2}{d}} \quad (6)$$

where n is a positive number or zero and is a characteristic of the material. Joblonski⁸⁵ noted that all the porosity equations apply only to values measured at atmospheric pressure. The conduction through the gas varies with pressure, causing the overall thermal conductivity to increase from a base level at vacuum up to a level representing the sum of two components, the solid and the gas. Another limitation of these theories is that they all disregard convection by considering only small pores less than a critical diameter (between 3 mm⁸² and 5 mm⁷⁹) with a temperature gradient across them no greater than 100 C.

1.4.2. Thermal Conductivity Measurement.

A good review of methods for measuring thermal conductivity has been made fairly recently by Willshee.⁸⁶ The BS 1902 apparatus⁸⁷ developed by Clements and Vyse⁸⁸ and the similar ASTM method are described after a brief outline of earlier techniques. Also included is a description of the split column

apparatus and a discussion of transient methods such as the heat pulse method and the hot wire test, which is reviewed in more depth by Davis and Downs.⁸⁹ Other means of measurement, not reported by Willshee,⁹⁰ include a transient numerically solved method⁹¹ and a rapid differential scanning technique.⁹¹ Improved versions of the hot wire test and the split column method have been developed by Morrow⁹² and Sutton⁹³ respectively, and the heat pulse technique has evolved into the laser flash method.⁹⁴

The BS and ASTM methods both measure the conductivity of a relatively large brick or test panel. The brick is arranged with a heat source at one face and a calorimeter opposite, possibly with lateral heating to promote unidirectional heat flow. Thermocouples are situated at hot and cold faces allowing the heat flow and temperature gradient to be measured at steady state, and the thermal conductivity can be determined from the steady state conduction equation -

$$k = \frac{q \cdot t}{A(\theta_1 - \theta_2)} \quad (7)$$

where k = thermal conductivity

q = heat flow

t = thickness

A = area

θ = hot face temperature
 θ_1
 θ = cold face temperature
 θ_2

The split column method is similar in concept, but the sample is cylindrical and is sandwiched between material of known thermal conductivity. Its advantage is the more specific temperature at which conductivity is measured, but radial heat losses cause large errors when the sample has a low thermal conductivity. The hot wire test is a transient method which can also measure thermal conductivity at specific temperatures, and it relies on the change in temperature of a heated wire embedded in a solid cylinder. The mathematics of calculating the result are quite complex, but the final value represents an average conductivity over two dimensions, which can be a considerable disadvantage when the material is anisotropic. The other main transient method is the laser flash or heat pulse technique, where a small disc is rapidly heated on one side by a laser pulse and the temperature rise of the cold face is monitored. Early versions using electron guns could not be used for many ceramics because the required specimen thickness for the low conductivity range was less than the grain size. Using a laser flash has allowed the thickness of the samples to increase to 2 mm, but there is still considerable variance for results obtained from refractories and similar materials.

2. INDUSTRY BASED STUDIES.

2.1. Data And Sample Selection.

Previous work concerned with the effect of water cooled sidewalls on arc furnace heat losses⁶⁴ had identified the slag accretion formed on the water cooled panels as being critical, and hence the first stage of the research program was direct observation of the phenomena. To support the subjective visual impressions and photographic records, samples of slag and related panel operating data were obtained to allow "post mortem" study of the slag build-up mechanism. The number of variables was limited by restricting the investigation to the sidewalls only of a single furnace, Stocksbridge's 80 tonne "B" unit⁹⁵ fitted with Korf/Fuchs type sidewall panels and either a refractory or tubular type water cooled roof. The layout of the furnace is shown in figure 1, with details of the panel configuration in figure 2, showing the exposed area of each panel.

The method and sequence of information collection and obtaining relevant samples was developed during the early visits, and the procedure used is given in Appendix I. Eight series of data/samples were collected together with numerous observation notes and photographs, although the latter were poor because of the difficult conditions.

2.2. Data And Sample Analysis.

All of the time and temperature data was transferred onto computer files for subsequent conversion to heat flux versus time graphs or tables. This conversion was achieved by a FORTRAN program which determined the heat flux to each panel (see Appendix II) utilising calibration data and flow resistance factors (see Appendix III). The resultant datafiles were then tabulated or plotted using FORTRAN programs incorporating CALCOMP subroutines (see Appendix IV).

The samples were assessed visually before being sectioned and the macrostructural features recorded on a standard proforma which defined the morphology as follows -

i) thickness of the layer and any sublayers of high porosity or metal content, which were identified by their distance from the cold face.

ii) percentage of each phase, with the metal divided into three distinct morphological types and the porosity into three grades of size, the distribution of each being defined using the cold face as the datum, as in i).

Some of the macrostructures were recorded photographically also, and parts of the sample mounted for microscopical examination. Considerable difficulty was encountered in mounting and polishing a material of mixed slag, metal and high porosity, even using low viscosity resins with evacuation and reimpregnation

techniques, and the polished finish was poor and susceptible to staining. Microstructural examination was possible however, including phase identification using a scanning electron microscope with an x-ray analysis facility.

3. THEORETICAL HEAT TRANSFER STUDIES.

3.1. The Development Of A Model For Heat Losses To Water Cooled Sidewalls.

This work is concerned with the heat losses from an arc furnace to its water cooled sidewall and roof, and a model which describes the mechanisms involved allows the prediction of heat losses for given situations. This is useful in assessing the likely effect of process variables, hence in identifying optimum conditions and in the design of water cooling systems or furnaces. Because the thermal characteristics and behaviour of electric arc furnaces are very complex it is necessary to make simplifications and assumptions when first establishing a heat transfer model.

Heat transfer in the arc furnace is not easily predictable due to the cyclic nature of its operation and the instability of the arc heat source, but approximate steady-state occurs when stable arcs are maintaining a flat bath at a constant temperature. Under these conditions, heat lost from the furnace interior to the water cooling will be constant provided the thermal resistances between the two are also constant. For a small area of the sidewall the heat flow from the hot face of the slag to the bulk cooling water can be considered linear, as shown in figure 4. The parameters which control the heat transfer at each stage and the thermal resistances are as follows -

a) Heat flux from the furnace interior to the slag hot face.

Heat transfer is by a combination of radiation from the arc, radiation and convection from the arc flame, and background radiation from the bath surface, lower sidewall and other water cooled or refractory surfaces. In section 3.2. the application of Montgomery's empirical equations for arcs is discussed and a resistance network for background radiation is developed.

b) Heat flux through the slag layer.

The mechanism for transfer is primarily conduction, but will depend on the amount and size of porosity in the slag. The thermal resistance is the thickness divided by the thermal conductivity. The thickness can vary immensely, but during steady-state conditions it is proportional to the heat flux and will be constant at any specific position (see section 6.2.1.). The thermal conductivity depends upon the structure of the slag layer, and is discussed in detail in section 3.3.

c) Heat flux across the slag/panel interface.

For the common panel designs this interface is never planar, and hence the heat flow is not linear. The box type panels approximate to a planar interface however, and when the slag is in intimate contact with the oxidized panel surface the increased surface area effect of the slag catchers is assumed to exactly counteract the interface resistance, i.e. $\theta_2 = \theta_3$. Where a

distinct gap exists the resistance is equal to the gap width divided by the thermal conductivity of the ambient gas, provided that convection cannot take place and radiation is negligible. Natural convection in air requires an interplanar dimension greater than approximately 5 mm, and the contribution of radiation across a gap is insignificant below 500 C.

d) Heat flux through the panel wall.

The mode of heat transfer is straightforward conduction, with the thermal resistance equal to the wall thickness divided by the thermal conductivity of the material of construction.

e) Heat flux from the panel wall to the bulk cooling water.

Heat transfer is by straightforward forced convection, with the thermal resistance equal to the inverse of the heat transfer coefficient.

The overall equation for heat transfer from the hot face of the slag to the cooling water is therefore -

$$q'' = \frac{\theta_1 - \theta_5}{\frac{1}{h_1} + \frac{1}{h_2} + \frac{1}{h_3} + \frac{1}{h_4}} \quad (12)$$

where

q'' = heat flux per unit area

θ_1 = slag hot face temperature

- θ = bulk cooling water temperature
- λ_5 = thermal resistance of slag layer
- λ_1 = thermal resistance of slag/panel interface
- λ_2 = thermal resistance of panel wall
- λ_3 = thermal resistance of panel/cooling water interface

Note: $\lambda_4 = \frac{1}{h}$ (13)

where h = convective heat transfer coefficient

To apply the above linear model to an actual furnace fitted with Korf/Fuchs type panels, the area being considered is taken as a single sidewall panel and the following assumptions made -

- i) edge effects due to panel/panel joins, panel/roof joins and conduction from the lower sidewall are minimal in comparison to the rate of heat flow from the furnace interior.
- ii) heat flux from the furnace interior is uniform over the panel area.
- iii) slag thickness, structure, adherence to the panel and hot face temperature are uniform over the panel area at any one instant.
- iv) the panel wall, because of it's high thermal

conductivity, is considered to be of uniform thickness and the presence of slag catchers and joins with internal baffles is ignored.

v) perfect mixing occurs in the bulk cooling water.

The validity of this model is tested in section 6. using appropriate values obtained from a real furnace situation.

3.2. Heat Transfer Within The Furnace.

3.2.1. Heat Transfer Characteristics Of Arcs.

The arcs are the main heat input during the flat bath period, although there may be significant contributions from exothermic reactions in the bath and from oxygen blowing or oxy-fuel burners when used. Montgomery⁶⁰ discusses all aspects of arc and arc flame heat transfer, and uses regression analysis on the results obtained from both observation of a production furnace and the study of laboratory generated arcs to propose empirical equations describing various properties of the arc and arc flame.

The geometry of arc flames was studied using photographic and cinematic techniques, and equations were derived for the variation of height and width along the length of the flame. The frequency distribution of the direction of the arc flame was also measured for a single phase system with a side bath connection, and this clearly showed how the current path dictates the directionality of the flame. Moveable calorimeters were used to measure the heat flux or "power density" associated with the arc flame, and the following equation was developed -

$$\dot{q}'' = 1.33 I (V - 105) / (e^{3.3x} - 1) \quad (14)$$

where \dot{q}'' = heat flux in kW m⁻²

I = mean arc current (see footnote p43)

V = mean arc voltage (see footnote p43)

x = distance from arc to calorimeter in m

Actual measured heat fluxes varied from around 10 kW m^{-2} at a distance of 1.23 m from the arc to 500 kW m^{-2} at 0.23 m. Although background radiation was accounted for, these values and the equation refer to a combination of convection and radiation from the arc flame and radiation from the arc. To measure arc radiation alone, a collimating apparatus was used with a thermopile detector, and an equation for graphite/steel arc radiation was derived -

$$R_{\text{arc}} = 4.81 \times 10^{-4} I (V - 80) \quad (15)$$

where R_{arc} = radiation from arc in MW

A similar apparatus was used to measure radiation from the arc flame, and the specific radiance of the flame (kW m^{-3}) was calculated for various conditions using the flame geometry equations previously obtained.

In his discussion, Montgomery used all of these equations to calculate the anticipated heat loading at the hot spot of a furnace with similar characteristics to the one used in the laboratory work, and arrived at a figure of 65 kW m^{-2} . This is superimposed on the background radiation in the furnace, and would be the heat flux measured by a calorimeter in a refractory wall. The only measurements known at that time,

-2

typically 115 kW m^{-2} , were for a larger furnace with different arc powers and dimensions and unknown flame lengths, and the equations could not be extrapolated to those conditions. Unfortunately, this also applies to this work, as flame lengths were not measured and the furnace involved is considerably larger in all respects.

However, although the application of Montgomery's equations is currently very limited, in the future it may be possible to predict the heat flux from the arcs and flames to any position around the sidewall, as more data from industrial furnaces becomes available and the equations are refined. This will enable the steady state conditions prevailing during the flat bath period to be defined from the furnace electrical input and the radiation network for any given furnace.

3.2.2. Radiation Networks.

A network for radiation and re-radiation between the bath, walls and roof is important in evaluating the level of background radiation to the panels during the flat bath period. It is also essential when considering the unsteady-state conditions at other times during the furnace cycle, particularly when the electrodes are raised to break the arc. The calculation of heat flux to one surface in an enclosure is well established ⁹⁶ using simultaneous equations. The data required is the

emissivity, reflectivity, temperature and area of each surface within the enclosure, and the view factors between surfaces. The interior of the arc furnace can be considered as four surfaces; the roof, the water cooled sidewall, the refractory lower sidewall and the bath.

The bath will generally be considered as the heat source, and its surface temperature and emissivity can be readily estimated ^{97,98,99,100} for both clear metal and slag cover.

The refractory lower sidewall can be considered as a re-radiator with an emissivity of 0 (reflectivity of 1).⁹⁶

The water cooled sidewall is the heat sink, and its surface temperature will be equal to the slag fusion temperature for steady state conditions. The emissivity will be that of the molten slag, the same as for a slag covered bath.

The roof can be either refractory (re-radiator as lower sidewall) or water cooled (heat sink as upper sidewall), and when removed the opening will act as a low temperature black surface.

All areas are easily derived from the furnace dimensions, and the view factors are calculated in Appendix V, including those for an empty furnace where the bath surface is replaced by the hearth.

Generally, radiation networks can be usefully solved for situations where reliable values for surface temperatures and emissivities are available, once the view factors and areas have been determined for the

furnace. The effect of the arcs on this network is difficult to assess, but the simplest method is to assume that they maintain the bath and refractory temperatures and that arc and background heat fluxes to the water cooled sidewall are additive.

Definition of Montgomery's electrical parameters -

Mean arc current for the period of the trial was obtained by electronically integrating a DC signal proportional to rms arc current, and dividing by the time of the trial.

Similarly, the mean arc power over a period of time was determined by integrating the instantaneous product of the arc current and voltage signals.

The mean arc voltage was then determined by dividing the mean arc power by the mean arc current.

3.3. The Thermal Conductivity Of WCP Slag Coatings.

3.3.1. Assumptions And Objectives.

One item of information that is vital for any calculation of heat losses to water cooled panels is the thermal conductivity of the slag layer on the panel face. These slag layers can vary considerably in their structure, particularly in the proportions of metal and porosity present (see section 5.), and this will affect the thermal conductivity. A vast number of thermal conductivity measurements would be needed to give sufficient data to cover all possible structures, and hence a model which could predict the conductivity of any combination of slag, metal and porosity would be very useful. The available theories apply only to two phase systems (see section 1.4.), and to overcome this certain assumptions are made -

i) the slag component is considered as effectively amorphous, ignoring variations in the non-metallic microstructure, and this is justified by the large difference in conductivities of the three components (at least an order of magnitude between each).

ii) for a dual phase solid containing porosity, the conductivity of the solid (k) is considered as that of an equivalent non-porous solid with the same proportion of phases. This involves a two stage calculation or the combination of two equations.

Because of the necessary repetition of calculations and the choice of available equations, it was decided to

develop the model as a computer program. This program had to be capable of calculating the conductivities of any combination of slag, metal and gas over a range of temperatures and using any theory or combination of theories to allow the following objectives to be met -

a) Comparison and evaluation of the various equations and combinations of equations.

b) Illustration of the effect of different variables on the thermal conductivity behaviour.

c) Prediction of the conductivities of specific structures for use in the furnace thermal model.

3.3.2. The Computer Program.

The equations incorporated into the program are Eucken's, Russell's, Russell's with a radiation allowance, Loeb's, and the simplified version of Loeb's. For non-porous slag/metal mixtures only the first two equations are applicable, whereas for porous slag or porous metal layers all five can be used. A three phase system will use one of the first two equations combined with any of the five. The forms of the equations used are as given on pages 25 to 27.

The program (see Appendix VI) consists of a short main program and 14 subroutines, with raw data being read from a data file at the start of the program or requested during running. The conductivity is calculated.

at 100 degree intervals from 0 to 1600 degrees C, and the output can be tabulated or graphical with various display options.

3.3.3. Derivation Of Data.

The information in the data file consists of the 17 temperatures from 0 to 1600 degrees C, and values of gas, metal and slag thermal conductivity and pore surface emissivity at each temperature. These values were estimated from data in the literature

97 98 99 100

102

and those for the slag revised when the experimental results (see section 5.3.) became available.

The composition of the gas in the pores is not known, but it is probably a mixture of nitrogen, oxygen, and carbon monoxide or dioxide, and values of thermal conductivity were estimated on this basis (Figure 6).

The metal in the system is an iron-carbon alloy of variable composition, which may include certain other alloying elements depending on the type of steels being produced. The conductivity curve for iron decreases at lower temperatures as the alloy content increases, and the slag layer metal has been assumed equivalent to a 1% carbon steel or a low alloy steel (Figure 7).

At the outset of this work, no values of slag thermal conductivity were found in the literature, and values were estimated by consideration of glasses and ceramic materials. Subsequently, data has been published for ESR slags by Taylor and Mills⁷³ and for ironmaking slags by

Nagata et al and, together with the results obtained from an EAF steelmaking slag (see section 5.), has formed the basis of revised values (Figure 8). Note that the gradient and exact position of the sudden drop in conductivity just below the fusion temperature are estimates, as are values above the fusion temperature.

The pore surface emissivity was estimated at a value within the range of various surfaces including those which might exist at a pore, such as oxidised iron or steel, or slags ¹⁰³. Other, similar materials considered were a range of glasses and ceramics (Figure 9).

The manual input data consists of the structural variables, rather than the physical properties, with volume fractions and pore size and shape being either specified or varied across a set range.

4. EXPERIMENTAL WORK.

4.1. Introduction.

Having identified conduction through the slag as the most critical factor in heat losses to the water cooling, it was decided in the absence of any published data to measure the thermal conductivity of the slag. Initially it was hoped that slags of various compositions would be measured, possibly with a metallic phase introduced to test the theoretical models, and even sections of material taken from a furnace sidewall. However, difficulties experienced with the samples, similar to those encountered by Taylor and Mills,⁷³ and with the apparatus restricted the scope of the work.

The choice of measurement method was based on the principle of simulating as closely as possible the conditions to which the results would be applied, i.e. one-dimensional heat flow with a large thermal gradient, and on practical considerations.

The hot wire method was rejected because it measures over two dimensions with fairly shallow thermal gradients, and difficulties were anticipated in the production of a reliable sample. The split column method is not suitable for low conductivity materials because of the high radial heat losses relative to the linear conductive heat flow. The heat pulse method can be used for low conductivity materials provided a high energy laser heat source is used and the sample is thin enough, but results for multiphase non-metals have been

unreliable due to the crystallite size approaching the thickness of the sample. The standard refractory brick methods were therefore the most attractive, being designed for measuring low conductivities with a large unidirectional thermal gradient. However, both the ASTM C201-47 and BS 1902 methods are designed to take standard bricks as the sample, using a panel of bricks either 9 inches square (BS) or 13.5 by 18 inches (ASTM). The production of slag bricks in the required quantities was envisaged as time-consuming and not practicable. The solution was to design and build a smaller apparatus based on the same principle as the standard methods, but using the simpler sample geometry of a circular disc.

4.2. Sample Development.

The possibility of using samples taken directly from the panel wall was considered first, but although a suitable core drill facility existed, the brittleness of the slag precluded any precise cutting operation. The samples therefore had to be formed to the required shape and be homogeneous, repeatable and representative of the slag component of the actual layers.

The raw material for producing thermal conductivity samples was obtained from a large piece of slag taken from a water cooled panel, which was initially broken up in a jaw crusher and the metallic layers removed. Following this, it was ground in a ball mill for 16 hours, and the powder was sieved to remove particles greater than 150 mesh, and then magnetically separated to remove high metallic content particles. Chemical analysis samples were taken before and after the comminution process to note any change in composition.

4.2.1. Fused Samples.

The initial approach to producing a solid thermal conductivity sample was to melt the slag powder and cast it into a shape suitable for the chosen method of measurement. A possible alternative was an enamelling technique, but when a sample of the powder was melted using an oxy-acetylene flame, the force of the flame tended to blow away both solid and liquid slag. Heating the slag in a plumbago crucible with the oxy-acetylene flame failed to achieve sufficient temperature to fuse

the slag. The plumbago crucible was then transferred into a H.F. induction furnace on a graphite receptor, and melting was achieved briefly before a violent reaction occurred between the slag and the crucible, causing gas evolution and resulting in the slag frothing out of the crucible and immediately solidifying.

Realising that the slag was too reactive to be contained in a graphite or plumbago crucible, it was decided to try fusing in situ, placing a 100 mm square, steel tray full of slag powder into a controlled atmosphere furnace set at 1350 C, under argon, for 40 minutes. The temperature of 1350 C was thought to be within the fusion range of the slag, a sample of which had been studied by Firth¹⁰⁴ to determine its fusion characteristics. Actual furnace temperature in the region of the sample was monitored using a supplementary thermocouple inserted through a port in the furnace door. The slag melted successfully but attacked the steel tray, dissolving the full steel thickness at one edge and escaping onto the furnace floor. It was then observed that the slag was totally molten at 1350 C, remained so down to 1250 C, and was still a viscous liquid below 1200 C. The reaction interface between the slag and the steel was examined, and both planar dissolution and intergranular attack were evident.

The highly reactive nature of the slag at high temperatures had to be overcome by finding a suitable

containing material, and a magnesite crucible was used in the following trial. The slag was melted at 1350 C to allow some superheating, and was to be cast into a cold metal tray. However, around half of the molten slag penetrated the wall of the crucible, and that which remained solidified before it could be cast. Although the magnesite was optically darker where penetration had occurred, microscopic examination failed to reveal any signs of reaction, and the slag appeared to have physically seeped through the open porosity of the refractory.

The procedure was then repeated using a magnesite crucible which had been lined with a silicon carbide slurry and baked, and this contained the molten slag and allowed it to be cast. The cast slag failed to fill the steel tray because of a considerable increase in viscosity as it chilled. On cold examination it was found that the slag contained a highly porous, glassy chill layer, a central plug of unfused powder, and a medallion of metal. The chilled slag had a microstructure of few fine dendrites in a glassy matrix, and the metal showed a ferrite/pearlite structure with areas of very fine pearlite surrounding graphite flakes, indicating a high carbon content.

The experiment was repeated, preheating the steel tray before casting and replacing the argon atmosphere with air to give a higher oxygen potential, in an attempt to prevent metal formation in the slag. Although the slag

cast evenly, it still contained a large metallic lump, and extensive gas evolution had caused gross irregular porosity. Because of this chemical activity and unpredictability of the slag in the molten state, it was decided to attempt to produce a thermal conductivity sample by the more controllable sintering process.

4.2.2. Sintered Samples.

Before sintering the slag, some knowledge of the fusion temperature range was required, so that the temperature used would allow partial fusion to take place. Samples of the slag powder were melted on a hot stage microscope under air and argon, and the pattern of melting observed. The results of several tests, summarised below, led to a sinter temperature of 1190 C being chosen.

1070 - 1090 C	first liquid
1160 - 1180 C	bulk softening
1200 - 1220 C	mostly liquid

A trial run was carried out with powder in a steel tray under argon, which was placed in the furnace and inspected after 10 minutes and 70 minutes. The slag sintered successfully, shrinking away from the tray sides, and there was no visible change between 10 and 70 minutes. The sinter was fairly strong with fine even

porosity, but was appreciably cracked, presumably from thermal stresses during heating or cooling.

A mould was made which would produce, from 100 g of slag powder, green sinters of 78 mm diameter and approximately 7 mm thick. The diameter used was determined by the size of steel stock available for making the mould, and the thickness was chosen by considering ease of handling, the degree of compaction and the need to minimise lateral heat loss during conductivity measurement. The slag was mixed with binder and ethyl alcohol and allowed to dry until reaching the texture of paste, when it was transferred to the mould and pressed with a unidirectional load of approximately 10 tonnes. The resulting compacts were then removed and allowed to air dry for 24 hours before being sintered.

Initially, three slag compacts were produced, containing 1%, 3% and 5% of ammonium chloride, the chosen binder. All had adequate green strength, and were sintered at 1190 C under argon for 15 minutes and then air cooled, apart from the 5% sample which was allowed to slow cool in the furnace. The 1% sample sintered well, with only hairline cracking appearing during cooling, and the microstructure showed very fine porosity with few larger pores and some fine cracks. The 3% sample was badly split, with a dome formed by a thin layer on the top surface rising and cracking due to rapid sintering and shrinkage at the edge of the compact. Microstructural examination revealed severe horizontal cracking. The 5%

slow cooled sample also had a dome, but had fewer internal cracks, although there was extensive gross porosity present. As a result of this trial, all subsequent compacts were made using 1% ammonium chloride binder.

The second sintering trial was an attempt to remove all cracking from the final structure by gentler thermal treatment, and to reduce the amount of porosity by increasing the temperature. One compact was slow heated under air to 1200 C and then slow cooled, and a second was treated similarly under argon. Both sinters were badly split and had increased in size to 84 mm and 82 mm diameter respectively, probably due to some transformation or reaction. It was decided to abandon extended heat treatments in favour of a rapid sinter followed by a fairly slow cool in an insulated box.

A further six compacts were prepared and then sintered in turn, under argon, in an attempt to produce a viable sample for measurement. The first was sintered on a steel plate for 10 minutes at 1200 C but fused to the plate and was broken when being dislodged. The furnace temperature was reduced to 1190 C to prevent this and the two subsequent compacts sintered for 10 and 8 minutes respectively. Both were whole and "solid", but a considerable concavity was noticed, presumably due to greater heat flux to the top surface increasing the degree of sintering. To prevent this, the remaining

three samples were sandwiched between two steel plates during sintering, and apart from a slight concavity on the fifth sample, this was successful. The fourth compact was sintered for 5 minutes and suffered only slight radial cracking at it's edge, and the fifth compact had a more severe edge split after a 6 minute sintering time. The final sample was sintered for 15 minutes and was flat and solid, but unfortunately cracked into two during cooling. It was noted from this trial that the diameter after sintering was dependant on the time spent in the furnace (see Figure 10), suggesting a minimum time of 10 minutes to give a reasonable degree of sintering and densification.

As regular sample production began, a further refinement of ceramic fibre packing around the compact was introduced to reduce the occurrence of edge cracking, and 12 minutes at 1190 C became the standard conditions. Even then, only 20% of the compacts produced made successful samples due to green breakages and cracking during or after sintering.

4.3. Development Of The Apparatus.

4.3.1. The Initial Design.

The basic design for the apparatus followed the BS or ASTM method of using a water cooled calorimeter and an electrical resistance heat source to promote and measure a linear heat flow through the material (see Figure 11). The heat source consisted of four 2.5 ohm elements connected in series and supplied by a variable mains transformer, with a silicon carbide radiation tile below to give a more even radiation source to the sample's upper face. A type S control thermocouple entered the heating element chamber from above and was connected to the transformer control unit. The sample rested on the calorimeter, with three type S thermocouples in contact with it's upper face and three in contact with the lower face to enable measurement of the thermal gradient. The calorimeter was of welded mild steel construction and was designed to cope with the maximum output of the heating elements without danger of nucleate boiling (see Figure 12). The dimensions of the inner and outer chambers, the baffles, and the water connections were all designed to give similar water velocities in the two chambers at flow rates giving equal heat extraction rates per unit area. The water supply was from a header tank via plastic tubing secured with clips, with flow controlled and measured by needle valve rotameters on the outlet side and discharge to an open drain. Just below the calorimeter inlet and outlet connections were

fittings with type T thermocouples (guard calorimeter inlet and outlet) or platinum resistance thermometers (inner calorimeter inlet and outlet) for measuring water temperature rise. The whole apparatus was enclosed and supported by a structure of alumina insulating bricks, with additional insulating wool and paper where necessary. During operation a metal cage prevented accidental burning or electrocution. All the thermocouples and the PRTs (platinum resistance thermometers) were connected to a Solartron data-logger which initially gave a printed output and a digital display.

The apparatus was tested for watertightness and proper operation of the thermocouples and PRTs before being assembled around a slag sample for a trial run. The increase in water temperature was extremely small, and it was noticed that the inner and outer flows appeared to be very similar, although the rotameter readings indicated a factor of four difference. To check this, the rotameters were calibrated by measuring actual volumes passing through in a set time. The inner rotameter was found to be in excess of the indicated value, and a smaller rotameter was fitted. The flowrate ranges of the rotameters used were approximately 0 to 2.5 l/min for the inner calorimeter and 0 to 10 l/min for the outer. The practice of calibrating rotameters was continued with the refined design, when even smaller

rotameters were used.

The trial run was repeated, with the temperature being increased in steps while monitoring the sample surface temperatures to determine the time taken to reach steady state. The inner and outer water flowrates were adjusted to reduce radial temperature differences to a minimum. The increase in water temperature was still much lower than anticipated, and the inner calorimeter water flow was reduced to a very low level, 170 ml/min, to try and maximise the temperature rise and hence reduce the error due to the PRT accuracy limit. Unfortunately this resulted in wild fluctuations of the outlet water temperature, thought to be due to natural convection, and the flow was increased to 300 ml/min to overcome this, with an outer calorimeter flowrate of approximately 1000 ml/min. Other problems became apparent as more experience was gained -

a) the increase in water temperature for the inner calorimeter was so small, even at 300 ml/min, that considerable inaccuracy and variability of the resulting thermal conductivity value was inherent at the lower temperatures. Use of conductive pastes to improve the thermal contact between the sample and the calorimeter was unsuccessful, and this problem was only overcome in the refined design.

b) the relationship between the water flowrates, the measured water temperature rise and the sample temperatures proved to be complex, with the calculated

value for thermal conductivity varying according to the set conditions. The water flowrates, as established in the trial run to give the maximum consistent water temperature rise and a minimum radial variation in sample temperature, were used for all subsequent experiments with the initial design apparatus.

c) the transformation observed during sintering which had caused cracking and expansion of the compact was also observed during the experimental heating cycle, both as a change in conductivity and from examination of the samples after cooling. This effect was reduced by careful heating but was always present in both original and refined apparatus.

d) the calorimeter's life was limited by internal and external corrosion due to the use of uninhibited oxygenated water and condensation formation during cooling.

4.3.2. The Refined Design.

It was realised from the problems encountered that the original design had some severe shortcomings, mainly caused by incorrect assumptions. The proportion of the heating system output reaching the cooling water was lower than expected, due to losses from the heating chamber and greater than predicted radial losses from the sample. As a result, the calorimeter and all the connecting pipework was larger than necessary and the

water flowrates were excessive, resulting in the small water temperature increase. A second calorimeter was designed and fabricated from aluminium. The plastic tubing and rotameters were replaced with a smaller system, and the thickness of the samples reduced from approximately 13 mm to 6 mm. The principle of creating similar flow conditions in the inner and outer calorimeters was used in conjunction with the experience gained to determine design details (see Figure 13).

The refined design allowed a wide range of flowrates to be used without significantly effecting the accuracy and variability of the result, and this enabled the apparatus to be calibrated by water flow adjustment using samples of known thermal conductivities. Finally, an Apple PC became available which enabled instantaneous evaluation of thermal conductivity values using pre-set data and the output of the data logger.

4.4. Experimental Technique.

4.4.1. General Operating Procedure.

Before each run the apparatus was checked for water leaks and any air locks, and then assembled around the sample (see Figures 14 -17). Particular care was taken to ensure that the six sample thermocouples were all in contact with the surface of the sample and sufficient insulation wool was packed around the calorimeter and sample. The temperature of the control couple was increased in either 100 or 50 degree steps by setting the control unit and increasing the transformer voltage to a value which attained the desired temperature without overshooting and hunting. In the initial design, the data logger display which cycled the thermocouple temperatures every 30 seconds was monitored until steady state was achieved and then a hard copy of approximately 7 sets of values taken. This number was thought sufficient to give a representative sample of results for quoting a mean value and a standard deviation. The water flowrates were kept constant throughout the run. The calibrated apparatus used a specific flow at each temperature setting which was entered into the PC and the calculated thermal conductivity values were then monitored. As before, when steady readings were obtained a print-out of approximately 15 values was taken. Temperature settings above 800 C were particularly closely monitored to determine the onset on the expansion transformation and to minimise it's effect by

reducing the rate of heating and increasing the time at each temperature. The maximum set temperature was 1400 C, and the cooling cycle was controlled and measured in the same way for the majority of the samples. At the end of the run the slag samples only were removed, sectioned and mounted for assessment of the volume fraction of porosity (and metal content where present). The porosity was determined from two components, the macro-cracking measured at X6 and the micro-porosity measured at X250, using a point counting method.

The thermal conductivity values were calculated from the steady state heat flow equation using the measured hot and cold face temperatures at the centre of the sample and the heat flux as calculated from the equation for a channel -

$$\dot{q} = \dot{m} C_P \Delta\theta \quad (8)$$

where \dot{q} = heat flow

\dot{m} = mass flowrate of fluid

C_P = specific heat capacity of fluid

$\Delta\theta$ = change in mean fluid temperature between inlet and outlet

4.4.2. Sequence Of Experiments.

The first two samples measured were slag samples of nominally 6 mm thickness (No.1 and No.2), and were used

to establish the operational practice of the rig and identify any problems. The subsequent four samples attempted to establish the effect of introducing flakes or spheres of steel into the slag, simulating the structures being observed in actual sidewall layers. To facilitate this, the sample thickness had to be increased to nominally 12 mm, and the samples were as follows -

No.3 - slag

No.4 - slag with steel flakes

No.5 - slag

No.6 - slag with steel spheres

At this stage it was realised that the calorimeter had severe limitations, due to greater than anticipated lateral and upward heat losses, and the revised version was designed and constructed. During this period, the specific density and the specific heat capacity of the sample slag was measured, using standard S.G. bottle and calorimetric techniques.

Reverting to the 6 mm nominal thickness, two slag samples, Slag 8 and Slag 4 (revised nomenclature), were measured on the improved apparatus, using much lower water flowrates which gave acceptable temperature increases. The actual flowrates used were selected as midrange for the rotameters, the inner at 0.99 ml/s (59 ml/min) and the outer at approximately 250 ml/min. The results obtained were much lower than those from the

initial rig, and it was decided that to validate any future results, the apparatus had to be tested using a sample of known thermal conductivity. To this end samples were prepared by core drilling from insulating bricks which had manufacturer's quoted values for thermal conductivity and from silica refractory bricks. The first insulating brick sample (IB 4) gave results higher than the quoted values, and on the final temperature setting the inner flowrate was varied between 0.44 ml/s and 1.57 ml/s to observe it's effect on the calculation. When the results had been converted to thermal conductivities (still a manual operation at this time), it was found that the lowest flowrate used, 0.44 ml/s, gave a result very close to the quoted value at that temperature. A second sample was then measured using the lower flowrate (IB 1), and this moved the results curve quite close to the quoted curve.

It was decided to then repeat the calibration exercise using silica samples, partly because their conductivity would be closer to that of the slag, and partly due to doubts concerning the manufacturer's figures for the insulating brick which it was thought might be optimistically low. Various data was available in the literature ^{97,98,99,100} for silica bricks, although there were no specific values associated with the material used. The first silica sample (Silica 2) ran at the same inner flowrate as IB 1, 0.44 ml/s, but as with IB 4 it became obvious that the flowrate was not giving

the anticipated results. In this case they were very low, and on the final temperature setting two higher flowrates, 0.99 ml/s and 1.57 ml/s were tried. After studying the results, another sample was taken up to a constant temperature and the inner flow varied throughout the range of the rotameter, but even the maximum flow of 4.07 ml/s gave results that appeared significantly lower than literature values.

At this time an Apple PC became available for linking to the data logger, allowing direct readings of thermal conductivity to be made by programming with the appropriate equations. This meant that the response of the measured conductivity to changes in flowrate could be monitored instantaneously, and therefore the flow conditions fine tuned. Following the disappointing results from the silica samples, it was decided to re-use sample IB 4, maintaining a constant inner flowrate of 0.44 ml/s and varying the outer flowrate as necessary. From this, the flow conditions at each set temperature were established, with the outer flow varying from 75 to 200 ml/min, which gave the quoted thermal conductivity value at the associated mean sample temperature. These flow conditions were used for the subsequent two slag samples, Slag 6 and Slag 5.

However, the low values obtained rekindled the doubts over the validity of calibrating against manufacturer's figures which were an order of magnitude smaller than

the slag conductivity, as anticipated from the earlier work and the literature review. To overcome this, a sample of a haemetite-olivine heat storage brick was obtained, which had had its thermal conductivity over a range of temperatures certified by the British Ceramic Research Association. Following a similar procedure for HSB 1 to that used with IB 4 revealed that the existing rotameters were not capable of measuring the required flowrates at the lower temperatures, as previously suggested by the silica samples, and larger rotameters were fitted. A second run with HSB 1 successfully established the flow conditions, the inner flowrate fixed at 10 ml/s and the outer varying from 0 to 750 ml/s, which reproduced the certified values.

These flow conditions were used for the final five samples, Slag 22, Slag 32, Slag 31, Slag 21, and Slag 24.

5. RESULTS.

5.1. Results Of Industry Based Studies.

5.1.1. Results Of Furnace Observations.

Although it was not possible to continuously monitor the slag covering on the water cooled sidewalls, certain trends became apparent from the intermittent observations. The thickness of the slag varied considerably, ranging from bare panels to massive aggregations more than one metre thick with the configuration of slag cover constantly changing.

Bare panels occurred where the slag layer had fallen from the panel face and this was observed to take place by "peeling off". Generally, most of the sidewall was covered to a thickness of a few centimetres, but two areas consistently had more substantial layers. These were the region of the slag door (panels 1 and 12) with layers commonly of 5 - 10 cm, and an area adjacent to the taphole (panels 7 and 8) where massive build-ups occurred (Figure 18). The results of these process observations were confirmed by the less subjective measurements taken on inspection of the cold furnace (Table I and Figure 19).

The hot face of the very thick layers was often metallic, with a smooth continuous surface showing evidence of molten metal running and dripping back into the bath. This made the removal of samples very difficult, and only 6 of the 66 samples taken were from panels 7 and 8. Behind the hard metal shell, highly

porous multi-layered structures with large air pockets were observed, and samples of similar structures were taken from the slag door position.

The thinner slag layers found on the majority of the sidewall panels were either coherent with the panel or had small air gaps at the slag-panel interface, in which case the slag adhesion relied totally on the mechanical keying effect of the slag catchers. Evidence of slag peeling and fracture, as observed during operation, was also found when examining the cold furnace, and it was common to find extensively cracked slag held together only by its metal content.

5.1.2. Results Of Sample Examination.

A total of 66 samples were examined, and the features which emerged from the extensive observations of surfaces, sections and microstructures are summarised below. The average thickness of all of the samples was 17.2 mm, but this did not include panels 7 and 8 because a full set of representative samples could not be obtained.

The hot face of the slag showed two distinct textures which are best described as "molten" and "frozen splash", with an intermediate "lumpy" texture which was also common (Figure 20). Although only 24% of the samples were totally frozen-splash having little subsequent fusion, 56% did show evidence of the frozen-

splash texture and in nearly all cases this type of surface consisted of metallic globules apparently chilled by cooler pre-existing slag or metal. In contrast, the molten surfaces examined were invariably slag because none of the metallic molten face layers observed in situ could be removed for examination.

The cold face of the slag was generally contoured to the panel and slag-catchers, and had an iron oxide surface layer. On many samples a pale powdery substance (analytically identified as zinc oxide) was found in the form of lichen-like white or yellow patches (Figure 21). The sectional structures examined varied considerably in the degree of metal and porosity content, both of which were classified by fraction, size and distribution. The average metal content was 22.4%, and it existed as either a continuous layer, isolated globules or in a finely divided form (Figure 22). 70% of the samples contained continuous or semi-continuous metal layers, 49% of which were positioned at or very near to the hot face. The isolated metal droplets, which averaged approximately 1 mm in diameter, were randomly distributed and were present in 82% of the observed structures. The finely divided metal appeared to be the result of the other metal morphologies being disseminated, and was common to 53% of the samples.

The average porosity was 22.6%, with some degree of random fine porosity (< 1 mm diameter) present in all of the slags. A third of the samples also contained coarse

porosity (> 3 mm diameter) which often occurred adjacent to the continuous metal layers (42% had associated coarse porosity). Many of the observed structures had a laminar appearance caused by the metal layers and variation of porosity and slag microstructure (Figure 23). In some cases two distinct layers with an air gap interface were distinguishable.

The microstructures of the slags contained at least six different phases in widely differing morphologies. Two phases which were the major constituents common to all of the samples examined were identified by SEM x-ray analysis as calcium silicate (glassy matrix) and a mixed oxide of iron, manganese and magnesium. The third most common phase was similarly identified as iron silicate, and the other observed phases which occurred less frequently and usually not in combination were thought to be complex oxides. The overall composition of the slag layer varied slightly, but was similar to that of a bath slag sample (Table II).

Toward the cold face of the slag the microstructure was very fine and sometimes vitreous, with clearly defined droplet boundaries (Figure 24). Elsewhere the structures tended to be coarse and in many areas dendritic (Figure 25), apart from a few samples which had an apparently sintered structure with fine angular porosity (Figure 26).

The dissemination effect observed on the macrosection

showed up more clearly under the microscope (Figures 27 and 28).

5.1.3. Results Of Water Temperature Measurements.

The results are presented as plots of heat flux for each panel versus time (Figures 29 - 39).

5.2. Results Of Theoretical Heat Transfer Studies.

The heat transfer model, including the thermal conductivity program, is critically discussed in Section 6. However, the results of the comparison between the various equations and the theoretical effects of variables are given here.

The two earliest theories, those of Eucken and Russell, were then compared for non-porous slags containing metal droplets and porous slags with no metal content (Figures 40 and 41). Russell's theory can include a radiation allowance when the disperse phase is a gas, and the effect of this can be shown by comparing Russell's simple result with the radiation adjusted result (Figures 42 and 43). A similar comparison can be made between Loeb's theory and it's simplified form (Figures 44 and 45), although the latter is only intended for use at temperatures below 500 C. Replotting all of these curves demonstrates the difference between Russell's and Loeb's theories (Figures 46 - 48) and highlights the dependence of radiation transfer on pore diameter. The impact of pore radiation relative to the thermal conductivity of the solid phase can be illustrated by comparing a porous metal (Figure 49) with a porous slag (Figure 48). The theories which allow for pore radiation are of most interest with respect to the conditions found in WCP slag layers, and certain characteristics of both Russell's and Loeb's theories can be demonstrated by showing how the conductivity curves change with

varying pore size (Figures 50 and 51).

For the purpose of comparing the various combinations of theories for a three phase composite, a typical slag structure derived from the results of the slag sample examination is used. This structure consists of a continuous slag phase with 20% metal content in the form of randomly distributed 1 mm spheres and 25% porosity of mean diameter 2 mm. All ten possible combinations of equations are considered (Figures 52 and 53), including those which do not account for pore radiation. The effect of non-spherical porosity on this structure can also be shown by considering ellipsoid pores (Figures 54 - 57).

5.3. Experimental Results.

5.3.1. Peripheral Work.

The full chemical analysis of the slag used for all of the thermal conductivity measurements was as follows -

CaO	-	34.7 %
Fe O	-	29.73 %
_{2 3}		
SiO	-	11.43 %
₂		
Al O	-	6.62 %
_{2 3}		
MnO	-	5.94 %
MgO	-	4.64 %
Cr O	-	2.19 %
_{2 3}		
ZnO	-	0.75 %
CuO	-	0.05 %

The results of the density and specific heat capacity measurements for the same material are given in Tables III and IV.

5.3.2. The Initial Thermal Conductivity Apparatus.

Sample No.1, a 6 mm thick slag compact, was allowed to equalise after setting the element chamber temperature to 200 C. This raised the temperature of the upper surface of the sample to around 50 C, and the difference between inlet and outlet water temperature was less than half a degree. At 300 C set temperature the slag increased to 85 C, but at 400 C set a decrease in water temperature was observed. This was found to be due to a water leak, which was repaired and the set temperature taken up to 500 and then 600 C. At this setting the slag

had a temperature gradient of over 200 degrees from top to bottom faces, and the increase in water temperature was around one degree. To determine the response time of the apparatus, temperatures were monitored every 60 seconds from the point when the set temperature was increased to 700 C (Figures 58 and 59). The run was continued, but at the 1000 C setting it was noticed that steady state was not being achieved, and the lower face temperatures were decreasing instead of increasing (Figures 60 and 61). Eventually the set temperature was increased, and at the higher settings this phenomenon was no longer apparent and this was evident when the raw data was converted to thermal conductivity values (Figure 62). At the highest temperature setting, 1400 C, the slag face temperatures were 1230 C and 70 C and the water temperature increase was four degrees.

Sample No. 2 was heated using 50 degree steps in the set temperature, and was closely monitored to establish the onset of the above phenomenon. It occurred at the 850 C setting, with the upper face of the slag at approximately 650 C and the lower at around 150 C, giving a mean temperature of 395 C (Figure 63). After an hour at this setting these had changed to 665 C and 135 C, maintaining the mean temperature of the slag, but increasing the temperature gradient across the sample by around 30 C. At the maximum setting the temperatures reached were similar to those recorded for the first

sample, apart from the cold face of the slag which was at 165 C. The cooling cycle of this sample was also monitored and controlled in 50 degree steps (Figures 64 and 65).

The four double thickness samples, including those containing metal, were measured on the heating cycle only using 100 degree steps in the set temperature (Figures 66 - 69). The drop in conductivity at around 400 C mean slag temperature was again apparent (Figure 70). These thicker samples contained large pores not present in the 6 mm samples, possibly caused by less effective compaction (Table V).

5.3.3. The Refined Apparatus.

The lower flowrates used with the replacement calorimeter had a considerable effect on the increase in water temperature which varied from two degrees at 400 C set, through 10 degrees at 900 C set to over 20 degrees at the maximum 1400 C set for the samples Slag 8 and Slag 4. This greatly reduced the fluctuations of the calculated conductivities at each set temperature (Figures 71 and 72). The cold face temperature of the slag was higher than for the previous runs at 300 and 400 C, making the conductivity drop phenomenon occur at a higher mean slag temperature (Figure 73). These samples showed larger temperature gradients horizontally across the sample diameter, over 30 degrees on the hot face and over 100 degrees on the cold face at the higher set

temperatures, with the centre of the sample being cooler. This was opposite to the effect of lateral heat flow away from the centre of the sample observed on the initial apparatus, where the temperature differences were much less. Although subsequent runs also showed this apparent imbalance, it was greatly reduced to less than half of the differences quoted above and varied depending on the water flow conditions.

The dramatic effect of altering the flow conditions was demonstrated during the attempts to calibrate the apparatus using insulating brick and silica brick, and proved to be the only effective way of controlling the heat flow within the rig to give the desired values (Figures 74 - 77).

The water flows established from the second run with sample IB 4 were used for samples Slag 6 and Slag 5, which were the first to be measured using the PC to process the data directly. By removing the lengthy hand calculation stage it was possible to record more results at each set temperature, and therefore only the mean values are plotted (Figures 78 and 79). Sample Slag 6 was measured in three stages, from 400 to 600 C, 600 to 1000 C and 1000 to 1400 C, with the heating and cooling cycle being controlled in each range. This was done to avoid the conductivity drop effect.

The heat storage brick sample, HSB 1, had a thermal conductivity in what appeared to be the ideal range at

the temperatures being used, and initial trials resulted in a change to the outer flow rotameter and the inner flowrate was optimised. A full calibration was then possible for the set temperature range 800 to 1400 C (Figure 80).

The water flow conditions established were maintained for the remaining slag samples, all of which were measured on both heating and cooling cycles (Figures 81 - 86).

6. DISCUSSION.

In previous sections the topics have been considered in the chronological order of the work carried out. In this section the sequence is changed to allow the logical construction of the overall model, which is assessed in the final part.

6.1. Experimental Work.

6.1.1. An Appraisal Of Experimental Technique.

6.1.1.1. Thermal Conductivity Measurement.

Some of the problems encountered during the development of the thermal conductivity rig have been discussed in section 4, but a further assessment of the difficulties and peculiarities, both general and specific to the apparatus used, is worthwhile.

Measuring the thermal conductivity of complex materials is difficult due to the possibility of inhomogeneity or directionality, although each can be minimised by optimising the selection or production route ⁷³ of samples. The grain size must be sufficiently fine to make the orientation of crystallites random and the proportion of individual phases along the line of measurement representative of the bulk. It was hoped that this would be achieved by chill casting and, after abandoning the melting route, by reducing the slag to a very fine powder prior to mixing and pressing. Inconsistent particle properties can make homogenous blending difficult and may result in particle alignment

during compression, although this was not observed. Porosity was shown to vary with the amount of binder used, and also varied across the sample due to uneven pressure during compaction, but variation from sample to sample was allowed for by a calculated adjustment (see section 6.1.2.).

A further source of structural inhomogeneity was sintering, where the geometry of the sample and the short furnace times resulted in different levels of consolidation depending on the heating rate and the maximum temperature reached. An inevitable consequence of that was the additional sintering that occurred during the operation of the rig, clearly demonstrated by the results (Figures 60 - 63). The sudden drop in observed thermal conductivity was found by subsequent porosity evaluations to be caused by extensive cracking in the sample, and was associated with an overall volume increase. This confirmed the observations made during the sintering trials with longer furnace durations. The severity of the effect was related to the heating rate (Figures 62 and 63), indicating that thermal stress was at least in part the cause, but it's persistent appearance at approximately the same temperature suggested that some phase change was occurring. The fact that iron was a major constituent of the slag and was primarily present as an oxide makes an M_2O_3 to MO transformation seem likely.

These factors not only lead to variability from sample

to sample but the latter effect also means that the material measured during the heating cycle was different to that of the cooling cycle.

One of the main difficulties associated with measuring the thermal conductivity of low conductivity materials is to promote and control the heat flow regime required. For example, where unidirectional heat flow is required there will always be lateral heat losses between the heat source and the heat sink. In this case such losses, initially underestimated, were evident by the dependence of results on the sample thickness and water flowrates and the lower than anticipated water temperature rise, even after redesigning to allow for greater heat losses. Not having access to the technical sophistication necessary to reduce these heat losses, the apparatus was limited in that the approximate conductivity of the sample material needed to be known, and a calibration sample of similar, but precisely known, thermal conductivity was required so that the water flow conditions could be established. However, within these limitations and subject to the sample difficulties discussed above, the rig gave reproducible results and, once watertight, proved reliable in operation.

6.1.1.2. Other Techniques.

The measurement of specific density and specific heat capacity are both standard techniques.

6.1.2. Discussion Of Results.

6.1.2.1. Thermal Conductivity Measurement.

Apart from the final five samples, the results obtained from the rig are not reliable measurements of the slag thermal conductivity. However, there are certain aspects of these other results which are worth discussing, not only in terms of experimental development, but with respect to the slag behaviour.

A hysteresis effect was first noticed on Sample No.2 (Figure 65) and was evident on subsequent samples which were measured on both heating and cooling cycles. Possible explanations are thermal inertia in the system, consolidation of the cracks produced during heating by high temperature sintering, or time dependent phase changes occurring. The effect was not always consistent, and was not very significant relative to the variability caused by other factors.

The experiments to measure the effect of metal in the slag were inconclusive, although the only sample which had any real metal content, Sample No.6, did show the highest conductivity (Figure 70). These thicker samples were less homogeneous than the 6mm samples, and this is reflected in the differing results for samples No.3 and No.5, which were both slag only compacts.

One thing common to all the measurements taken for the slag samples was the shape of the conductivity curve, increasing gradually with temperature, which is in

agreement with the published findings for other slags.

The purpose of the experimental work was to determine absolute values of slag thermal conductivity for inclusion in the theoretical model. To achieve values for solid slag, the results of the final five samples (Figure 86) were adjusted by calculating back to zero porosity using Russell's equation and the average porosity of the slag. The best straight line through these was used to give the required values for the thermal conductivity computer program (Appendix VI and Figure 8).

6.1.2.2. Other Results.

The average of ten density determinations for the as-collected slag was 3.15 g/ml, which compares well with published data for similar materials⁷². The sintered slag gave an average of 3.88 g/ml, the difference probably being due to reduced levels of closed porosity. The average of five specific heat capacity determinations is 723.5 J/kg K, which again compares⁷² favourably with Chester's data for a steelmaking slag.

6.1.3. Errors And Accuracy.

6.1.3.1. Thermal Conductivity Measurements.

Some of the errors inherent in the method have already been discussed, but in this section the errors of the individual measurements made, using the final rig design

for the determination of the thermal conductivity, are appraised. The equation used for this calculation is as follows -

$$k = \frac{\dot{v} \rho C \Delta \theta_w t}{\Delta \theta_{sl}}$$

where \dot{v} = volume flow rate

ρ = density of water

C = specific heat capacity of water

$\Delta \theta_w$ = water temperature rise

t = sample thickness

$\Delta \theta_{sl}$ = temperature difference across slag sample

Density and specific heat capacity values for water were taken to four significant figures from standard tables using the mean water temperature. The variation with temperature across the range involved is less than 0.1% for both properties, and therefore the error is insignificant in comparison with the measured variables and can be ignored.

a) Volume flow rate :

This was measured by taking a visual reading from a rotameter, and once a steady flow was established there was no visible variation during the course of the experiment. It is estimated from the rotameter

graduation that the accuracy was ± 0.5 ml/s.

b) Water temperature difference :

This was measured by PRTs (platinum resistance thermometers) having an accuracy of ± 0.1 C situated just below the calorimeter. The error due to heat losses from the water before reaching the exit PRT can be assumed to be the same under calibration and measurement conditions, and therefore ignored. Variable flow patterns could introduce errors caused by the degree of mixing, assumed to be perfect in the calculation. Such variable flow patterns produce significant fluctuations in the exit temperature, as observed for the very low flowrates at the lowest temperature setting.

c) Sample thickness :

This was measured using a micrometer, taking a mean of five readings around the sample. Micrometer error can be ignored as insignificant compared with sample variability of ± 0.1 mm.

d) Temperature gradient across slag :

Both hot and cold face temperatures were measured using Pt/PtRh thermocouples which have an accuracy of ± 5 C. Contact between the couple and the face of the sample is essential, and this was checked during assembly and after each experiment. It is possible that the hot face couple may be affected by direct radiative heating, but this cannot be quantified. Treating these data errors as absolute errors, relative errors can be taken for typical values and used to

calculate the relative error of the thermal conductivity results.

For $\dot{v} = 10$ ml/s the relative error = 0.05

For $\Delta\theta_w = 10$ C the relative error = 0.02

For $t = 5$ mm the relative error = 0.02

For $\Delta\theta_{s1} = 500$ C the relative error = 0.01

The sum of relative errors = 0.1

Therefore the relative error of the thermal conductivity results is approximately $\pm 10\%$.

6.1.3.2. Specific Density.

The accuracy of the method used depends on the quality of the sample. Errors can be caused by inhomogeneity of the sample or failure to crush the material sufficiently to expose all closed porosity. Another possible source of error is the presence of air bubbles on the particles in the S.G. bottle during weighing. Actual measurement errors are very small, with weighing errors of approximately ± 0.0005 g. The density of the water is taken from the temperature using standard tables, giving an error of only ± 0.0001 g/ml. From the equation for density calculation -

$$\rho_s = \frac{M_s \rho_w}{M_w - (M_{s+w} - M_s)}$$

where ρ_s = density of slag
 M_s = weight of slag
 ρ_w = density of water
 M_{s+w} = weight of slag and water

For $M_s = 1 \text{ g}$; relative error = 0.0005

For $\rho_w = 1 \text{ g/ml}$; relative error = 0.0001

For $M_w - (M_{s+w} - M_s) = 0.5 \text{ g}$;
 relative error = 0.003

The sum of relative errors = 0.0036

Therefore the relative error of the specific density measurements is $\pm < 0.5\%$.

The variation in the results obtained suggests that the significant sources of error are not those of measurement, but are probably due to the experimental factors given above.

6.1.3.3. Specific Heat Capacity.

The major errors in this manual method are the inconsistent heat losses during transfer of the sample from the oven to the calorimeter and the insulation

efficiency of the calorimeter. Errors due to accuracy of weighing and oven and water temperature measurement are insignificant, and the results are therefore likely to be lower than the true values.

6.2. Water Cooled Panel Slag Layers.

6.2.1. Formation Of Slag Layers.

Slag/metal layers on water cooled sidewalls are formed by the impingement of molten particles projected from the arcs during operation. Using Bowman and Fitzgerald's results⁵⁸ from their study of these particles, the expected structure of a slag layer removed from a cold furnace can be surmised. There should be a metal layer at the hot face, created just prior to tapping the final cast when the slag has been largely removed from the bath and the arc splash is primarily metal. Behind this, there would be a slag layer with a thickness of between 1 and 2 cm, based on a 2 hour tap-to-tap practice. Behind the slag layer there would be another metallic layer formed during the penultimate cast, and so on.

A structure similar to that just described was observed in this work, with isolated droplets of metal in the slag due to the varied composition of the impinging particles, probably caused by steel entrainment in the bath slag. It should be noted that, in over 80% of cases, the diameters of these droplets were estimated as < 1 mm or between 1 and 3 mm, which is in agreement with Bowman and Fitzgerald's experience.

One difference from the expected structure was the absence of the second metallic layer in a large number of the samples. In many instances the slag layer was quite thin, suggesting that it is common to have bare panels in the early stages of a cast. For the thicker

samples, the metal may have been oxidised by the mechanism discussed in section 6.2.2., and there was some evidence of partially disseminated layers.

Having established how the build-up of slag/metal layers occurs, the parameters which limit their thickness must be determined. One factor is the thermal conditions under which the panel layers exist, and the effect of these conditions can be shown by considering the formation of a slag layer at a constant rate of slag splashing from the bath to the panel.

The driving force for heat transfer from the hot face of the panel to the cooling water is a function of hot face temperature and water inlet temperature. The thickness of the slag, and hence the thermal resistance to heat transfer from the hot face to the cooling water, will increase as the cast proceeds. If the heat flux to the panel from the furnace interior is constant, then the temperature difference across the slag increases, until a situation arises such that the hot face temperature of the slag exceeds its fusion temperature. Any further slag splashing on to the hot face will remain molten and run off back into the bath, and should the slag layer be removed it would be reformed to the same limiting thickness. In fact, the heat flux will not remain constant during the build-up of the layer, because it is influenced by the hot face temperature such that, even for stable arcs at a constant power, the heat flux is

lower for thick layers than thin layers. However, should a stable slag layer be formed, with its hot face at the fusion temperature and the arcs steady, the situation of slag splashes running off into the bath will occur. If the heat flux from the arc is reduced, the hot face will cool down and splashes will solidify, increasing the thickness of the layer. Conversely, if the heat flux from the arc increases, then the slag layer will overheat at the hot face resulting in melting back and a reduction in thickness. Ignoring for the moment other factors, it follows that the steady state slag thickness is a direct function of the heat flux from the arc. As this is greater at the hot spot positions, then the slag layer thickness should vary around the furnace, being greatest at the cold spots.

The monitored furnace had a major hot spot at a position corresponding to panels 9 and 10, and lesser hot spots at panels 2 and 6. This explains the thicker layers observed at the 7/8 panel cold spot, and possibly the thicker than average layers on panels 12 and 1. These latter panels are above the slag door, which is used for access to the furnace and hence any large accretions are mechanically removed as a matter of course. The third projected cold spot at panels 3 and 4 had only thin layers, but the heat generated by oxygen lancing through the port below panel 3 may have eliminated the cold spot effect.

Further evidence for the limitation of thickness by the

slag melting temperature is the surface fusion found on 76% of the samples and the coarse remelted dendrites in the slag microstructure. Also, when the bath slag is removed and metal is splashed on to the panel slag layer, the surface temperature is not sufficient to keep the metal molten, and this results in the frozen-splash surface.

Because of the higher fusion temperature and the lower thermal resistance of the metal, a high metal content layer would have a greater steady state thickness than a totally slag layer for similar furnace conditions, and this thickness is attained at the panel 7/8 position, as evidenced by the fused metal hot face. The higher metal content may be caused by extra metal splashed up by the oxygen blown in from a position diametrically opposite in the furnace. Alternatively, the steady state thickness of the slag-rich layer at this point may be such that the closer proximity to the arcs results in a greater proportion of the denser metallic droplets impinging on the hot face. Although closer to the arc, the heat flux to the slag would be less than that at the hot spot because of the directional nature of the arc flame.

The overall effect of geometry and arc directionality is to cause a variation around the furnace in the amount of material splashed on to the sidewall, although generally the thickness controlling mechanism appears to be the

hot face temperature limit and not the material arrival rate. However, a lower rate of slag transfer to the wall between the two widely spaced hot spots at panels 2 and 6 would partially explain the thinner layers found on panels 3, 4 and 5, assuming that the periodic shedding of slag layers from the sidewall is random and frequent. The shedding of slag is the other major factor limiting the thickness of the panel layers, (see section 5.1.1.), but it is intrinsically a more difficult process to study or predict. To enable a portion of the slag/metal layer to fall from the sidewall, both separation at the panel/layer interface and fracture within the layer must occur. Separation appears to be common, with air gaps forming between the panel face and the slag layer, and this is probably caused by the thermal cycling during furnace operation. Within these small air gaps the lichen-like growths are formed, almost certainly from zinc in the furnace atmosphere being deposited by a condensation/oxidation reaction. Whether these zinc oxide patches encourage or inhibit panel/slag adherence is not known, but it seems unlikely that they have any significant effect.

The air gap also acts as a barrier to heat flow, creating an additive thermal resistance which results in either rapid melting back or softening and peeling of the slag layer when the furnace is at high temperature. At low temperatures the slag is very brittle and most fractures occur during charging (by direct impact or

thermal stresses) or meltdown (by intense vibrational shock). Accretions containing continuous metal layers often survive substantial shattering of the slag, although such layers are more susceptible to high temperature peeling. Observations and structural evidence suggest that the shedding of layers can occur as frequently as every cast, but the maximum layer life is not known. The thicker layers may tend to last longer, although all types of covering, including the massive metal-fronted build-ups, are shed from the panels during furnace operation.

Finally, an alternative model of layer formation is required to account for the slag structures observed to contain extensive fine angular porosity. It seems likely that furnace dust, which is occasionally deposited on the sidewall as a powdery coating, can sinter in situ when exposed to the heat of the arcs.

6.2.2. Chemistry Of Slag Layers.

The microstructures of the slag layers observed suggest that there is considerable chemical activity taking place at high temperatures prior to the layer being chilled. This is not surprising when one considers the complexity of the situation, both in the number of metallic, non-metallic and gaseous phases coexisting and in the dynamic nature of the process that supplies the sidewall with droplets. During the steelmaking cycle,

the composition and degree of oxidation of the steel, slag and furnace atmosphere all change, and where different grades of steel are being produced these factors will vary from cast to cast also. However, there are certain phenomena which were common to a large proportion of the samples taken.

Oxidation of the metal in the slag layers was evident, visual examination showing that isolated droplets and semicontinuous layers had been disseminated to clusters of tiny metal particles. Under the microscope, it appeared that these clusters were individual grains of metal isolated by preferential attack at the grain boundaries of the original droplet or layer. The non-metallic phase surrounding the remaining metal was confirmed as iron oxide using EDAX analysis on an SEM sample.

The porosity noticed at the interface between the metal and slag layers indicated that some reaction which involved gas evolution had taken place, possibly decarburisation of the steel producing carbon monoxide. Interactions between the slag phases were widespread and extremely varied, with the only common factor the presence of glassy structures where the cooling rate had been sufficient to prevent phase formation.

6.2.3. The Effect Of Slag Layers On Heat Losses.

The plots of heat flux against time demonstrate many of the characteristics of the furnace and process being

studied, although some of the plots are offset due to water temperature gauge calibration errors (Figures 29 - 33).

There is considerable variation in the measured heat fluxes from cast to cast, both in their magnitude and their fluctuation during the cycle. This is mainly caused by the scrap, depending on the way it is packed, how it falls on charging, and how the channels are formed and settling occurs during meltdown. However, in addition to this, the thickness of the panel slag layer, and hence it's thermal mass, will also have an effect. To overcome this variability, the data has been plotted as numerical parameters, such as maximum heat flux or rate of increase of heat flux during meltdown, which can be averaged for each panel or directly correlated with the slag cover observed on the cold furnace (Table I).

Starting with the cycle at the charging stage, the effect of the introduction of cold scrap on the heat flux is universally apparent, for example at 200 minutes in Figure 29. The dramatic reduction is primarily due to the shielding effect, minimising radiation from the other surfaces in the furnace and from the arc when it is struck. The rate of cooling is related primarily to the thermal mass of the slag present on the panel, as can be seen by comparing Figure 87 with Figure 19. The base level to which it falls is a function of conduction through the lower sidewall, convection of hot gases

through the scrap and the thermal mass of the panel slag layer. The first of these is probably the most important because the base levels are very similar for most of the panels regardless of position or slag cover (Figures 34 - 39).

During meltdown the scrap heats up, convection increases and the shielding effect diminishes, resulting in a general rise in the heat flux to the sidewall. As gaps or channels are formed in the scrap at the hot spot positions, the panels are exposed to the high powered arcs and rapid rises in the heat flux can occur. This is clearly shown by panel 10 in Figures 36 - 39 and in Figure 88, while the protection offered by the slag layer is demonstrated in Figure 89. The steepest gradient appears anomalous, but from the records made for that panel at that time it is almost certain that the slag examined cold became detached from the panel very early on in the cast, and that the actual slag cover during meltdown was zero.

The sequence of charging and meltdown is repeated for the second basket, and as the heat flux becomes excessive the power tap setting is reduced to prevent refractory or panel damage. In Figure 34 the tap setting was reduced from 1 to 3 at 152 minutes, and then to tap 4 at 168 minutes. The same graph also illustrates the next stage of the cycle where a flat bath of molten metal exists and the heat fluxes to the sidewall remain fairly constant. The maximum heat flux measured will

occur during either of these two stages, and will therefore represent either channeling or the approximately steady-state heat loss, and be related to hot and cold spots and possibly slag cover. Figure 90 shows both effects at panels 10 and 8 respectively, and the odd point in Figure 91 corresponds to that in Figure 89 (see above).

The flat bath stage is the only time during the cycle where steady state heat flow is even approached, and the hot spot effect is perhaps more evident in Figure 34 where panels 6,5,10 and 1 have the highest heat fluxes.

The final part of the cycle, which is usually curtailed by the following cast being charged, is the natural cooling after tapping, and this is shown on Figures 29 - 34,36 and 38. The rate of cooling depends on the panel temperature and the thermal mass of the slag layer, as illustrated by Figures 92 and 19.

To summarise, the heat losses to the water cooled sidewalls vary with time and position in the furnace, and are related to the thickness of the panel slag layers in addition to other process variables (e.g. arc power, bath slag depth, scrap packing).

6.2.4. Errors And Accuracy.

6.2.4.1. Slag Cover Assessment.

Assessments of slag cover during furnace operation are totally subjective and therefore unreliable, but cold

examination allowed some measurement to assist in estimating the percentage of panel covered. Estimates of mean slag thickness and mean air gap were made from a limited number of measurements, and the magnitude of error on such values is difficult to assess without sufficient data for statistical analysis. Estimates of the errors are given below -

- a) percentage of panel covered : $\pm 5\%$ of total
panel area
- b) mean slag thickness : up to $\pm 30\%$
up to $\pm 15\%$ when samples taken
- c) mean air gap : up to $\pm 50\%$

6.2.4.2. Slag Layer Examination.

The classification of the surface appearance of the samples was subjective, but because extensive comparisons were possible the categories are consistent. This also applies to the metal type and the classification of metal droplet and pore sizes, although the latter was assisted by check measurements using a rule.

Thickness measurements were accurate to ± 1 mm, with the variability of thickness throughout the sample being generally less than $\pm 10\%$.

Because of the large number of samples, the assessment of percentage of each phase was made using a subjective coarse grid method, and hence the resulting errors can

only be estimated as $\pm 5\%$ of the total observed area.

6.2.4.3. Heat Flux Calculations.

Certain assumptions have been made regarding water flow in the panels and their feed system and in the heat flow path from the furnace to the cooling water, and the effect of these assumptions on the result of the calculation are unknown. From the equation for heat flux to a panel -

$$\dot{q}'' = \frac{\rho \dot{V} \Delta\theta C_p}{A}$$

where ρ = density of water
 \dot{V} = volume flowrate of water
 $\Delta\theta$ = increase in water temperature
 C_p = specific heat capacity of water

Density and specific heat capacity values for water were taken from standard tables.

a) Overall volume flowrate was taken from a chart to an accuracy of $\pm 6 \text{ m}^3/\text{hr}$. The factors used to calculate individual panel flowrates were based on theoretical principles and the error introduced is uncertain, so a nominal relative error of 0.05 will be used.

b) Water temperature values were taken from digital readings given to the nearest 0.1 C, the quoted accuracy

of the device. However, these readings were often unstable during the operation of the electromagnetic stirrers of the furnace, and the value would fluctuate across a range of approximately 0.5 C. Hence, the accuracy of the readings must be taken as ± 0.3 C.

It was discovered during the course of the work that the water temperature sensors were subject to large offset errors, which were corrected for on the later data-sets by measuring the offset on the cold furnace.

c) The area of each panel was calculated from it's overall dimensions, ignoring edge effects, internal baffles and slag catchers. The values are accurate to $\pm 0.002 \text{ m}^2$.

For a total flow of $180 \text{ m}^3/\text{hr}$,

the relative error of $\dot{V} = 0.08$

For a $\Delta\theta_w$ of 10 C, relative error = 0.06

For an A of 1.5 m^2 , relative error = 0.003

The sum of the relative errors = 0.146.

Therefore the relative error of the calculated panel heat fluxes is approximately $\pm 15\%$.

6.3. A Heat Transfer Model.

6.3.1. Theories Of Thermal Conductivity.

The heat transfer model for conduction through the panel/slag layer must include an equation for calculating the thermal conductivity of that layer based on it's structure and the thermal conductivities of it's components. The theories have been compared by using a computer program to give conductivity vs temperature curves for various combinations of slag, metal and porosity.

Eucken's and Russell's theories give very similar results for porous slags (Figure 40), but are not so close for a high conductivity disperse phase (Figure 41). The introduction of a radiation allowance to Russell's equation has little effect at low temperatures, and becomes more significant as the pore size increases (Figures 42 and 43). This is also true for the radiation effect in Loeb's theory (Figures 44 and 45), which gives similar results to the other theories for porous slag (Figures 46 - 48). Comparing Russell and Loeb for porous metal, there is still little difference between the two (Figure 49), although Loeb is again suggesting a slightly greater conductivity than Russell. However, if the range of pore size is increased some interesting characteristics of the two theories emerge (Figures 50 and 51). For small pore diameters Loeb's equation gives higher values of thermal conductivity at all temperatures, but as the pore

diameter increases then Russell's theory shows conductivity increasing considerably above 700 C and exceeding that predicted by Loeb. These curves suggest that the critical pore diameter above which the radiation effect does not increase is smaller for Loeb's theory than for Russell's theory at any given temperature. The importance of this is somewhat diminished by the fact that neither theory allows for the convection within the pore that can take place when the pore diameter exceeds 3 mm.

For porous slag/metal mixtures, the combined theories fall into two bands, depending on the equation used for the solid (Figures 52 and 53), highlighting the difference between the theories of Eucken and Russell. The secondary equations applied behave as for porous slags, although the difference between Loeb and Russell with radiation allowance is more marked. When non-spherical pores are introduced, depending on their orientation, this difference is either emphasised or slightly reduced (see section 6.3.2. and Figures 54 - 57).

From this study of the characteristics of the various theories it is not clear which are the most suitable for inclusion in the model, as little is known about the thermal conductivity behaviour of these types of materials. The two preferred combinations are Russell/Russell Radiation, because it offers a universal

equation, and Eucken/Loeb Radiation where both theories have some supportive experimental evidence in the literature.

6.3.2. Thermal Conductivities Of Complex Structures.

Although there are some discrepancies between the theories included in the thermal conductivity program, they are generally in close enough agreement to allow the predicted effects of structural changes to be studied meaningfully.

The most striking aspect of dual structures of widely differing component conductivities is the importance of continuity in determining the composite conductivity. Note that a structure of 60% continuous metal with 40% porosity has a conductivity over twice that of 75% dispersed metal in 25% slag (Figures 40 and 49). When the dispersed phase is of a higher conductivity, the relationship between its volume fraction and the composite conductivity is almost exponential, with the conductivity rapidly increasing to that of the dispersed phase as the volume fraction approaches 100% (Figures 40 and 94). However, with a lower conductivity dispersed phase the relationship is closer to linear (Figures 41 and 93).

Radiation across the pores appears to be important, with both theories indicating that for large pores the conductivity of a porous material can be greater than that of the solid equivalent at high temperatures

(Figures 50 and 51). For pore sizes where convection can be ignored, this effect can only occur when the thermal conductivity of the solid phase is low (Figure 49).

The possible effects of pore shape have been examined in Figures 52 - 57, where the volume fraction of porosity is constant but ellipsoid pores have been introduced with the 2 mm dimension in both longitudinal and cross-sectional planes. Both theories are sensitive to the changes in cross-sectional volume fraction of porosity and the longitudinal dimension of the pores which are the result of changing the pore shape, but the radiation effect of Loeb's theory appears to be enhanced to a greater degree.

6.3.3. Heat Flux Within The Arc Furnace.

A method for calculating the heat flux to the sidewall was outlined in section 3.2, and it was intended that these equations be used to give a first assessment of the furnace on which this work was based. However, investigative calculations using the data available have given results that vary by as much as an order of magnitude, depending on the assumptions made, for both the arc heat flux and the radiation network calculations. The problem in both cases is the lack of accurate data for a number of the key variables, and it is apparent that meaningful results can only be gained from an extensive monitoring and recording program

beyond the scope of this work.

6.3.4. Heat Flow To The Water Cooling.

6.3.4.1. Conditions For Testing The Model.

A model for heat transfer from the furnace to the water cooling was outlined in section 3.1., and although part a) regarding heat transfer within the furnace cannot be included (see section 6.3.3.), the other components can be used to compare measured heat fluxes with calculated values. This will test the assumptions made in the model, as described in section 3.1., and the additional assumptions that ;

a) the theoretical calculation of thermal conductivity of a complex structure based on Russell's equation is valid.

b) the values of slag thermal conductivity taken from the experimental results and used in a) are true.

To facilitate any comparison, the situation for which the measured heat flux is available must be compatible with the conditions under which the model is considered valid. Hence the following criteria have been applied to the results obtained from Stocksbridge's "B" furnace :-

i) Calibration factors for the water temperatures must have been taken to ensure that the heat fluxes are true values.

ii) Data from the last cast of the week must show steady heat fluxes during the refining period prior to tapping.

iii) The panel, on cold inspection, must be fully covered with an adherent slag layer of constant thickness.

iv) A sample must have been taken and examined.

Five of the samples taken meet all of these criteria, and for these the heat flux from the hot face of the panel slag layer to the cooling water can be theoretically determined and compared to a value derived from the water temperature data.

6.3.4.2. Samples Used In Testing The Model.

The five samples are :

1) B5-06 (panel 5, dataset 06)

This sample was taken from a layer which was described as constant in thickness and covering over 90% of the panel, which had a "molten" hot face appearance with patches of "frozen splash". The layer was 6 mm thick with no observed air gap, and the sample had 25% porosity, all fine, with very few isolated metal globules. During the 30 minutes prior to tapping the last cast of the week, the heat flux was steady at approximately 155 kW/m^2 , rising slightly on tapping to approximately 165 kW/m^2 (Figure 34 b).

2) B10-06 (panel 10, dataset 06)

This sample was taken from a layer which was described as constant in thickness and covering over 95% of the panel, which had a glassy, "molten" hot face appearance with fine blowholes. The layer was 7 mm thick with no observed air gap, and the sample had 15% porosity, all fine, with 15% metal as isolated globules. During the 30 minutes prior to tapping the last cast of the week, the heat flux was fairly steady between approximately 125 kW/m^2 and approximately 135 kW/m^2 (Figure 34 b).

3) B3-07 (panel 3, dataset 07)

This sample was taken from a layer which was described as constant in thickness and covering over 95% of the panel, which had a "molten" hot face appearance. The layer was 20 mm thick with indications of an air gap in places, and the sample had 15% total porosity, 10% fine and 5% medium, with 1% metal as isolated globules. During the 60 minutes prior to tapping the last cast of the week, the heat flux was steady at approximately 50 kW/m^2 (Figure 35 b).

4) B5-07 (panel 5, dataset 07)

This sample was taken from a layer which was described as constant in thickness and covering over 85% of the panel, which had a "lumpy" hot face appearance. The layer was 23 mm thick with no observed air gap, and the sample consisted of six distinguishable sublayer structures -

- a) 0-1 mm metal
- b) 1-7 mm slag with 15% fine porosity and 1% metal
- c) 7-10 mm metal
- d) 10-13 mm slag with 15% fine porosity
- e) 13-14 mm metal
- f) 14-23 mm slag with 15% porosity, mostly fine,
some medium

During the 60 minutes prior to tapping the last cast of the week, the heat flux was steady at approximately 60 kW/m^2 (Figure 35 b).

5) B5-08 (panel 5, dataset 08)

This sample was taken from a layer which was described as a thick layer covering 90% of the panel, with 5% of the panel having a thinner layer and the remaining 5% bare. The hot face appearance was "frozen splash" with some remelting, and there were indications of air gaps over part of the panel area. The sample was 20 mm thick and consisted of four distinguishable sublayer structures -

- a) 0-10 mm slag with 25% fine porosity and 5% metal
- b) 10-12 mm continuous metal with 50% slag
- c) 12-17 mm slag with 25% fine/medium porosity and
5% metal
- d) 17-20 mm metal with 25% fine/medium porosity

During the 60 minutes prior to tapping the last cast of the week, the heat flux varied between approximately 80 kW/m^2 and 100 kW/m^2 (Figure 36).

6.3.4.3. Data Used For Testing The Model.

The calculation requires values for the hot face temperature of the slag, the bulk cooling water temperature, the surface heat transfer coefficient at the panel/water interface, and the thickness and thermal conductivity at each conduction stage including the panel wall and the sublayers of the slag.

The slag hot face temperature is taken as 1200 C, based on the surface appearance of the samples and the measured slag fusion temperature of 1190 C. During the period of steady heat flux, the layer would have been stable and is unlikely to have changed substantially during tapping. The hot face metal layer in sample B5-08 could have been formed at that time due to the metal bath being exposed, but the thermal resistance of the metal sublayer is in any case insignificant.

The bulk cooling water temperature is taken as 35 C, based on an assessment of inlet and outlet temperatures, and is consistent for datasets 06,07 and 08.

Convective surface heat transfer coefficients are calculated from the standard equation

$$Nu = 0.023 Pr^{0.4} Re^{0.8} \quad \text{(Indices for water in circular ducts)}$$

where Nu = Nusselt number

Pr = Prandlt number

Re = Reynolds number

Details of the calculation are given in Appendix VII.

Conduction through the steel wall of the panel is the same in every case, with a thickness of 25 mm and a thermal conductivity estimated as 20 W/mK.

Air gaps are ignored (refer to section 3.1.).

The thickness of the slag sublayers is known from the sample examination, and values for thermal conductivity have been taken from the output of the computer calculation for Russell's combined theory applied to the observed sublayer structures (see Table VI). The actual values used are shown in the summary of the calculation of heat flux (Table VII), and are based on a consideration of the mean temperature of the sublayer.

6.3.4.4. Results Of Testing The Model.

Table VII shows the actual heat fluxes and the final calculated values, and is therefore the crux of the comparison. The correlation is generally good, except for sample B10-06 which predicts a much higher heat flux than that observed. Sample B5-06 shows close agreement, while samples B3-07, B5-07 and B5-08 predict values slightly higher than actual.

The most likely explanation for predicted values being higher than actuals is the presence of air gaps or cracks in the slag, which, even when very small, can introduce significant thermal resistances. It would appear that the assumption that air gaps at the slag/panel interface are balanced by the enlarged area of surface contact is generally a reasonable one, but

cracks and air gaps in the slag are not accounted for. Hence sample B5-06 at only 7 mm in thickness is less affected than the three thicker samples where the possibility of gaps between sublayers is greater. Sample B10-06 requires further consideration, and several possible reasons for the marked difference in values can be proposed. These are -

a) As this was the only sample of the five to come from the "hot" side of the furnace, it could be that the simple linear model does not apply where the heat fluxes and rates of slag splashing vary rapidly due to the behaviour of the arc.

b) This sample had the highest metal content of the five, and this had the effect of approximately doubling the calculated thermal conductivity, and hence doubling the theoretical heat flux. Two possibilities are suggested ;

i) the sample was unrepresentative of the bulk layer.

ii) the conductivity theory does not hold for high metal contents.

c) A significant air gap existed between the slag and the panel over a large proportion of the interface.

d) The layer was unchanged from earlier in the melting cycle when higher powered arcs were in use and

the heat flux was actually at around 220 kW/m^2 (see figure 34 b). This would mean that virtually no slag splashing occurred during the final 45 minutes of the heat.

Some of the explanations given, if correct, introduce limitations to the application of the model. However, even subject to possible limitations, the model has shown to be valid as a general representation of heat transfer through the slag layer. The values of thermal conductivity for the slag, which are the major influence on the thermal resistance, are therefore confirmed.

6.3.4.5. Errors And Accuracy.

The theoretical calculation includes slag conductivity data with an accuracy of $\pm 10\%$, but the values used are based on an estimate of the temperature. There are also many estimates and assumptions involved in the final stage of the calculation, and a realistic assessment of the accuracy of the resulting heat flux is not possible, but it probably exceeds $\pm 20\%$.

The measured values of heat flux have an accuracy of $\pm 15\%$, but this will be greater for the mean levels taken from the graphs.

Hence the theoretical and measured values are, with the exception of sample B10-06, sufficiently close for their error bands to overlap.

7. CONCLUSIONS.

7.1. The Formation And Structure Of Slag Layers.

1) Slag layers are formed through splashing caused⁵⁸ by the arcs, as described by Bowman and Fitzgerald.

2) The thickness of a layer is dependent on its melting temperature, the material arrival rate, the frequency of shedding and the arc heat flux.

3) The structure of a layer is, typically, alternate sublayers of slag and metal, which are related to the state of the bath during the melt cycle.

4) Layers are shed from the panel frequently, predominantly during the early stages of the melt, and often every cycle.

7.2. Heat Transfer Through The Slag Layer.

5) The heat flux from the furnace to the cooling water is influenced by the thickness of the panel slag layer.

6) A simple linear model can be applied to heat flow from the hot face of the panel slag layer to the water cooling.

7.3. Properties Of Slags.

7) The thermal conductivity of the steelmaking slag of the composition given in Table II increases linearly from 1.45 W/mK at 300 C to 1.54 W/mK at 800 C.

8) The specific heat capacity of the same slag at room temperature is 724 J/kg K.

9) The density of the same (unsintered) slag at room temperature is 3.15 kg/m³.

7.4. Experimental Technique.

10) The described apparatus can be used to measure the thermal conductivity of materials between approximately 300 and 800 C, provided the approximate conductivity is known so that a suitable similar material can be used for calibration.

11) The best practical method of producing samples of slag for thermal conductivity measurement is by the compaction and sintering of powdered slag.

8. FURTHER WORK.

8.1. Slag Layer Control.

The conclusions in sections 7.1. and 7.2. are based on observations of a single furnace, although there is no reason to suppose that similar large steelmaking furnaces would show different behaviour for the same melting practice.

The appended case study explores the benefits of being able to reduce heat losses by control of the slag layer. It concludes that potential heat savings of 20 kWh/tonne are available and suggests how these might be achieved.

The areas of development work required are -

- a) Hot water cooling, using water at high pressure with an inlet temperature of approximately 150 C.
- b) Improved slag catcher design to reduce occurrence of layer shedding and maintain thicker layers.
- c) Deliberate splashing of steel for short periods to create stronger panel layers and hence reduce shedding.
- d) Increased shielding of the arc by the bath slag.
- e) Furnace design with respect to -
 - i) maximising the arc to panel distance.
 - ii) reducing the hot spot effect.

The scope of slag layer control is however limited because of the restrictions imposed by other parameters of the process. For example, productivity and melt analysis control considerations will generally outweigh any heat loss cost benefits.

8.2. Heat Transfer Models.

Having established that the sidewall can be considered as a linear heat flow problem, further work is required to adapt Montgomery's equations ⁶⁰ such that the heat losses can be related to the arc conditions during the flat bath period. Extending the model to cover the whole melt cycle, where the heat transfer can not be approximated to steady state, creates a very complex problem.

The simple linear model itself requires refinement to better account for the factors discounted by the assumptions made, such as the slag catchers and air gaps. Also, the calculation of thermal conductivity of multicomponent layers has not really been fully tested, and a program of work could be undertaken to determine whether the combined Russell's equation applies across the whole range of possible structures.

8.3. Thermal Conductivity Measurements.

There are three areas in which the experimental work could form the basis for future investigations.

Firstly, in the determination of the thermal conductivities of slags of different compositions, particularly as there is so little published data on this subject.

Secondly, the measurement of samples containing metal, which was touched upon, could be extended across a range of metal contents both to test the theory based on Russell's equation and to compare with actual slag layer samples.

Finally, the method of measuring thermal conductivity which was developed has proved to be an effective economic alternative to the existing standard methods for materials such as slags, and offers scope for future work in thermal conductivity measurement of other similar materials.

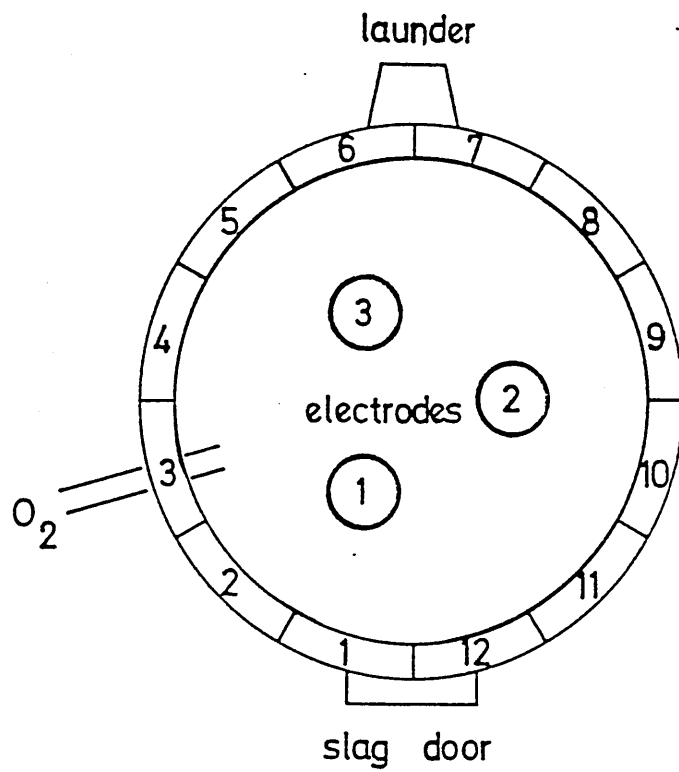


Figure 1. Furnace Layout Showing Panel Numbers.

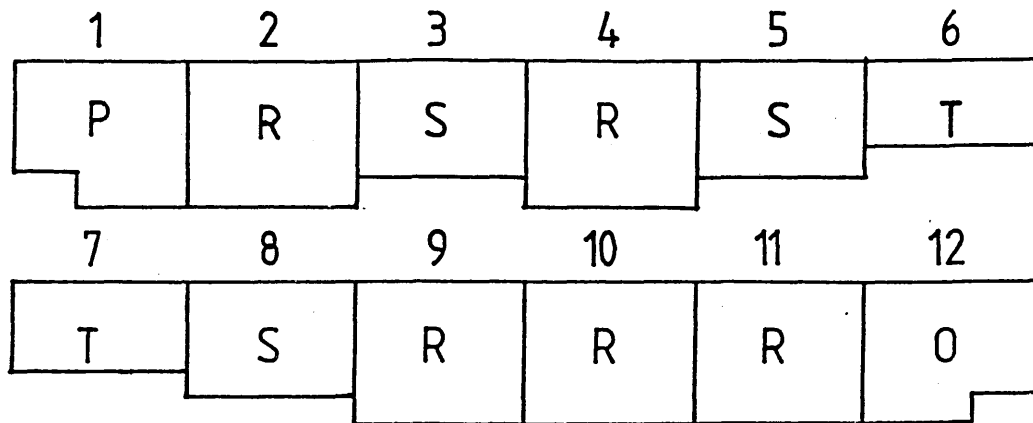


Figure 2. Detail Of Panel Configuration Showing Panel Types.

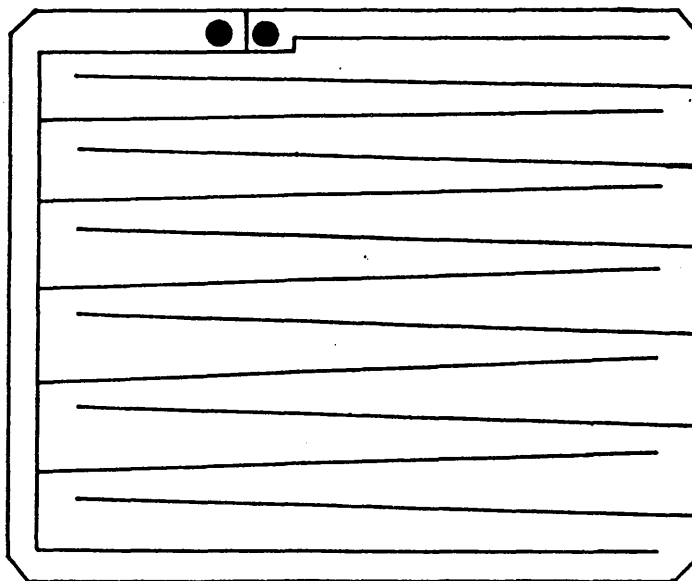


Figure 3. Schematic Diagram Of Internal Baffle System Of An "R" Type Panel.

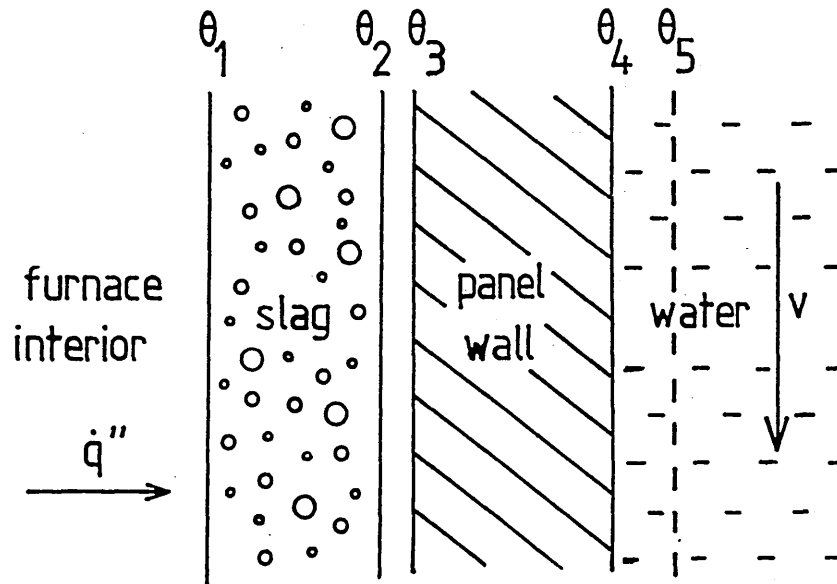


Figure 4. Schematic Diagram Illustrating Path Of Linear Heat Flow From Furnace Interior To Cooling Water.

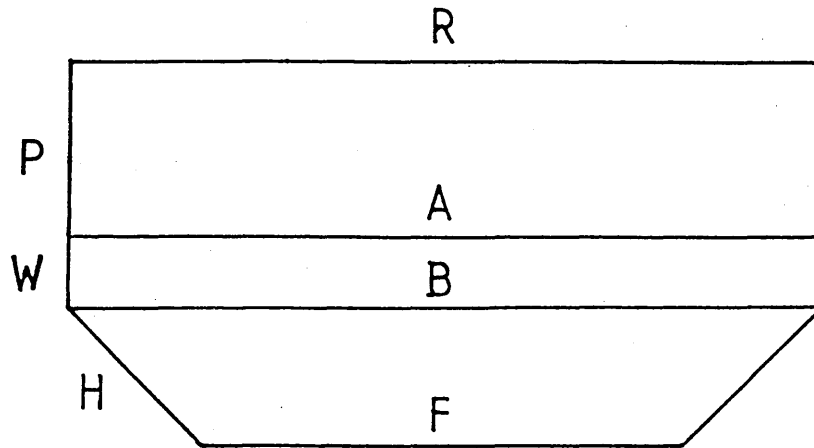


Figure 5. Simplified Geometry Of An Arc Furnace.

- R = roof
- P = water cooled sidewall panels
- W = refractory lower sidewall
- H = sloping side of hearth
- F = floor of hearth
- A = imaginary plane used in calculation
- B = surface of the bath

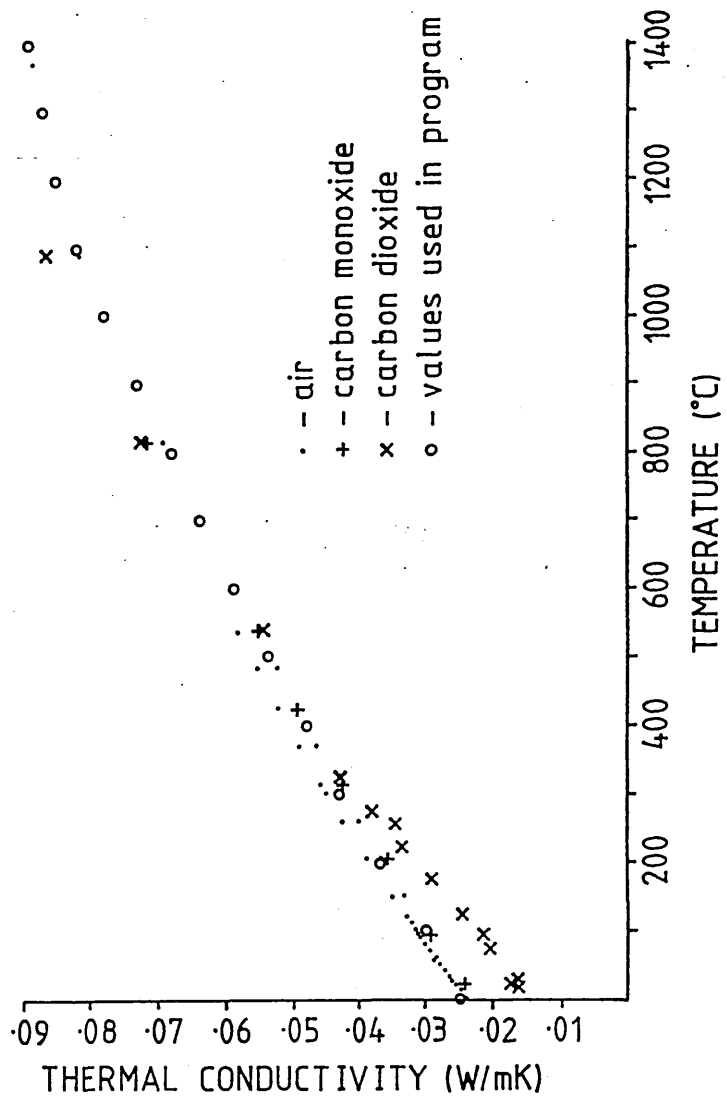


Figure 6. Thermal Conductivities Of Various Gases.

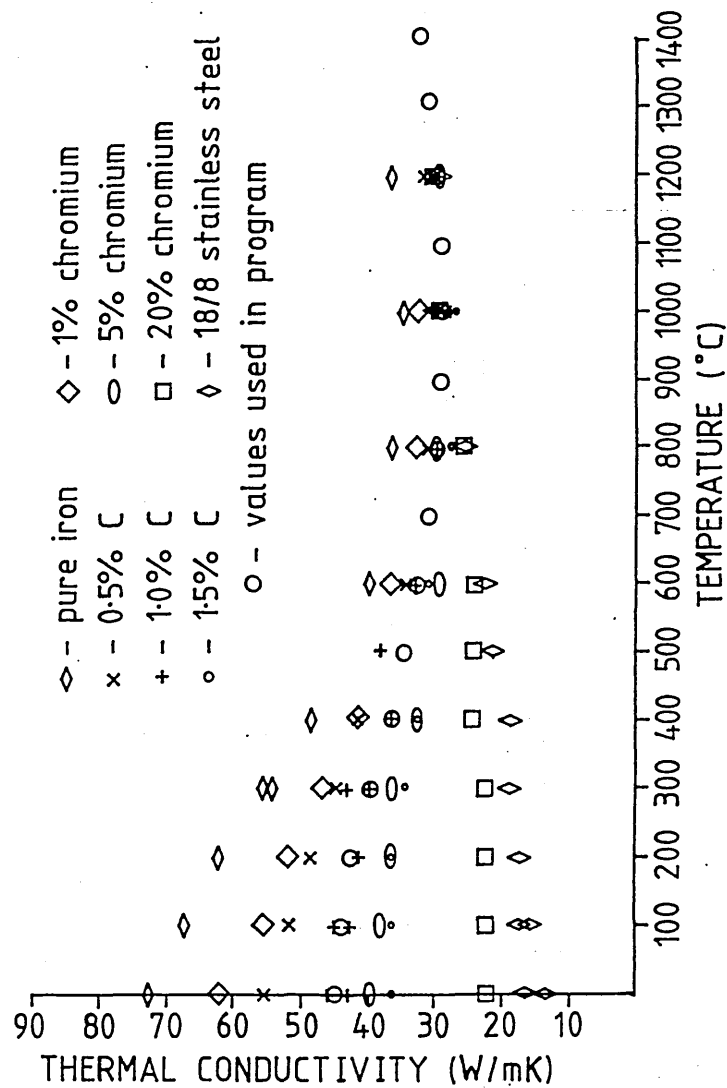


Figure 7. Thermal Conductivities Of Various Iron Alloys.

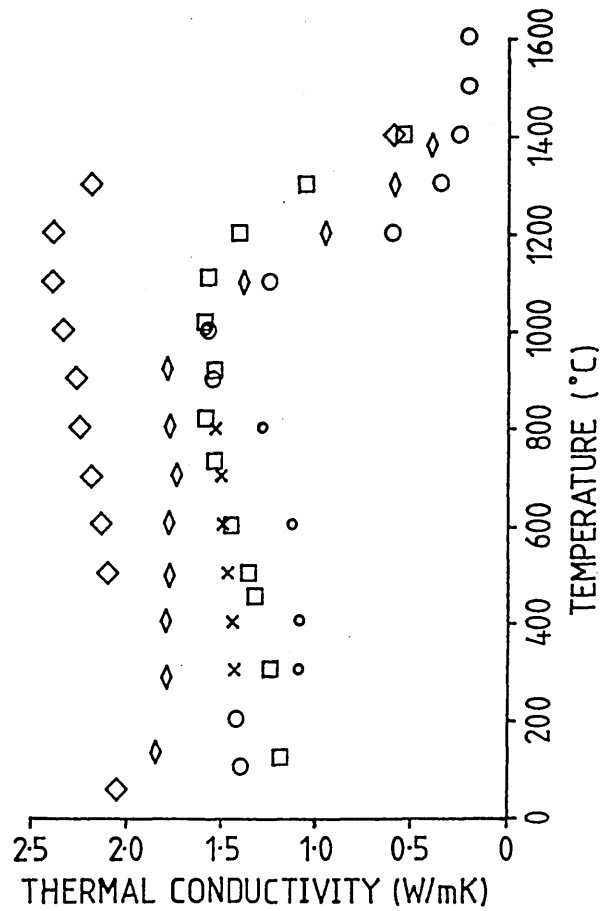


Figure 8. Thermal Conductivities Of Various Slags.

- ◇ - Blast Furnace Slag.
- ◇ - 24 CaO, 47 SiO₂, 29 Fe₂O₃.
- - 40 CaO, 40 SiO₂, 20 Al₂O₃.
- - 14 CaF₂, 43 CaO, 43 Al₂O₃.
- × - EAF Steelmaking Slag (used in program).
- - Estimated values used in program.

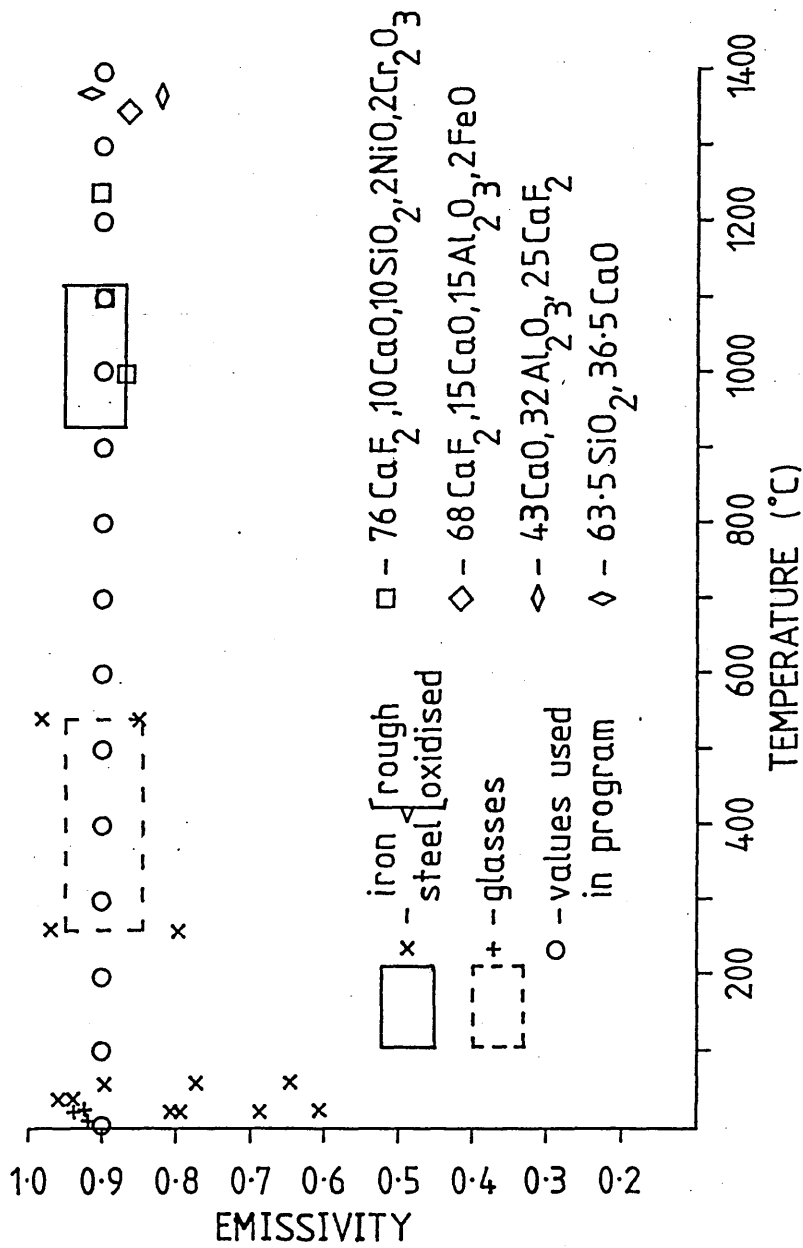
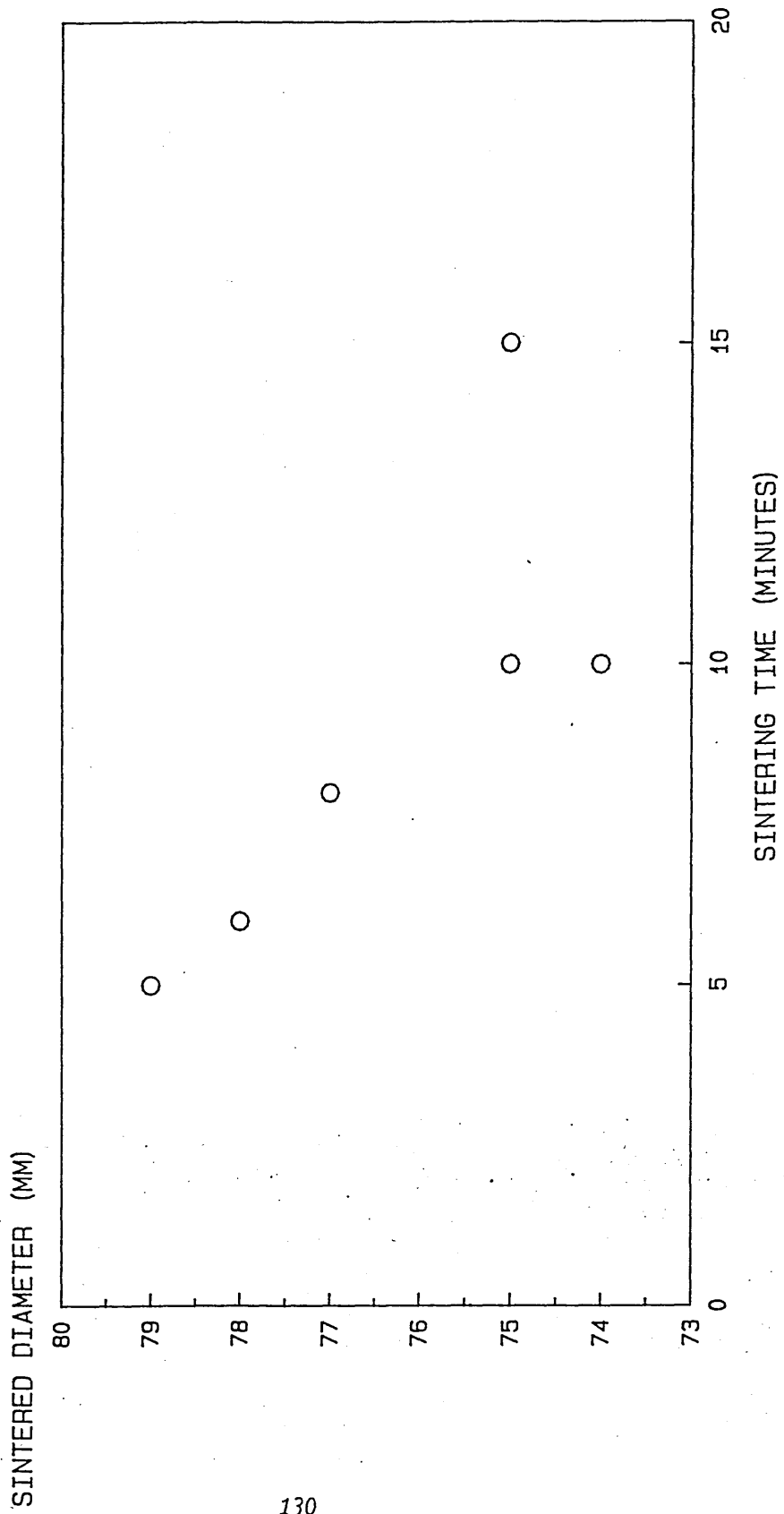


Figure 9. Emissivities Of Various Materials.

FIGURE 10. Dependence Of Sintered Diameter On The Time In The Furnace.



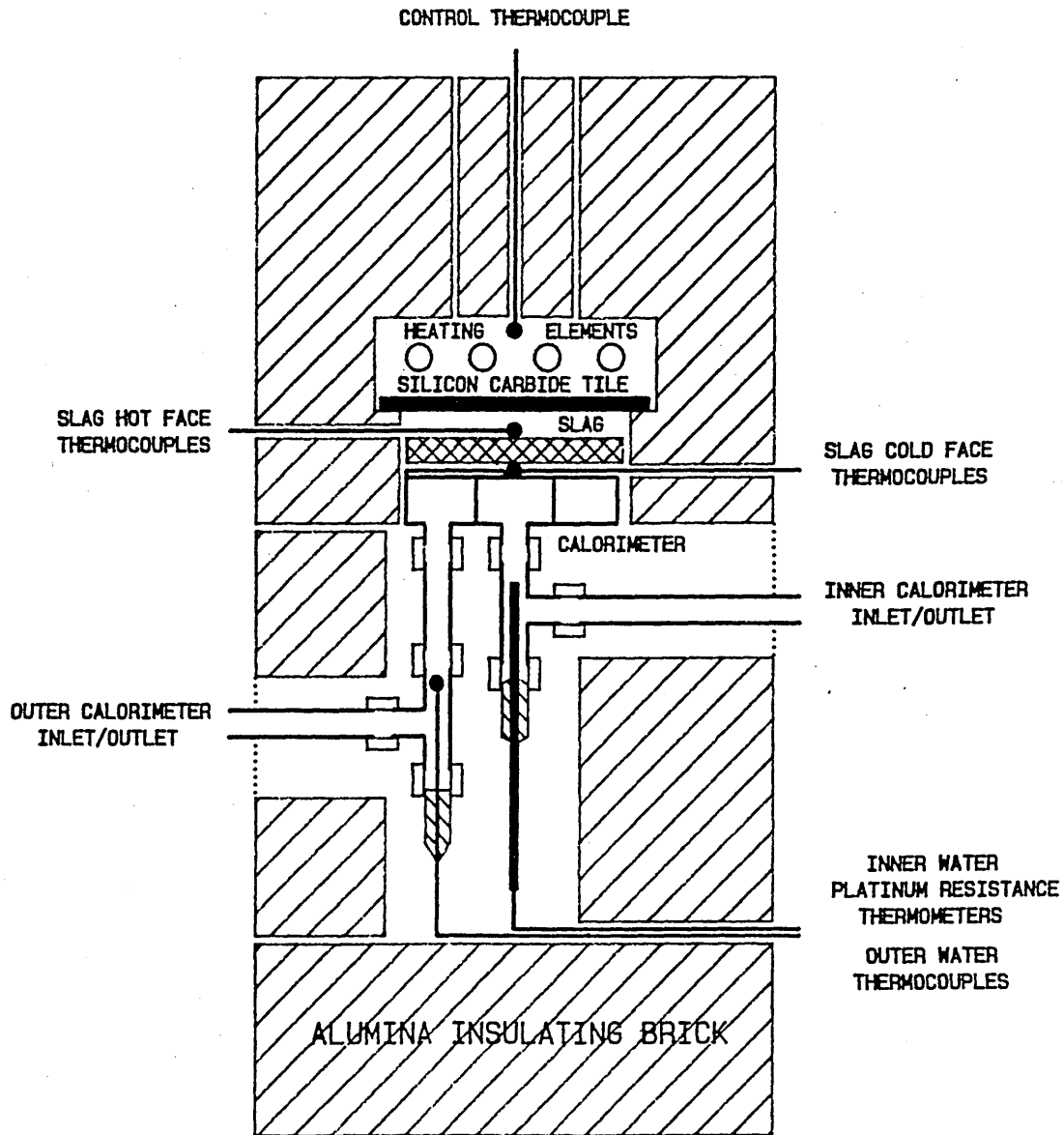
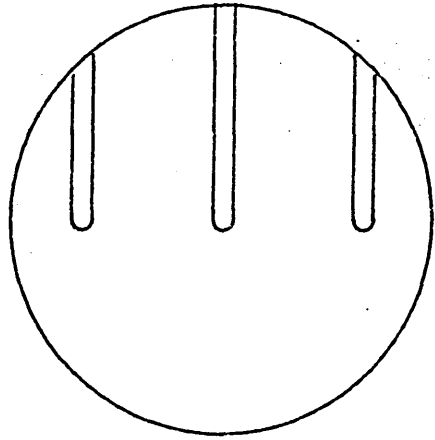
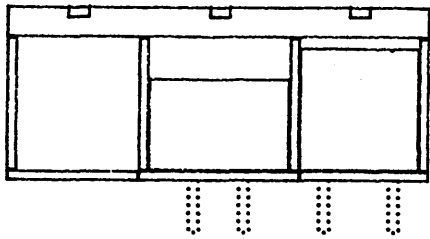


Figure 11. Schematic Diagram Of The Thermal Conductivity Measurement Apparatus.

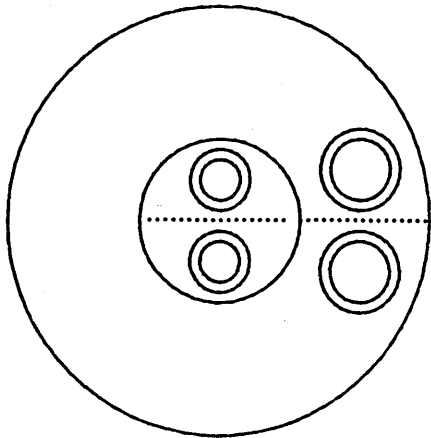


TOP VIEW



SECTION

50 mm



BOTTOM VIEW

Figure 12. Diagram Of The Initial Design Calorimeter.

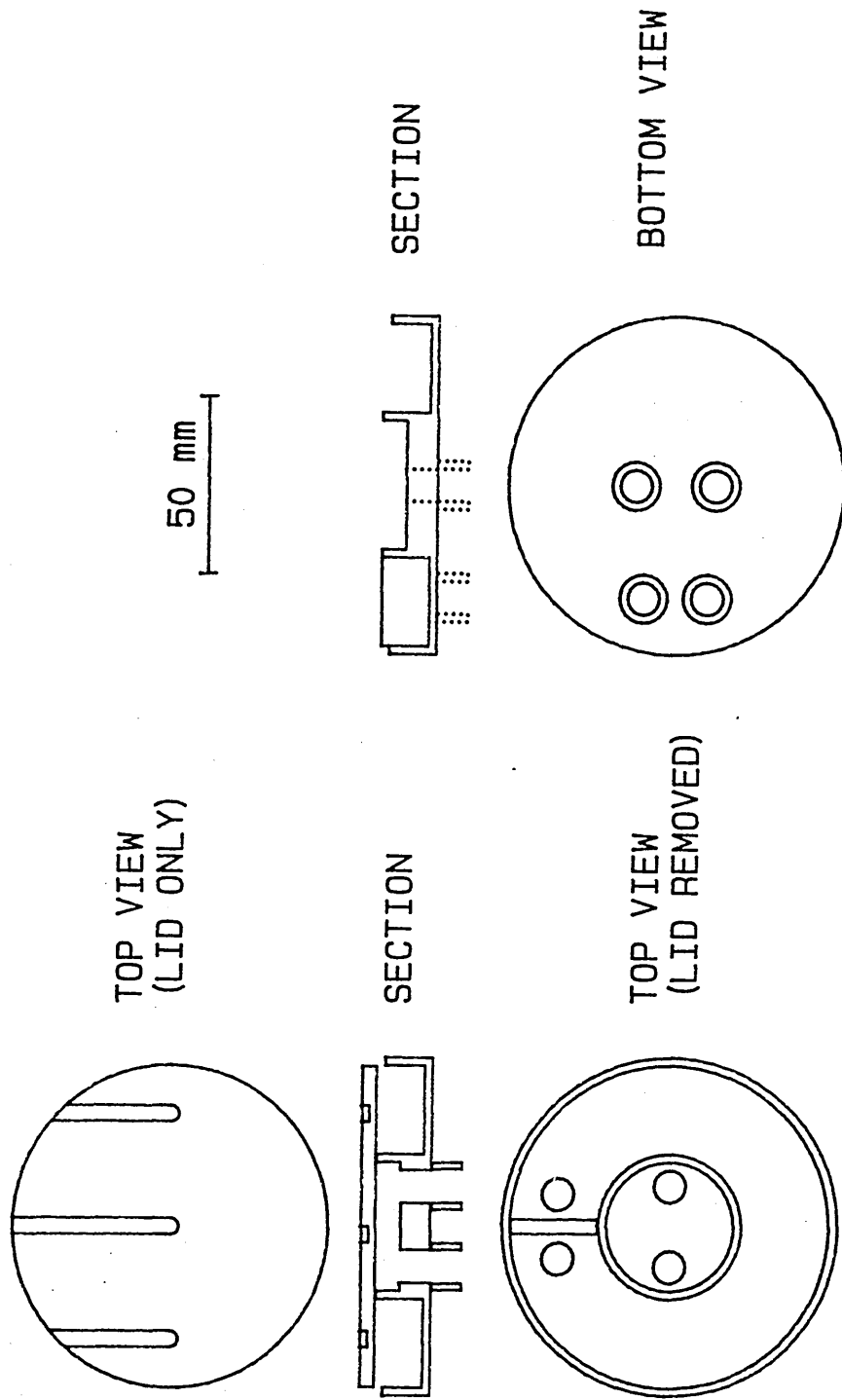


Figure 13. Diagram Of The Refined Design Calorimeter.

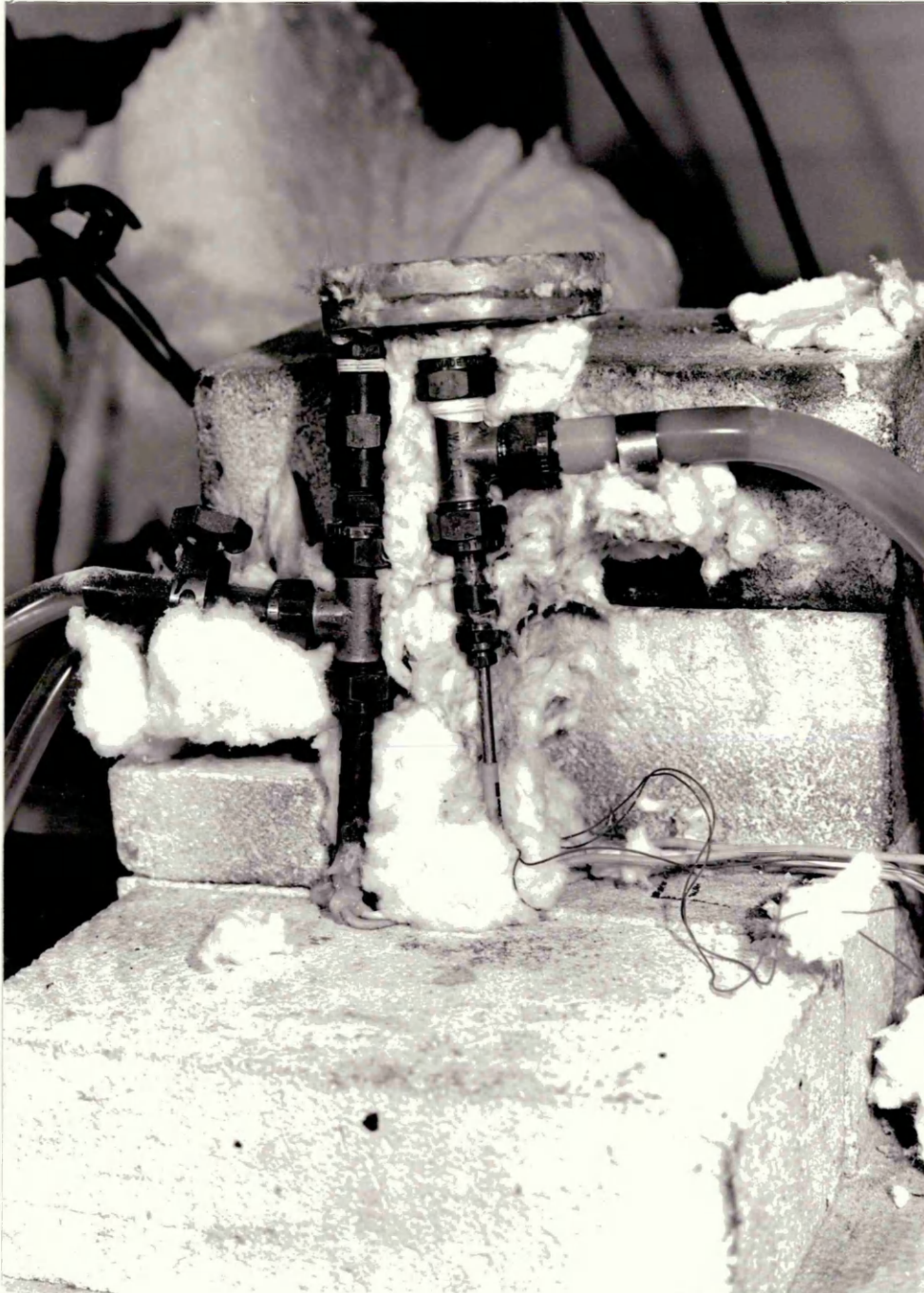


Figure 14. View Of Calorimeter In Position Showing The Water Connections And Thermometers.



Figure 15. View Of Calorimeter With Rig Partially Assembled Showing The Thermocouple Positions.



Figure 16. View Of Partially Assembled Rig Showing
The Sample, Radiation Tile And Resistance
Heating Elements.

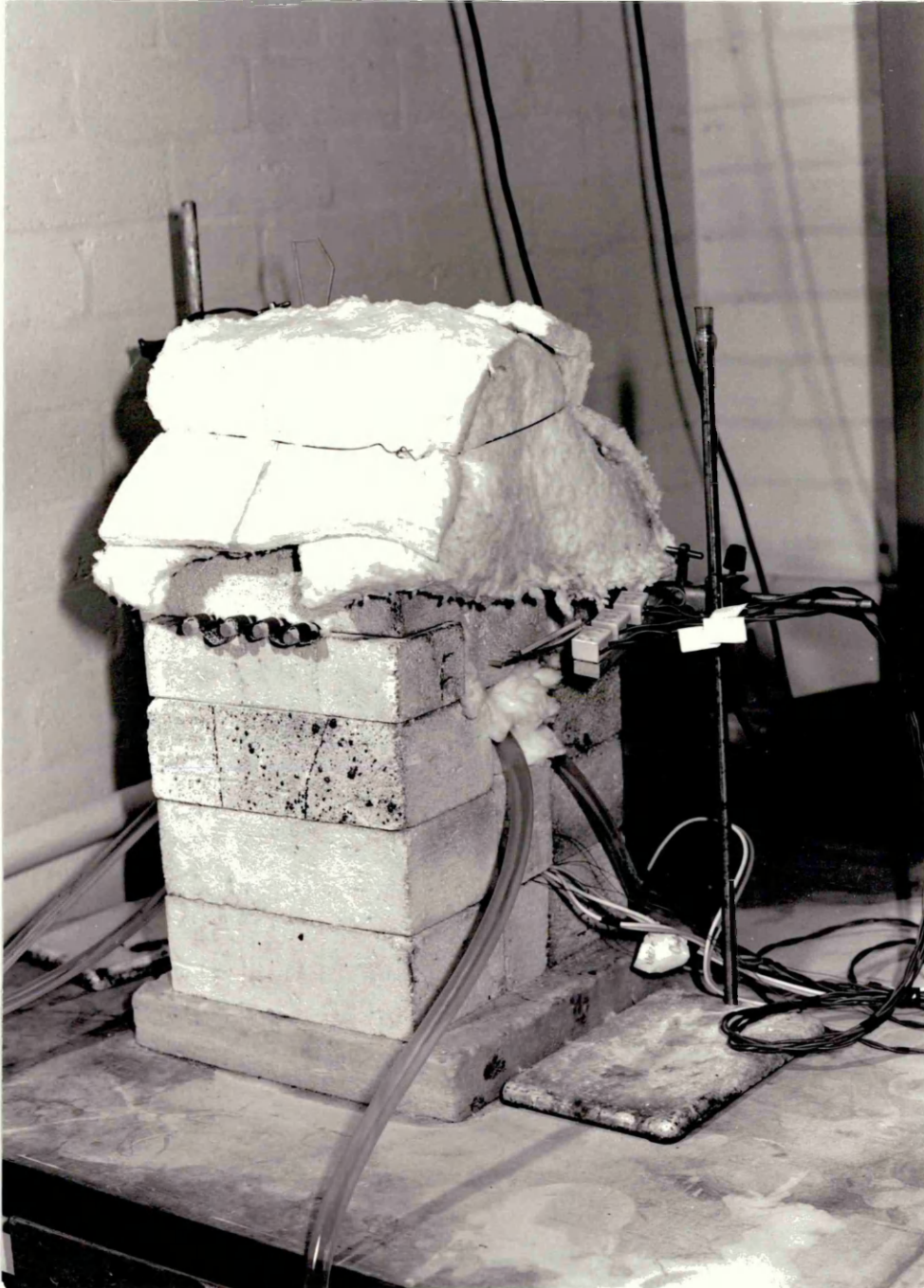


Figure 17. View Of Assembled Rig.

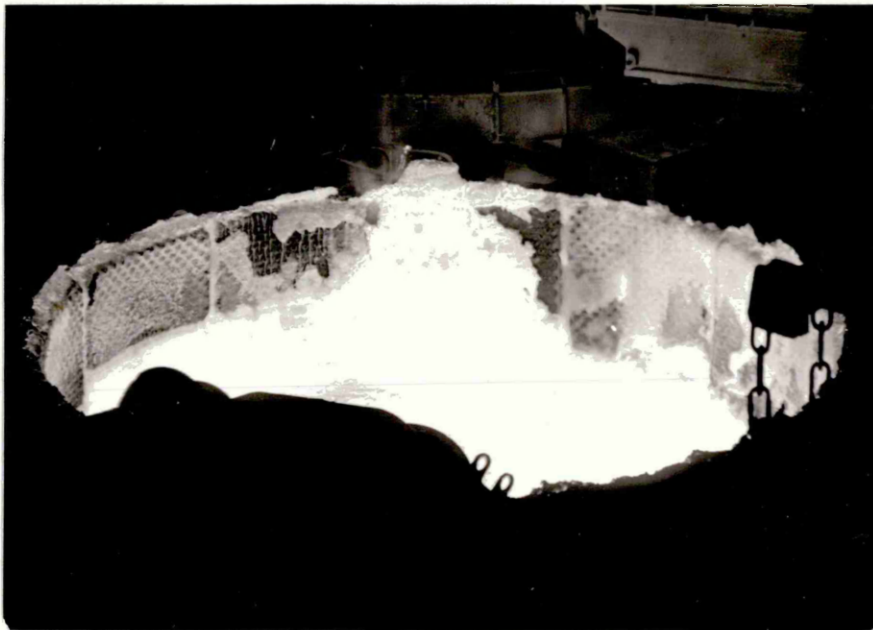


Figure 18. Slag Build-up In The Panel No. 8 Position.

FIGURE 19. Variation Of Slag Cover Around The Furnace.

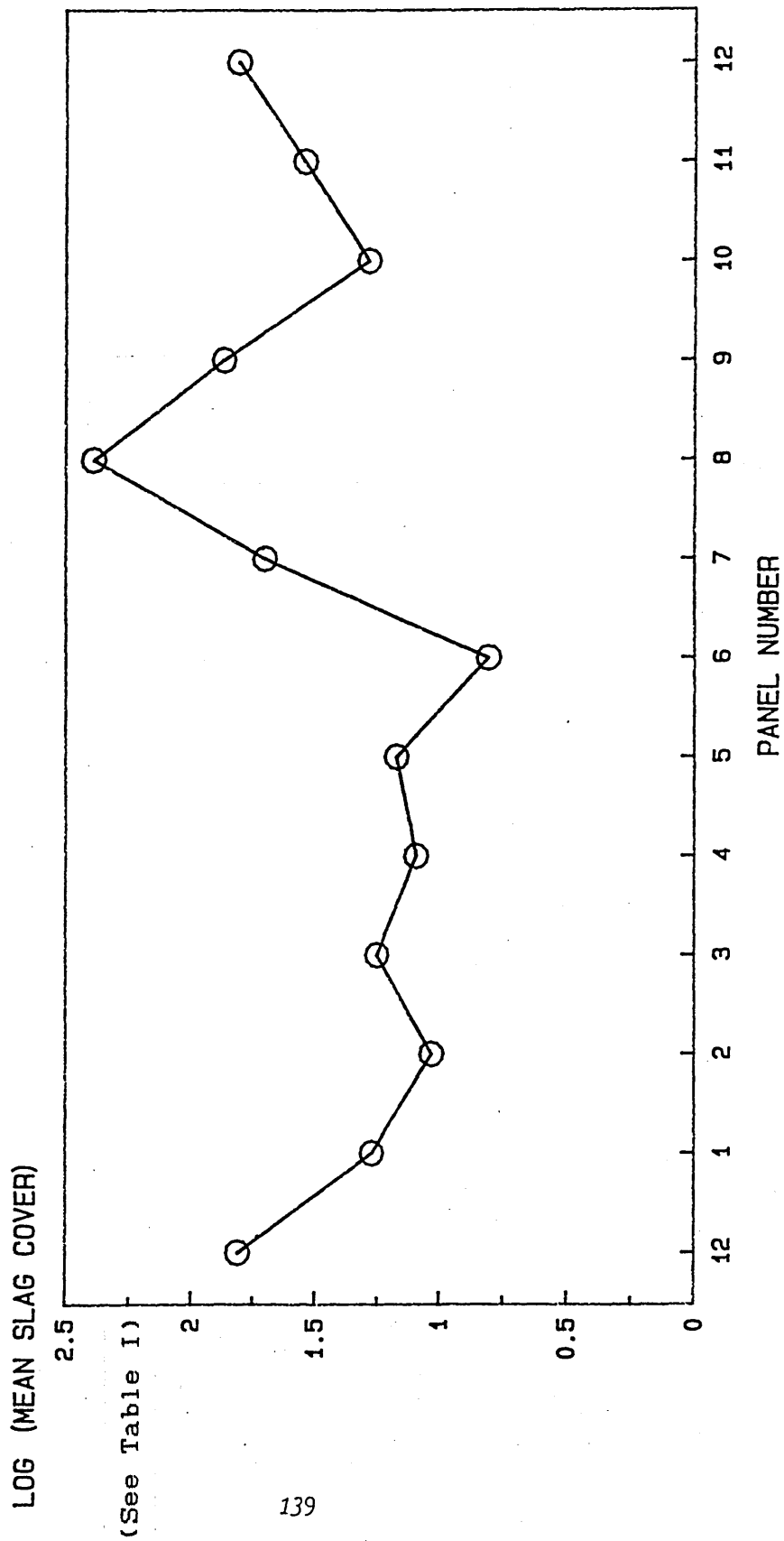




Figure 20 a) . Slag Layer Hot Face Of "Molten"
Appearance (x1) .



Figure 20 b) . Slag Layer Hot Face Of "Frozen Splash"
Appearance (x1) .

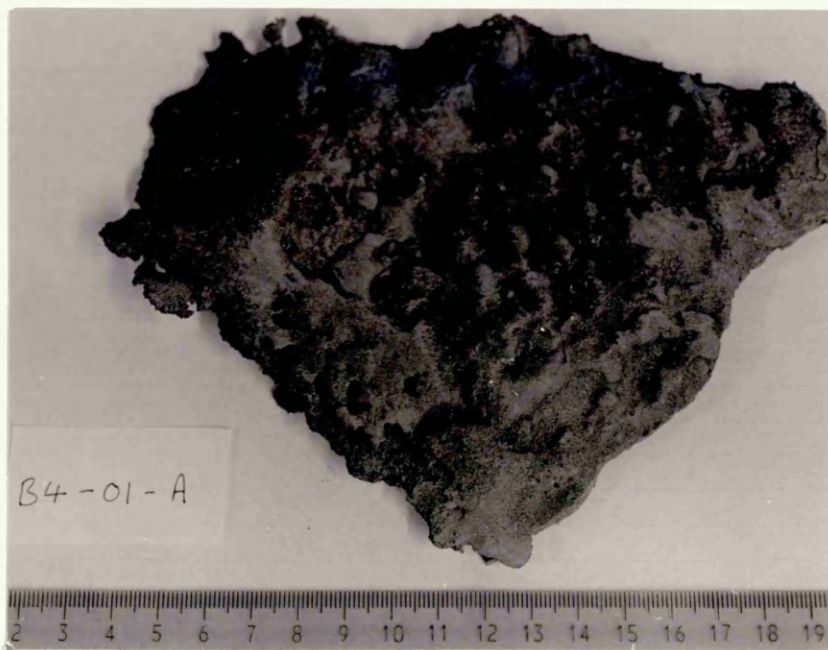


Figure 20 c). Slag Layer Hot Face Of "Lumpy" Appearance (x0.6).

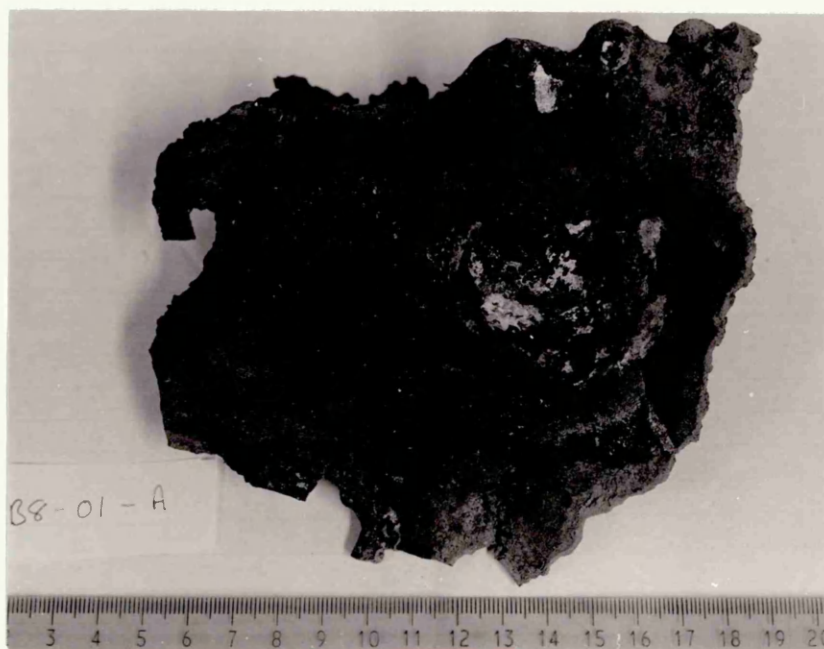
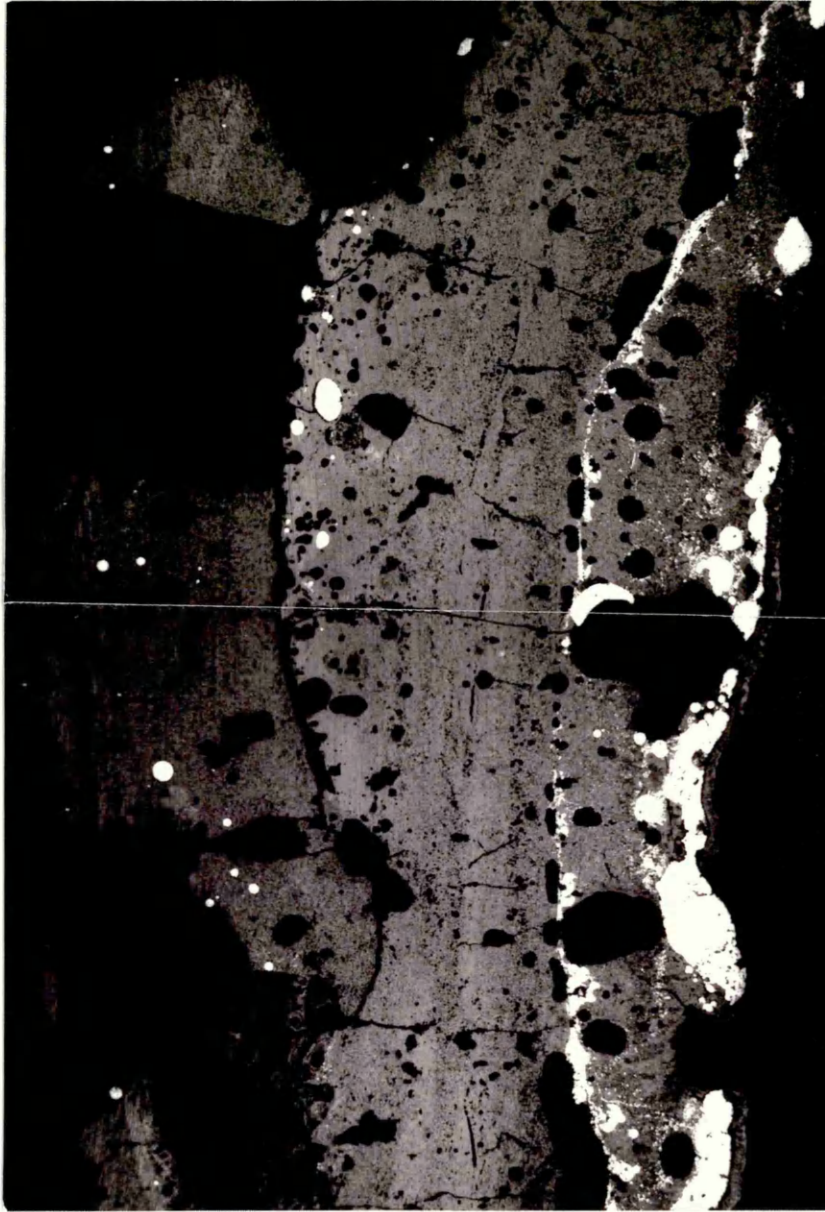


Figure 21. Slag Layer Cold Face Showing Patches Of Zinc Oxide (x0.6).



HOT FACE

Figure 22. Section Through Slag Layer Showing Various Metal Morphologies (x6).

HOT FACE

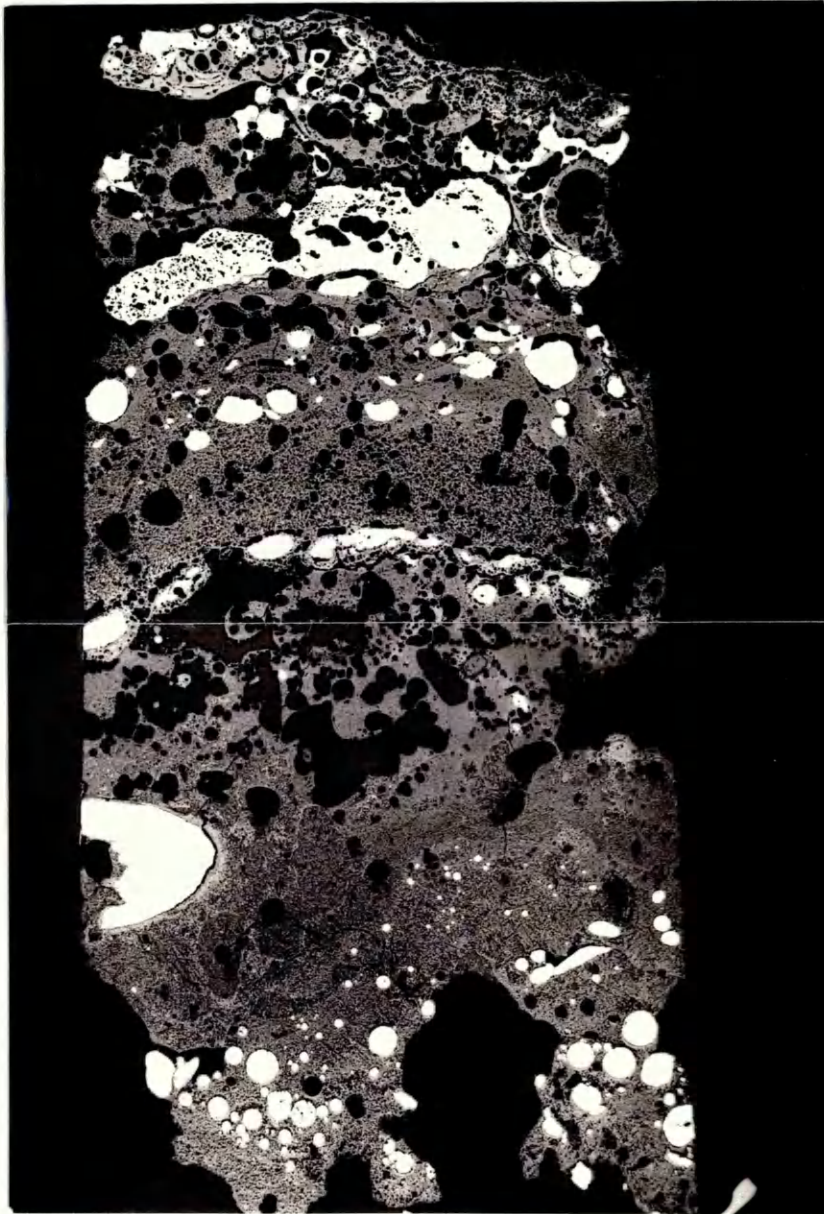


Figure 23. Section Through Slag Showing Layered Structure (x6) .

HOT FACE

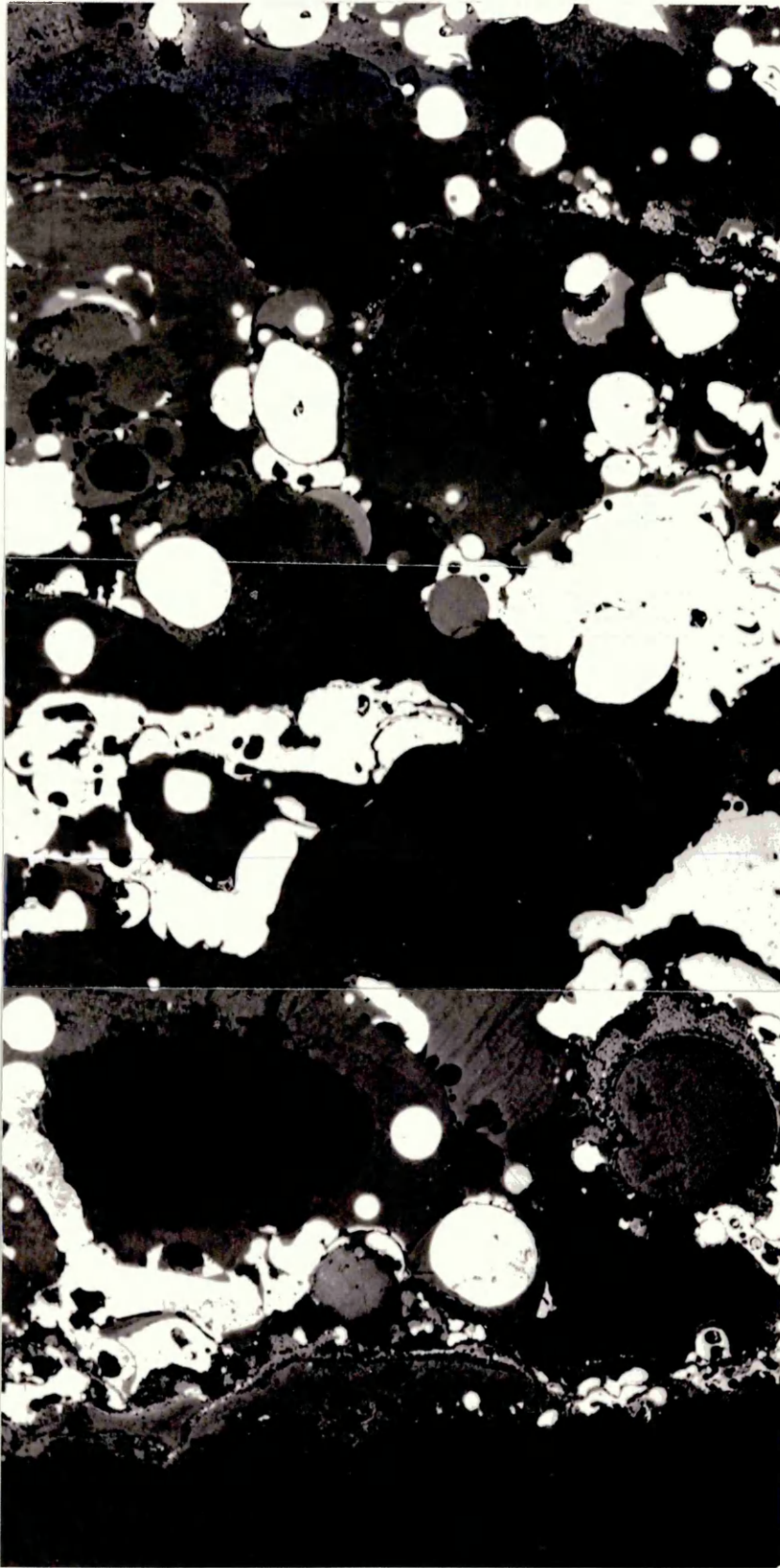


Figure 24. Section Through Slag Showing "Chilled" Structure (x65).

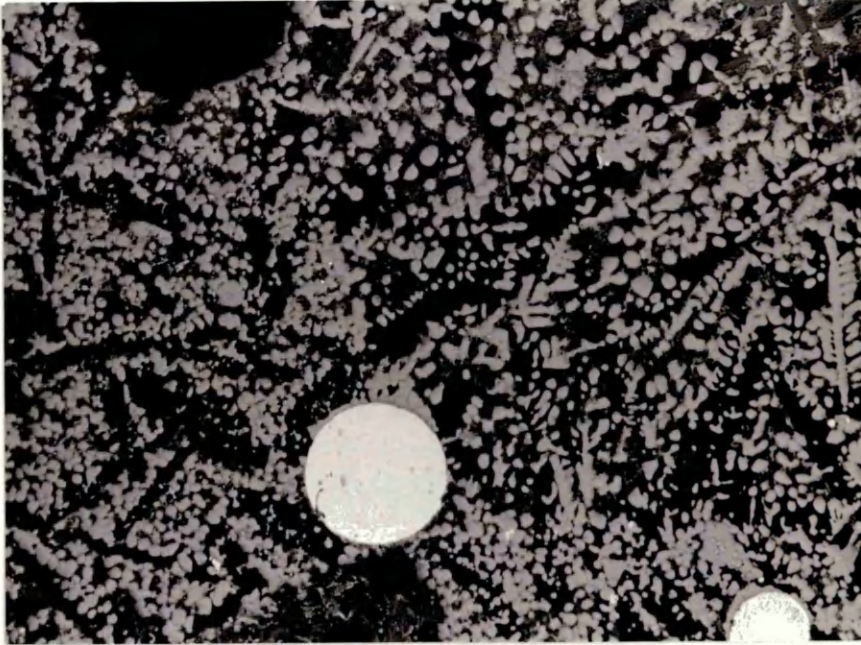


Figure 25 a) . Typical Slag Structure (x125) .



Figure 25 b) . Typical Slag Structure (x250) .

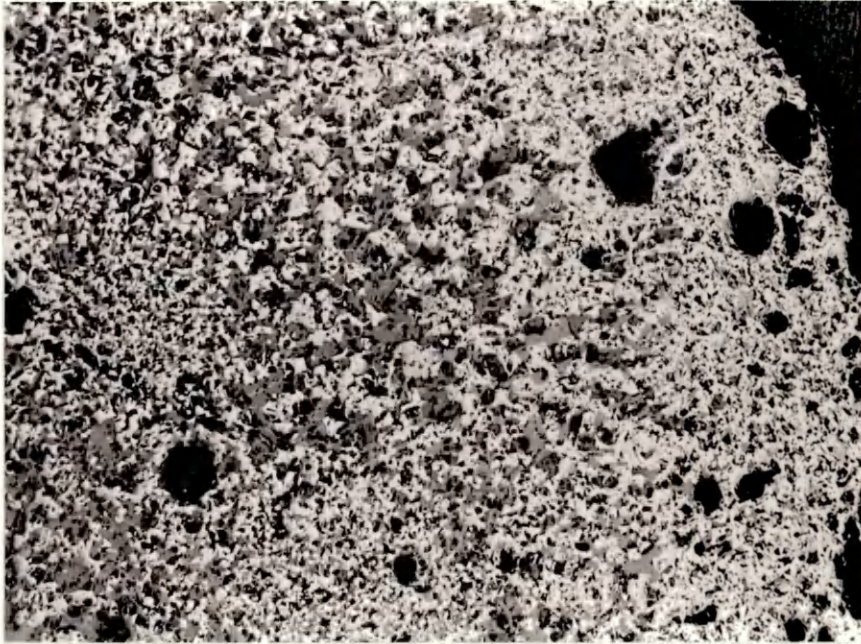


Figure 26 a) . Sintered Type Slag Structure (x125) .

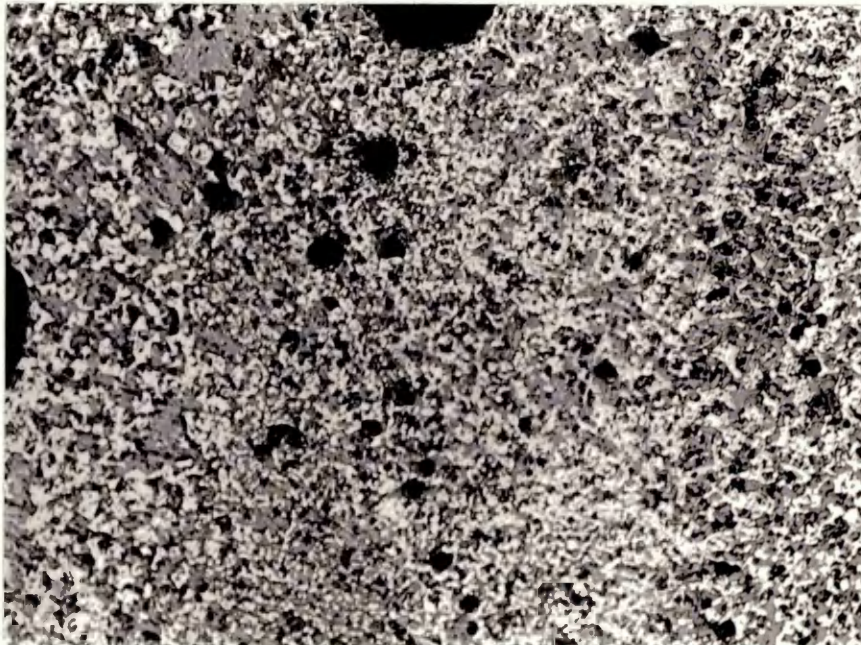


Figure 26 b) . Sintered Type Slag Structure (x250) .



Figure 27 a). Dissemination Of Metal Droplets
In The Slag (x250).

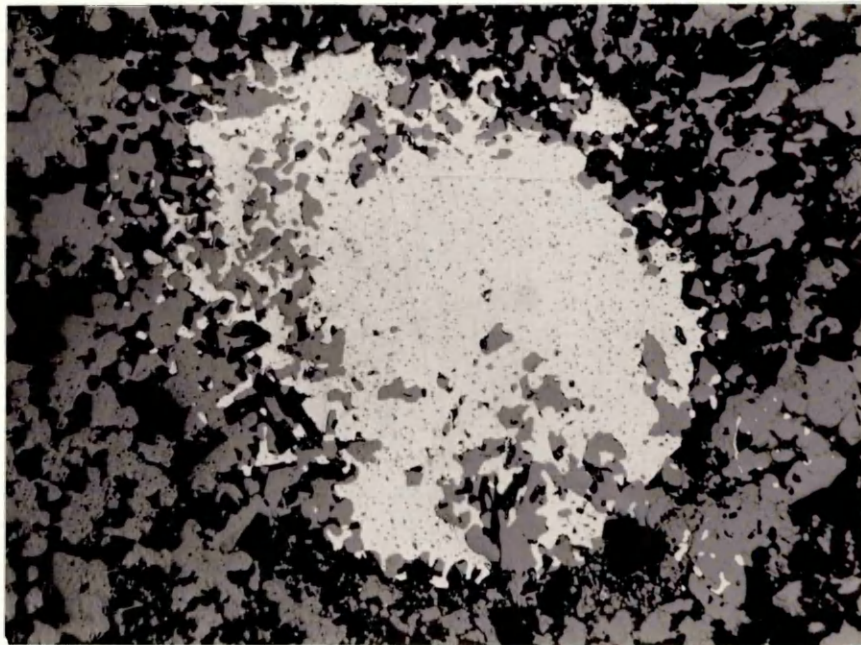


Figure 27 b). Dissemination Of Metal Droplets
In The Slag (x250).



Figure 28 a). Dissemination Of Metal Droplets
In The Slag (x250) .

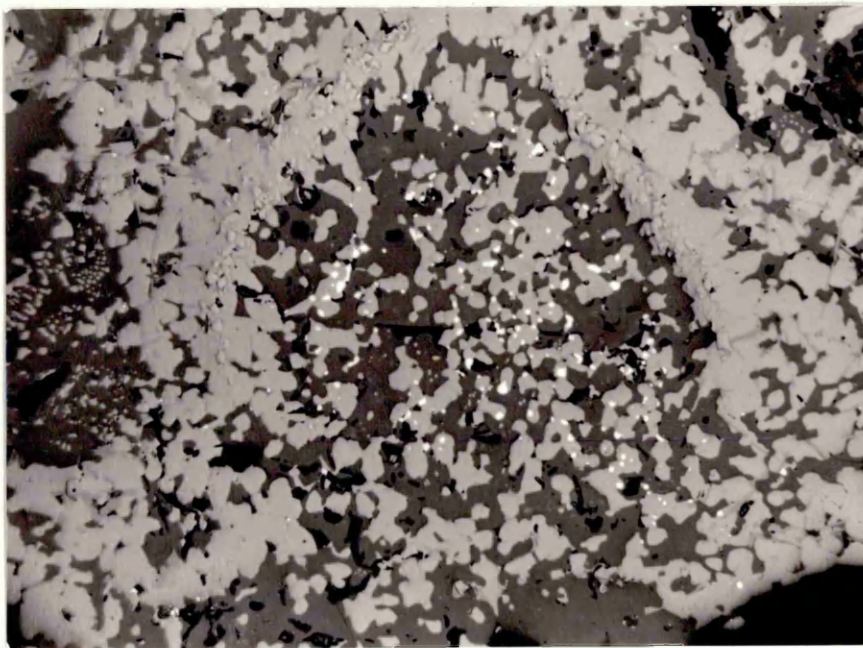


Figure 28 b). Dissemination Of Metal Droplets
In The Slag (x250) .

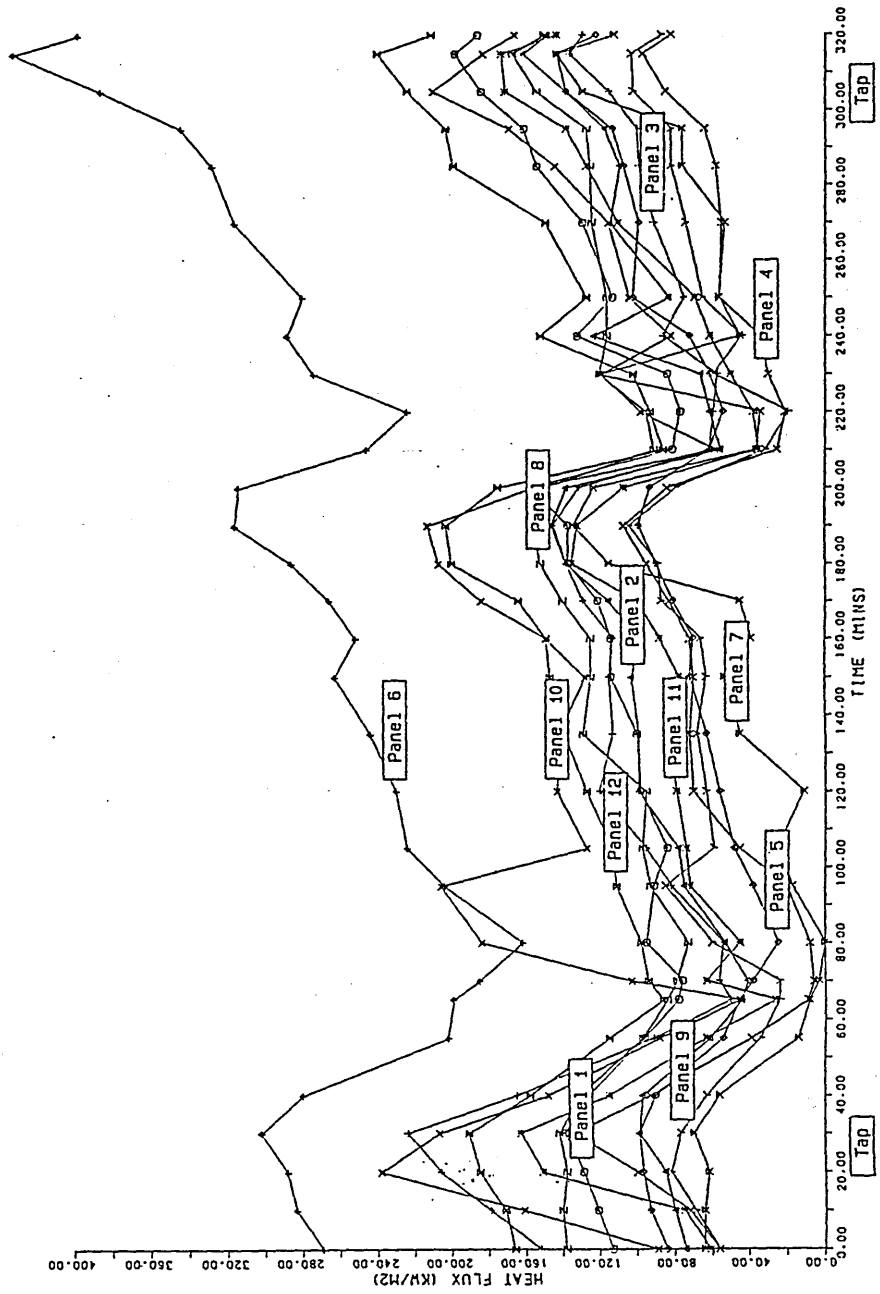


Figure 29. Variation Of Heat Flux With Time
(last cast of week - Dataset 01).

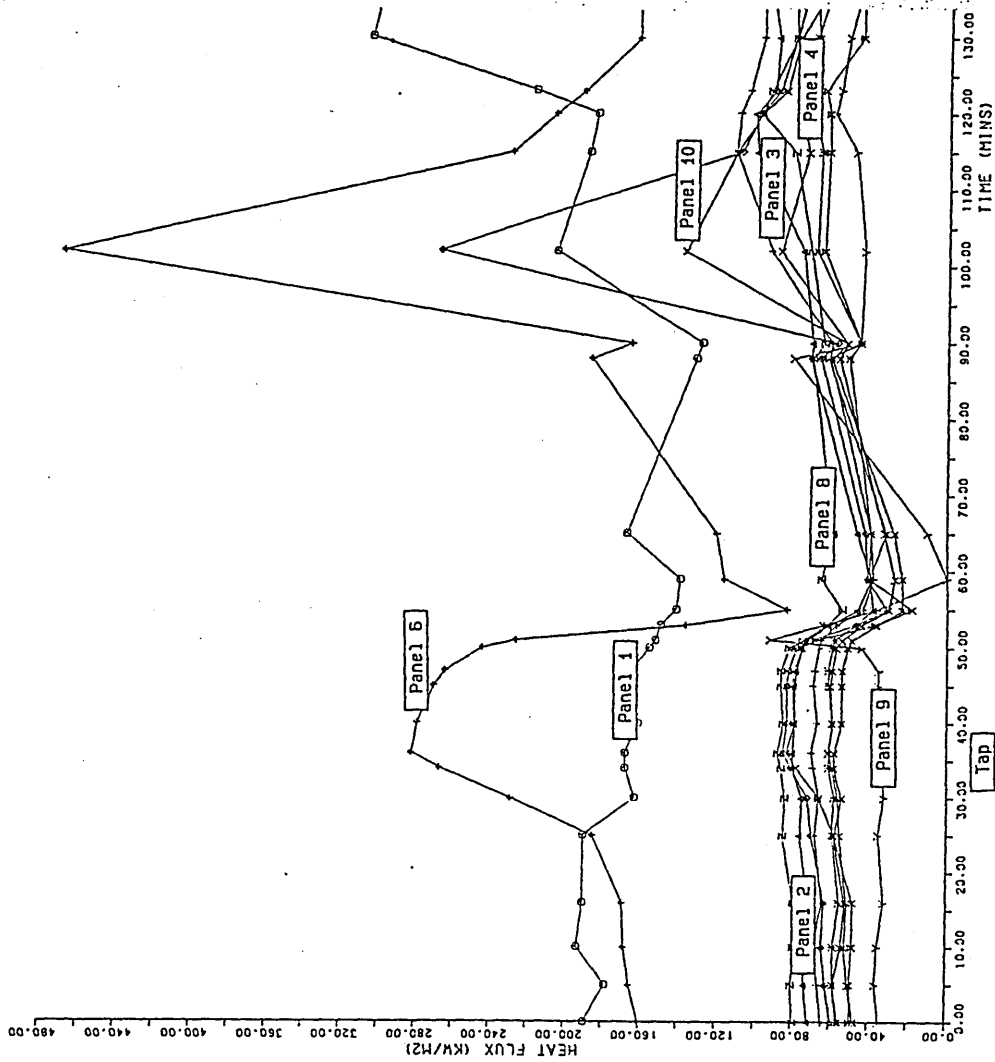


Figure 30 a). Variation Of Heat Flux With Time
(last cast of week - Dataset 02).

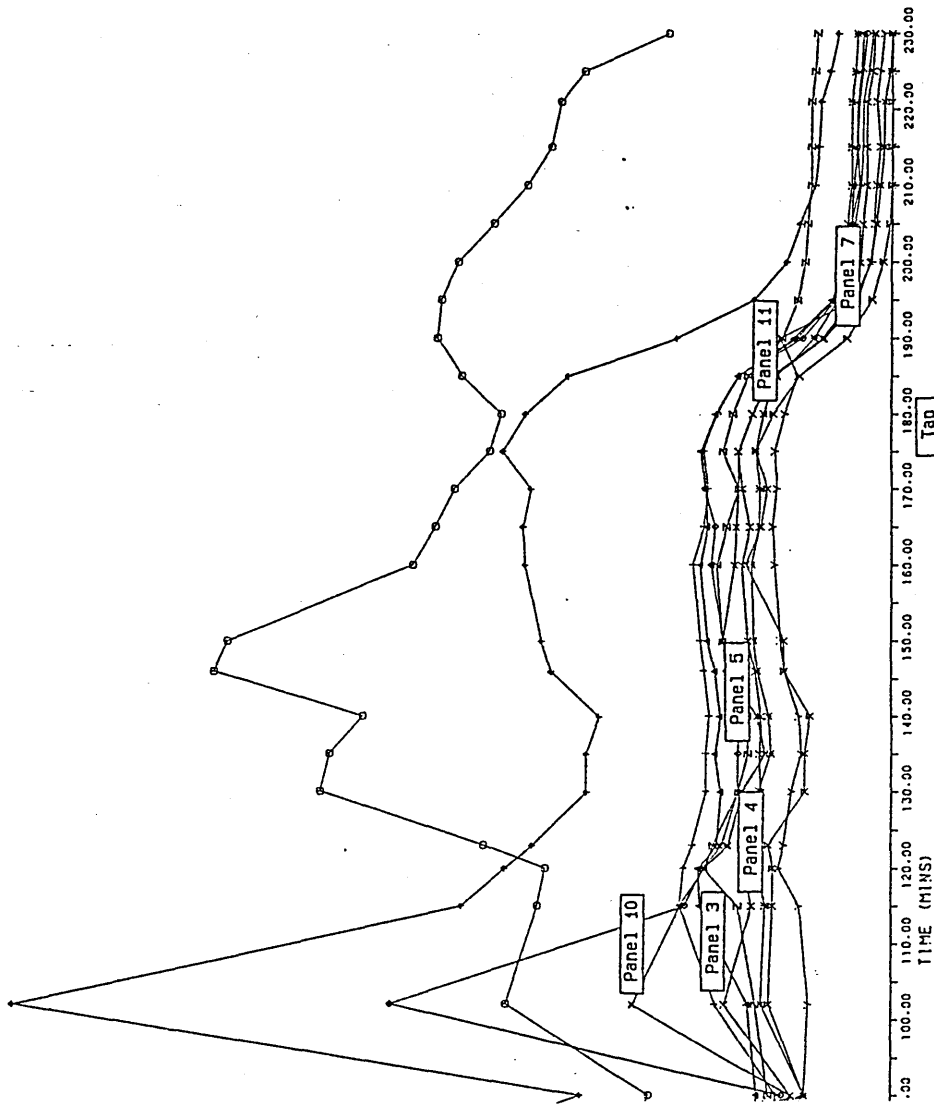
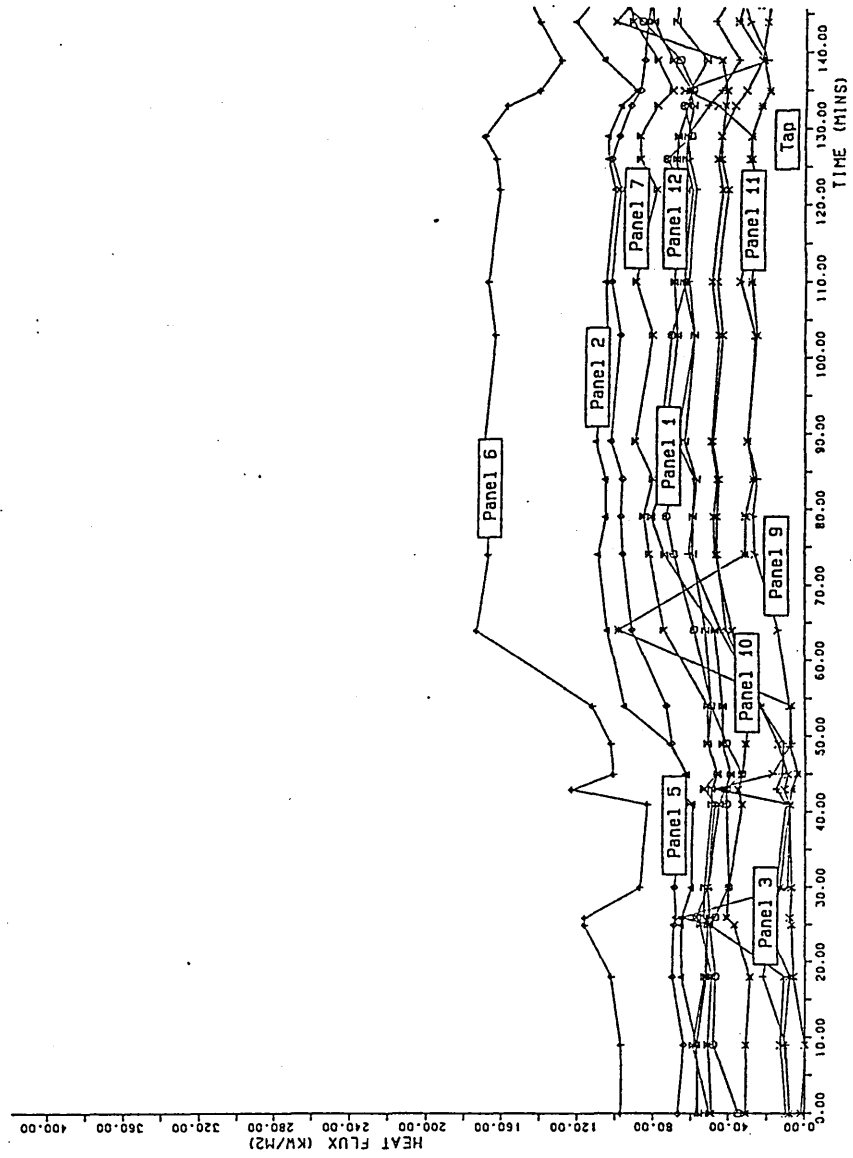


Figure 30 b) . Variation Of Heat Flux With Time
 (last cast of week - Dataset 02) .



**Figure 31 a) . Variation Of Heat Flux With Time
(last cast of week - Dataset 03) .**

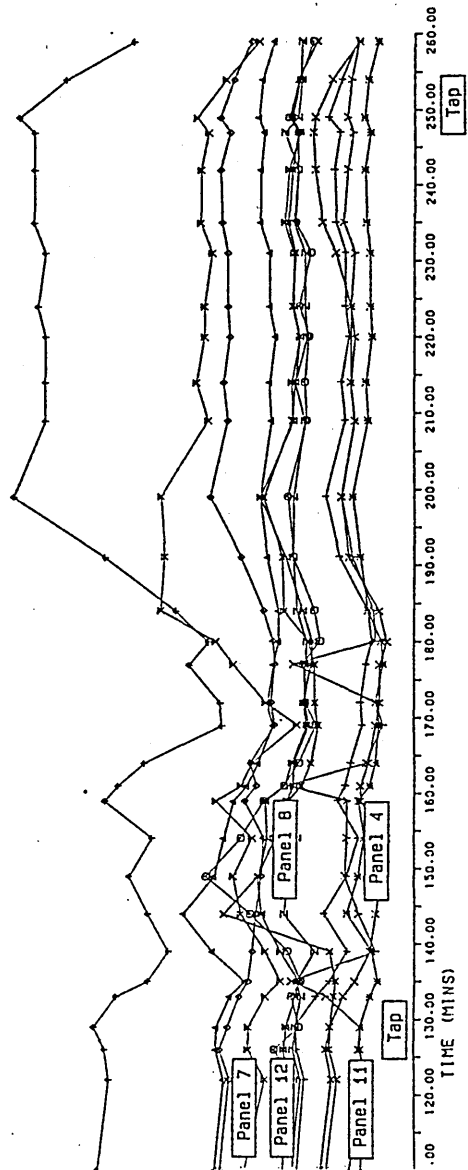


Figure 31 b) . Variation Of Heat Flux With Time
(last cast of week - Dataset 03) .

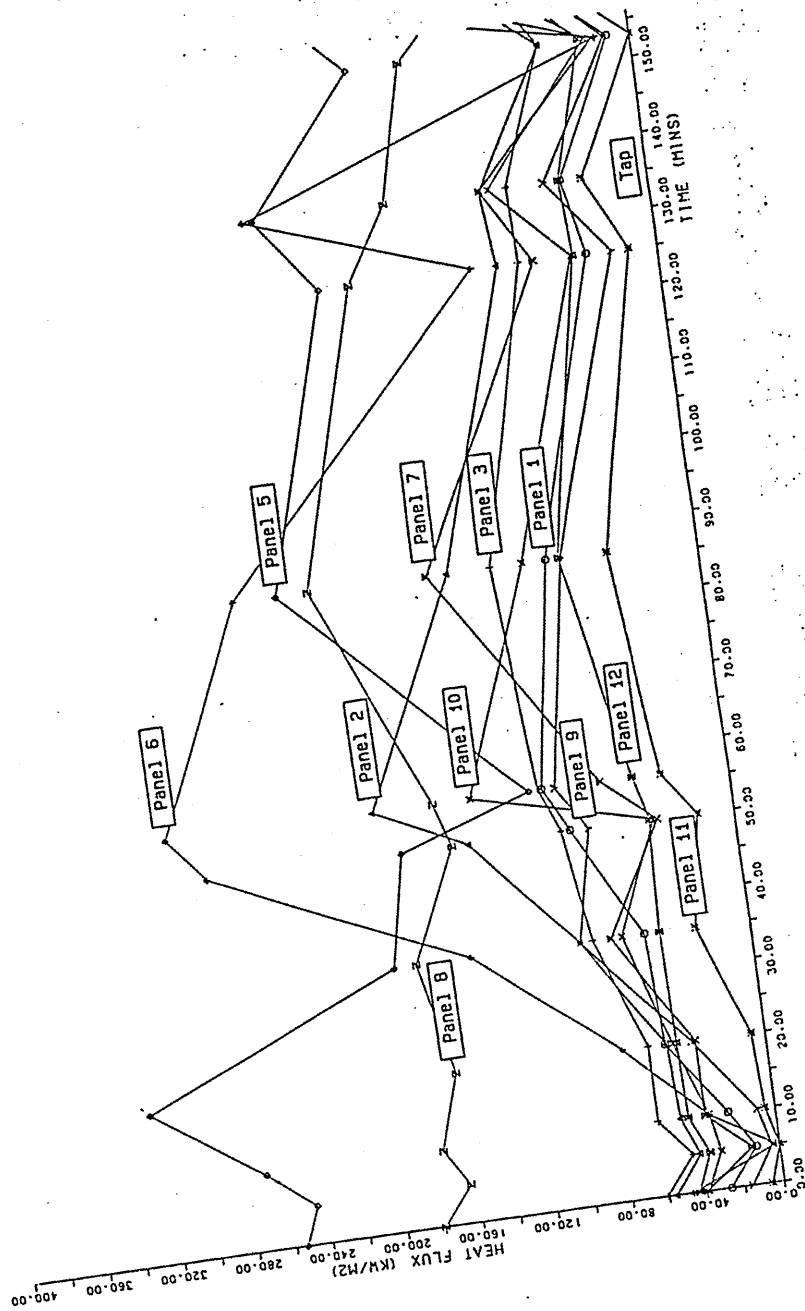


Figure 32 a). Variation Of Heat Flux With Time
 (last cast of week - Dataset 04).

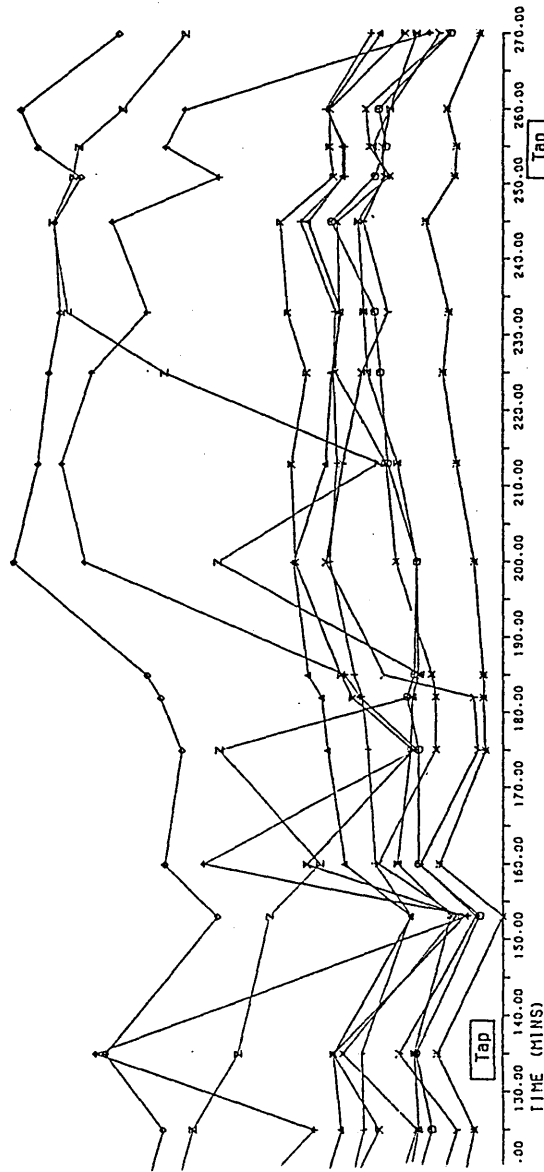


Figure 32 b) . Variation Of Heat Flux With Time
(last cast of week - Dataset 04) .

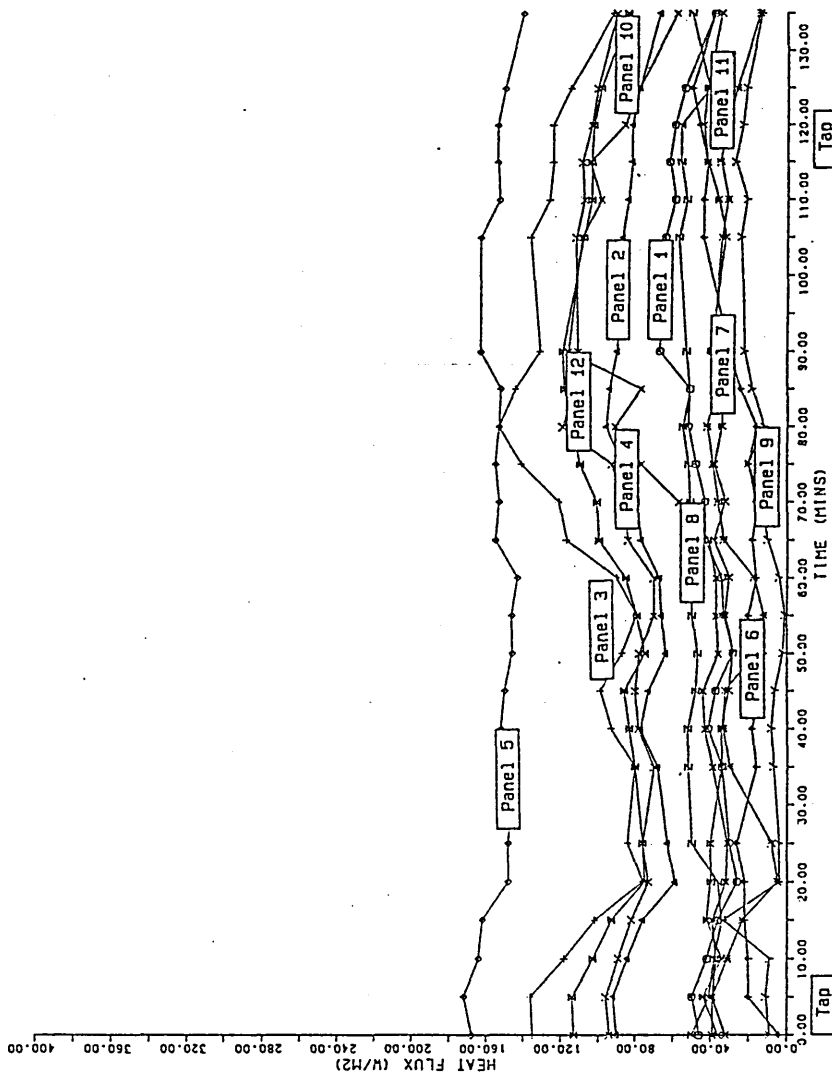


Figure 33. Variation Of Heat Flux With Time
(last cast of week - Dataset 05).

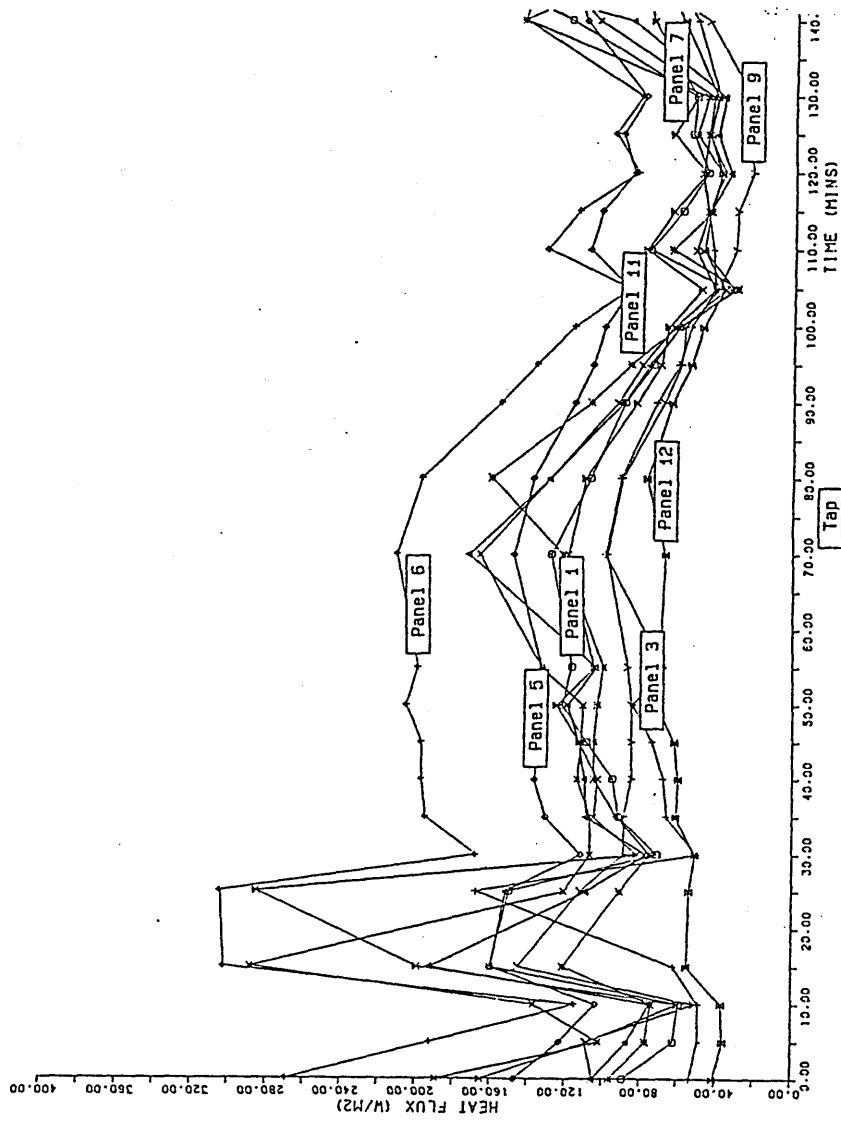


Figure 34 a). Variation Of Heat Flux With Time
(last cast of week - Dataset 06).

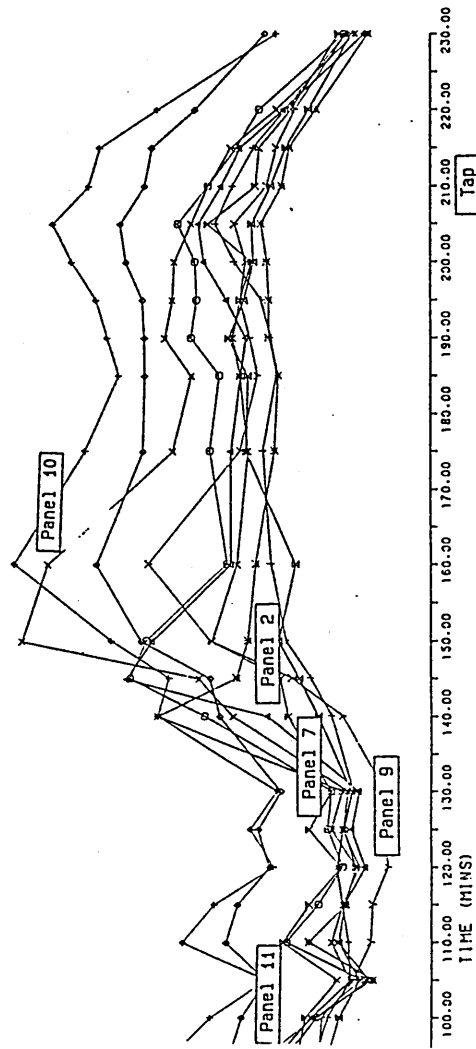


Figure 34 b) . Variation Of Heat Flux With Time
(last cast of week - Dataset 06) .

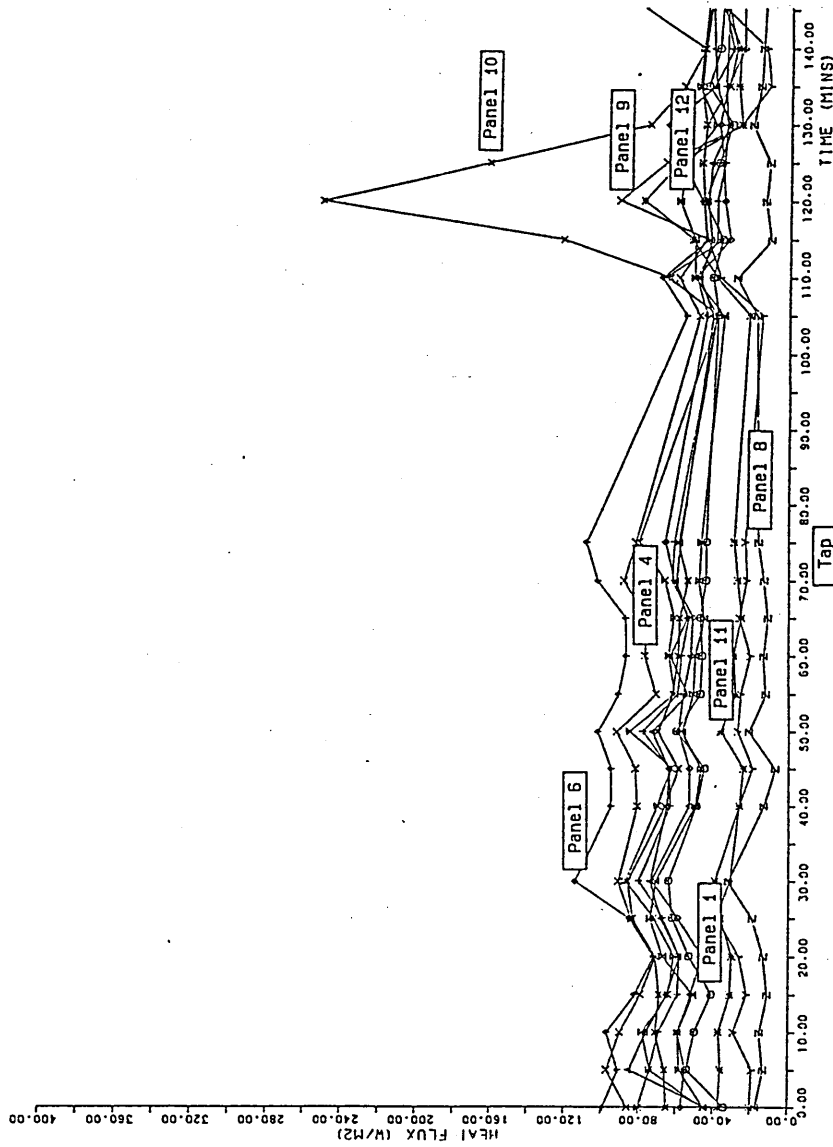


Figure 35 a). Variation Of Heat Flux With Time
(last cast of week - Dataset 07).

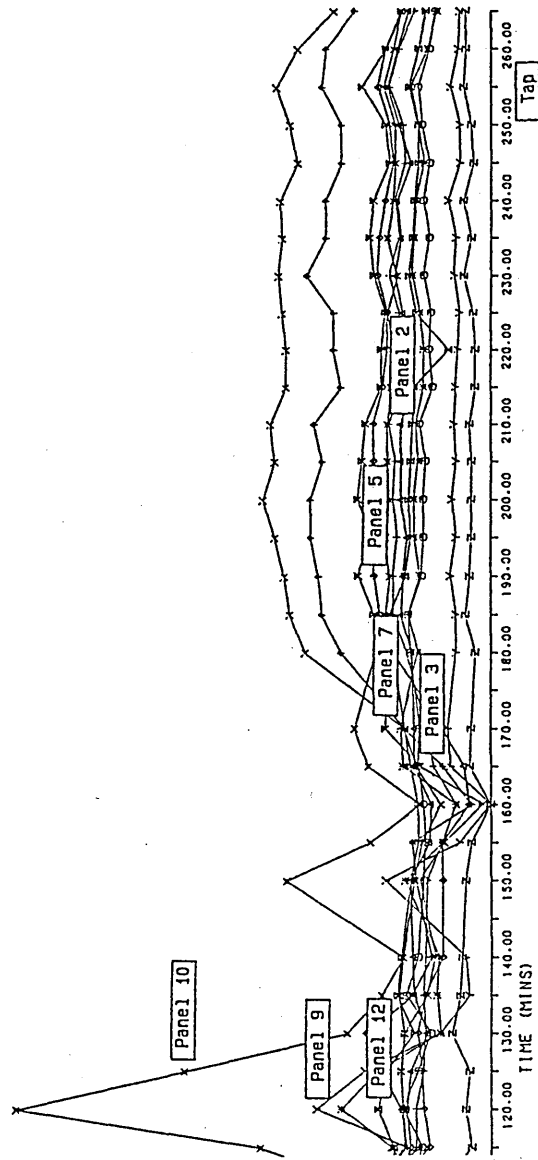


Figure 35 b) . Variation Of Heat Flux With Time
(last cast of week - Dataset 07) .

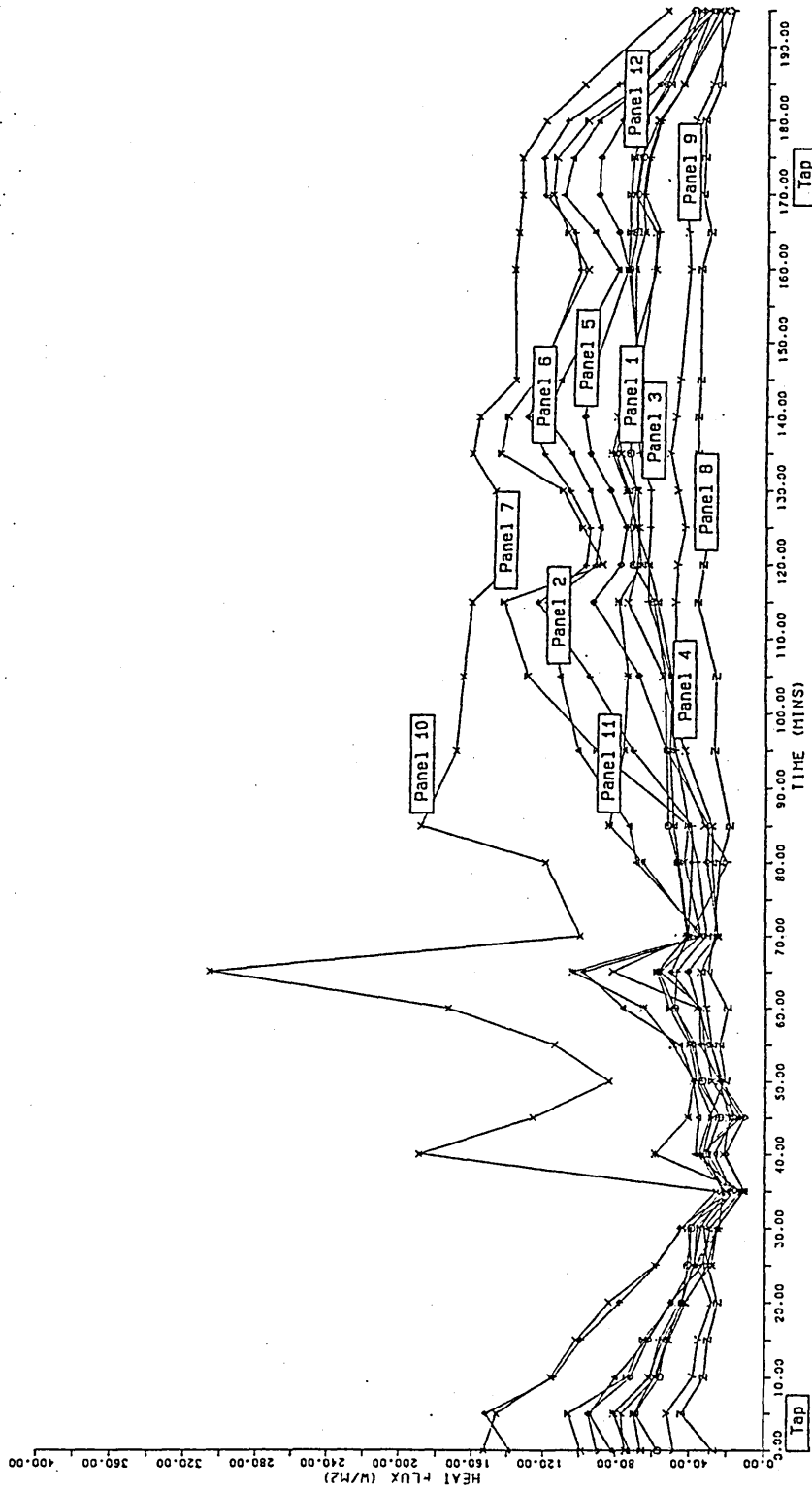


Figure 36. Variation Of Heat Flux With Time (last cast of week - Dataset 08).

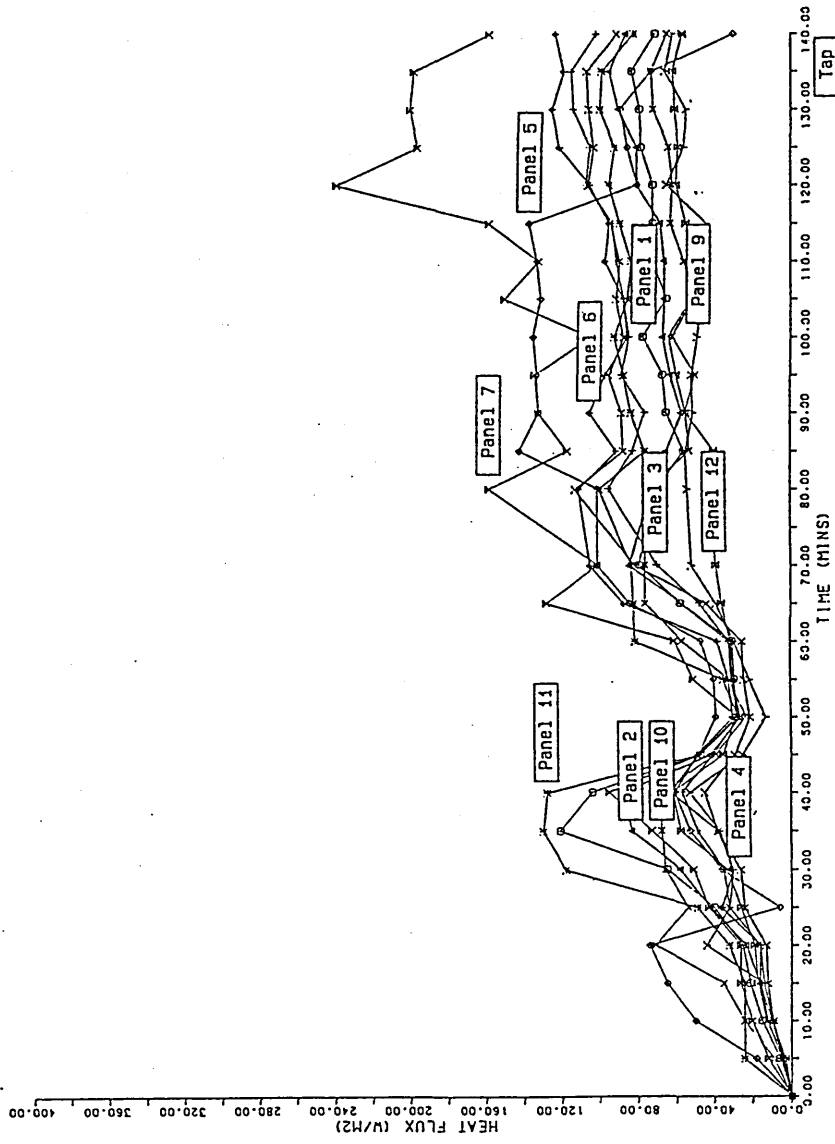


Figure 37. Variation Of Heat Flux With Time
(first cast of week - Dataset 06).

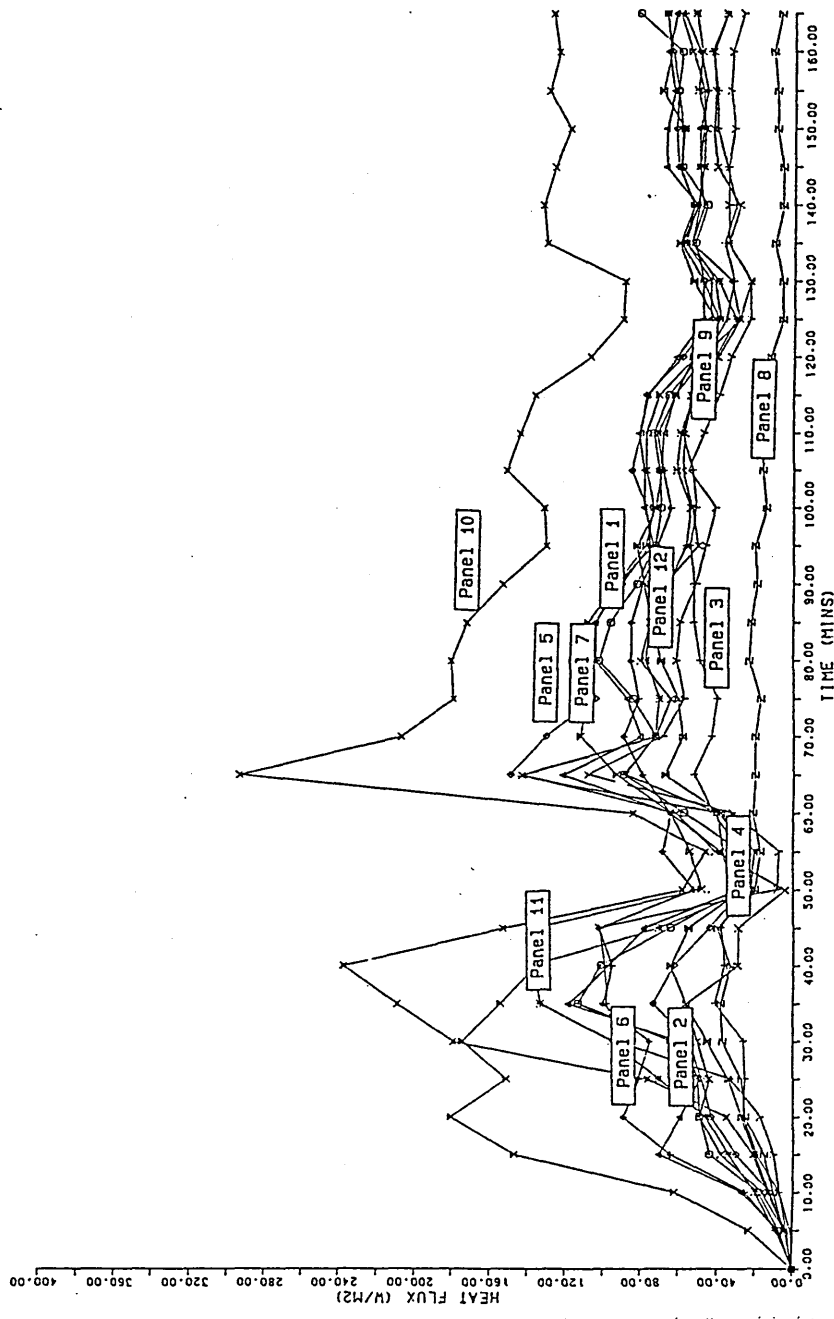


Figure 38. Variation Of Heat Flux With Time (first cast of week - Dataset 07).

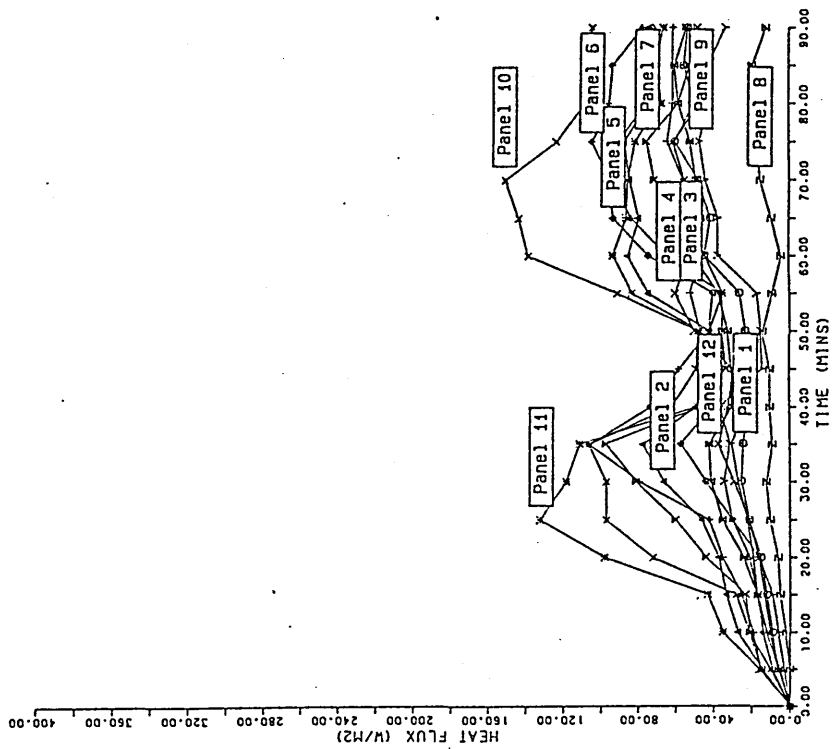


Figure 39. Variation Of Heat Flux With Time
(first cast of week - Dataset 08).

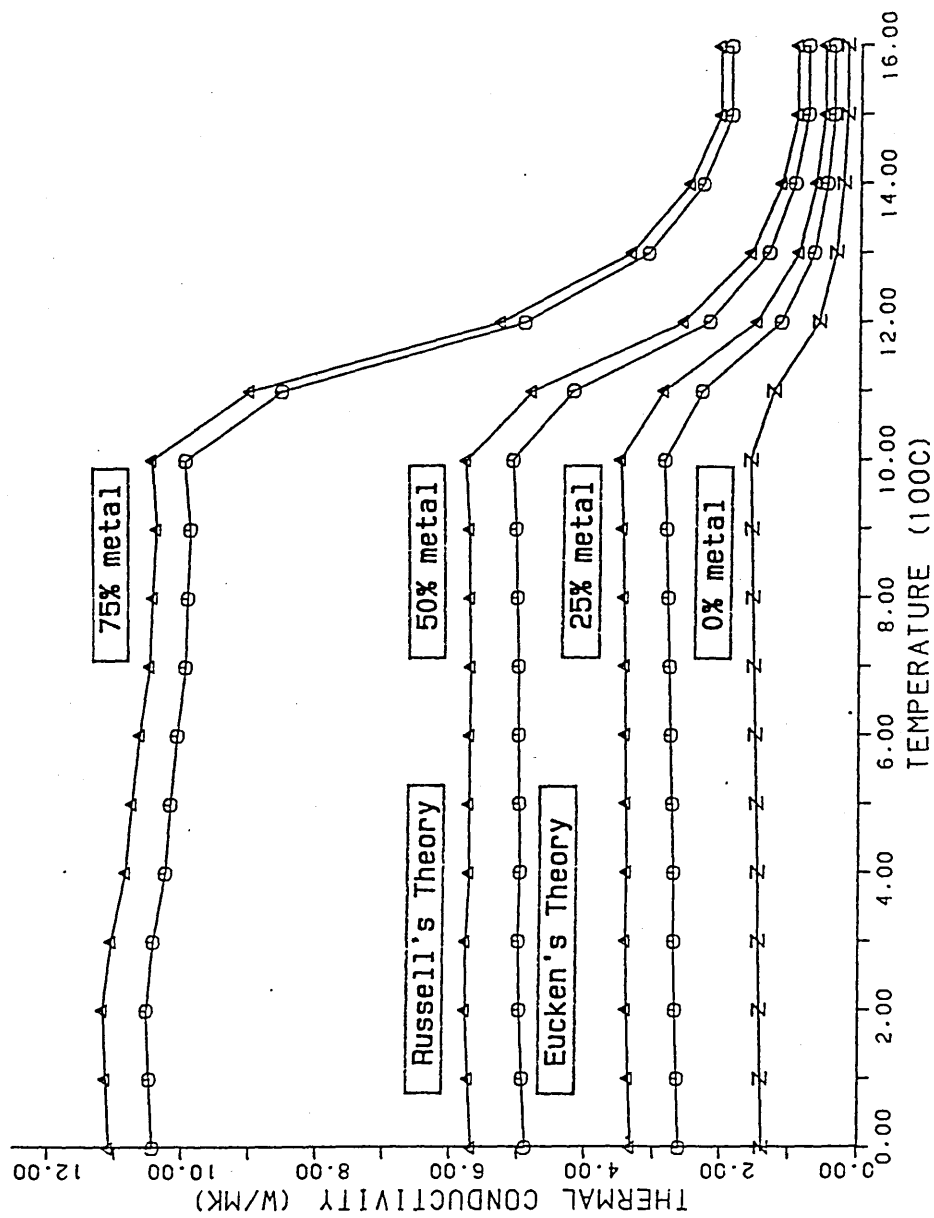


Figure 40. Comparison Of Russell's And Eucken's Theories For Slag With Various Metal Contents.

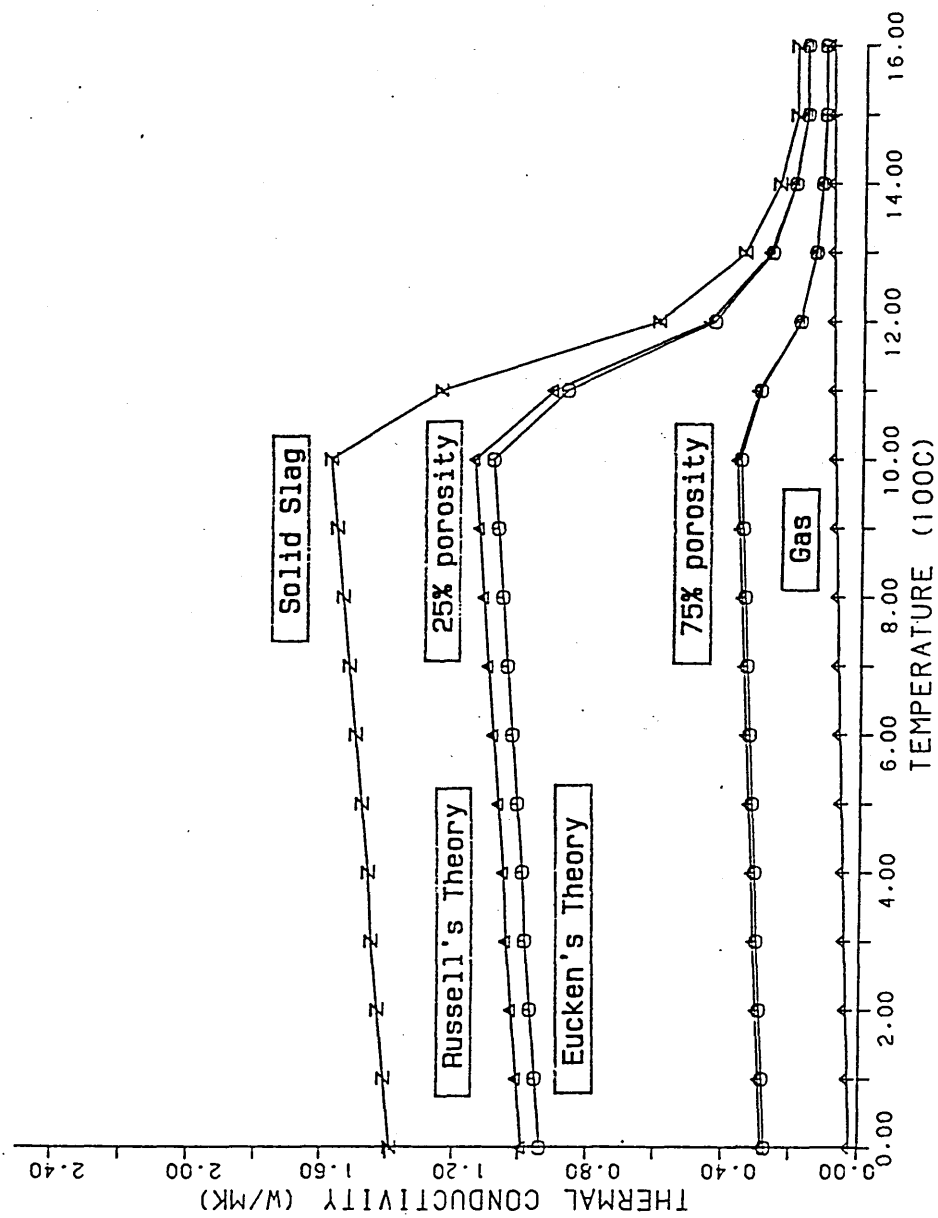


Figure 41. Comparison Of Russell's And Eucken's Theories For Slag With Various Gas Contents.

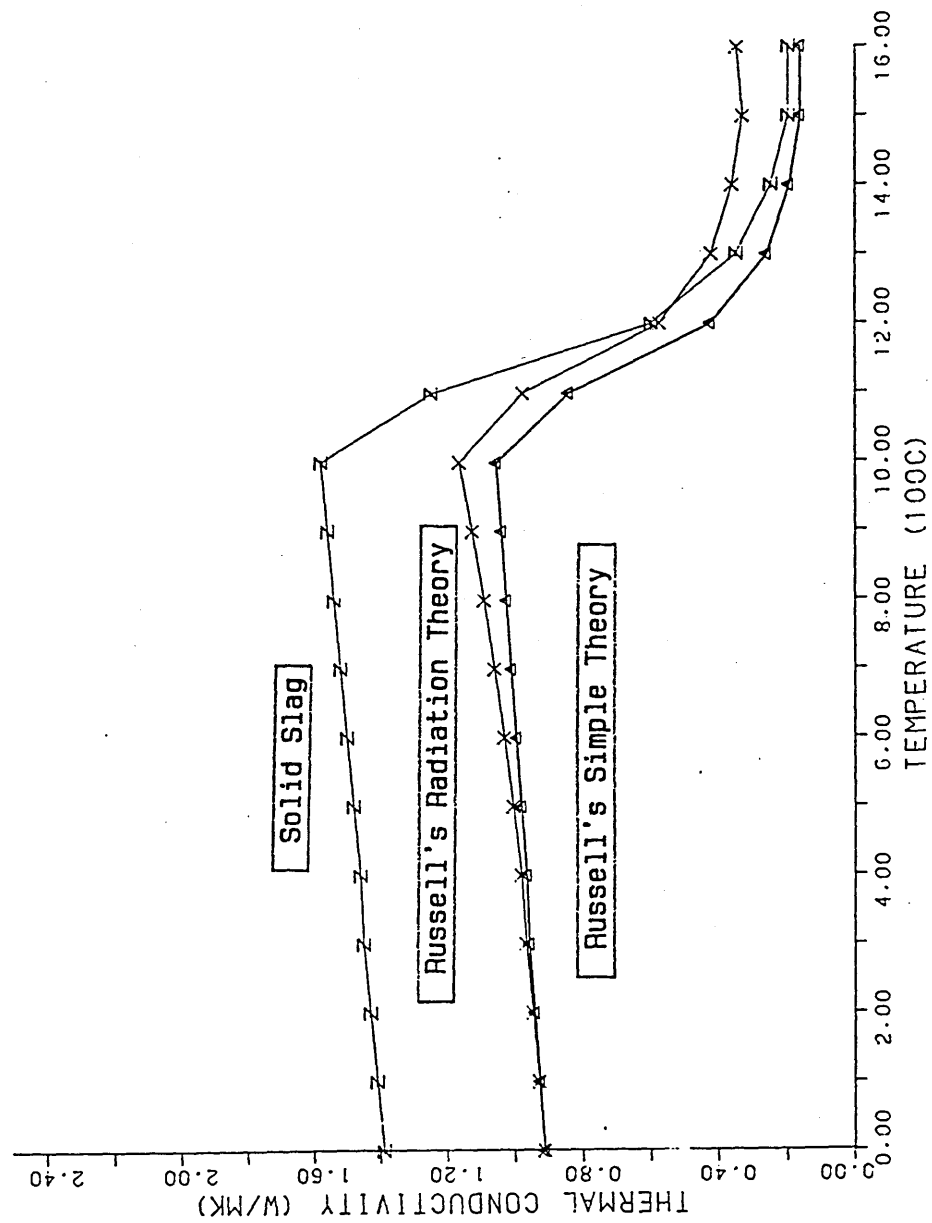


Figure 42. The Effect Of Russell's Radiation Allowance

porosity = 30% pore diameter = 1mm
 shape factor = 0.67 emissivity = 0.9

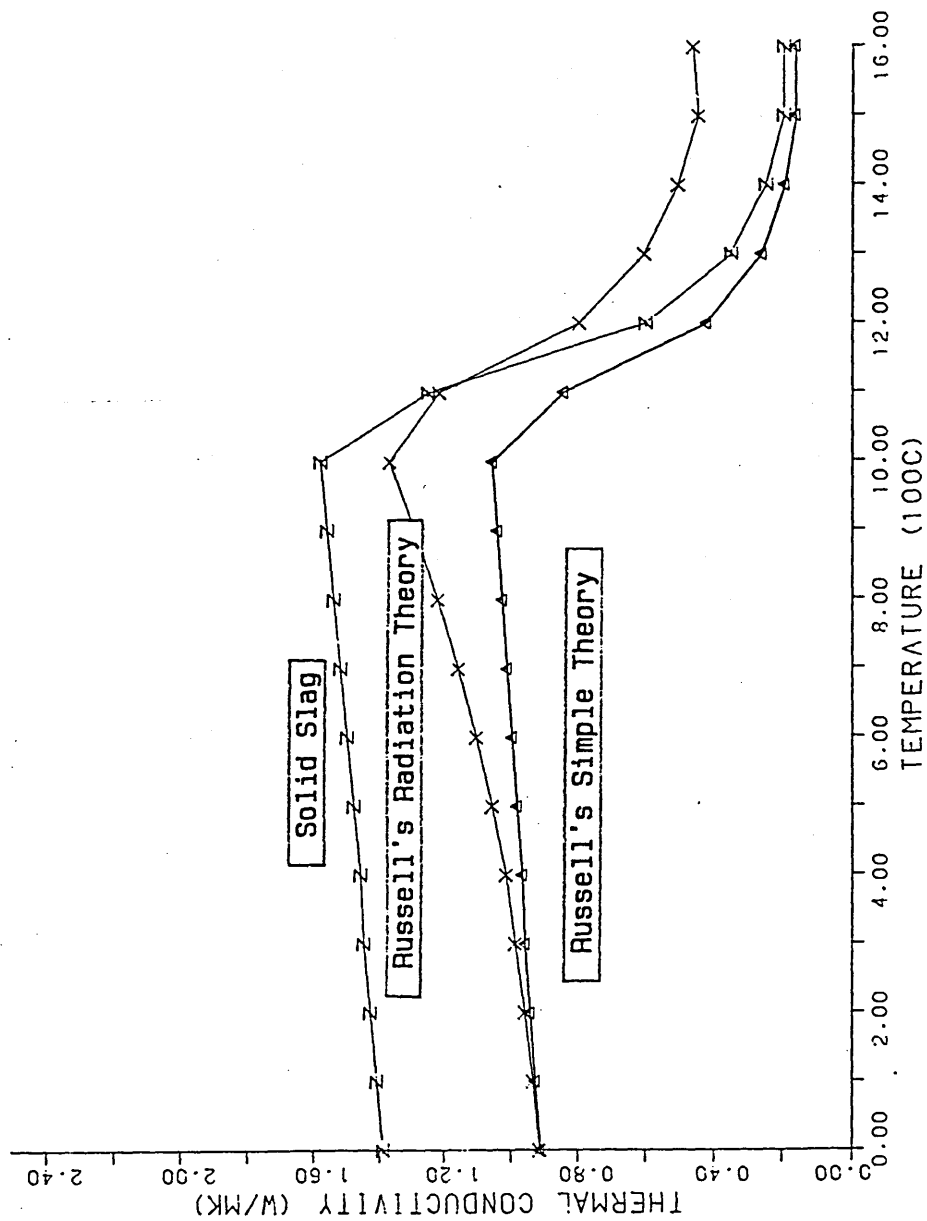


Figure 43. The Effect Of Russell's Radiation Allowance

porosity = 30% pore diameter = 3mm
 shape factor = 0.67 emissivity = 0.9

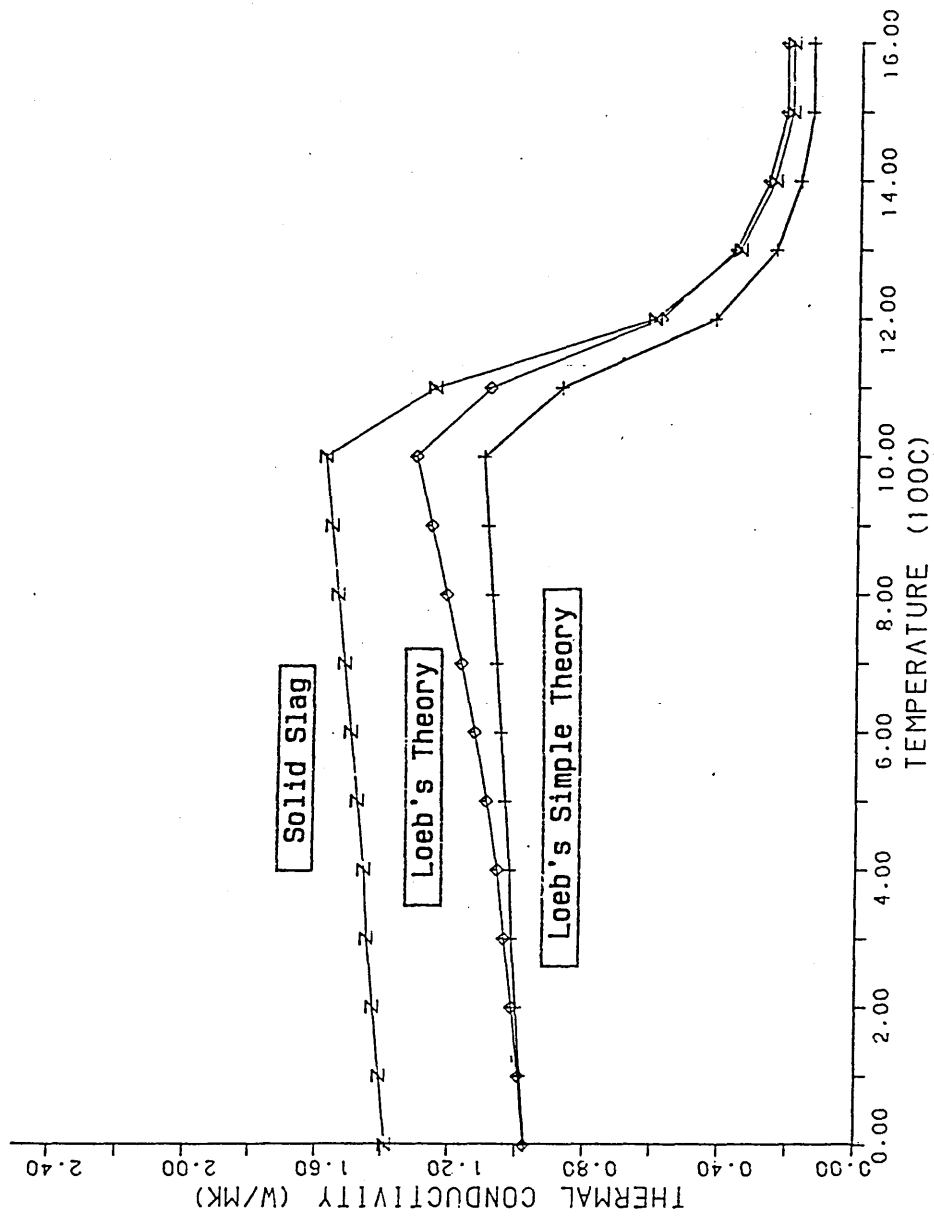


Figure 44. Loeb's Theory.

porosity = 30% pore diameter = 1mm
 combined pore factor = 0.60

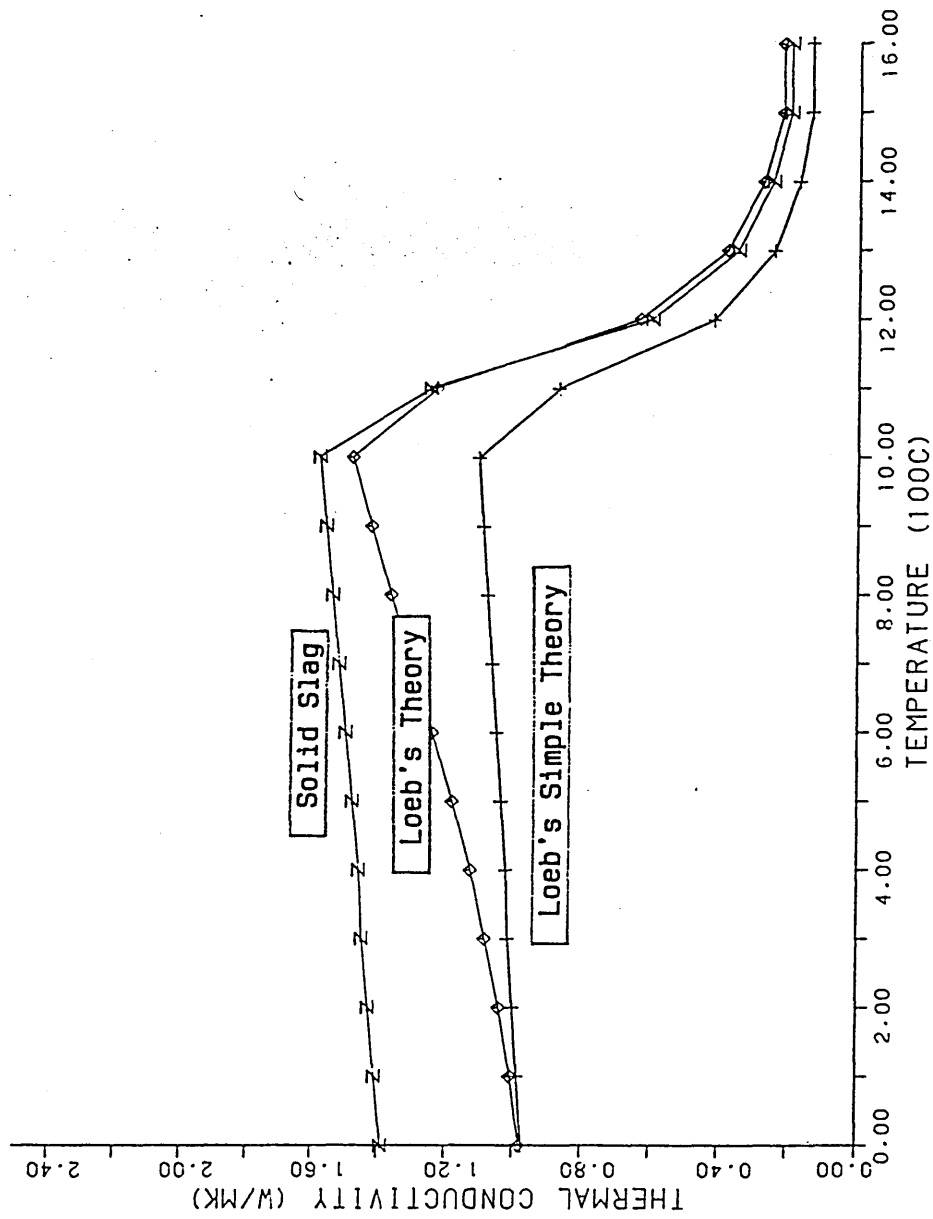


Figure 45. Loeb's Theory.

porosity = 30% pore diameter = 3mm
 combined pore factor = 0.60

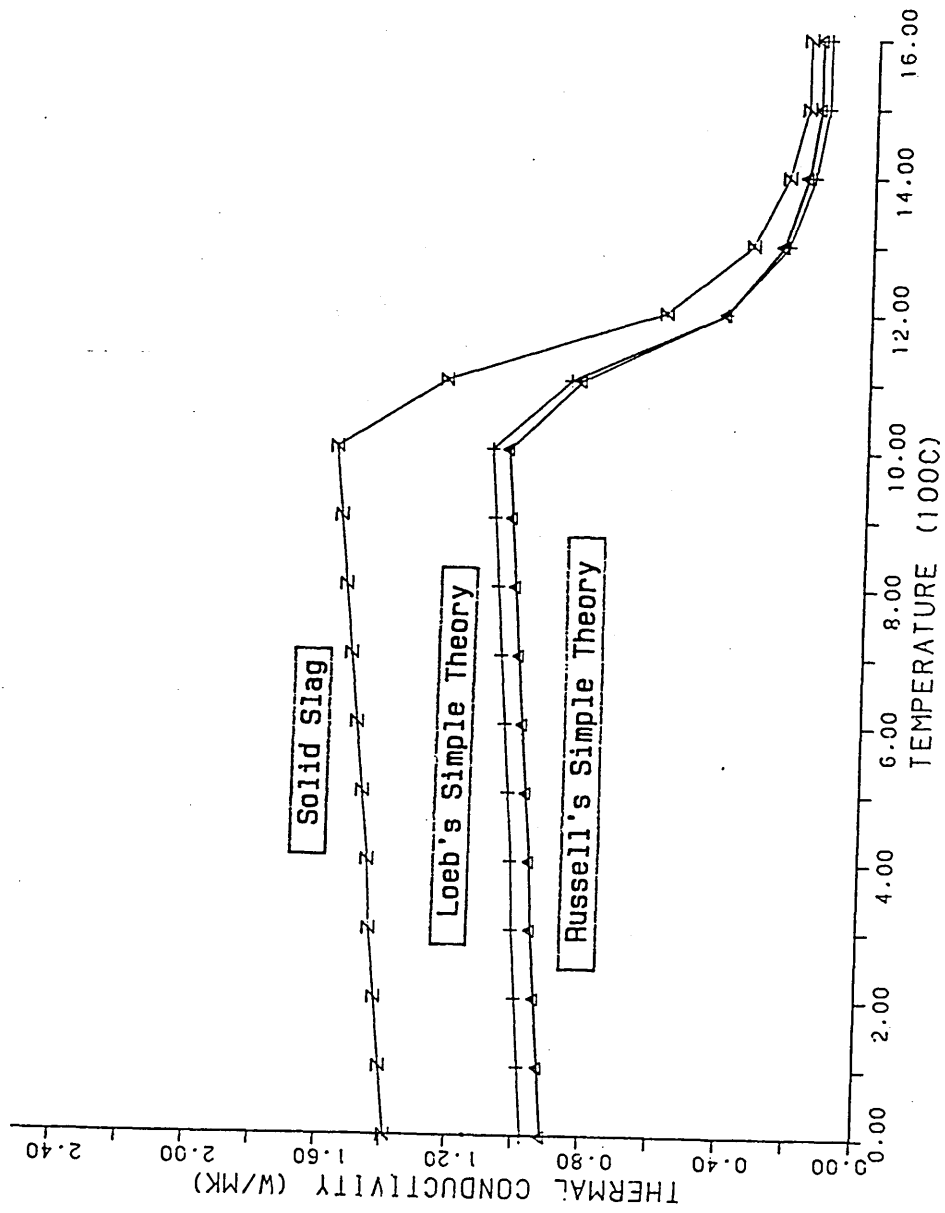


Figure 46. Russell's And Loeb's Simple Theories.

porosity = 30%

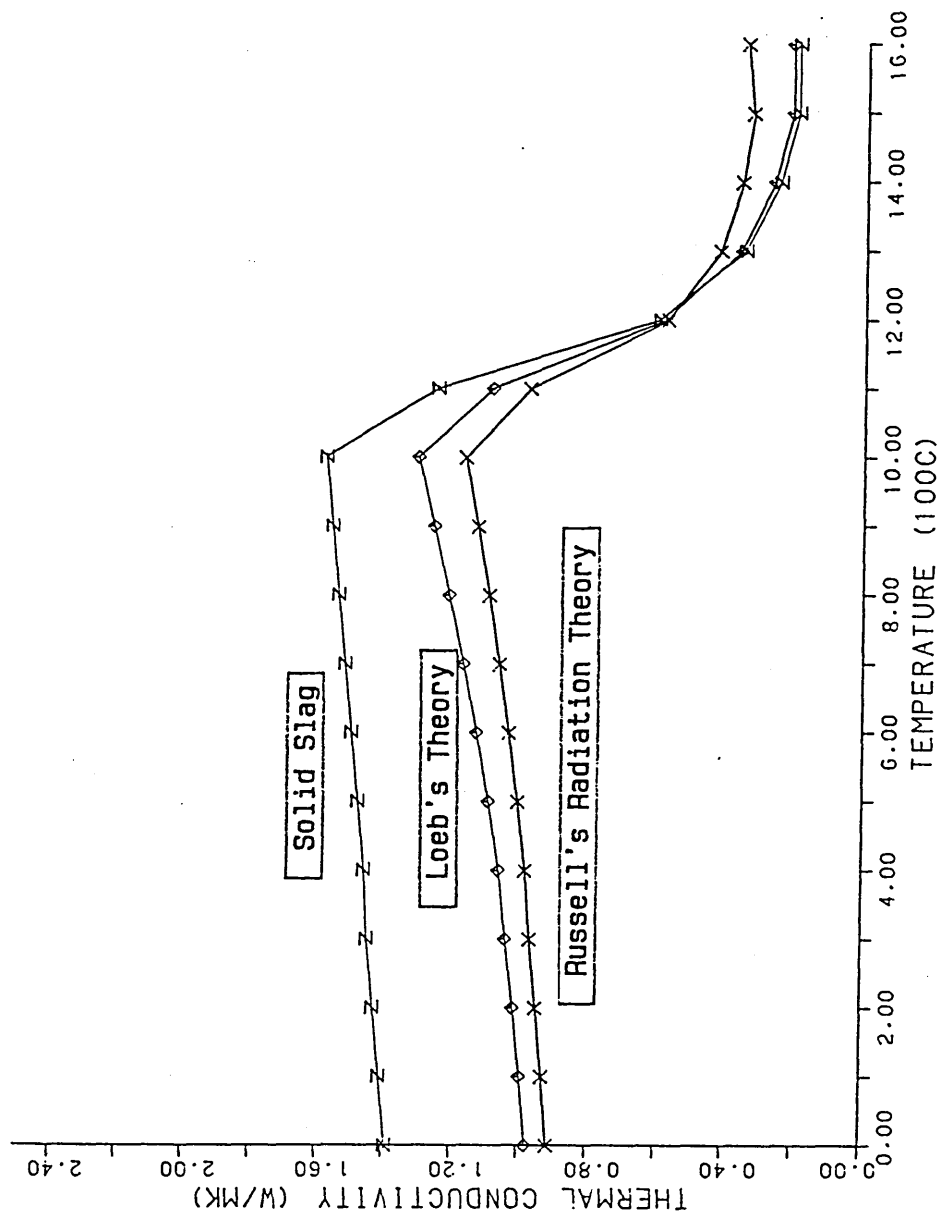


Figure 47. Russell's And Loeb's Theories With Radiation Allowance.

porosity = 30% pore diameter = 1mm
 shape factor = 0.67 emissivity = 0.9
 combined pore factor = 0.60

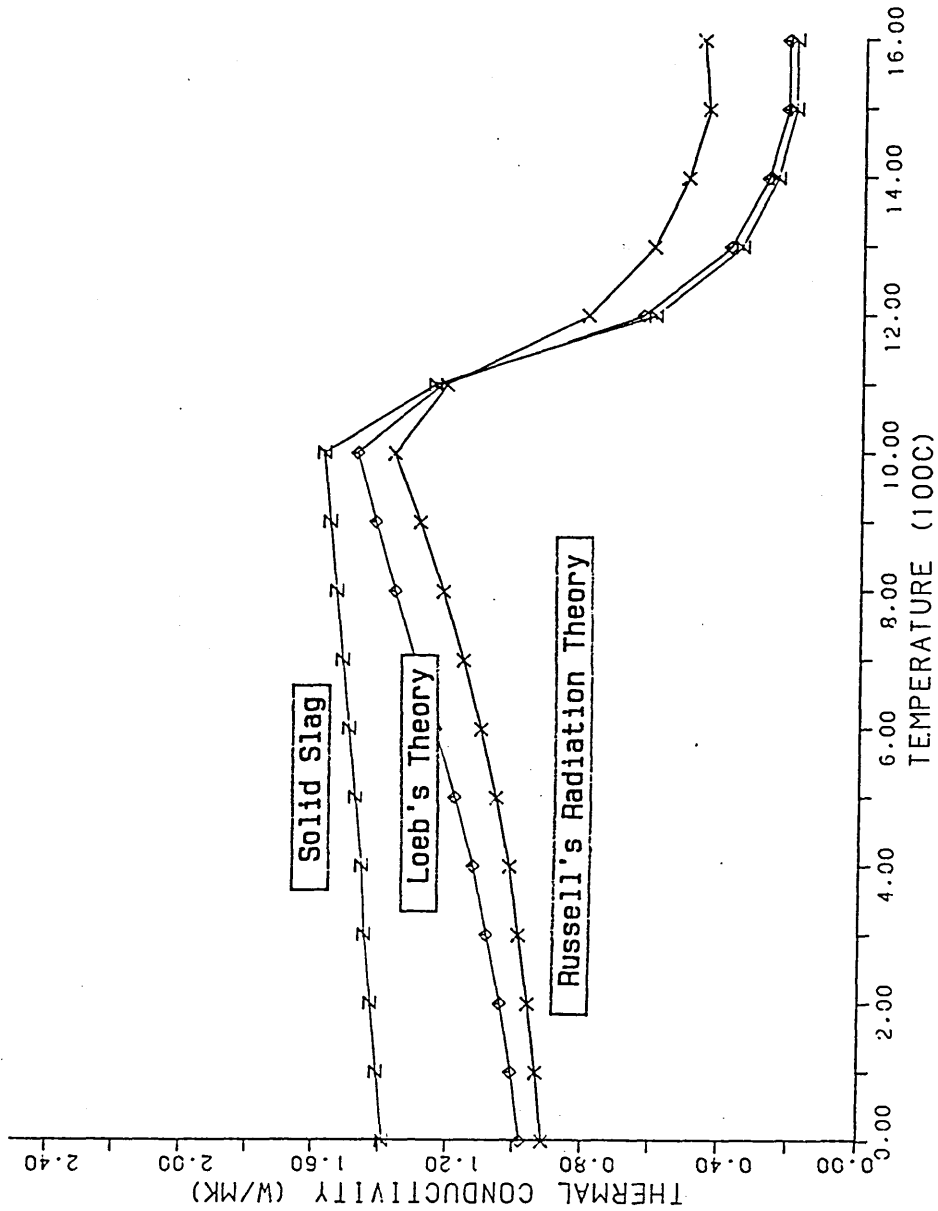


Figure 48. Russell's And Loeb's Theories With Radiation Allowance.

porosity = 30% pore diameter = 3mm
 shape factor = 0.67 emissivity = 0.9
 combined pore factor = 0.60

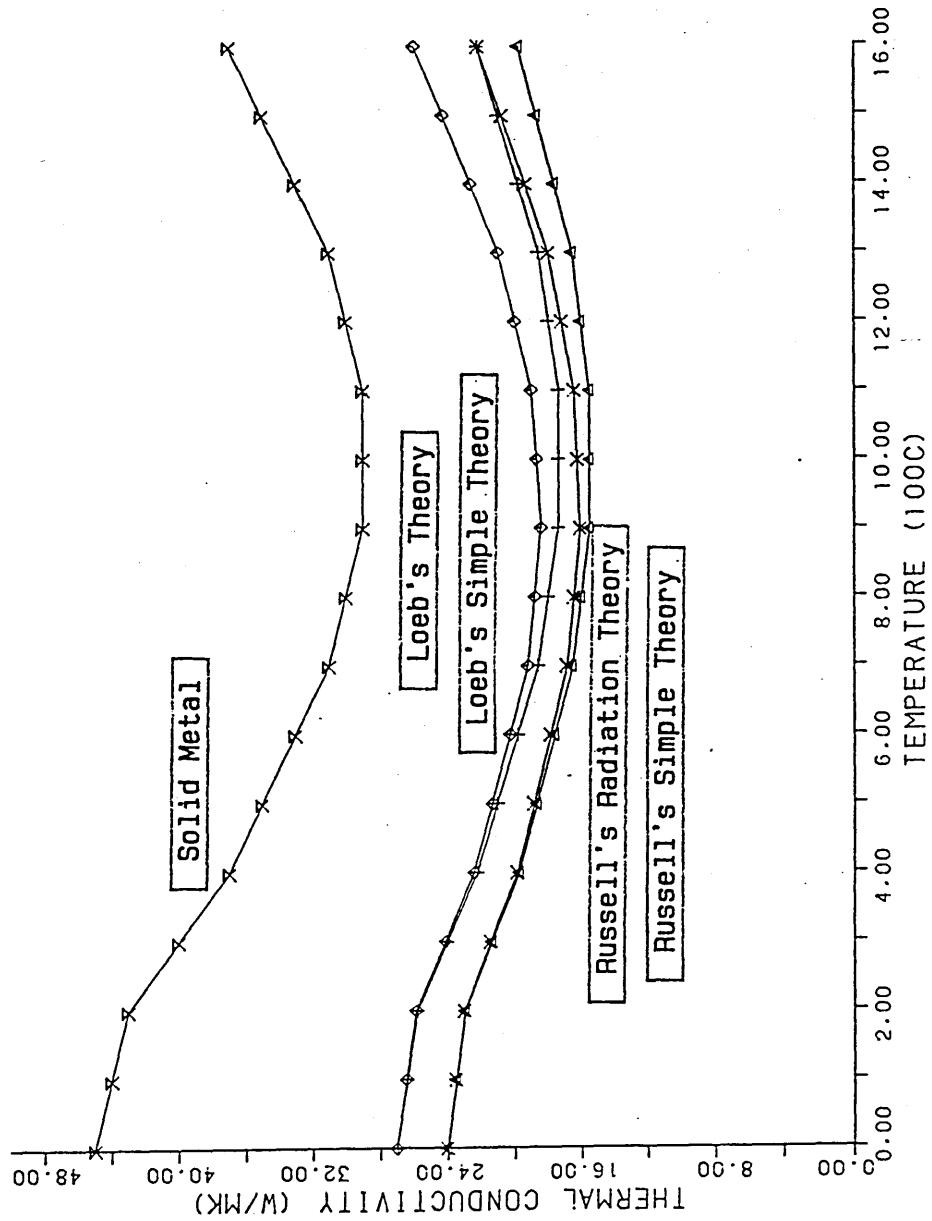


Figure 49. Comparison Of Theories For A Metal Layer.

porosity = 40% pore diameter = 5mm
 shape factor = 0.67 emissivity = 0.9
 combined pore factor = 0.60

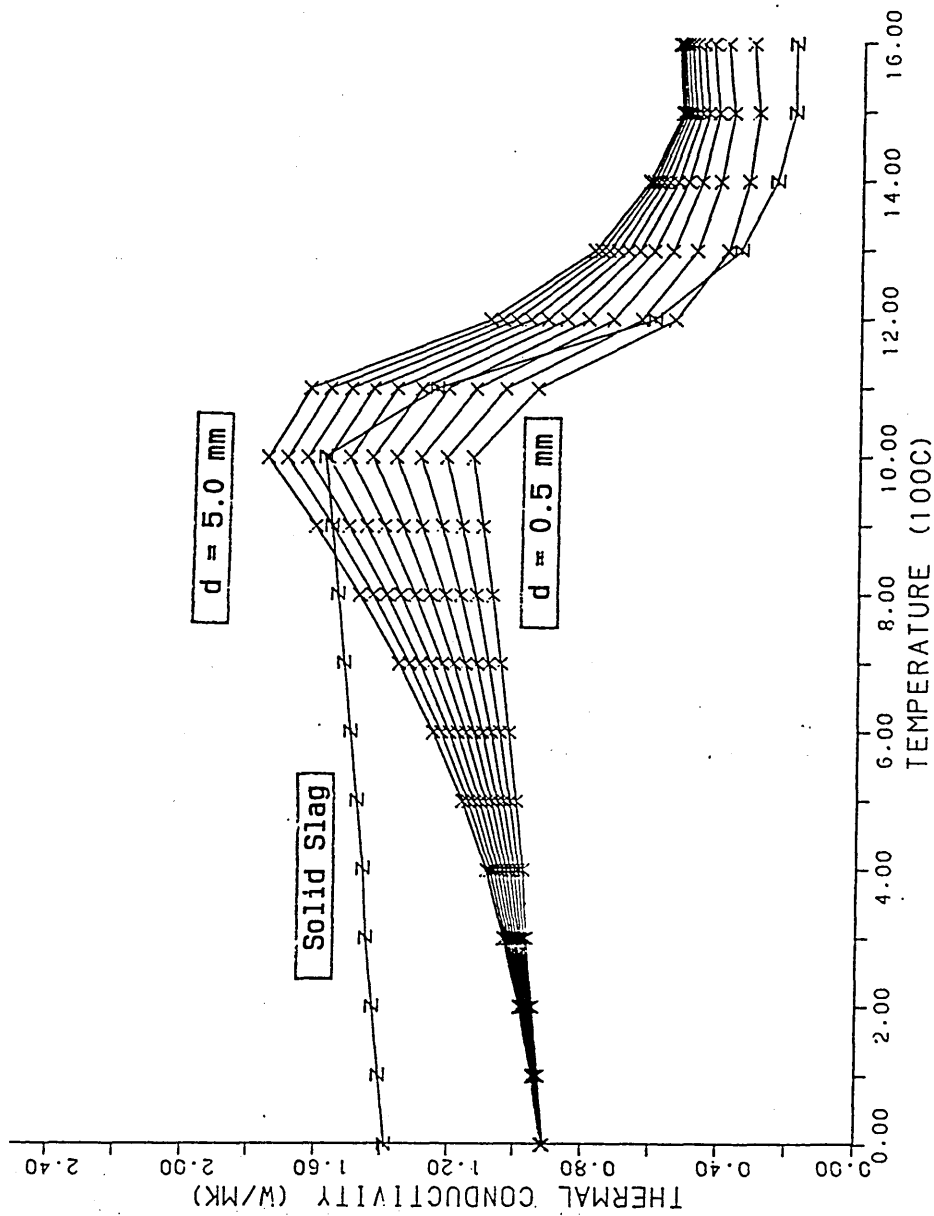


Figure 50. The Effect Of Pore Diameter On Russell's Theory.

porosity = 30% shape factor = 0.67
 emissivity = 0.9

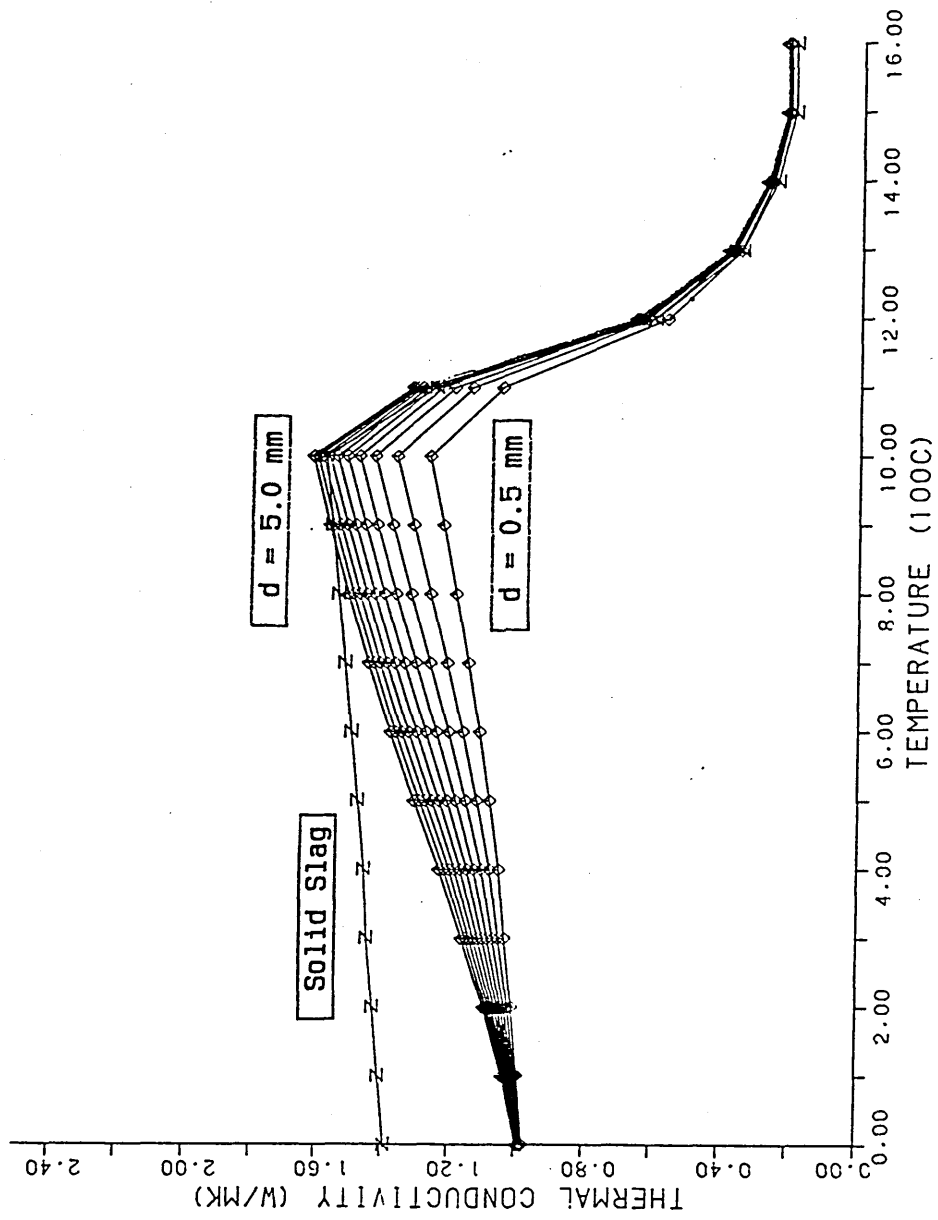


Figure 51. The Effect Of Pore Diameter On Loeb's Theory.

porosity = 30% combined pore factor = 0.60

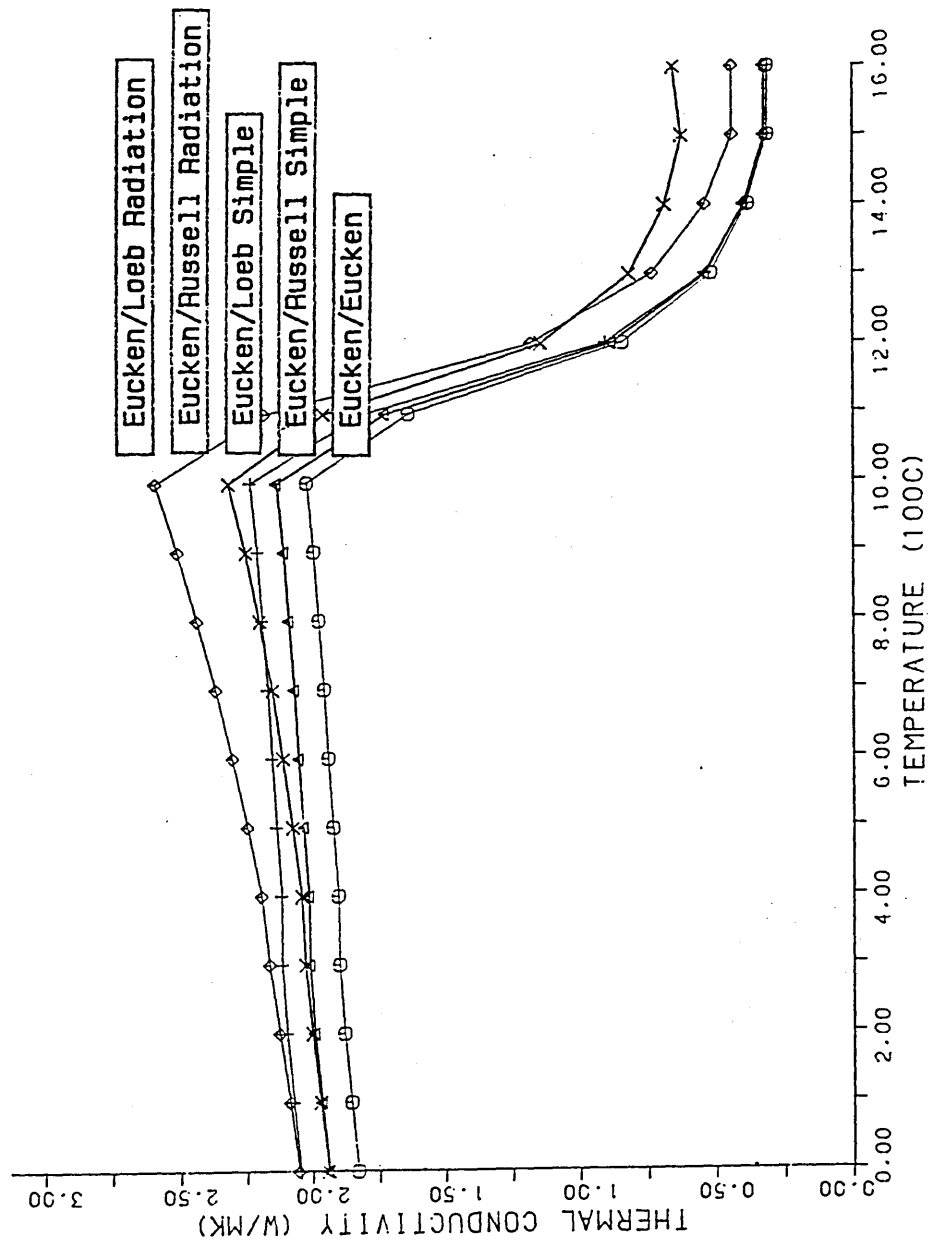


Figure 52. Combinations Based On Eucken's Theory For A Typical Layer.

porosity = 25% metal content = 20%
 pore diameter = 2mm shape factor = 0.67
 emissivity = 0.9 combined pore factor = 0.60

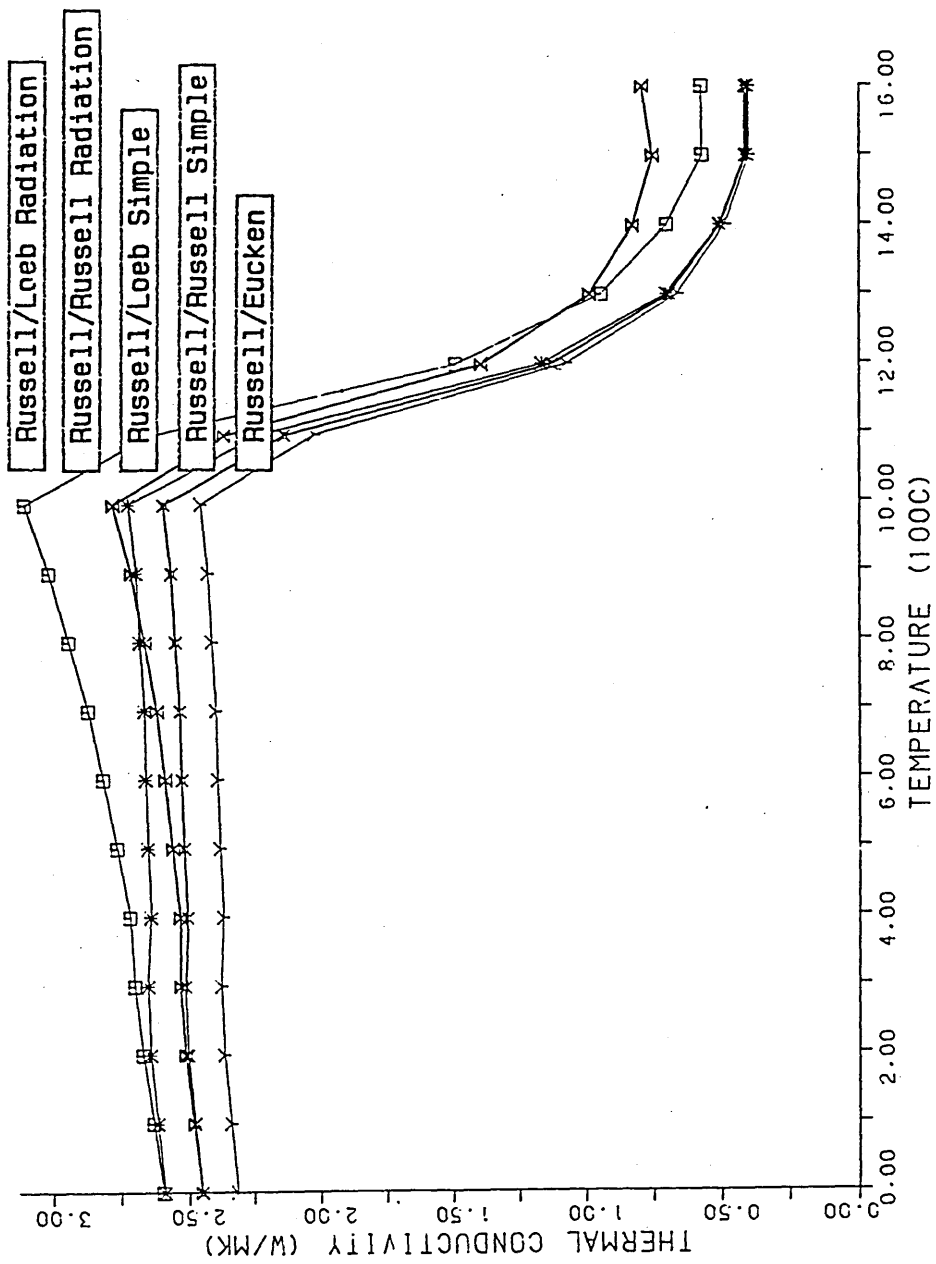


Figure 53. Combinations Based On Russell's Theory For A Typical Layer.

porosity = 25% metal content = 20%
 pore diameter = 2mm shape factor = 0.67
 emissivity = 0.9 combined pore factor = 0.60

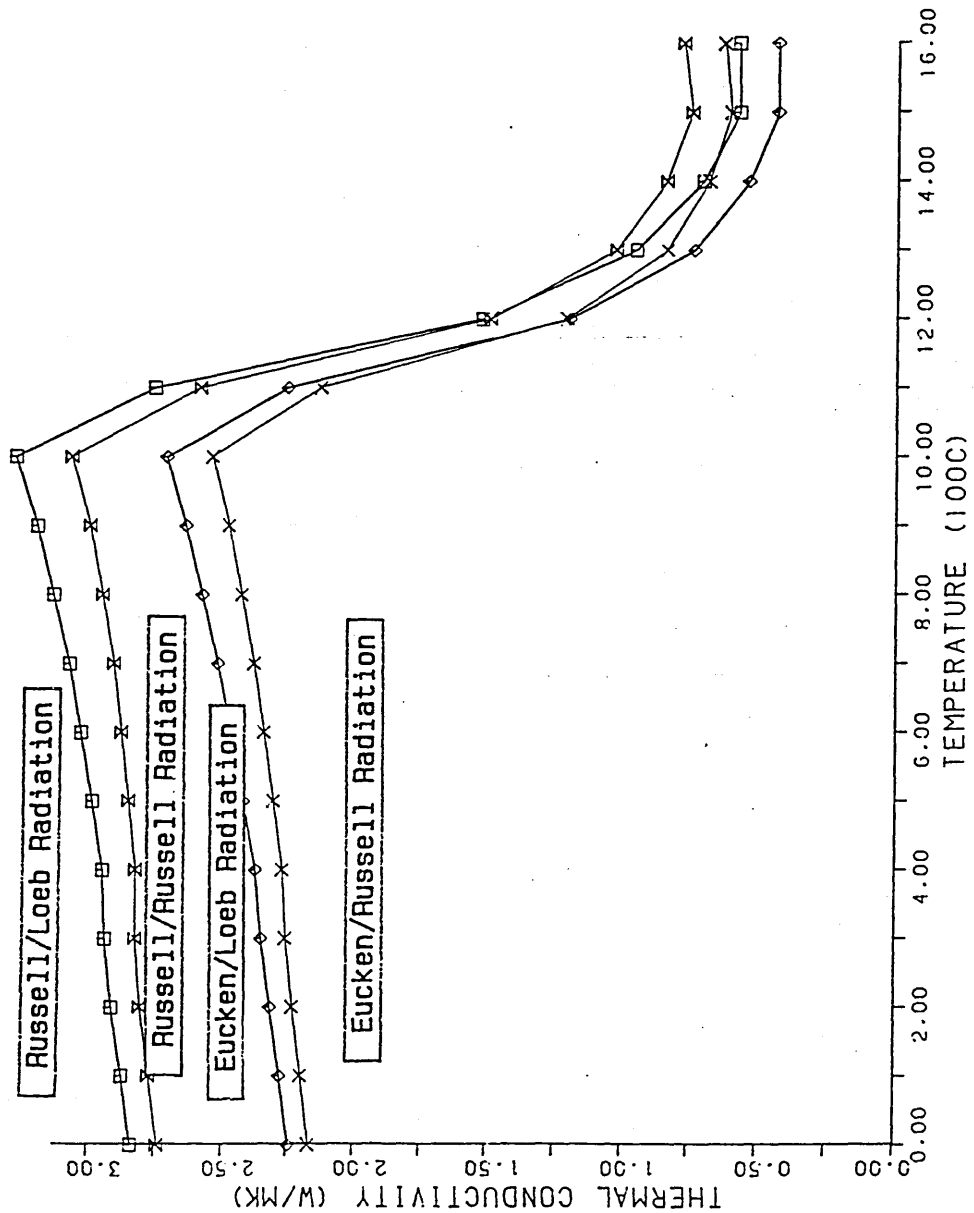
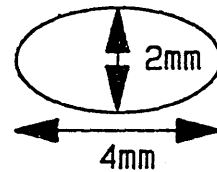


Figure 54. Effect Of Pore Shape.



pore dimension = 2mm emissivity = 0.9
 shape factor = 0.75 combined pore factor = 0.675
 total porosity = 25% longitudinal porosity = 18%
 cross-sectional porosity = 32% metal content = 20%

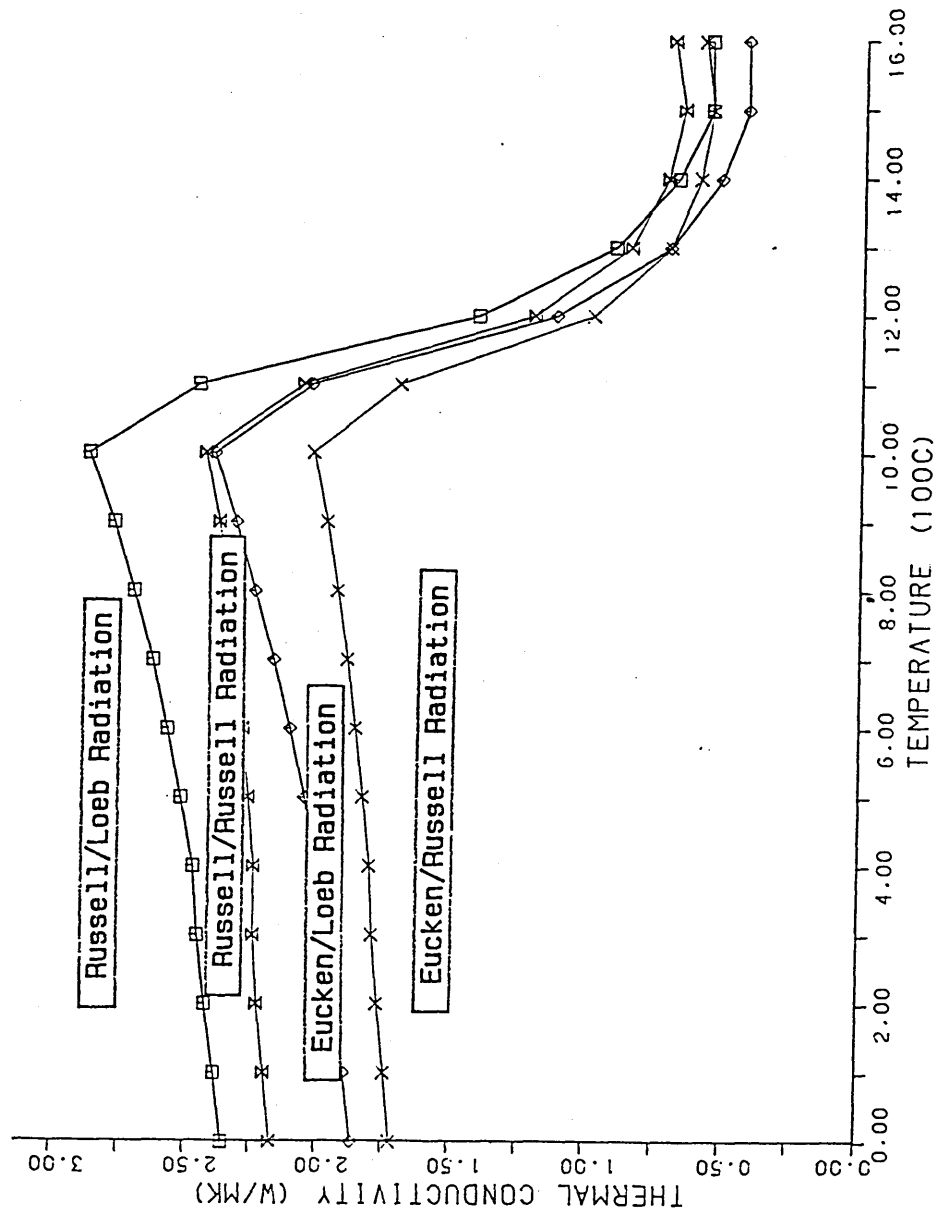
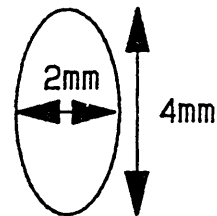


Figure 55. Effect Of Pore Shape.

pore dimension = 4mm emissivity = 0.9
 shape factor = 0.9 combined pore factor = 0.81
 total porosity = 25% longitudinal porosity = 32%
 cross-sectional porosity = 18% metal content = 20%



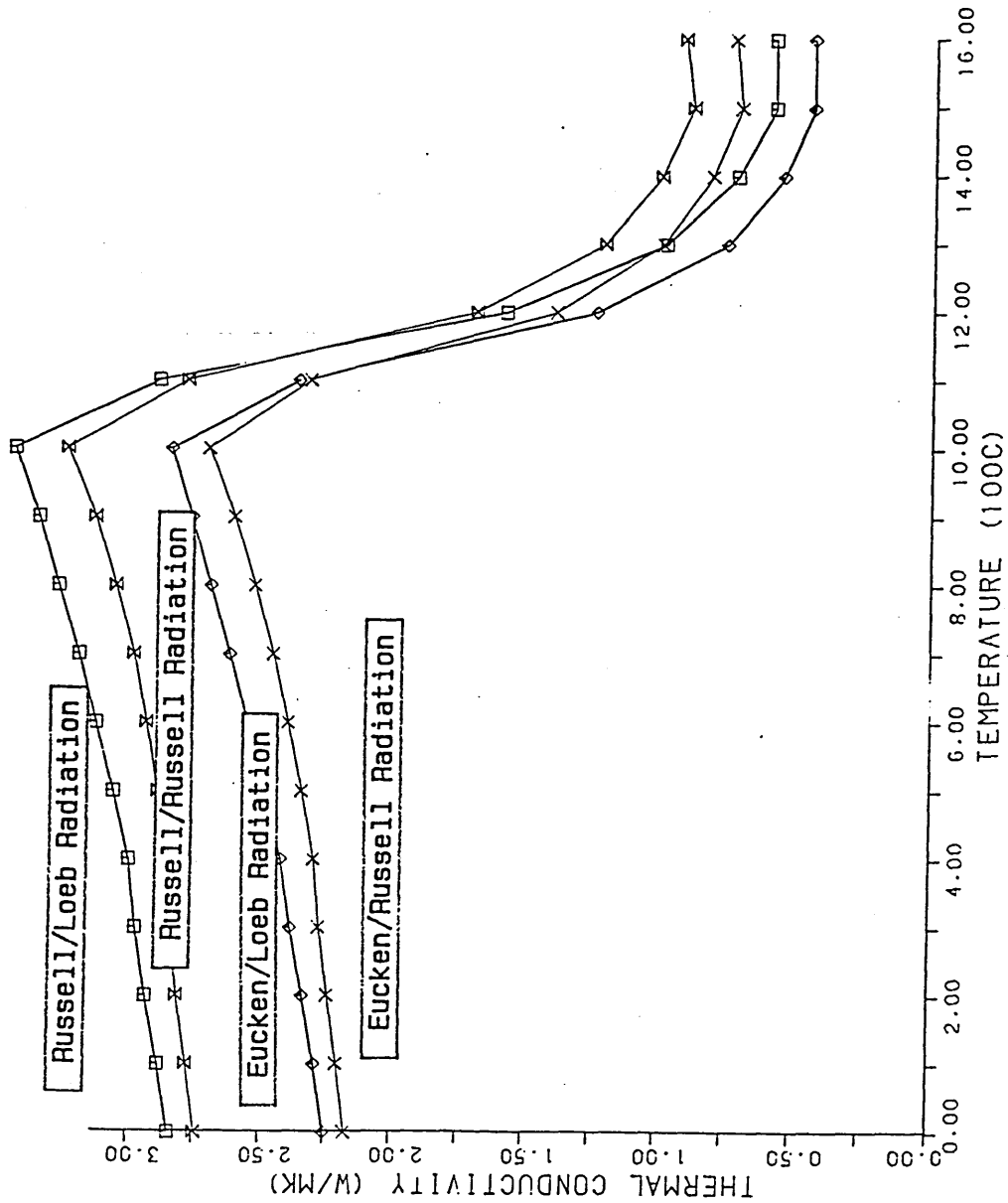
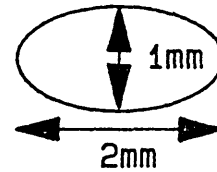


Figure 56. Effect Of Pore Shape.



pore dimension = 1mm emissivity = 0.9
 shape factor = 0.75 combined pore factor = 0.675
 total porosity = 25% longitudinal porosity = 18%
 cross-sectional porosity = 32% metal content = 20%

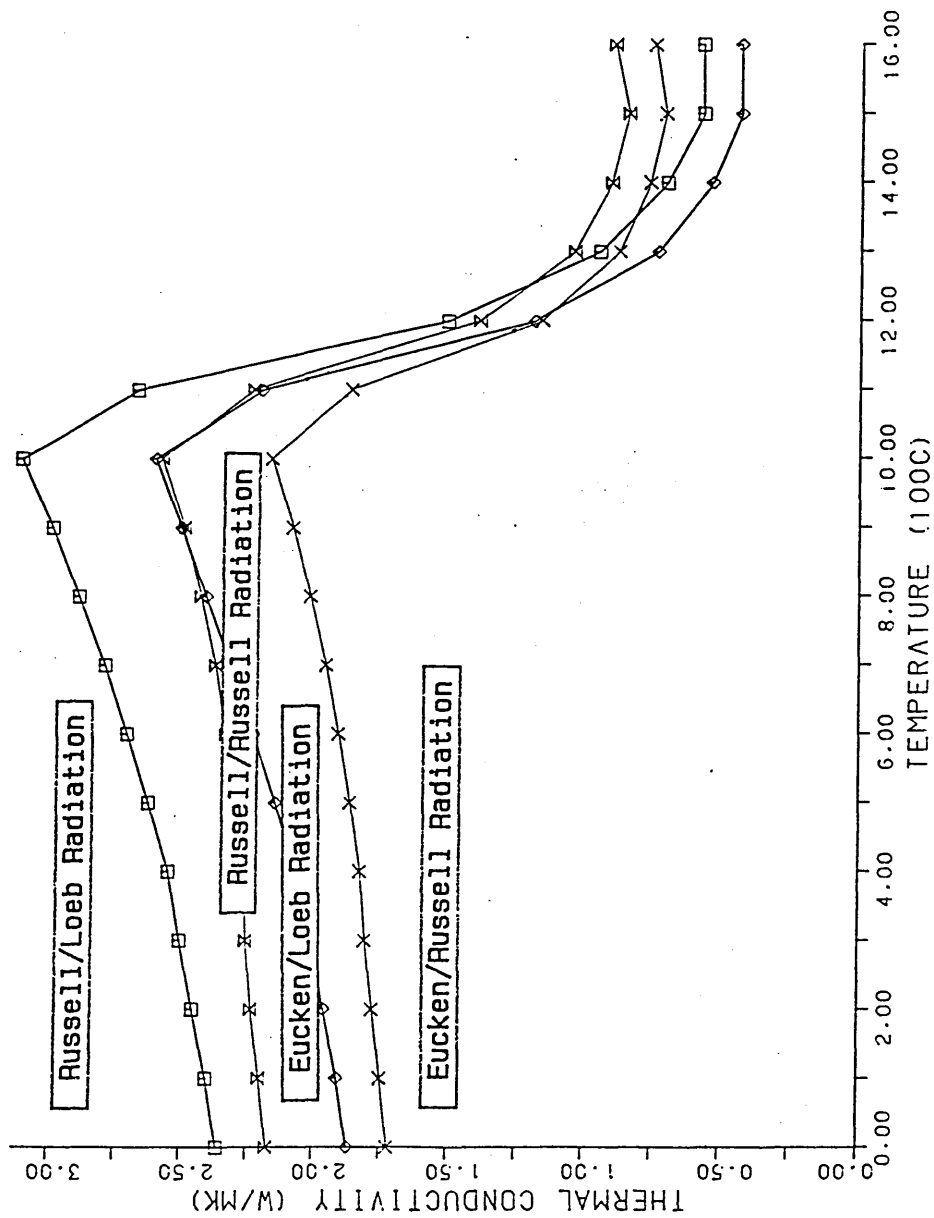


Figure 57. Effect Of Pore Shape.

pore dimension = 2mm emissivity = 0.9
 shape factor = 0.9 combined pore factor = 0.81
 total porosity = 25% longitudinal porosity = 32%
 cross-sectional porosity = 18% metal content = 20%

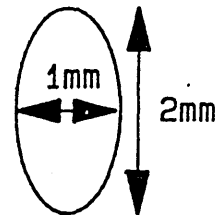


FIGURE 58. Hot Face Thermocouple Temperatures
(Sample No.1) After Changing Set
Temperature From 600 To 700 C.

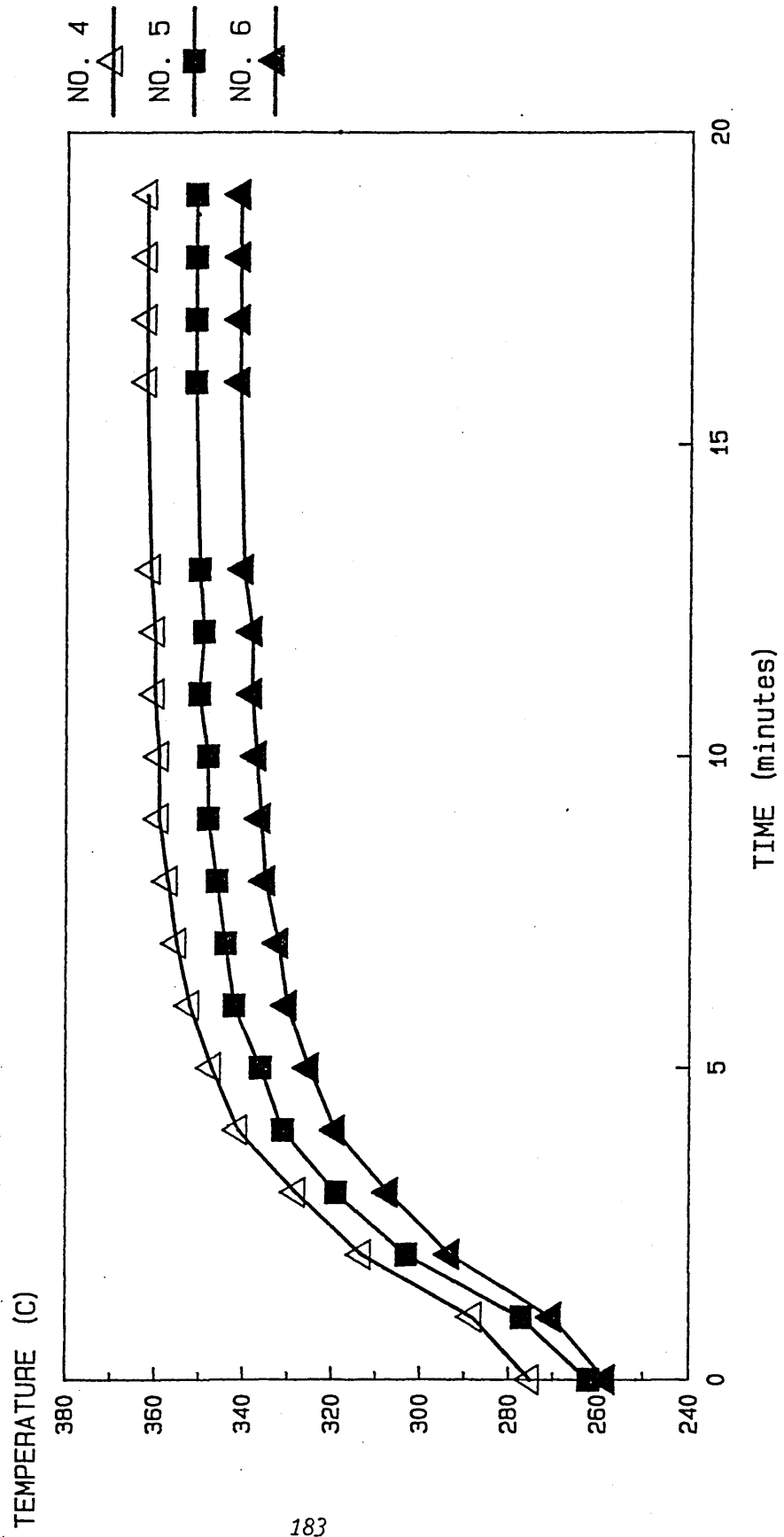


FIGURE 59. Cold Face Thermocouple Temperatures
 (Sample No.1) After Changing Set
 Temperature From 600 To 700 C.

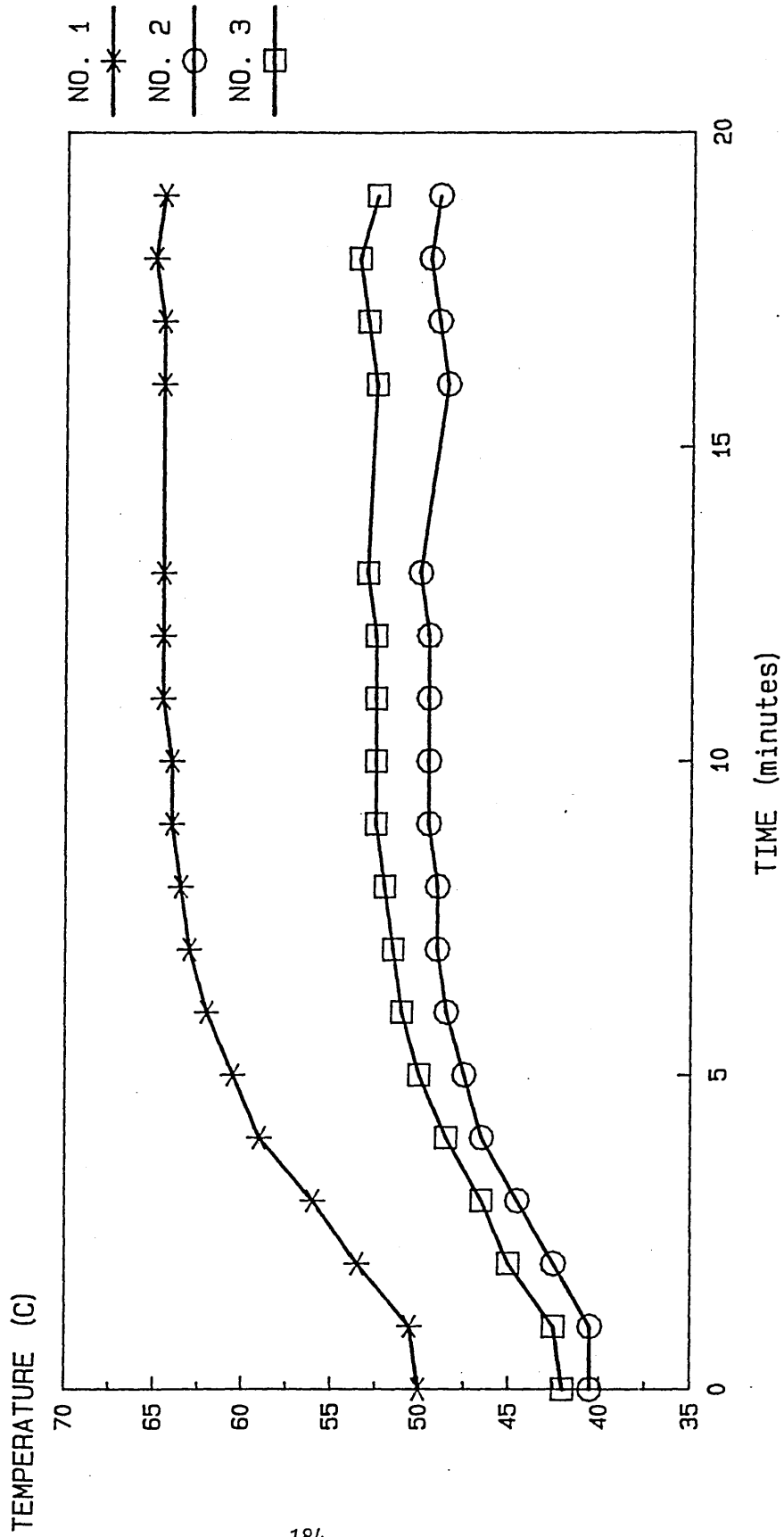


FIGURE 60. Hot Face Thermocouple Temperatures
(Sample No.1) After Changing Set
Temperature From 900 To 1000 C

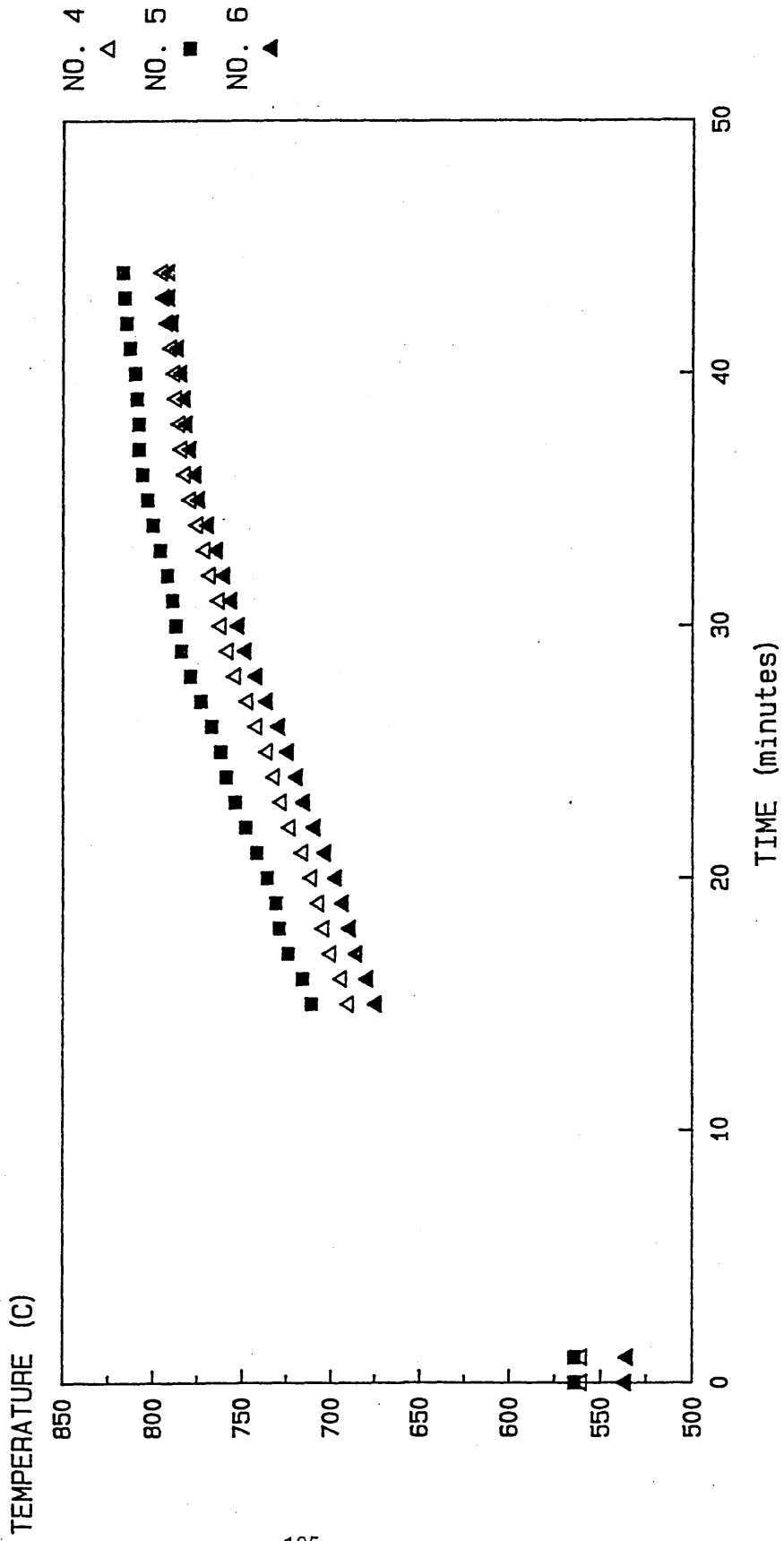


FIGURE 61. Cold Face Thermocouple Temperatures
 (Sample No.1) After Changing Set
 Temperature From 900 To 1000 C

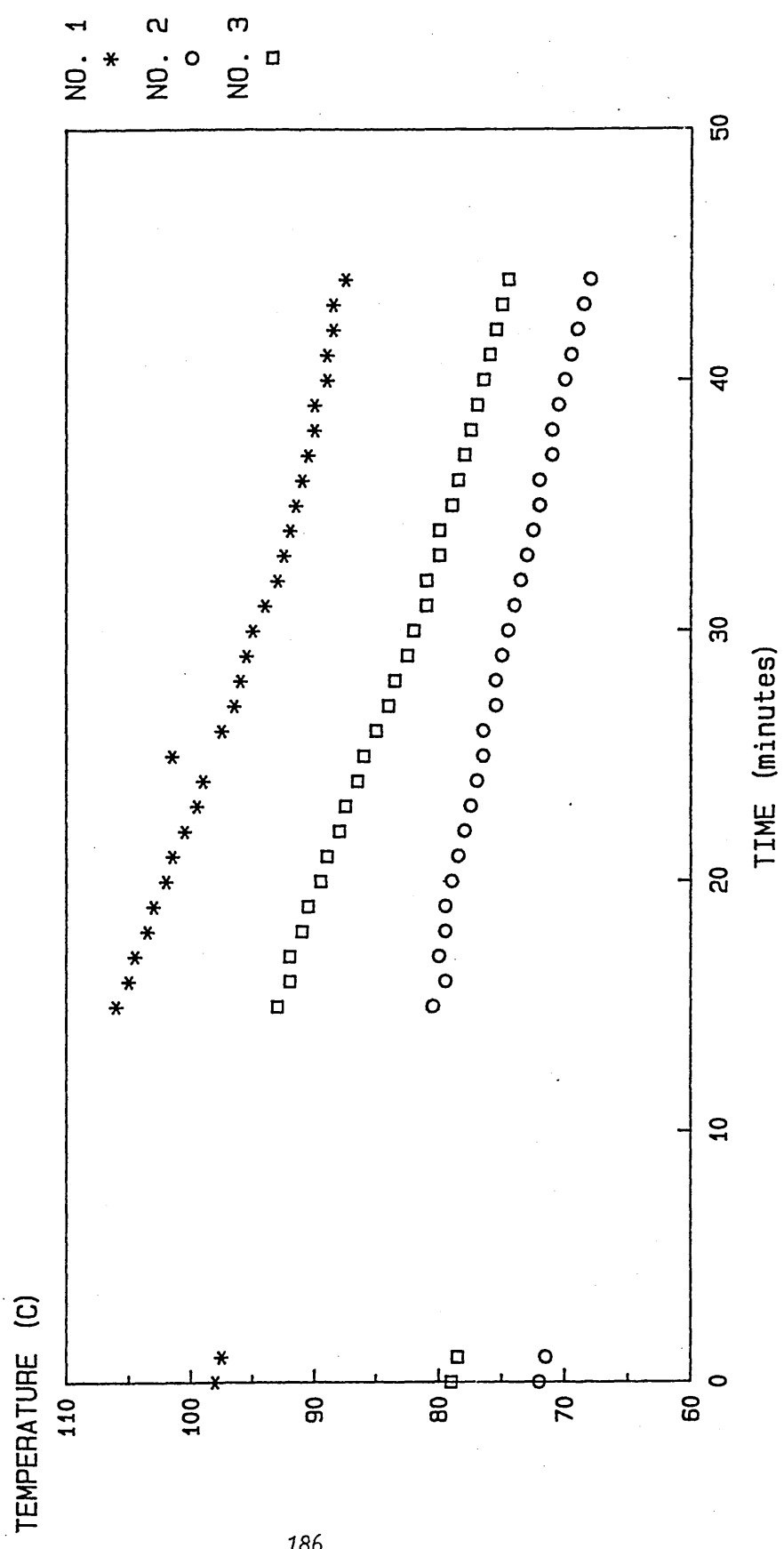


FIGURE 62. Measured Thermal Conductivity vs
Mean Sample Temperature For Sample
No.1 (Heating Cycle).

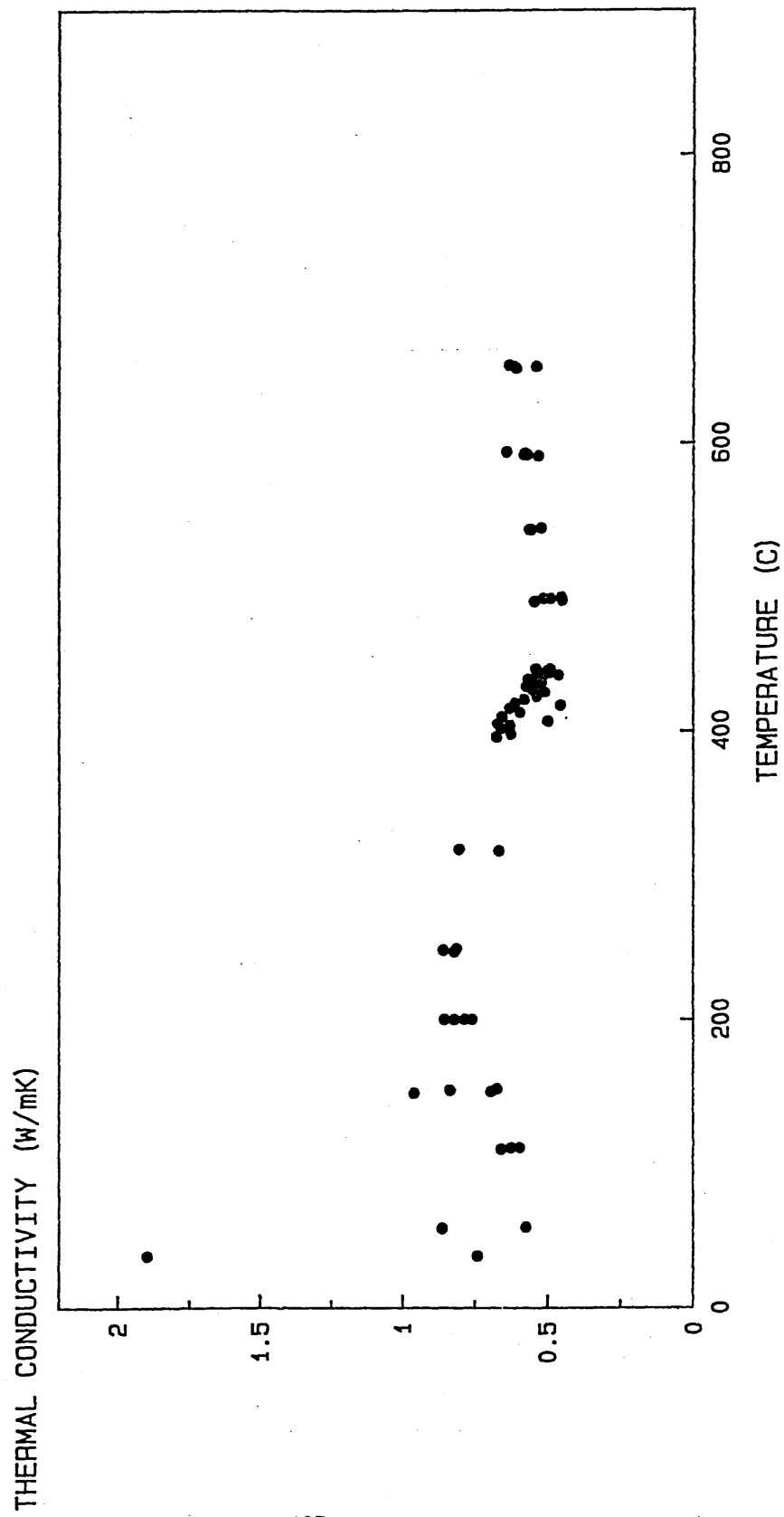


FIGURE 63. Measured Thermal Conductivity vs
Mean Sample Temperature For Sample
No.2 (Heating Cycle).

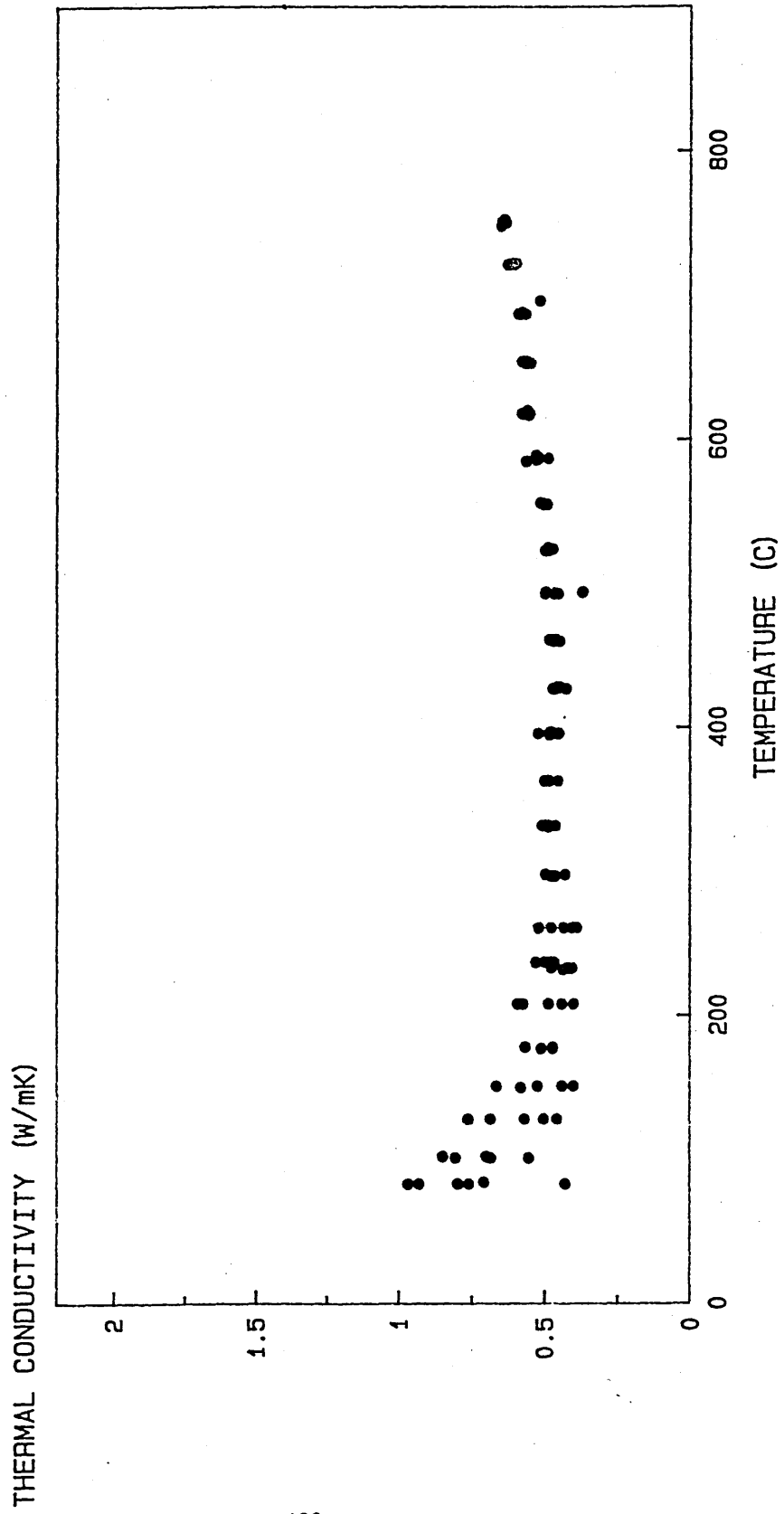


FIGURE 64. Measured Thermal Conductivity vs Mean Sample Temperature For Sample No.2 (Cooling Cycle).

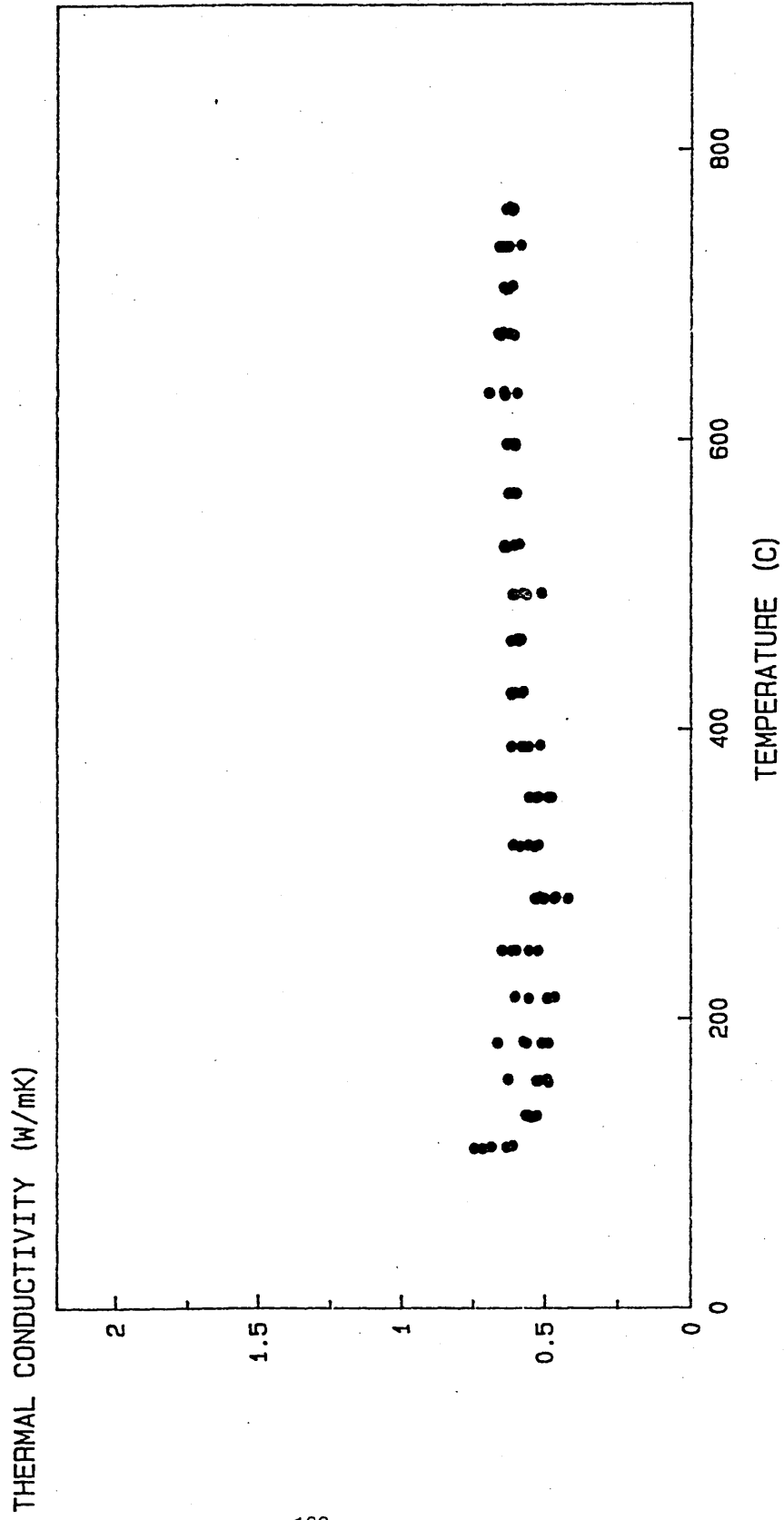


FIGURE 65. Average Conductivity Values For Sample No.2 (Heating And Cooling Cycles).

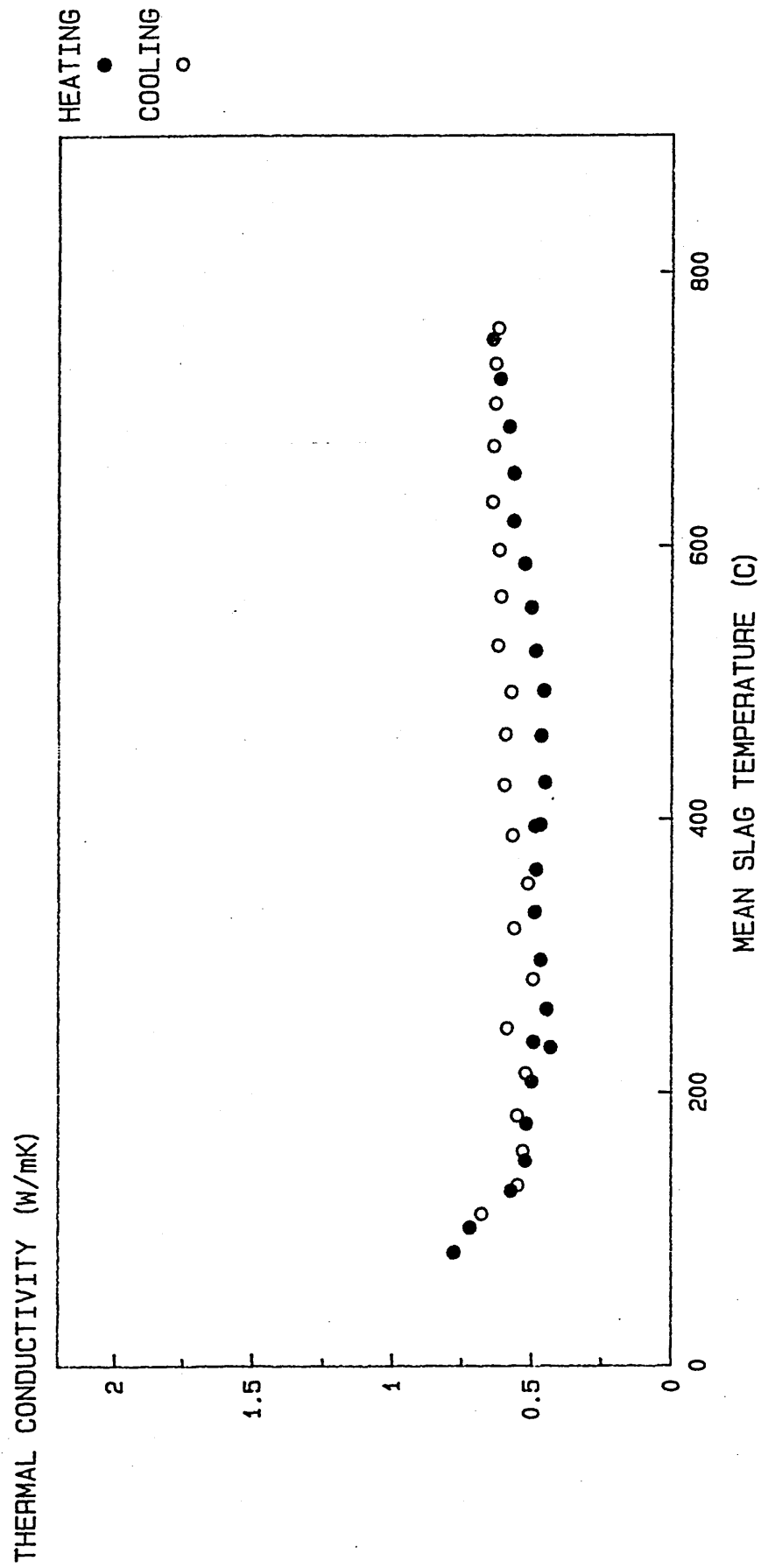


FIGURE 67. Measured Thermal Conductivity vs Mean Sample Temperature For Sample No.4 (Heating Cycle).

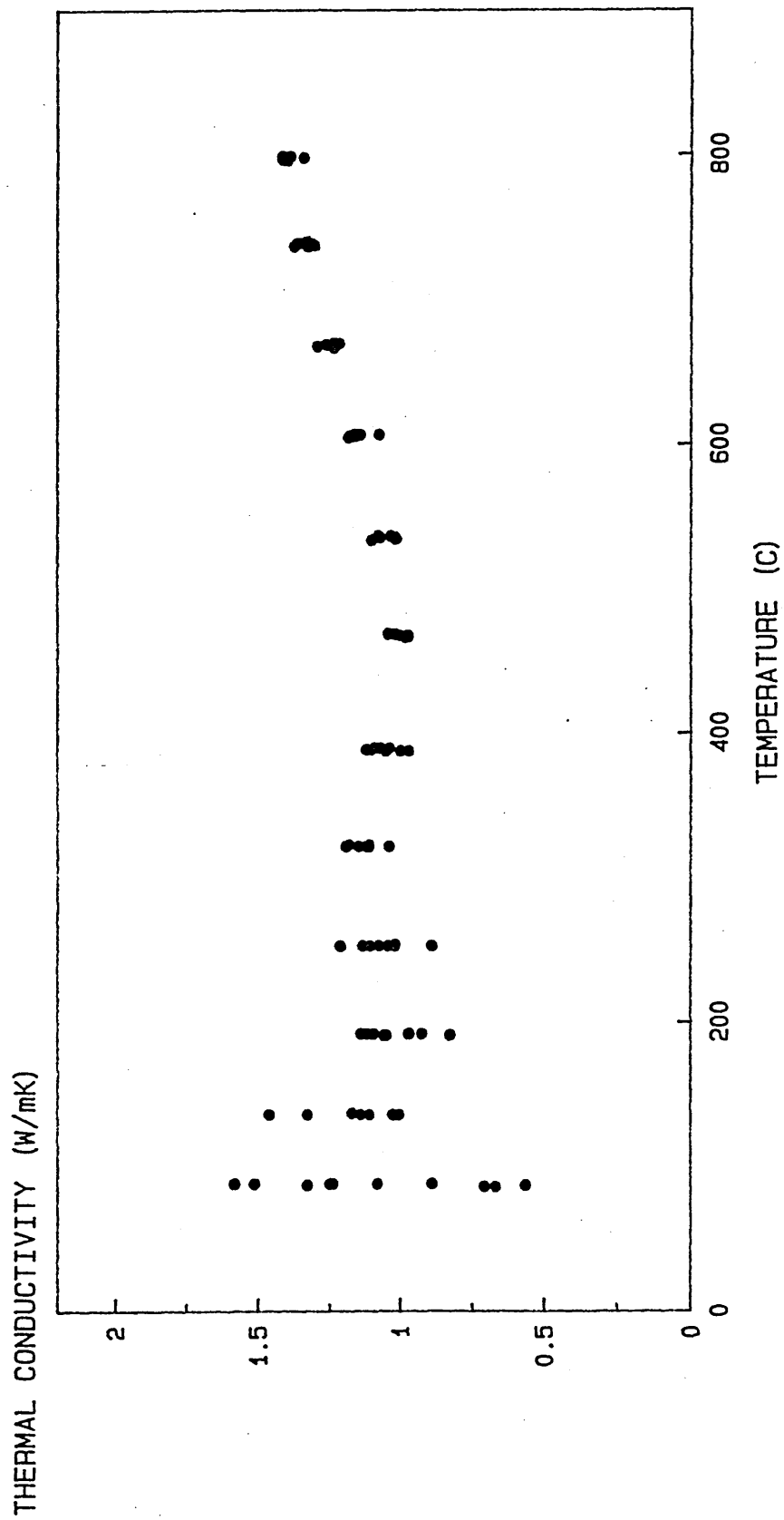


FIGURE 68. Measured Thermal Conductivity vs Mean Sample Temperature For Sample No.5 (Heating Cycle).

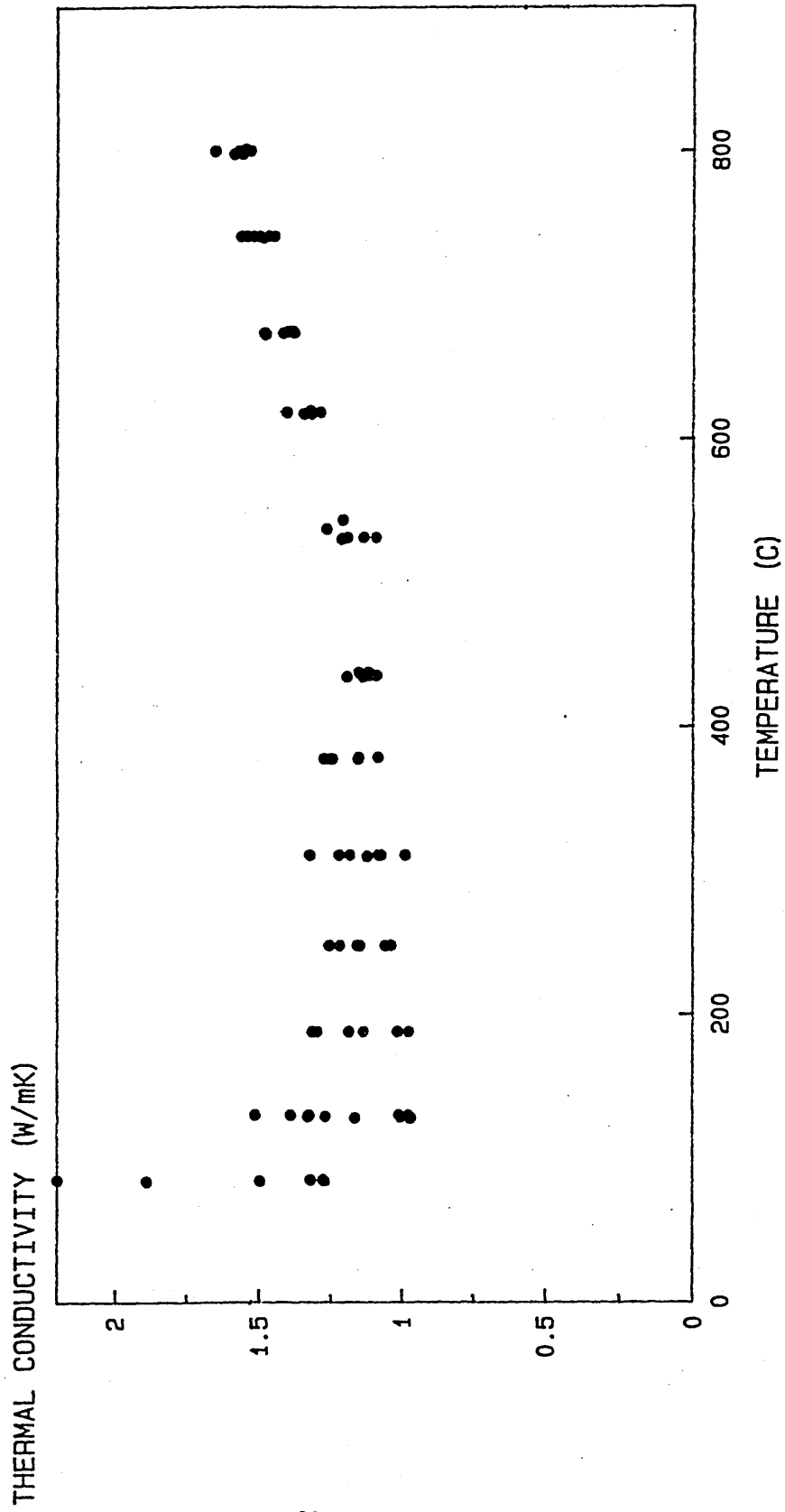


FIGURE 69. Measured Thermal Conductivity vs Mean Sample Temperature For Sample No.6 (Heating Cycle).

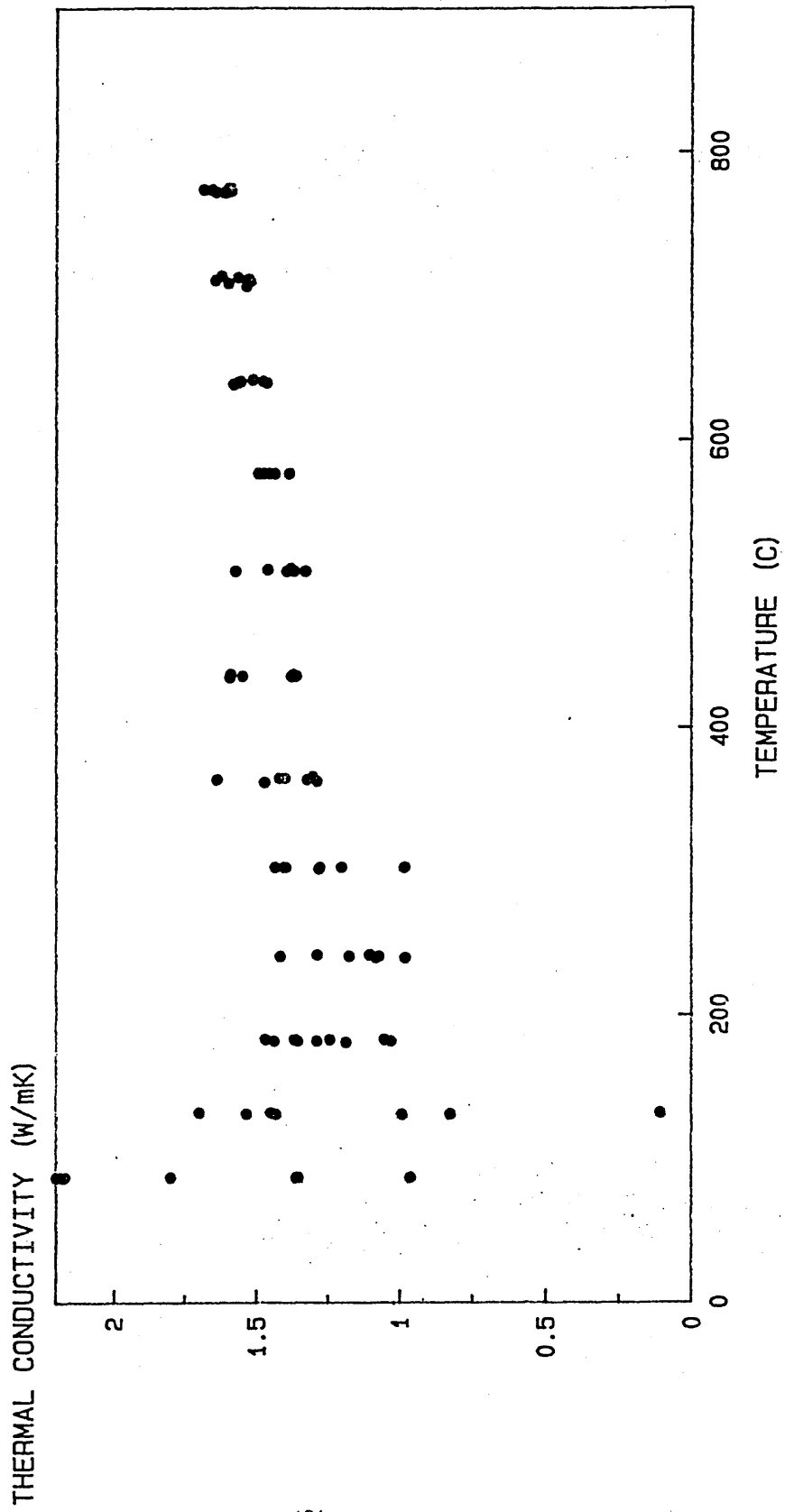


FIGURE 70. Average Conductivity Values For Samples No.3, No.4, No.5 And No.6 (Heating Cycles).

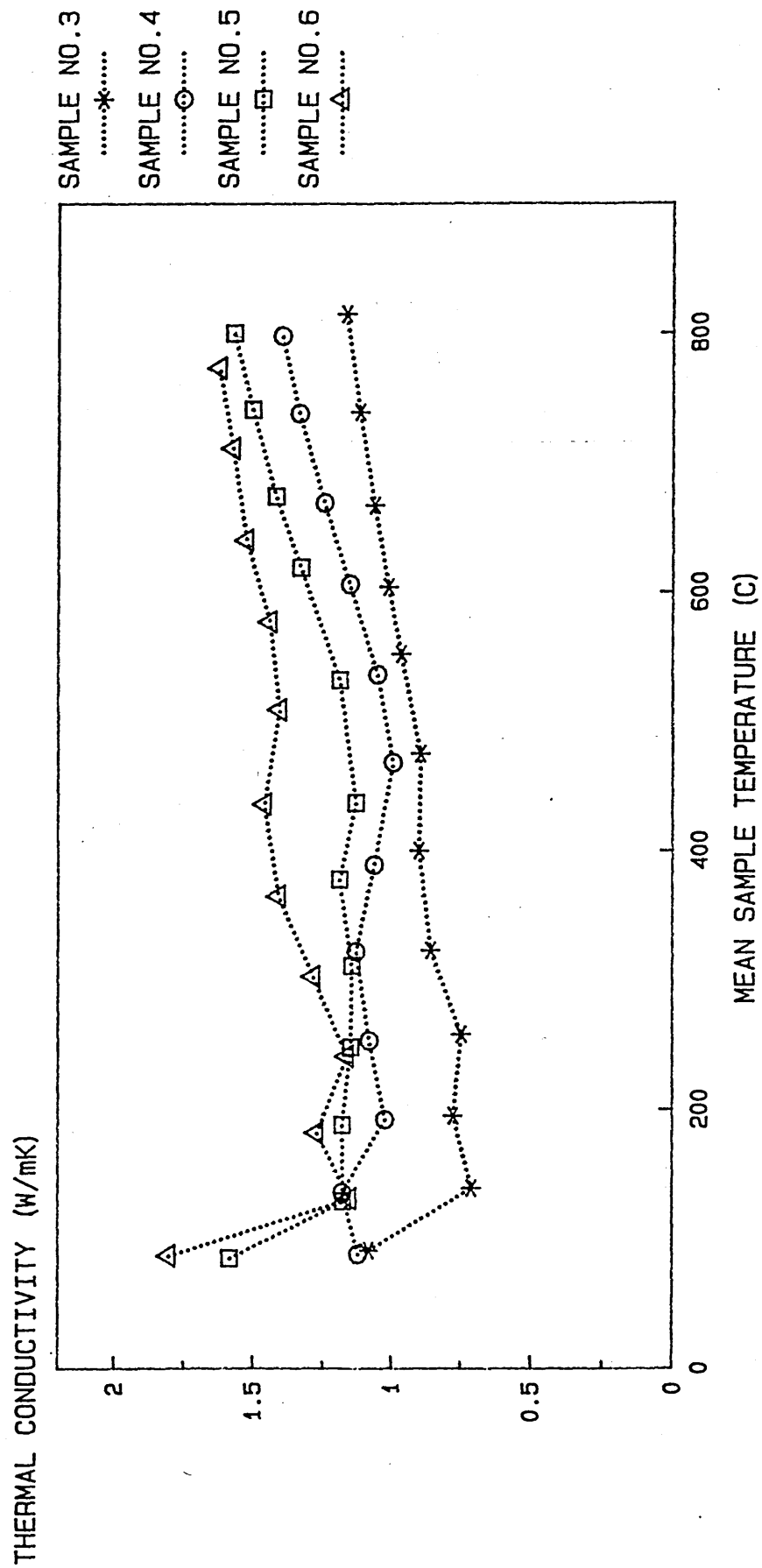


FIGURE 71. Measured Thermal Conductivity vs
Mean Sample Temperature For Sample
SLAG 8 (Heating Cycle).

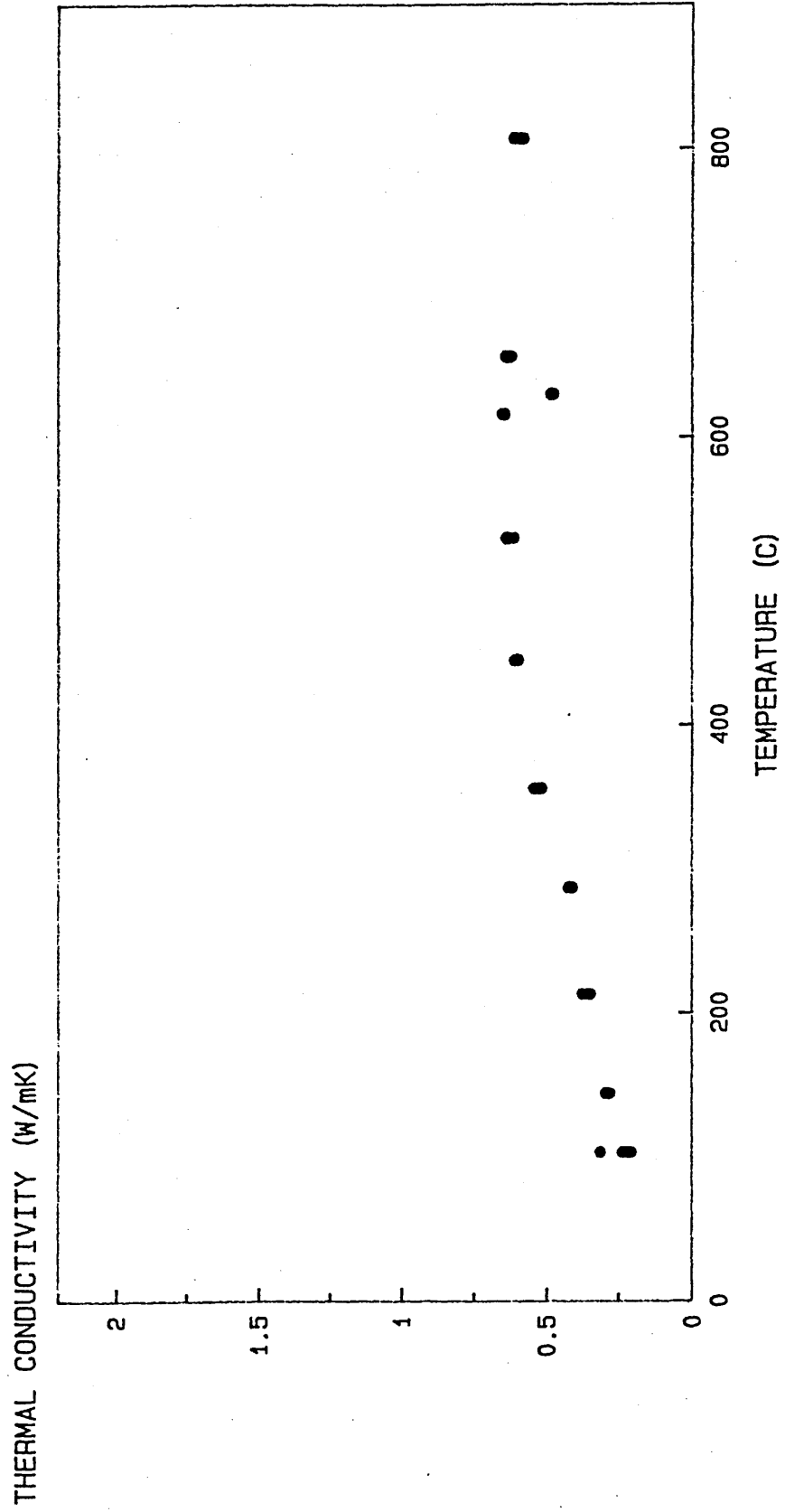


FIGURE 72. Measured Thermal Conductivity vs Mean Sample Temperature For Sample SLAG 4 (Heating Cycle).

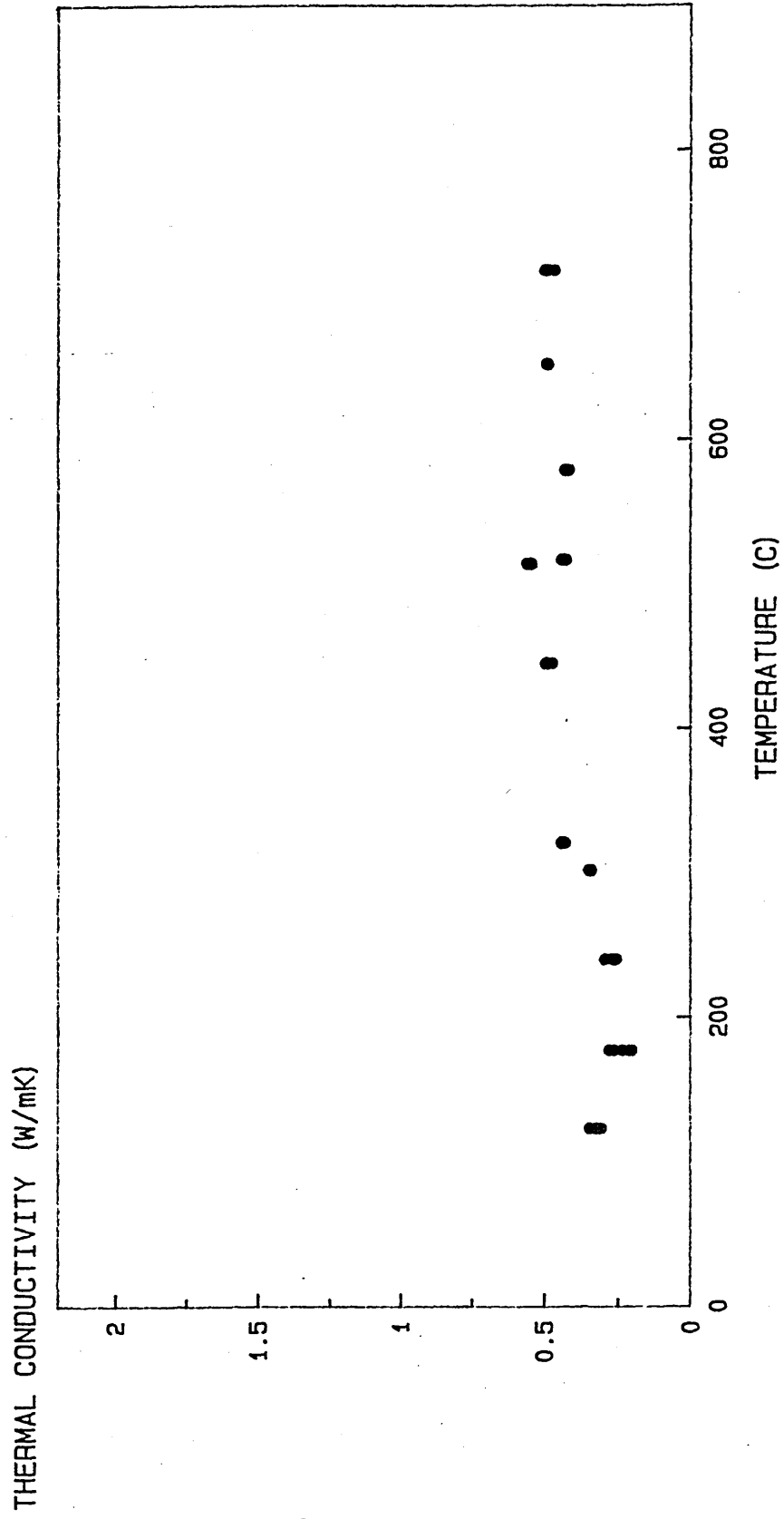


FIGURE 73. Average Conductivity Values For Samples SLAG 8 And SLAG 4 (Heating Cycles).

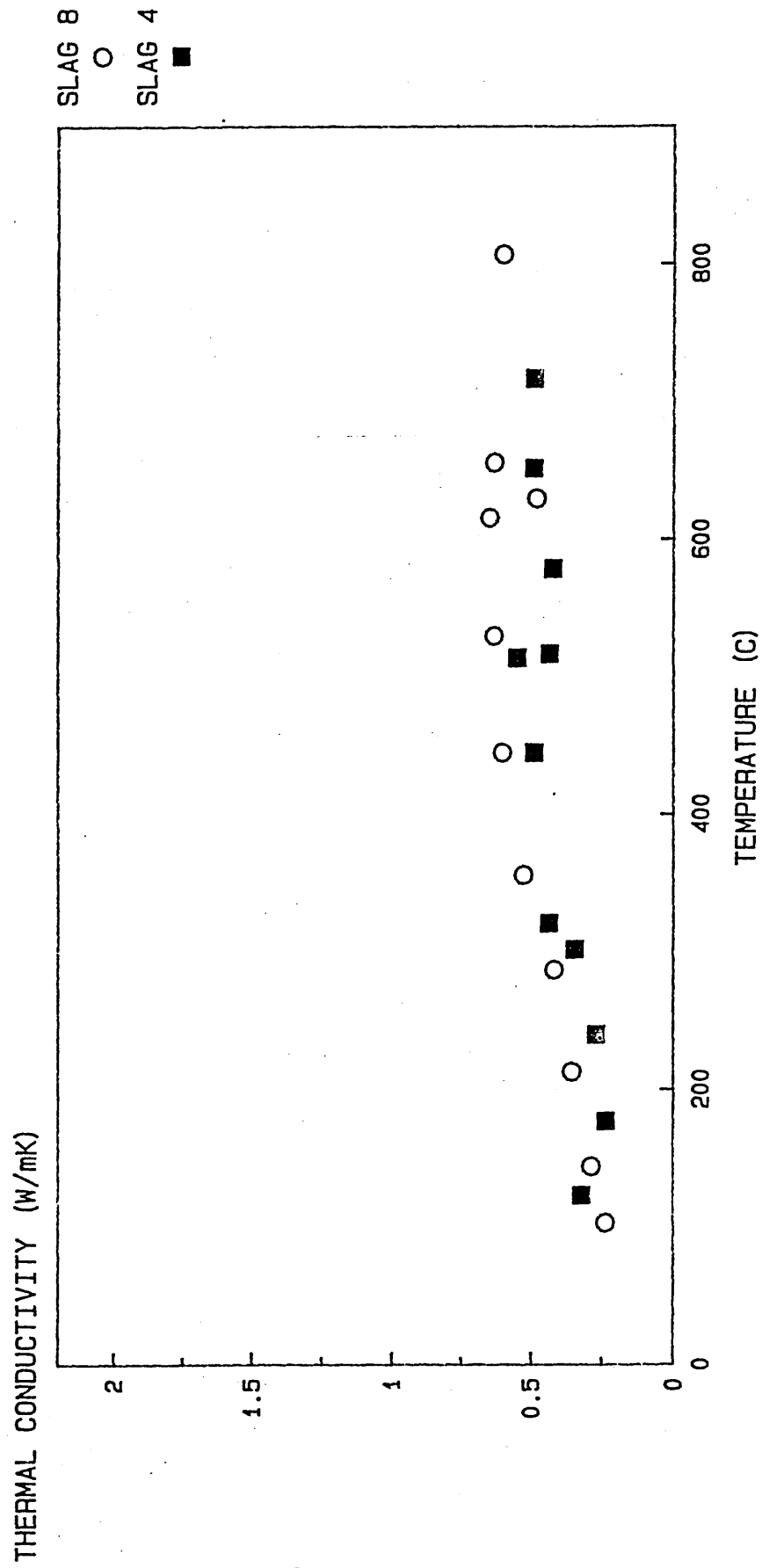


FIGURE 74. Average Conductivity Values For Sample IB4 (Heating Cycle).

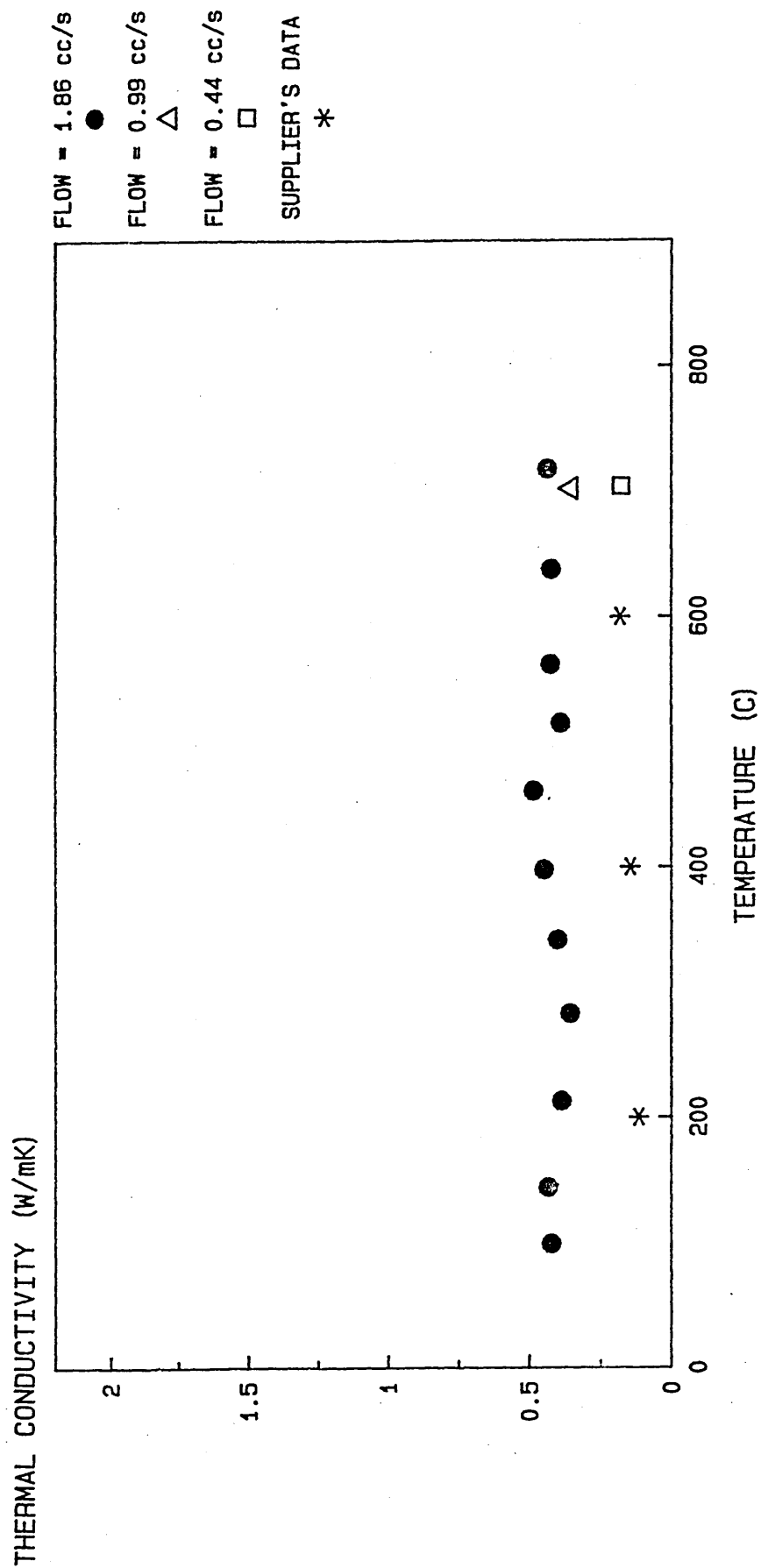


FIGURE 75. Average Conductivity Values For Sample IB1 (Heating Cycle).

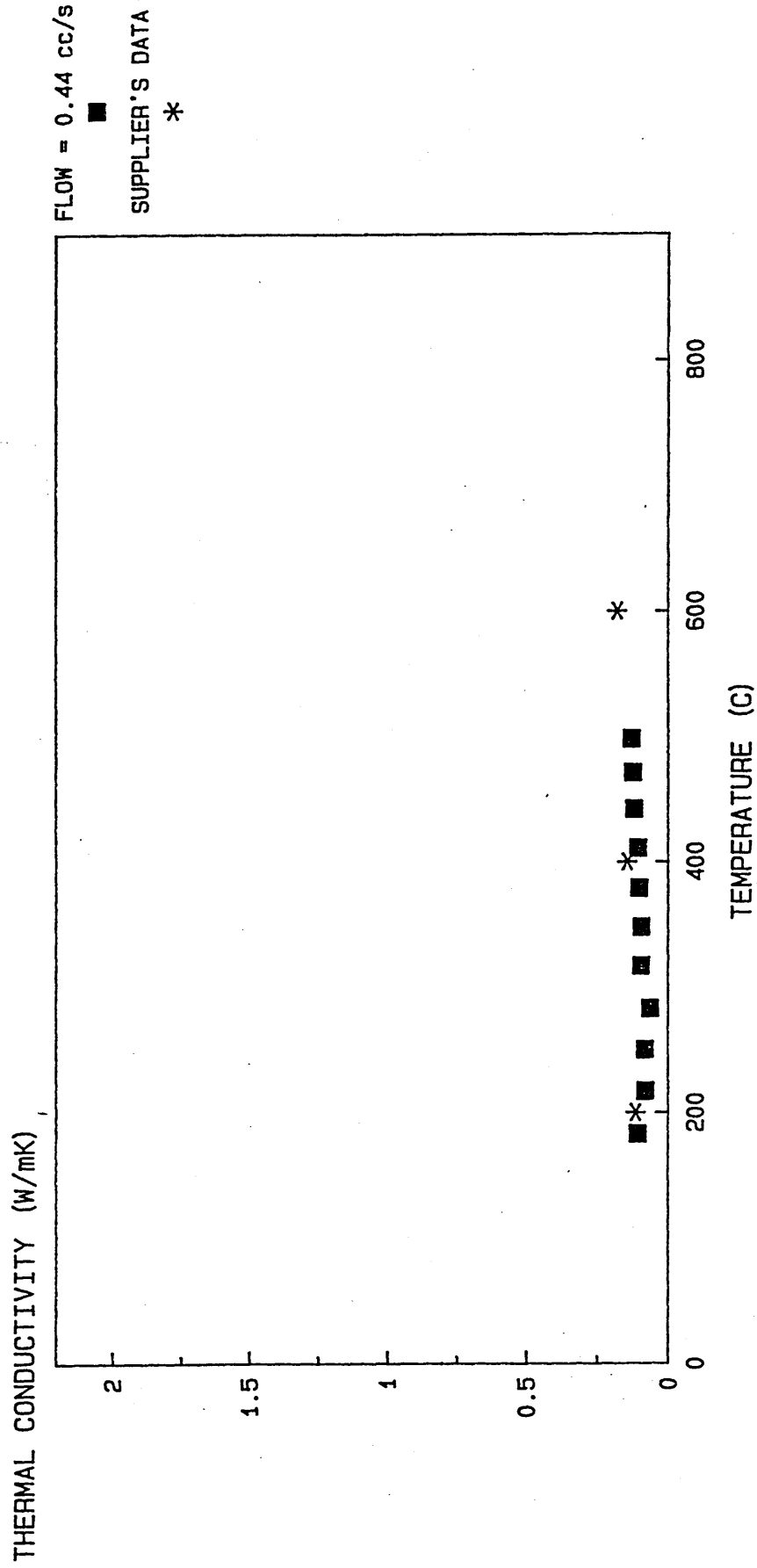


FIGURE 76. Average Conductivity Values For Sample SILICA 2 (Heating Cycle).

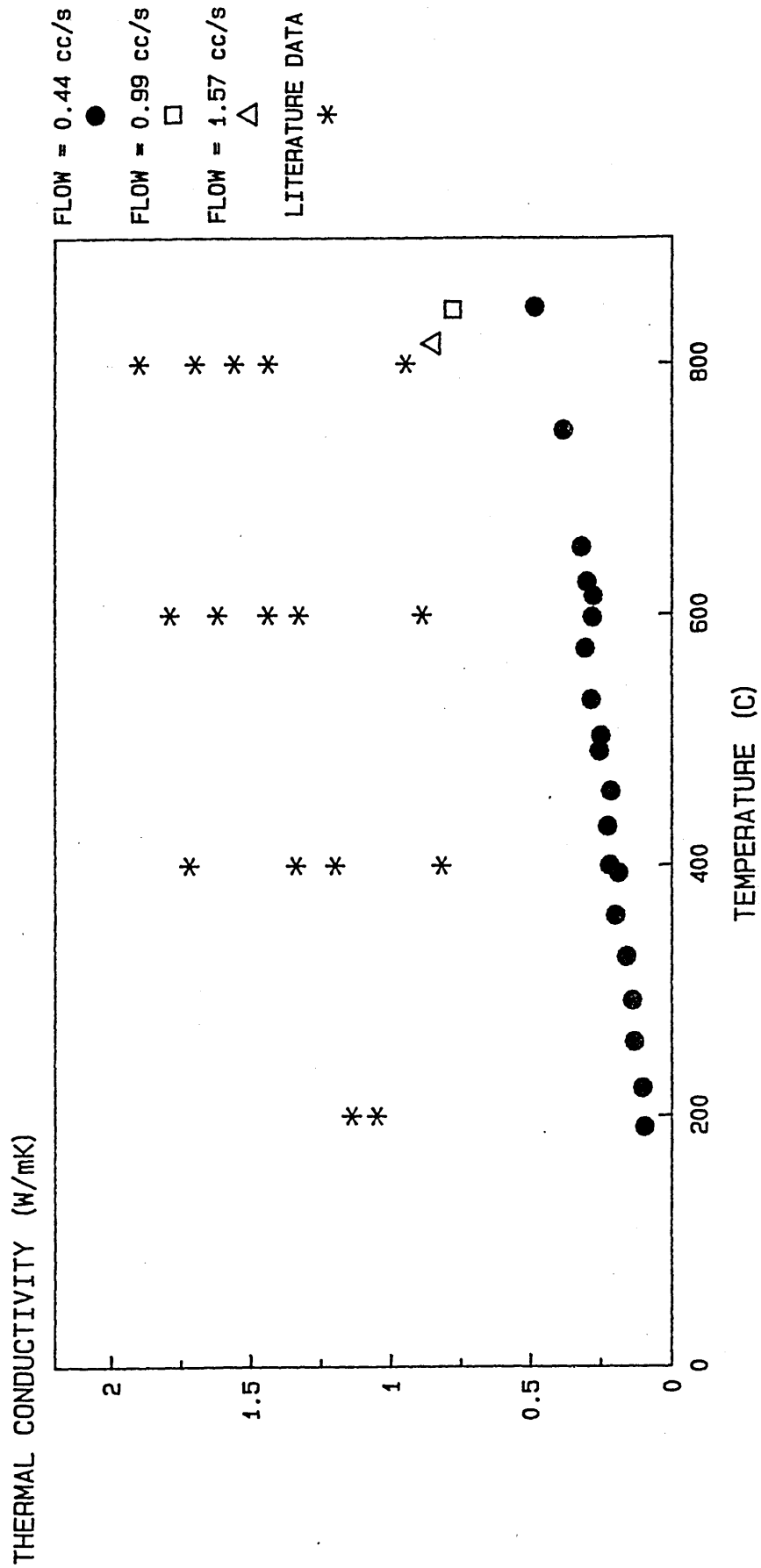


FIGURE 77. Average Conductivity Values For Sample IB4 Re-run (Heating Cycle).

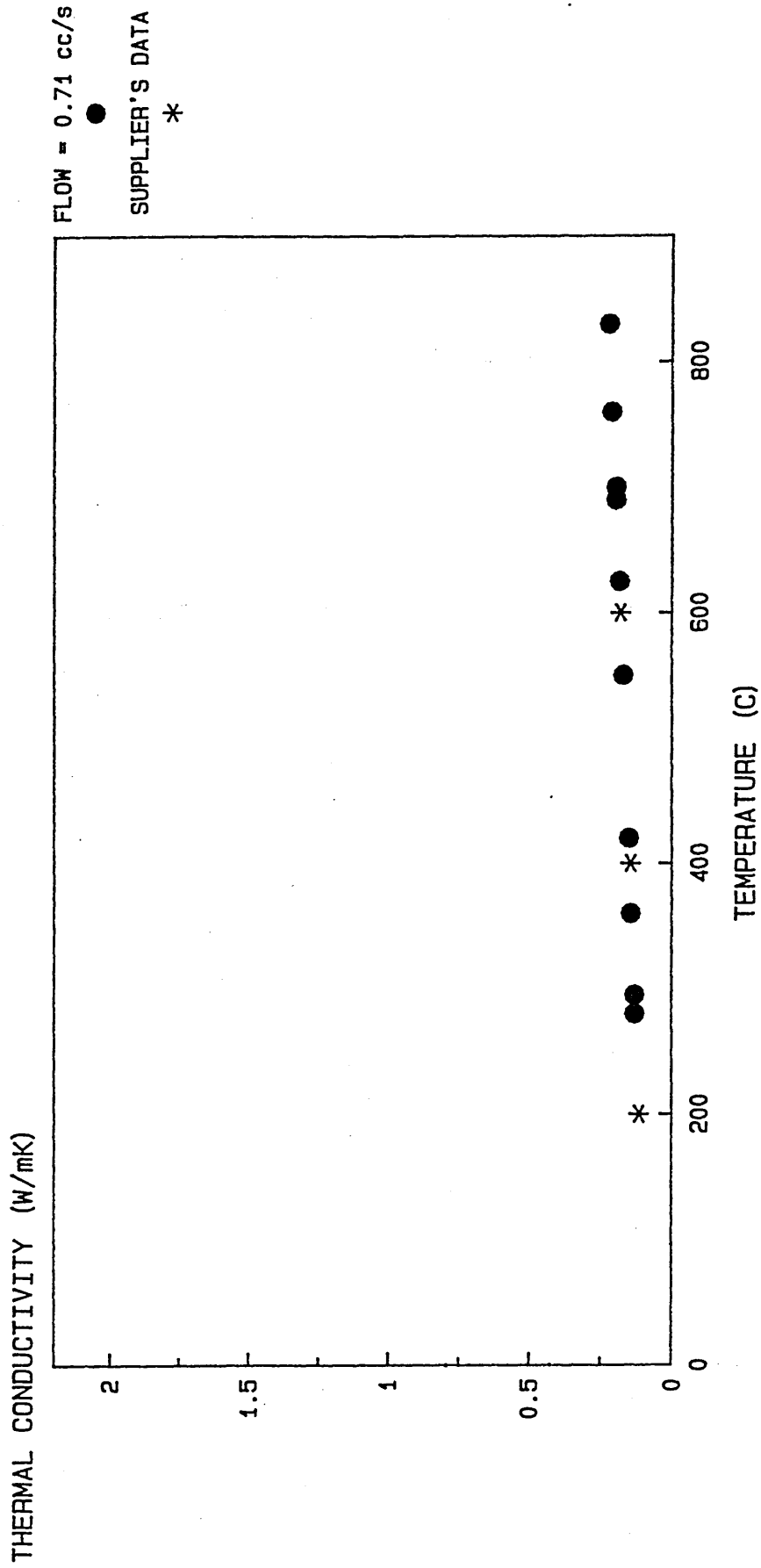


FIGURE 78. Average Conductivity Values For Sample SLAG 6 (Heating Cycle).

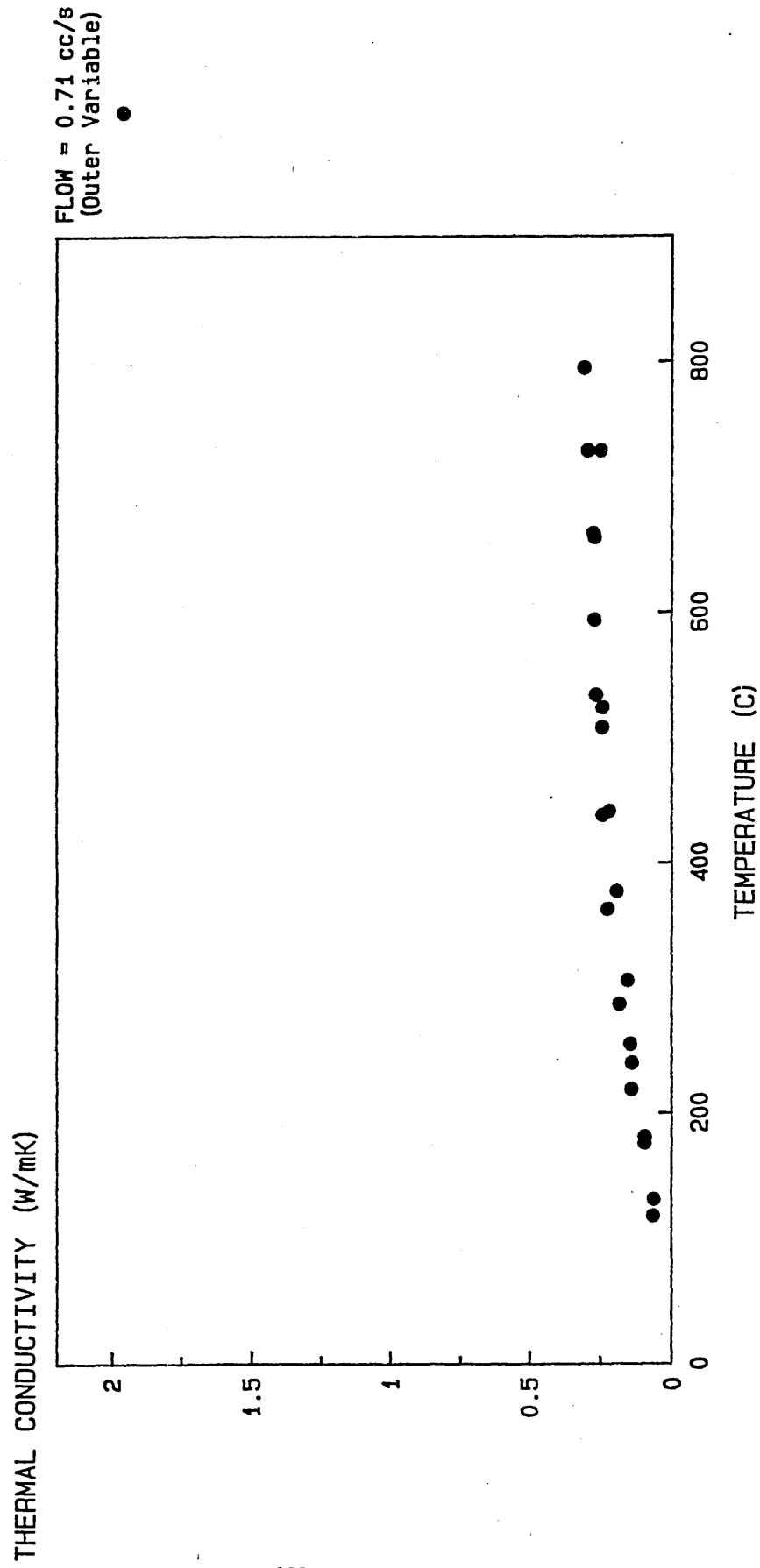


FIGURE 79. Average Conductivity Values For Sample SLAG 5 (Heating Cycle).

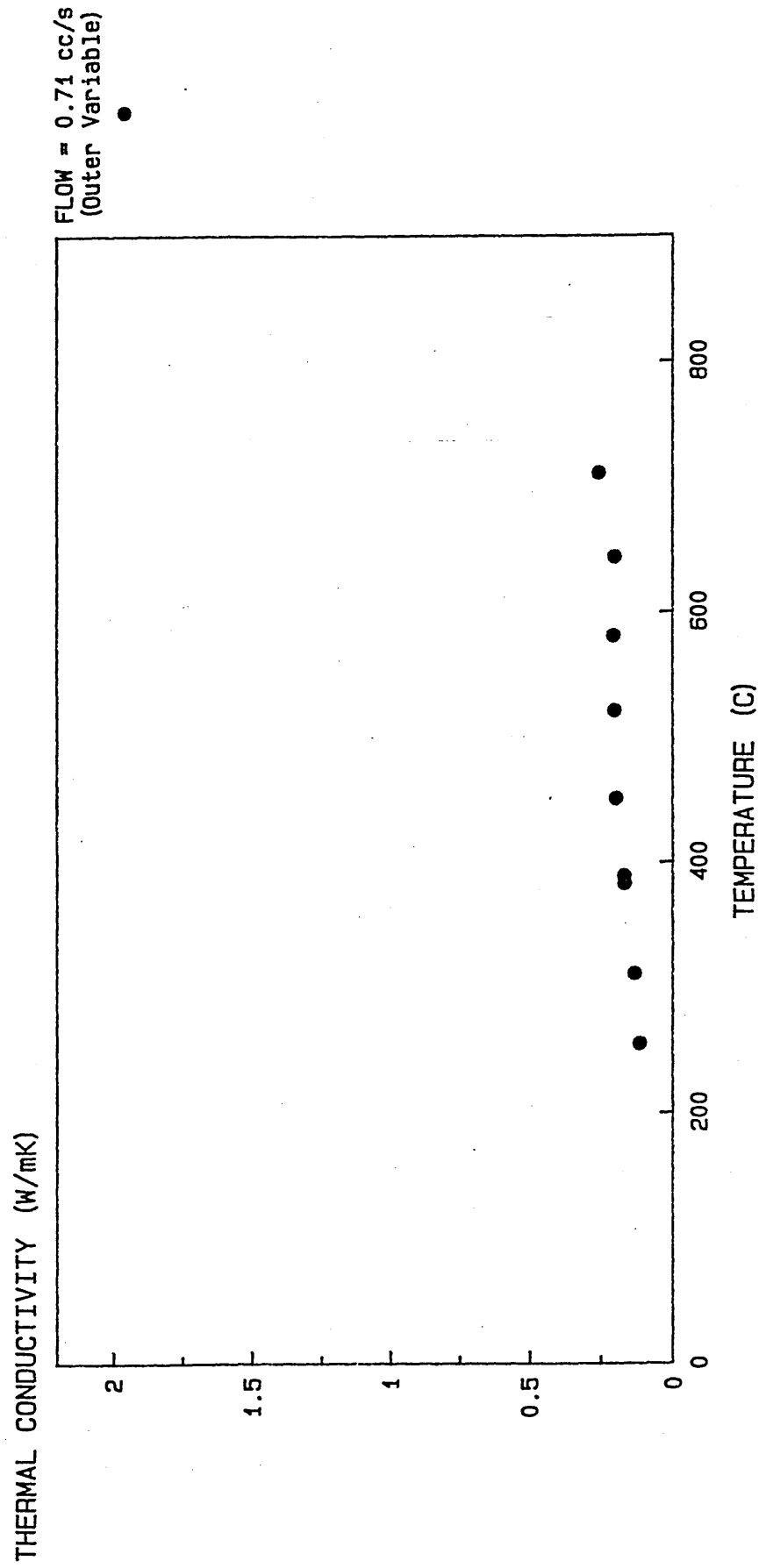


FIGURE 80. Average Conductivity Values For Sample HSB 1 (Heating Cycle).

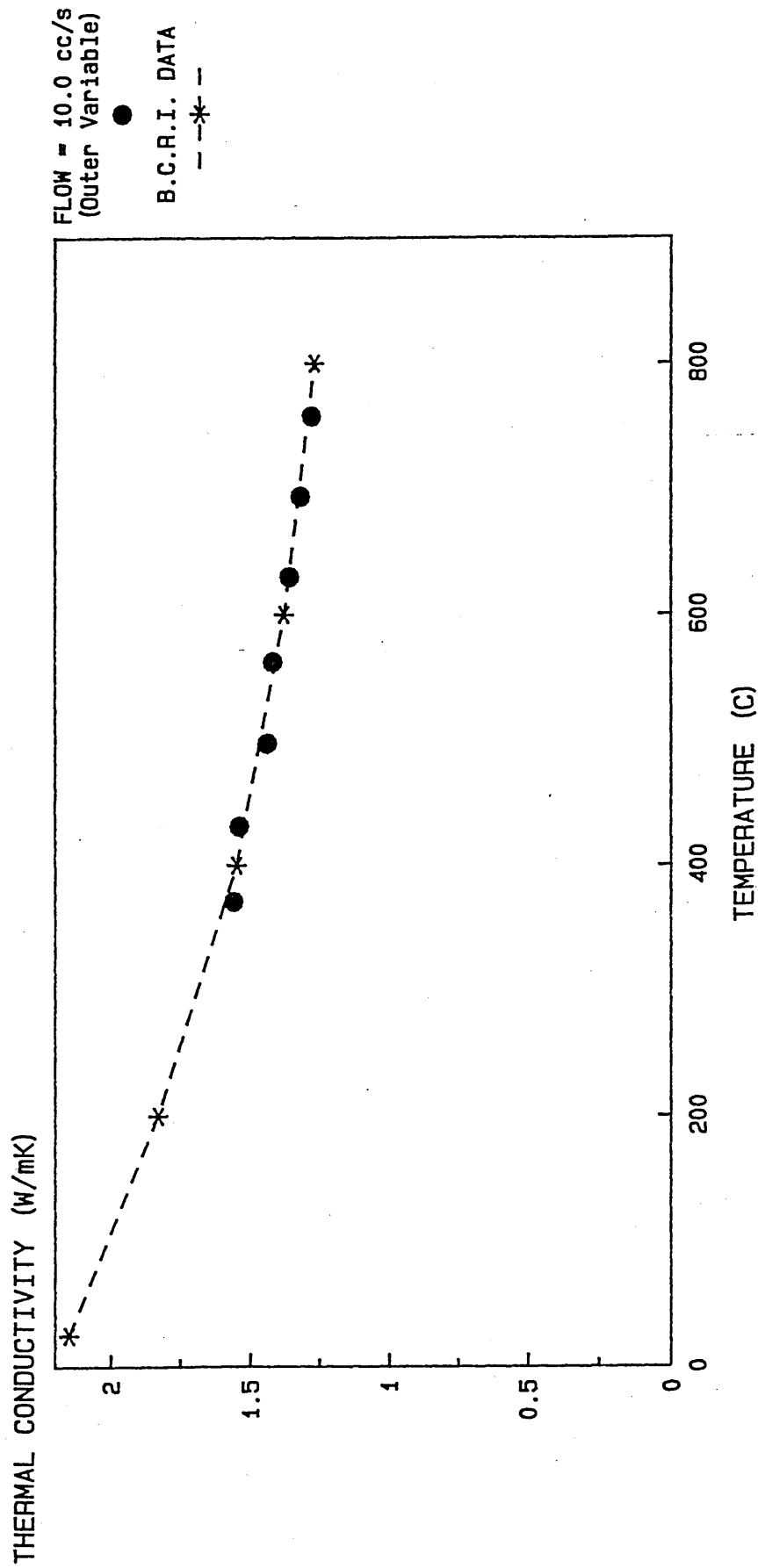


FIGURE 81. Average Conductivity Values For Sample SLAG 21 (Heating And Cooling Cycles).

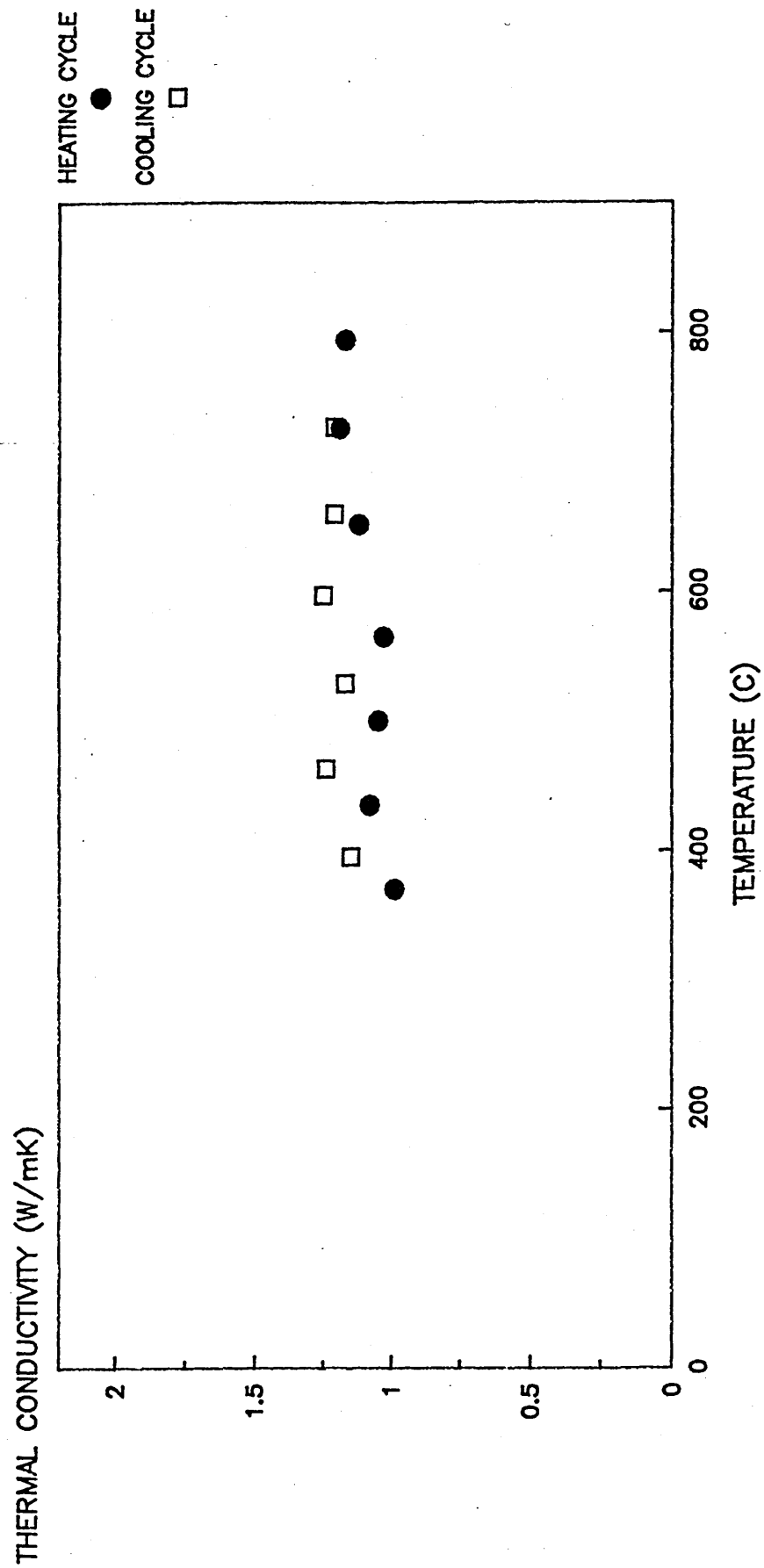


FIGURE 82. Average Conductivity Values For Sample SLAG 22 (Heating And Cooling Cycles).

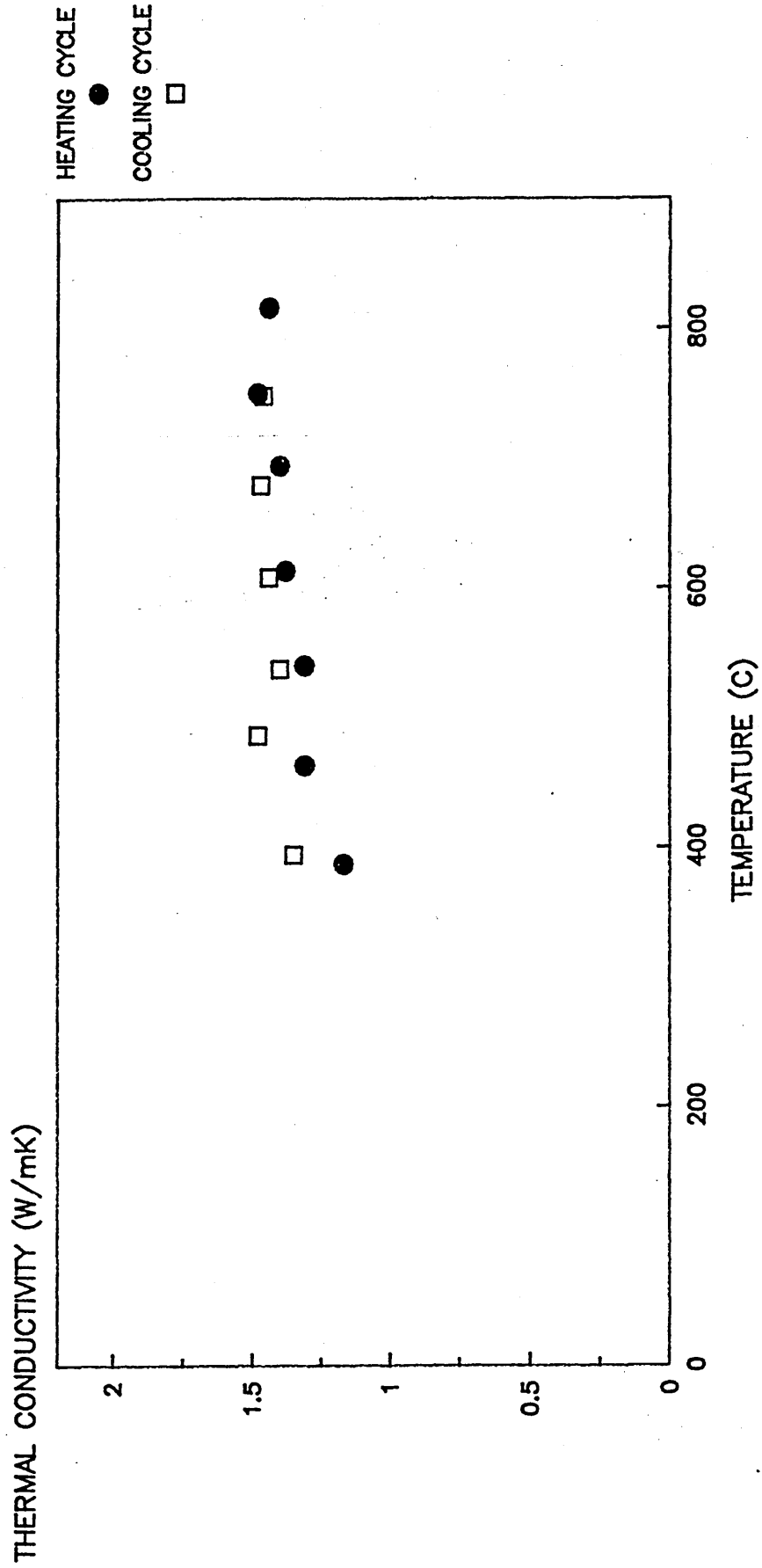


FIGURE 83. Average Conductivity Values For Sample SLAG 24 (Heating And Cooling Cycles).

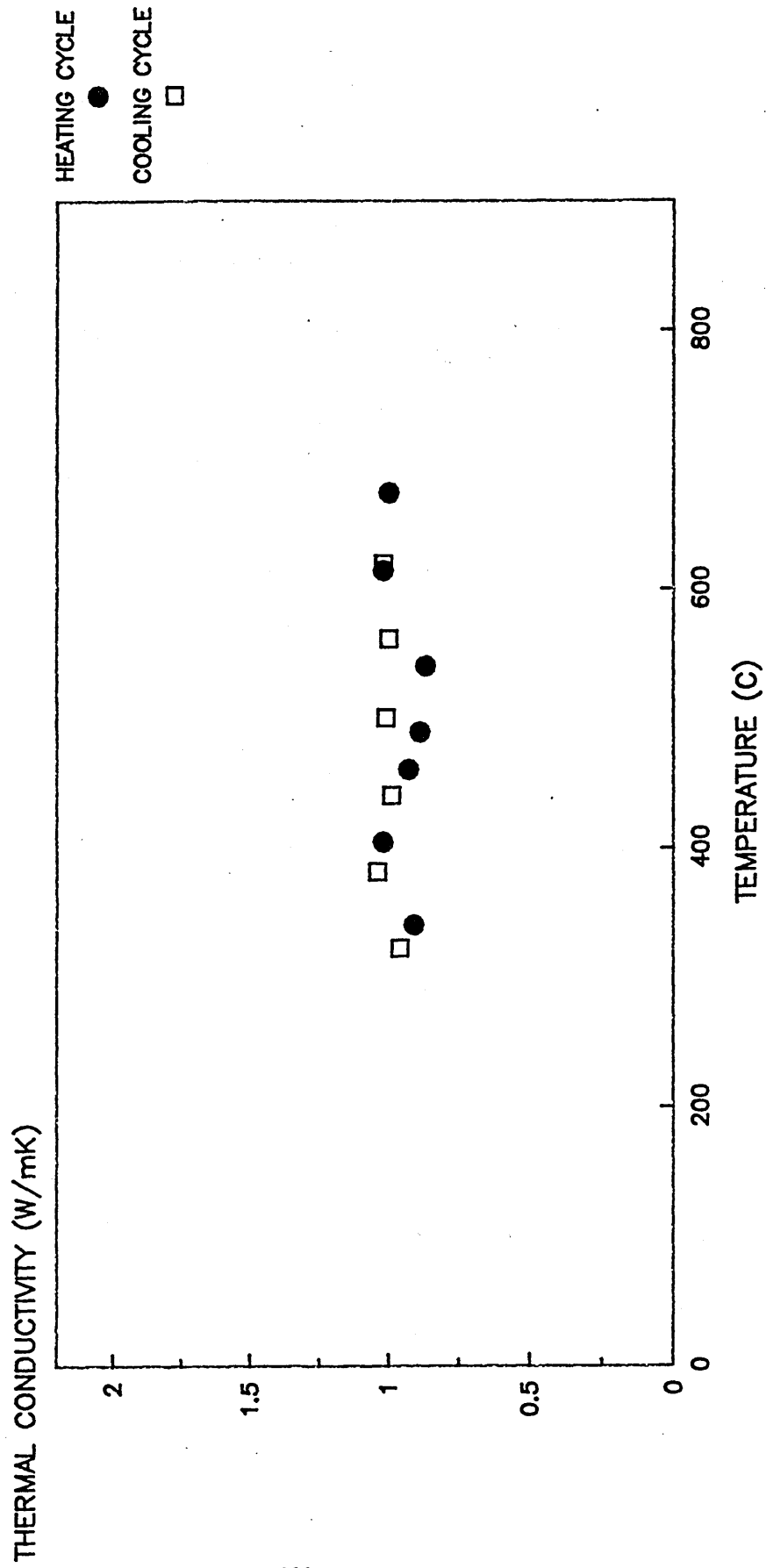


FIGURE 84. Average Conductivity Values For Sample SLAG 31 (Heating And Cooling Cycles).

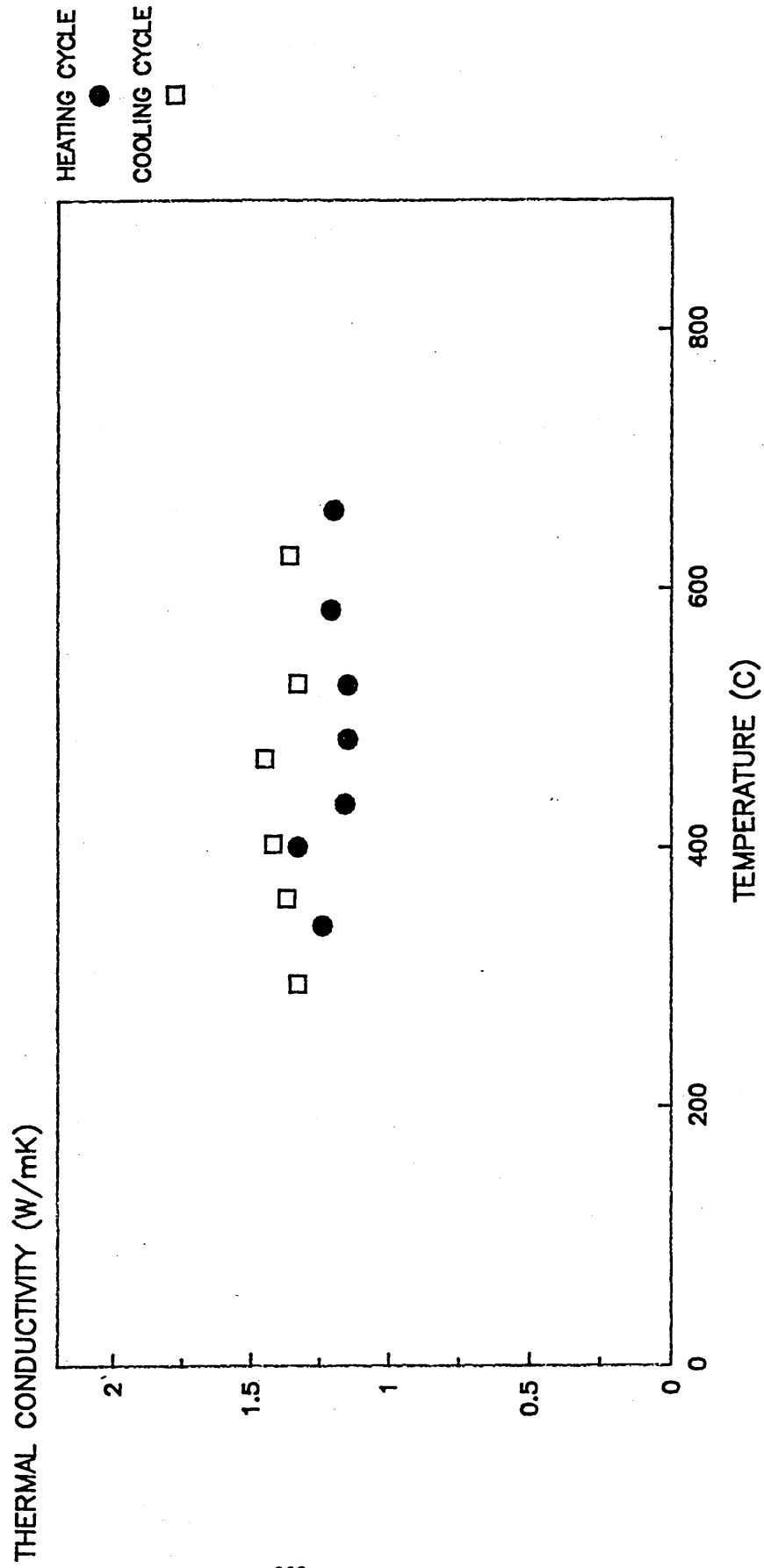


FIGURE 85. Average Conductivity Values For Sample SLAG 32 (Heating And Cooling Cycles).

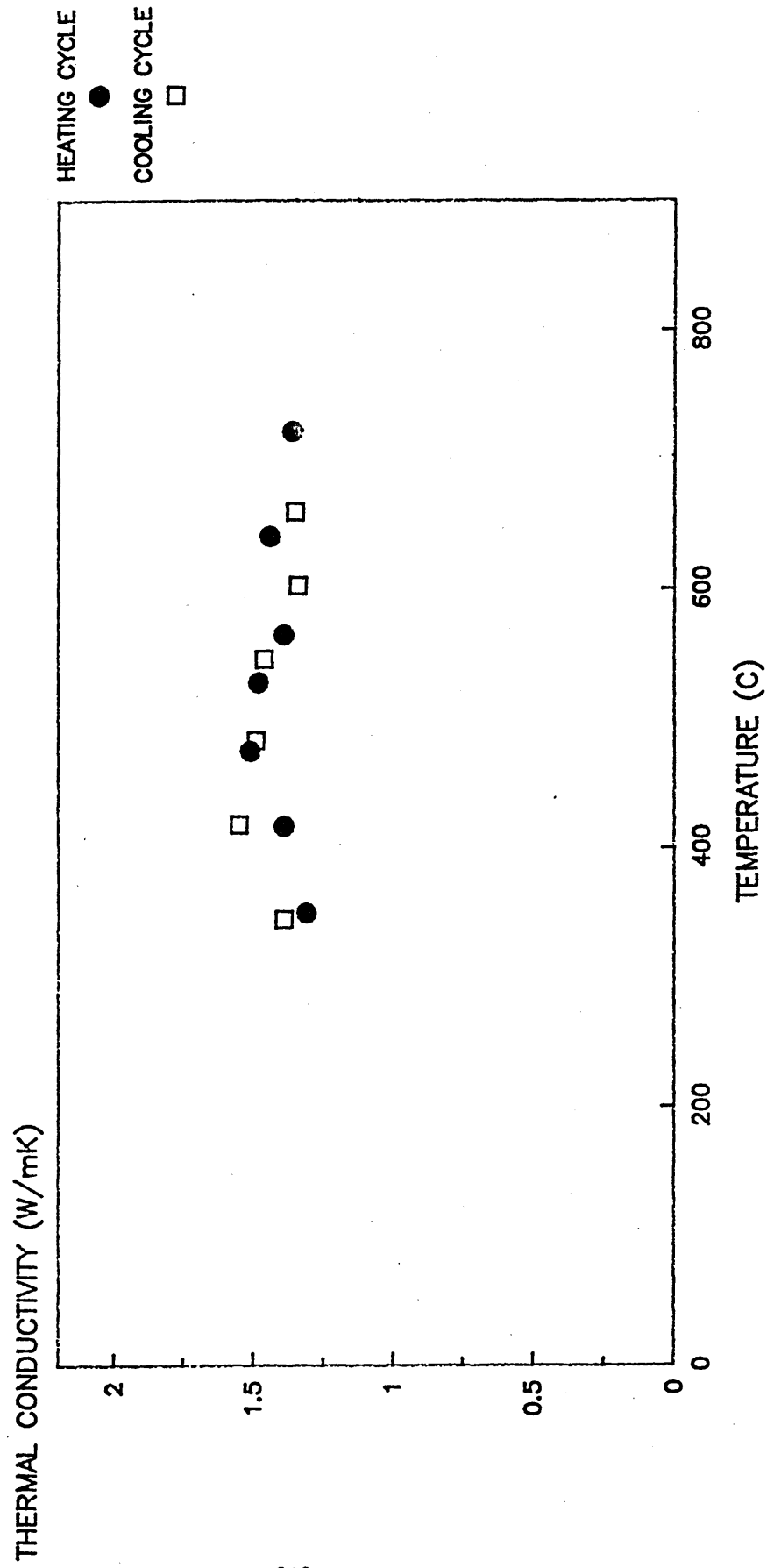


FIGURE 86. Average Conductivity Values For Samples SLAG 21, SLAG 22, SLAG 24, SLAG 31 And SLAG 32 (H + C Cycles).

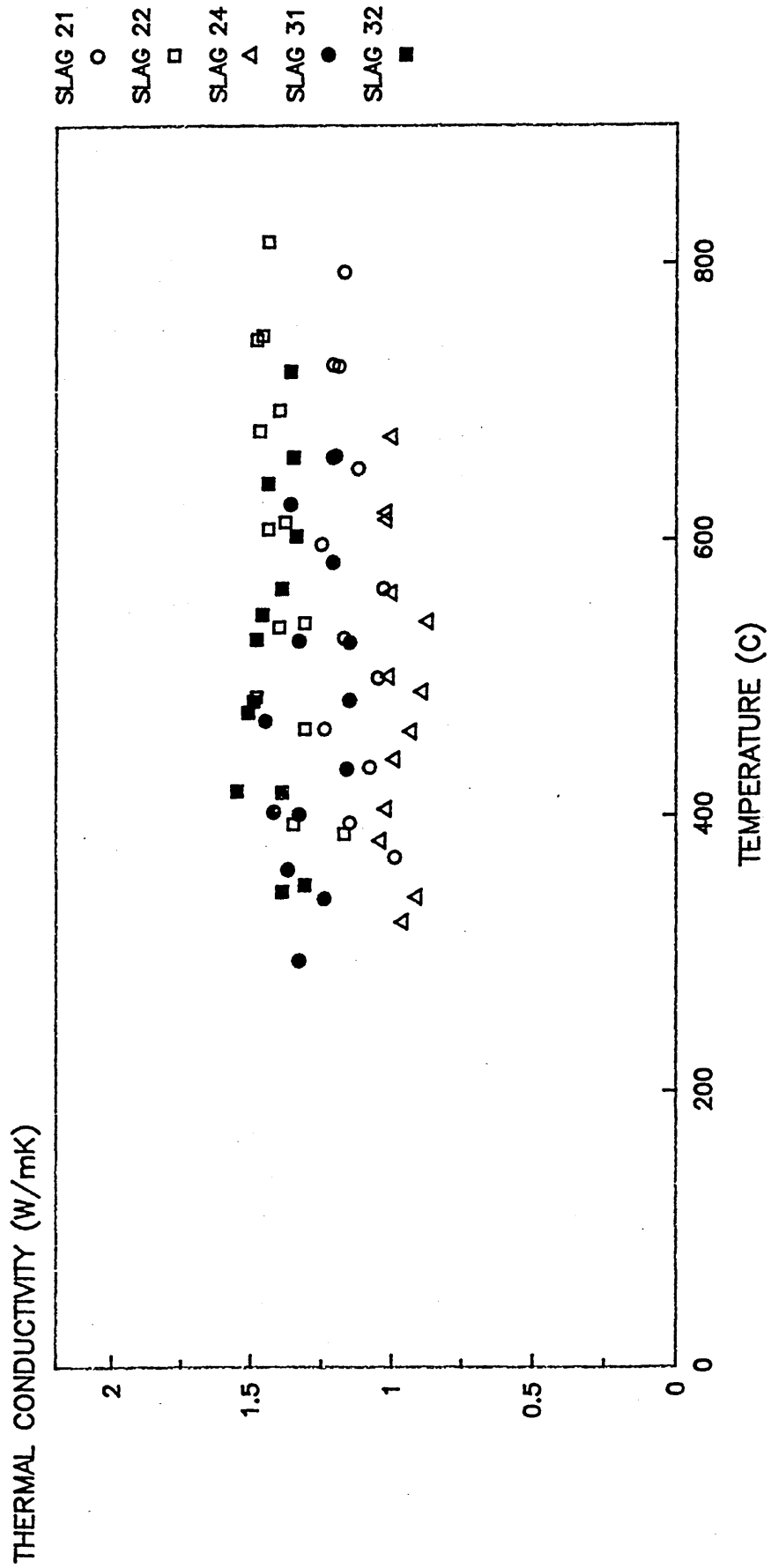


FIGURE 87. Mean Gradient Of Heat Flux Decrease After Charging Scrap vs Panel No.

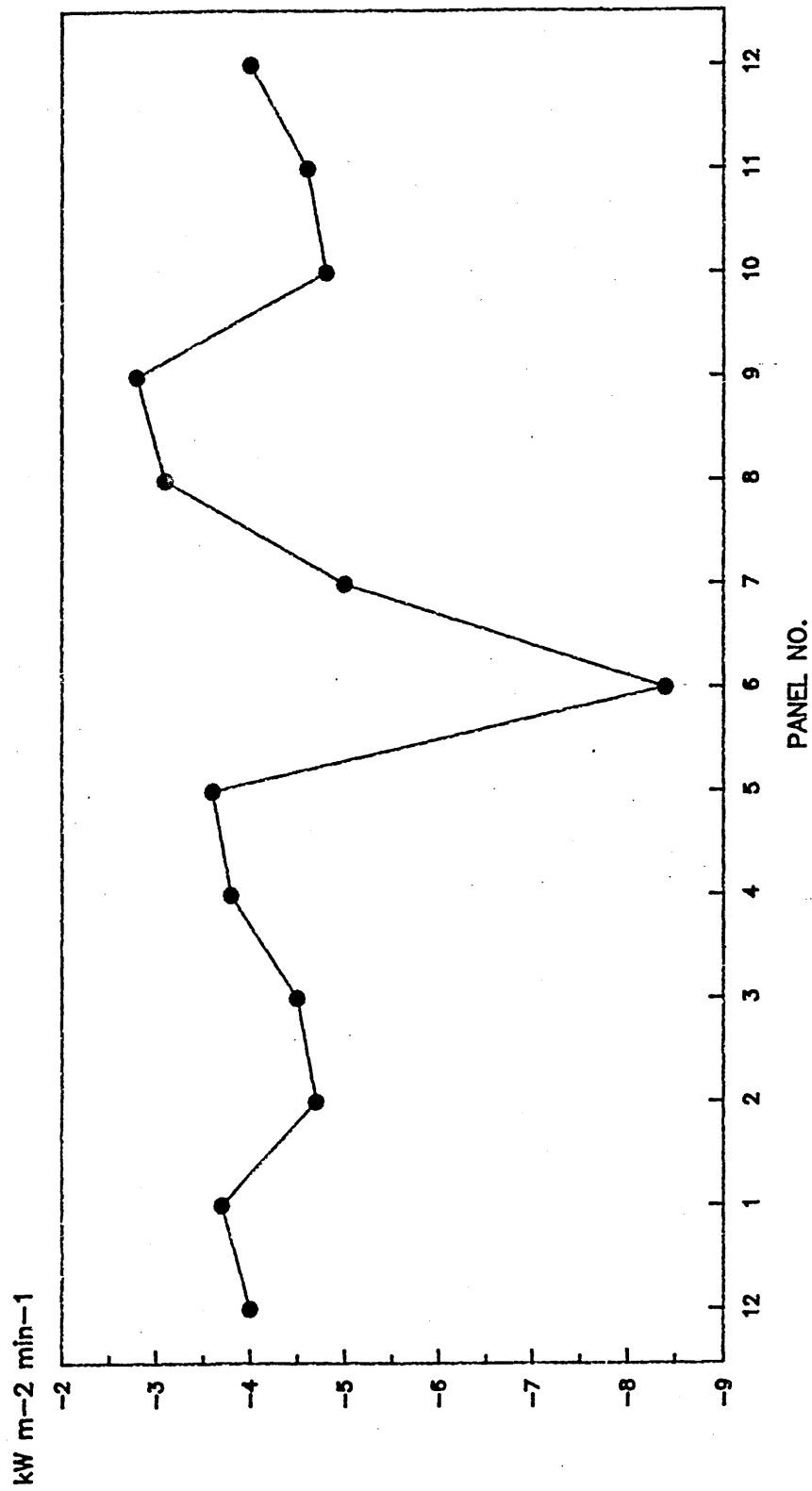


FIGURE 88. Mean Gradient Of Heat Flux Increase
During First 30 Minutes Of Meltdown
vs Panel No.

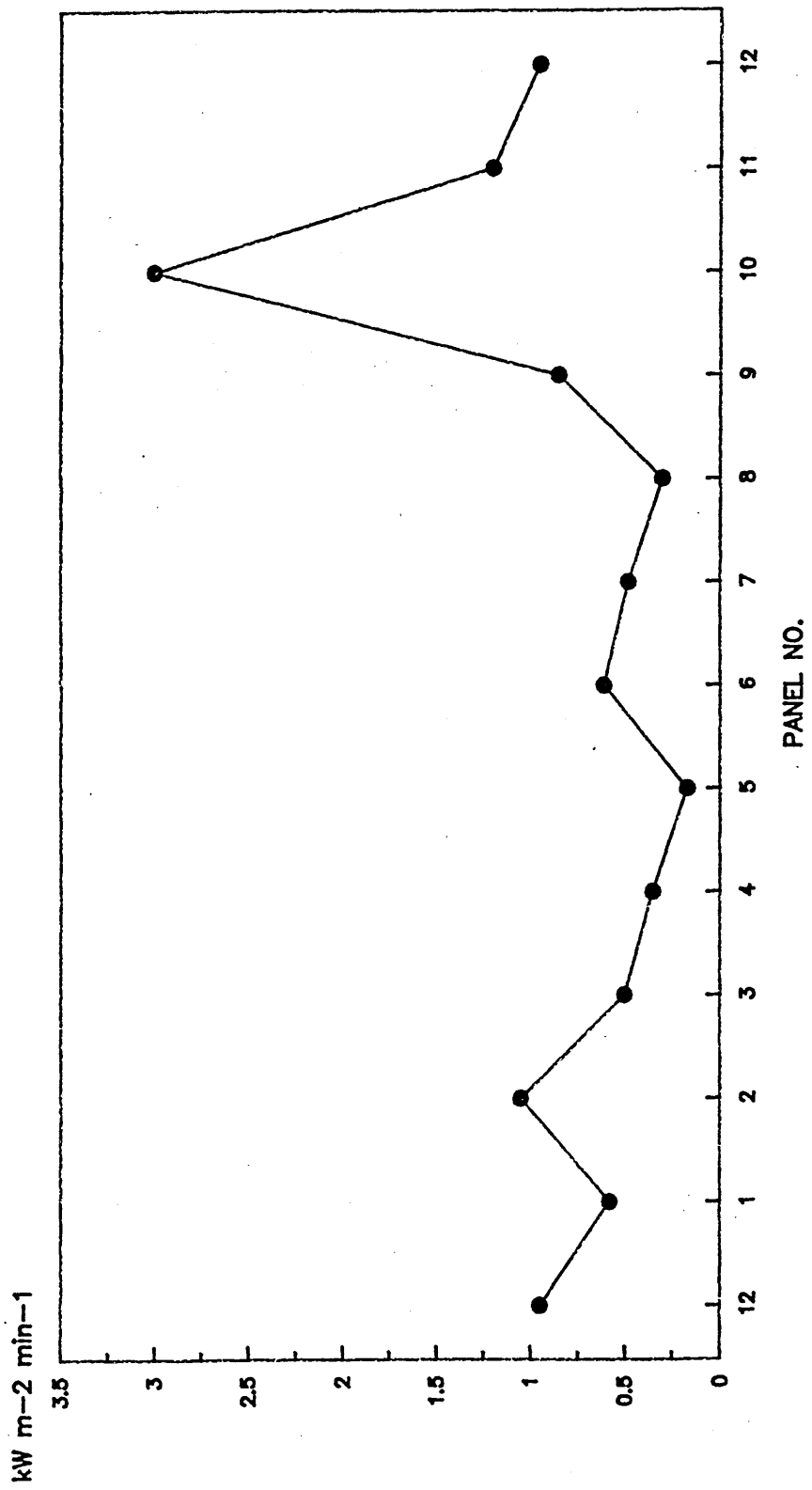


FIGURE 89. Mean Gradient Of Heat Flux Increase
During First 30 Minutes Of Meltdown
vs Log Slag Cover.

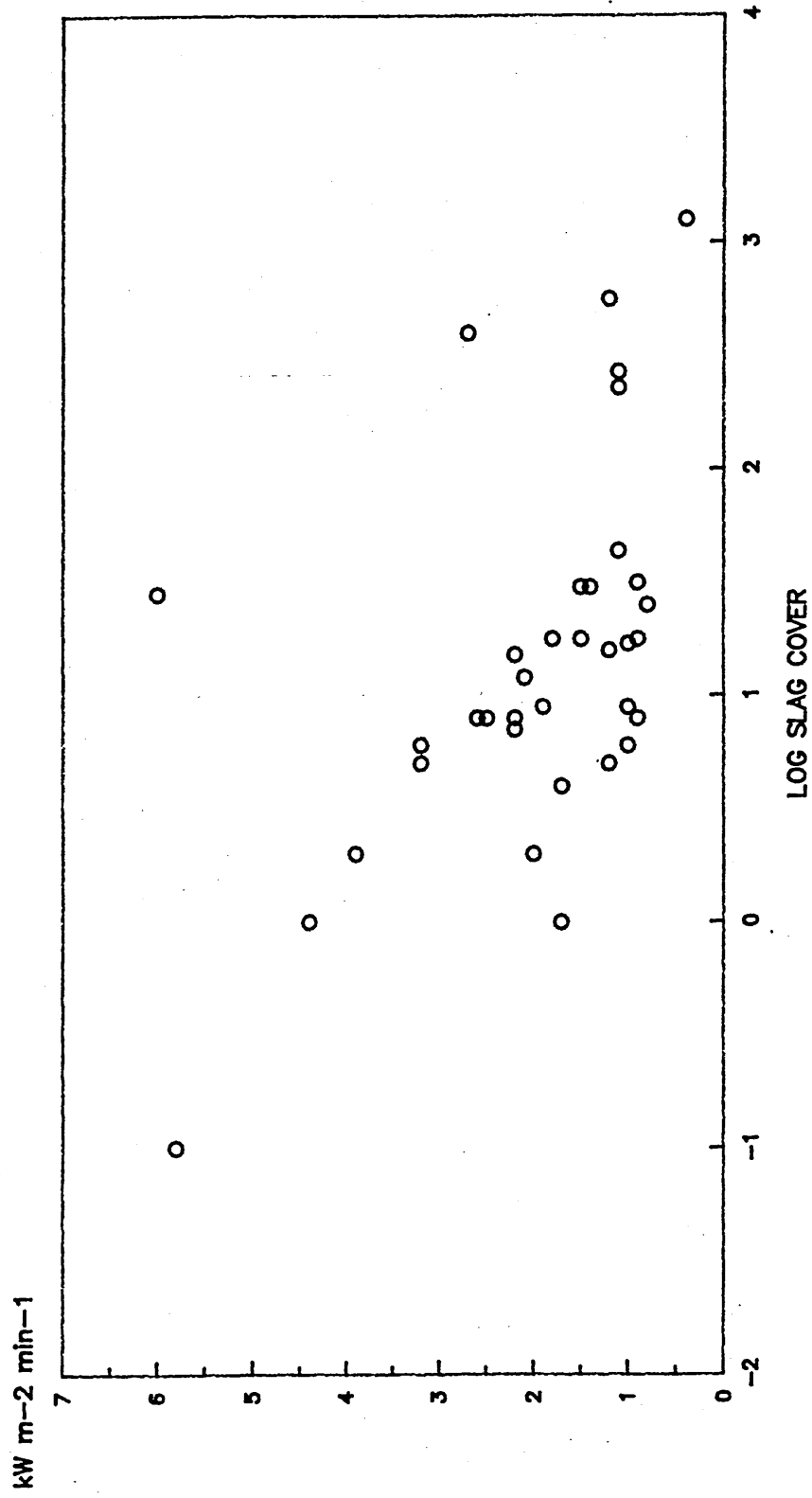


FIGURE 90. Mean Maximum Heat Flux vs Panel No.
(Datasets 06 - 08 Only).

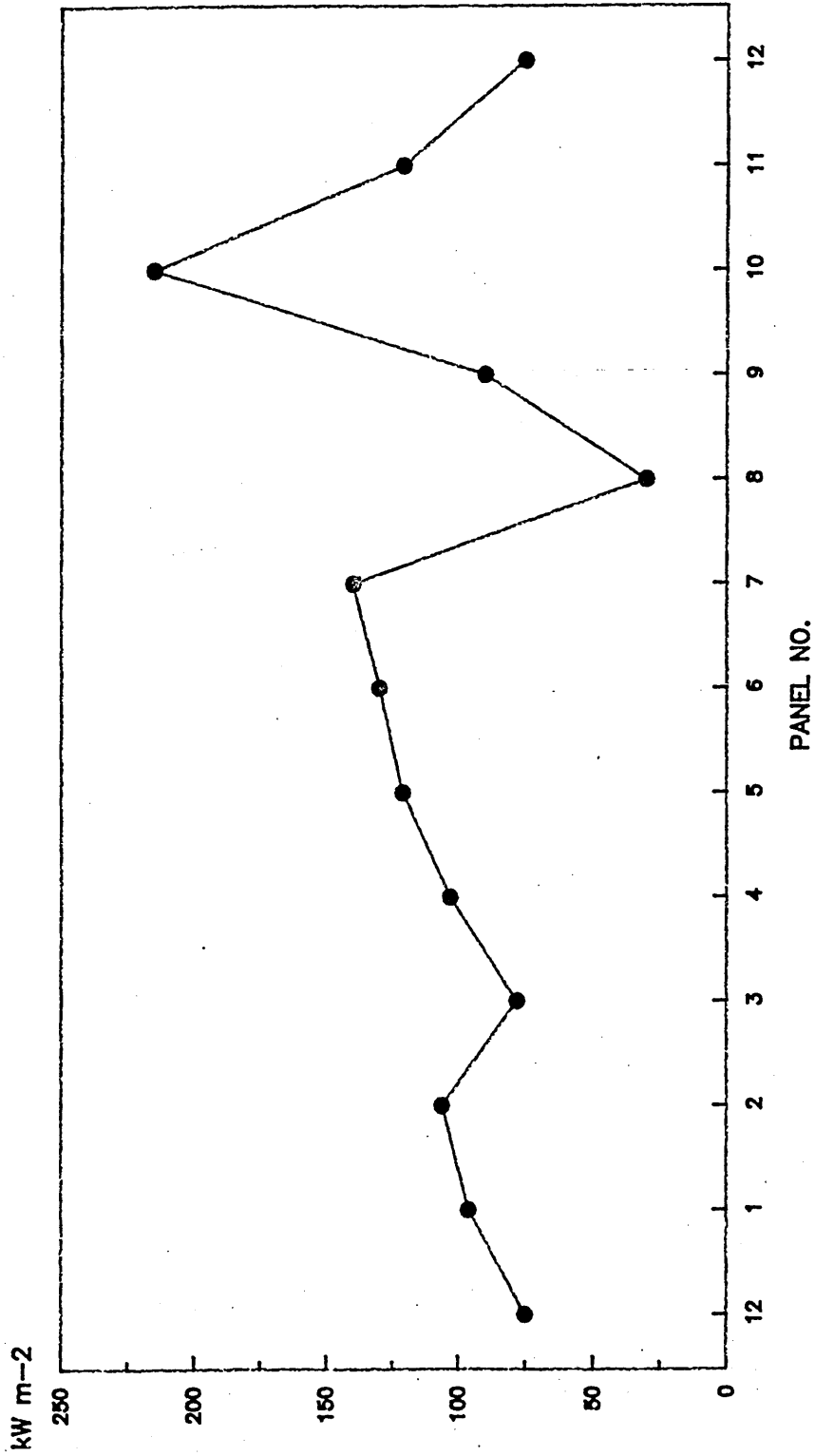


FIGURE 91. Mean Maximum Heat Flux vs Log Slag Cover (Datasets 06 - 08 Only).

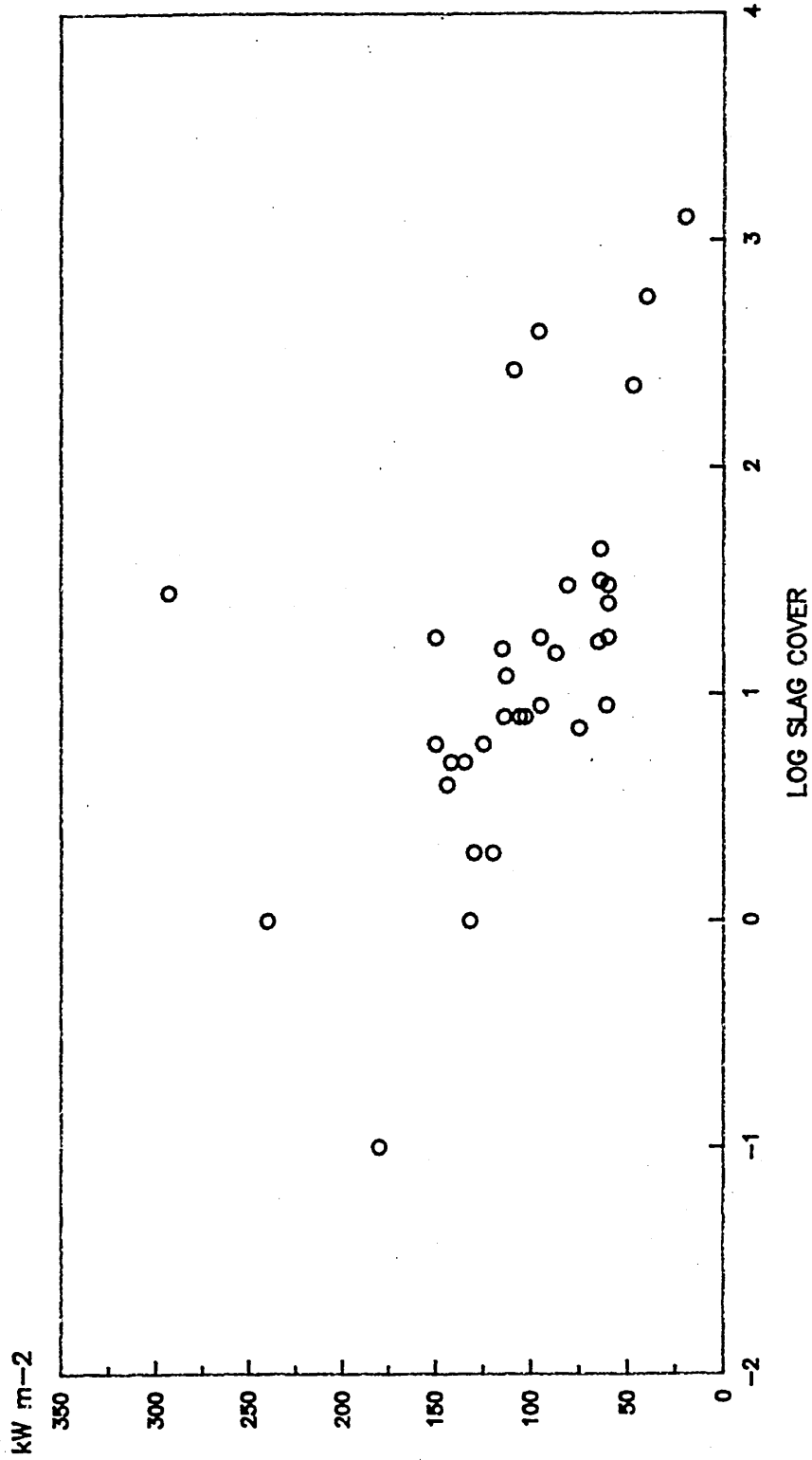


FIGURE 92. Mean Gradient Of Heat Flux Decrease
After Tapping vs Panel No.

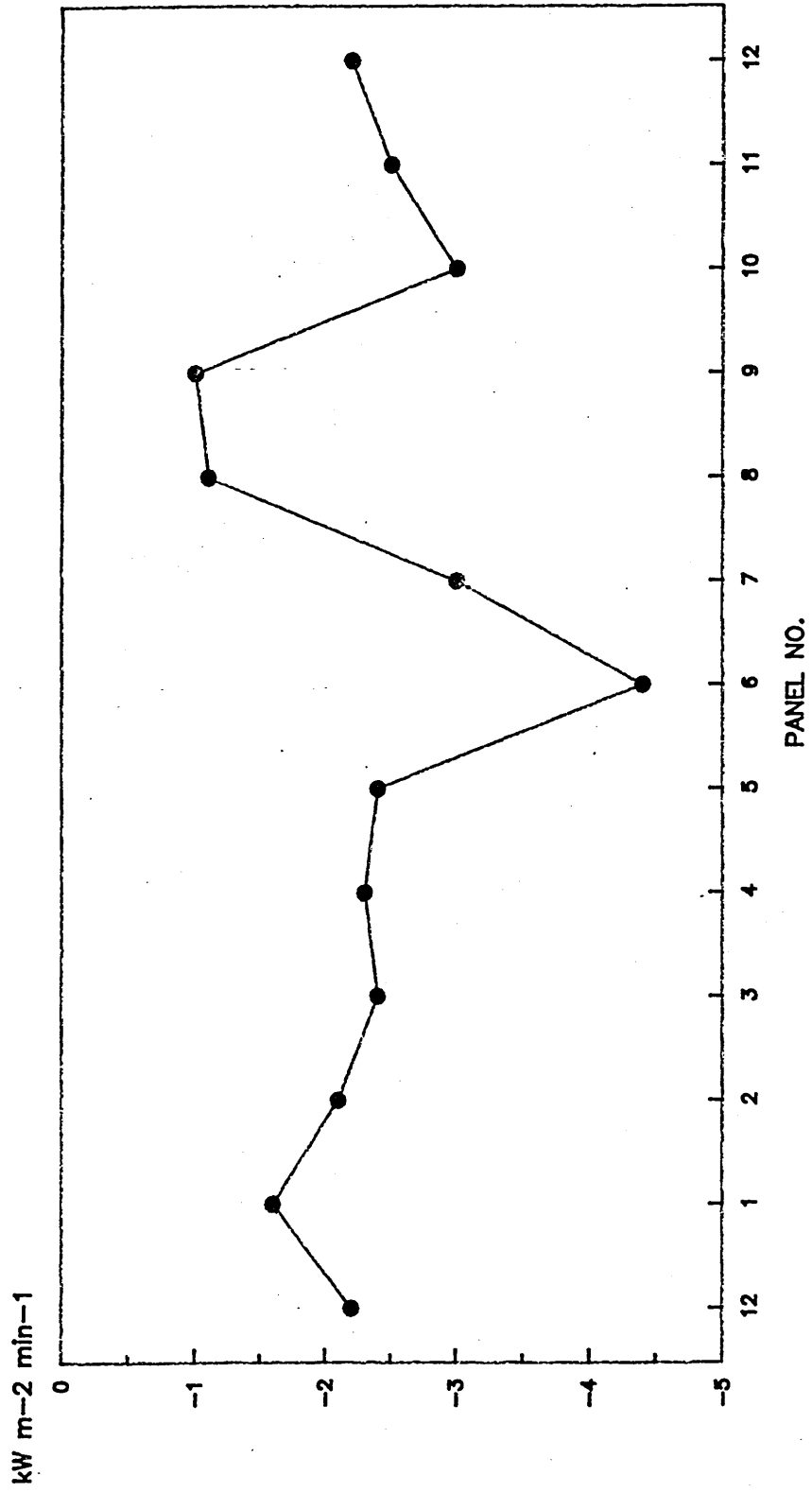


Figure 93. Thermal Conductivity Of Slag/Metal Structure With Continuous Metal

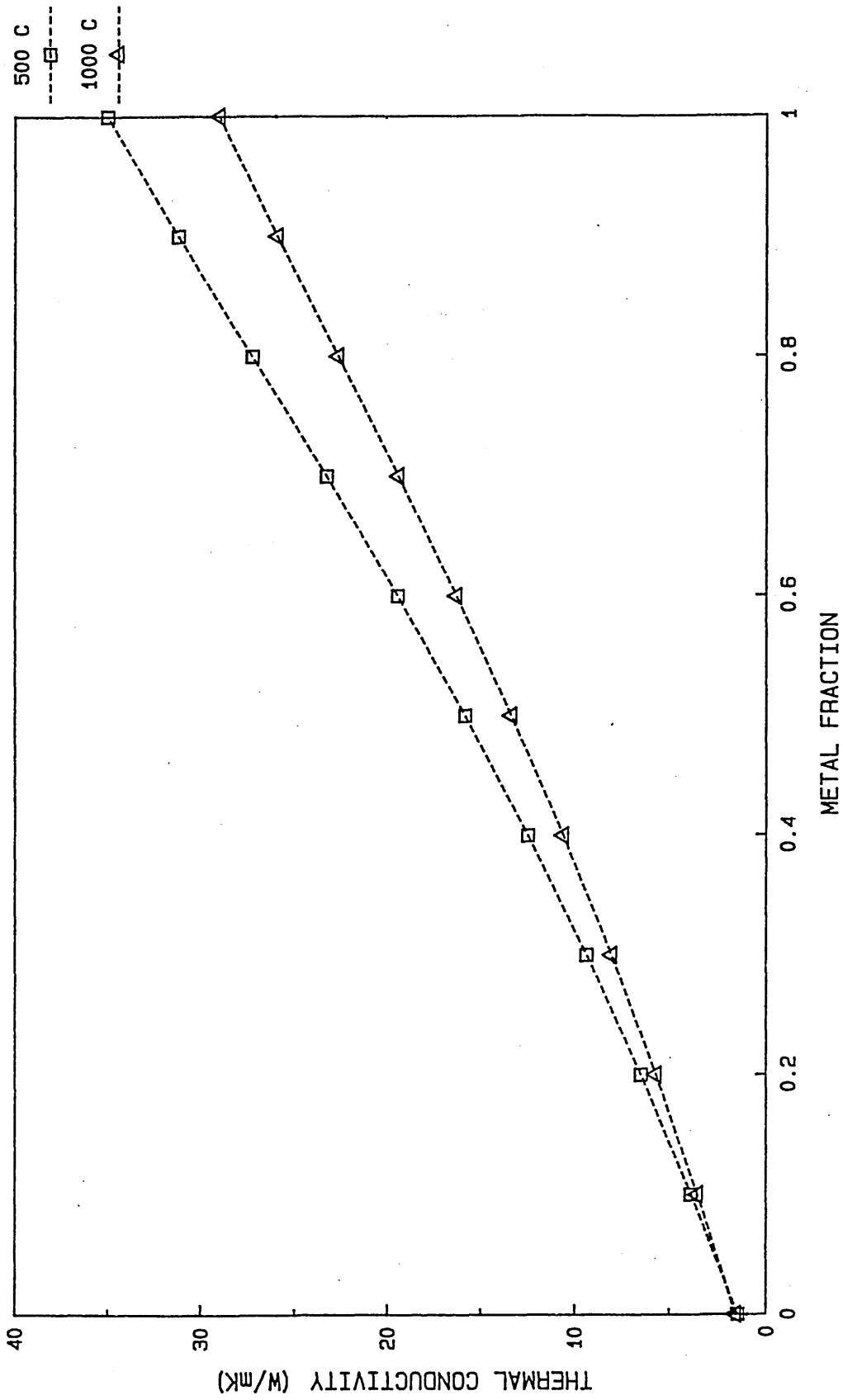


Figure 94. Thermal Conductivity Of Slag/Metal Structure With Continuous Slag

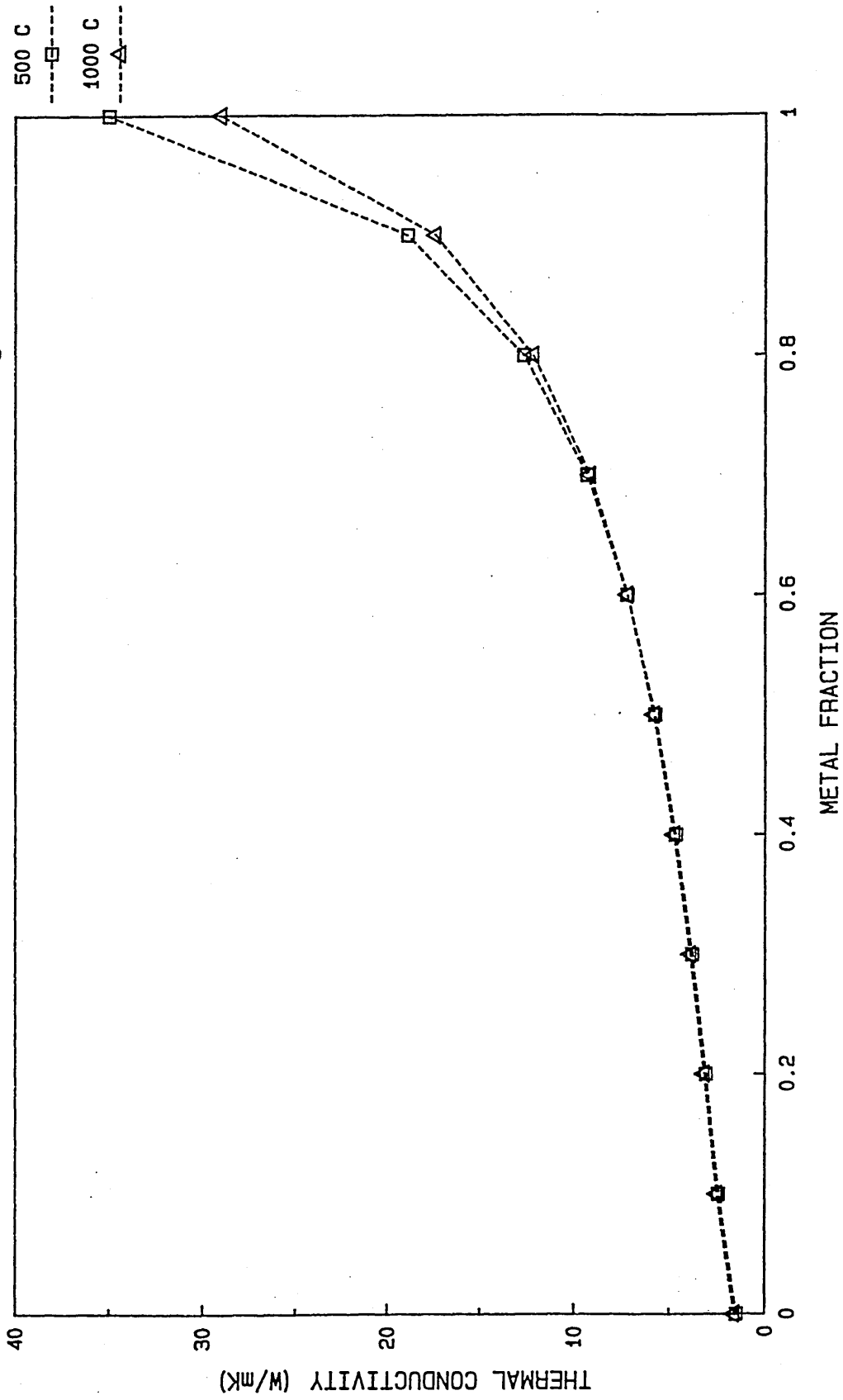


TABLE I. SIDEWALL SLAG COVERAGE

slag cover = $\sum(t \times Ft)$ t=slag thickness (mm)

Ft=fraction of panel covered by slag thickness t

	PANEL NO.1	PANEL NO.2	PANEL NO.3	PANEL NO.4	PANEL NO.5	PANEL NO.6
DATASET 01	26.00	10.00		10.00	32.00	
DATASET 02	22.00	6.00	17.00	6.00	14.00	9.00
DATASET 03	18.00	8.00	20.00	8.00	6.00	2.00
DATASET 04	17.00	20.00	7.00	34.00	9.00	6.00
DATASET 05	18.00	16.00	15.00	19.00	15.00	4.00
DATASET 06	8.00	9.00	16.00	8.00	5.00	6.00
DATASET 07A	16.00	2.00	19.00	5.00	20.00	10.00
DATASET 07B	12.00	2.00	18.00	4.00	18.00	8.00
DATASET 08	25.00	15.00	31.00	9.00	18.00	8.00
MEAN	18.00	9.80	17.90	11.40	15.20	6.60
DATASET 01 LOG	1.41	1.00		1.00	1.51	
DATASET 02 LOG	1.34	0.78	1.23	0.78	1.15	0.95
DATASET 03 LOG	1.26	0.90	1.30	0.90	0.78	0.30
DATASET 04 LOG	1.23	1.30	0.85	1.53	0.95	0.78
DATASET 05 LOG	1.26	1.20	1.18	1.28	1.18	0.60
DATASET 06 LOG	0.90	0.95	1.20	0.90	0.70	0.78
DATASET 07A LOG	1.20	0.30	1.28	0.70	1.30	1.00
DATASET 07B LOG	1.08	0.30	1.26	0.60	1.26	0.90
DATASET 08 LOG	1.40	1.18	1.49	0.95	1.26	0.90
LOG MEAN	1.27	1.03	1.25	1.09	1.17	0.81

Panels 1 to 6

cont..

TABLE I. (CONTINUED)

	PANEL NO.7	PANEL NO.8	PANEL NO.9	PANEL NO.10	PANEL NO.11	PANEL NO.12
DATASET 01	0.10	8.00	5.00	5.00	8.00	5.00
DATASET 02	2.00	0.10	24.00	15.00	5.00	20.00
DATASET 03	0.10	26.00	27.00	26.00	3.00	45.00
DATASET 04	1.00	100.00	16.00	8.00	0.10	3.00
DATASET 05	0.10	20.00	5.00	15.00	7.00	19.00
DATASET 06	1.00	28.00	17.00	7.00	2.00	44.00
DATASET 07A	0.10	570.00	265.00	73.00	253.00	350.00
DATASET 07B	0.10	570.00	265.00	28.00	5.00	30.00
DATASET 08	400.00	1,210.00	232.00	6.00	1.00	30.00
MEAN	44.90	281.30	95.10	20.30	31.60	60.70
DATASET 01 LOG	(1.00)	0.90	0.70	0.70	0.90	0.70
DATASET 02 LOG	0.30	(1.00)	1.38	1.18	0.70	1.30
DATASET 03 LOG	(1.00)	1.41	1.43	1.41	0.48	1.65
DATASET 04 LOG	0.00	2.00	1.20	0.90	(1.00)	0.48
DATASET 05 LOG	(1.00)	1.30	0.70	1.18	0.85	1.28
DATASET 06 LOG	0.00	1.45	1.23	0.85	0.30	1.64
DATASET 07A LOG	(1.00)	2.76	2.42	1.86	2.40	2.54
DATASET 07B LOG	(1.00)	2.76	2.42	1.45	0.70	1.48
DATASET 08 LOG	2.61	3.08	2.37	0.78	0.00	1.48
LOG MEAN	1.70	2.39	1.87	1.29	1.54	1.81

Panels 7 to 12

TABLE II. SLAG ANALYSIS RESULTS.

	Bath Sample 1	Bath Sample 2	Panel Sample 1	Panel Sample 2	Thermal Conductivity Sample
% SI 02	18.00	13.80	15.00	14.90	11.43
% AL2 03	6.62	5.33	5.16	8.10	6.62
% CR2 03	5.91	3.37	1.46	1.50	2.19
% MN 0	7.23	4.64	5.12	7.26	5.94
% FE2 03	19.01	21.44	23.99	25.76	29.73
% MG 0	2.27	3.97	3.34	2.80	4.14
% CA 0	40.70	47.25	45.93	39.68	34.70

TABLE III. SPECIFIC DENSITY RESULTS.

	Powdered Slag (g/ml)	Sintered Slag (g/ml)
Determination 1	2.42	3.88
Determination 2	3.54	3.91
Determination 3	3.82	4.27
Determination 4	2.81	3.72
Determination 5	3.45	3.87
Determination 6	3.35	3.86
Determination 7	2.47	3.83
Determination 8	3.25	3.85
Determination 9	3.35	3.77
Determination 10	3.08	3.88
Mean	3.15	3.88
Standard Deviation	0.46	0.14

TABLE IV. SPECIFIC HEAT CAPACITY RESULTS.

	Cp (J/kg K)
Determination 1	657
Determination 2	656
Determination 3	769
Determination 4	812
Mean	724

TABLE V. POROSITIES OF CONDUCTIVITY SAMPLES.

	Metal %	Porosity %
Sample 1		7.4
Sample 2		10.6
Sample 3		36.0
Sample 4	0.6	35.9
Sample 5		21.4
Sample 6	28.1	27.8
Sample 21		15.2
Sample 22		14.1
Sample 24		13.2
Sample 31		10.0
Sample 32		19.7

TABLE VI.
THERMAL CONDUCTIVITIES OF SLAG LAYER SAMPLES

	B5-06	B10-06	B3-07	B5-07 Sublayer 2	B5-07 Sublayer 4	B5-07 Sublayer 6
PORE DIAMETER (MM)	0.50	0.50	1.50	0.50	0.50	1.00
POROSITY FRACTION	0.25	0.15	0.15	0.15	0.15	0.15
METAL FRACTION	0.00	0.15	0.01	0.01	0.00	0.00
SLAG FRACTION	0.75	0.70	0.84	0.84	0.85	0.85
TEMPERATURE (C)						
0	0.99	2.35	1.17	1.17	1.16	1.16
100	1.01	2.57	1.18	1.18	1.17	1.17
200	1.03	2.40	1.20	1.20	1.19	1.19
300	1.04	2.41	1.23	1.22	1.21	1.22
400	1.06	2.41	1.24	1.23	1.22	1.23
500	1.08	2.43	1.26	1.25	1.24	1.25
600	1.10	2.44	1.29	1.27	1.26	1.28
700	1.12	2.45	1.32	1.29	1.28	1.31
800	1.14	2.47	1.35	1.31	1.30	1.34
900	1.16	2.49	1.38	1.34	1.33	1.37
1000	1.19	2.53	1.41	1.35	1.35	1.40
1100	0.96	2.08	1.17	1.09	1.08	1.15
1200	0.52	1.11	0.64	0.56	0.55	0.62

TABLE VII Calculation Of Heat Fluxes Through Actual Slag Layers.

	SAMPLE IDENTITY				
	B5 06	B10 06	B3 06	B5 07	B5 08
theta 1	1200	1200	1200	1200	1200
theta 2	35	35	35	35	35
convective HTC	1924	1730	1847	1847	1769
t steel	0.025	0.025	0.025	0.025	0.025
k steel	20	20	20	20	20
t air	0	0	0	0	0
k air	0.04	0.04	0.04	0.04	0.04
t slag1	0.006	0.007	0.02	0.001	0.01
k slag1	1.1	2.4	1.3	45	1.55
t slag2	0	0	0	0.006	0.002
k slag2	1	1	1	1.2	16
t slag3	0	0	0	0.003	0.005
k slag3	1	1	1	40	1.6
t slag4	0	0	0	0.003	0.003
k slag4	1	1	1	1.25	20
t slag5	0	0	0	0.001	0
k slag5	1	1	1	30	1
t slag6	0	0	0	0.009	0
k slag6	1	1	1	1.3	1
omega1	0.000519	0.000578	0.000541	0.000541	0.000565
omega2	0.00125	0.00125	0.00125	0.00125	0.00125
omega3	0	0	0	0	0
omega4	0.005454	0.002916	0.015384	0.000022	0.006451
omega5	0	0	0	0.005	0.000125
omega6	0	0	0	0.000075	0.003125
omega7	0	0	0	0.0024	0.00015
omega8	0	0	0	0.000033	0
omega9	0	0	0	0.006923	0
sum omega	0.007224	0.004744	0.017176	0.016245	0.011666
delta theta	1165	1165	1165	1165	1165
heat flux W/m2	161261	245537	67827	71714	99855
kW/m2	161	246	68	72	100
measured value	155-165	125-135	50	60	80-100

REFERENCES.

1. Ligot G.A. & Salomon P.J. - Metal Bulletin Monthly, (143), 7, 9, 12-13.
2. Schwabe W.E. - Electric Furnace Conference, (20), 195-206.
3. Schwabe W.E. - Electric Furnace Conference, (20), 349-357.
4. Schwabe W.E. - Electric Furnace Conference, (32), 48-54.
5. Schwabe W.E. - Iron & Steel Engineer, Sept. 1969, 132-137.
6. Seecs H.A. - Industrial Heating, 50, (9), 39-40.
7. B.S.C. - Steel Research, 1978/79, 5-8.
8. Swinden D.J. - "The Arc Furnace." - Electricity Council.
9. Wasem J.W. - Modern Casting, 73, (2), 16-18.
10. Roberts R.W. & Sochacky M.R. - Electric Furnace Conference, (34), 25-33.
11. Bowman B. - Ironmaking & Steelmaking, 1974, (4), 212-214.
12. Jordan J.R. - Ironmaking & Steelmaking, 1978, (4), 177-183.
13. Bowman B. - Ironmaking & Steelmaking, 1975, (4), 248-252.
14. Howes R.S. - 74th BISRA Steelmaking Conference, 1970, 9-16.
15. Markworth E. - Stahl & Eisen, 100, (10), 532-534.
16. Stenzel O. & Schumann J. - Iron & Steel

- International, 55, (4), 212-216.
17. Freeman E.R. & Medley J.E. - Electric Power Applications, 1, (1), 17-24.
 18. Nikolskii L.E. & Zinurov I.Yu. - Metallurg, 1981, (5), 21-24.
 19. Waldmann T. et al - Electric Furnace Conference, (40), 217- 223.
 20. Dowsing R.J. - Metals & Materials, April 1976, 31-34.
 21. Gill L.L. & Hill D. - Mini Mills (One day discussion), 1978, 3, (9), 38-43.
 22. Gill L.L. - Ironmaking & Steelmaking, 1978, (5), 217-223.
 23. Vaistaro N. & Saarelainen E. - 1st European Electric Steel Congress, Aachen, 1983, B2.
 24. Zollner D.H. et al - Electroheat For Metals Conference, Sept. 1982, 1.3.
 25. Blank J.R. et al - 1st European Electric Steel Congress, Aachen, 1983, G4.
 26. Prenn O. et al - Electric Furnace Conference, (40), 313-318.
 27. Rodal D. - 1st European Electric Steel Congress, Aachen, 1983, C3.
 28. Ebmann H. & Grunberg D. - Steel Times, 1984, (1), 13-17.
 29. Nilsson A. et al - 1st European Electric Steel Congress, Aachen, 1983, K5.

30. I.I.S.I. - "The Electric Arc Furnace." - I.I.S.I.
31. Strohmeier B. - Electric Furnace Conference, (39), 156-167.
32. Daido Steel Co. - 15th Refractory Sub-committee, June 1974, Japan Iron & Steel Institute.
33. Klein K.H. et al - S.E.A.I.S.I. Quarterly, 1979, 8, (2), 27-32.
34. Ameling D. et al - Stahl & Eisen, 1978, (9), 429-433.
35. Parkin B. & Sluiter G.T. - Electric Arc Steelmaking For The Eighties (One day discussion), Dec. 1979, 49-56.
36. Assenmacher R. et al - Metallurgical Plant & Technology, March 1978, 5-20.
37. Noda T. et al - Taikabutsu Overseas, 1, (2), 10-19.
38. Herridges P.R. - Electric Furnace Conference, (38), 307-309.
39. Braverman E.M. et al - Metallurg, 1983, (2), 23-25.
40. Iwanami Y. & Funazaki M. - Productivity And Maintenance Conference Proceedings (SEAISI), March 1981, 471-492.
41. I.R.F.I. - British Steelmaker, 45, (3), 17-18.
42. Druppel J. & Zieshang J. - Steel Times, April 1983, 201-204.
43. Bleimann K.R. & Cartales P. - Electric Furnace Conference, (36), 291-293.
44. Cartersville - 33 Metal Processing, Sept. 1978, 56-57.

45. Elsner E. et al - World Steel And Metalworking Export Manual, 1979, 68-72.
46. Bleimann K.R. et al - Electric Furnace Conference, (35), 100-103.
47. Palmer L.W. - Electric Furnace Conference, (38), 75-81.
48. Zangs L. - Steel Times, Oct. 1978, 912-916.
49. Farkas S. - Iron & Steelmaker, 6, (7), 14-21.
50. Roberts K.S. - Electric Furnace Conference, (36), 198-199.
51. Marlin L.G. - Electric Furnace Conference, (39), 287-289.
52. Sosonkin O.M. & Kudrin V.A. - Stal, 1981, (5), 25-28.
53. Spencer E.B. - Electric Furnace Conference, (38), 303-306.
54. Bleimann K.R. - Electric Furnace Conference, (38), 310-314.
55. B.S.C. - "Water Cooled Panel Safety Procedure." - Internal Document, 1979.
56. Kudrin V.A. & Sosonkin O.M. - Stal, 1983, (10), 39-40
57. Ameling D. et al - Steel & Energy Conference, Brussels, Feb. 1983, 353-374.
58. Bowman B. & Fitzgerald F. - Journal Of The Iron And Steel Institute, March 1973, (211), 178-186.
59. Sapiro V.S. et al - IZU.V.U.Z Cheryana Metall., 1981, (3), 63-66.

60. Montgomery R.W. - Commission Of The European Communities Pamphlet EUR No.5716 Pp 135.
61. Bowman B. - Electrowarme International B, Dec. 1979, 37, (6), 315-319.
62. Nanjo T. et al - Aceria Electrica (I.L.A.F.A.), 1974, J/1-J/22.
63. B.S.C. - " Water Cooled Linings For EAFs. " - Working Party Report, 1978.
64. Simon M.J. - Project Thesis, Sheffield City Polytechnic, 1982.
65. Pirozhnikov V.E. - Stal, March 1967, 222-224.
66. Ramous E. et al - Metallurgical Transactions, 1981, 12B, (2), 403-407.
67. Sasaki M. et al - Nippon Steel Technical Report No. 17, 1981, 1-8.
68. Chavepeyr G. et al - Silicates Industriels, 44, (10), 217-233.
69. Levin E.M. et al - " Phase Diagrams For Ceramists. " - American Ceramic Society, 1964.
70. Allmand T.R. - " Microscopic Identification Of Inclusions In Steel. " - B.I.S.R.A., 1962.
71. Kiessling & Lange - I.S.I. Special Report 90, Publication No. 100.
72. Chesters J.H. - Refractories Production And Properties. " - Iron And Steel Institute, 1973.
73. Taylor R. & Mills K.C. - Arch Eisenhüttenwes, 53, (2), 55-63.

74. Nagata K. et al - Journal Of The Iron And Steel Institute Of Japan, Sept. 1983, 69, (11), 1417-1424.
75. Rosenberg H.M. - " The Solid State. " - Oxford Physics Series No.9, Clarendon Press, 1978.
76. Kingery W.D. - Journal Of The American Ceramic Society, 38, (7), 251-255.
77. Kingery W.D. - Journal Of The American Ceramic Society, 42, (12), 617-627.
78. Eucken A. - Forsch. Gebiete Ingenieurw., B3, Forschungsheft No. 353, pp 16.
79. Russell H.W. - Journal Of The American Ceramic Society, 18, (1), 1-5.
80. Loeb A.L. - Journal Of The American Ceramic Society, 37, (2), 96-99.
81. Francl J. & Kingery W.D. - Journal Of The American Ceramic Society, 37, (2), 99-107.
82. Cooper C.F. - Journal Of The British Ceramic Society, 3, (1), 115-123.
83. Rhee S.K. - Materials Science And Engineering, 1975, 20, 89-93.
84. Aivazov M.I. & Domashnev I.A. - Poroshkovaya Met., 8, pp 51.
85. Jablonski W. - Szklo I Ceramica, 29, (12), 321-322.
86. Willshee J.C. - Proc. British Ceramic Society, 1980, (29), 153-173.
87. B.S. 1902 : Part 1A, 67-78.
88. Clements J.F. & Vyse J. - Trans. Brit. Ceram. Soc., 53, 134-155.

89. Davis W.R. & Downs A. - Trans. Brit. Ceram. Soc., 79, (2), 44-52.
90. Buzbee B.L. & Dorr F.W. - Instruments And Control Systems, Sept. 1971, 117-119.
91. Chiu J. & Fair P.G. - Thermochima Acta, 34, 267-273.
92. Morrow G.D. - Bull. Amer. Ceram. Soc., 58, (7), 687-690.
93. Sutton W.H. - J. Amer. Ceram. Soc., 43, (2), 81-86.
94. Bucknam M.A. et al - Trans. Brit. Ceram. Soc., 82, (1), 18-23.
95. Wright F. - Business Extra, Sheffield Morning Telegraph, 25th May, 1983.
96. Gray W.A. & Muller R. - " Engineering Calculations In Radiative Heat Transfer. " - Oxford Pergammon Press, 1974.
97. Krieth F. - " Principles Of Heat Transfer. " - International Textbook Company, 1969.
98. Holman J.P. - " Heat Transfer. " - McGraw Hill Inc., 1963.
99. Gebhart B. - " Heat Transfer. " - McGraw Hill Inc., 1971.
100. Ede A.J. - " An Introduction To Heat Transfer Principles And Calculations. " - Pergammon Press Ltd., 1967.
101. Wong H.Y. - " Handbook Of Essential Formulae And Data On Heat Transfer For Engineers. " - Longman, 1977.
102. Welty J.R. - " Engineering Heat Transfer. " - Wiley & Sons Inc., 1974.

103. Keene B.J. & Mills K.C. - Arch. Eisenhuttenwes,
1981, 52, 311-316.

104. Firth D. - Project Thesis, Sheffield City
Polytechnic, 1984.

APPENDIX I.

Data And Sample Collection Procedure.

Initially two preliminary samples were collected and observations recorded using a notebook, and the problems encountered with respect to the working environment and time restrictions were overcome in subsequent visits, culminating in the procedure outlined below.

1) General observations of slag splashing were made through the slag door and the variation of panel cover was monitored from a vantage point above the furnace each time the roof was removed to facilitate charging, usually over a span of several casts. All observations were recorded verbally using a small tape recorder and subsequently transferred to a written report.

2) During the final cast of a week's campaign the following were recorded from the furnace's installed panel water monitoring system every five minutes throughout the cast -

i) total manifold water flow rate, taken from a chart recorder.

ii) manifold water inlet temperature from the same chart recorder.

iii) each panel outlet temperature from individual LED displays.

The stages of melting were also recorded based on observation, noting the voltage tap settings and any stoppages due to electrode breakages, furnace power tripping etc. All records were made verbally using the

tape recorder, and subsequently entered into tables.

3) When the furnace had cooled sufficiently, representative samples of slag were removed from the sidewall panel faces, identified and marked at the top hot face position, and placed in bags. The individual panel water outlet temperatures were compared with the manifold outlet temperature to give calibration constants. The slag cover of the sidewall was then assessed in detail as to the percentage of cover and the thickness of the layers, and recorded as above.

4) During the first cast of the subsequent week's campaign, the same information as in 2) was recorded throughout the cast.

APPENDIX II.

Calculation Of Specific Heat Flux To Each Panel.

The FORTRAN program was not retained due to the need for disc storage space, but it performed the following calculation for all the temperature difference values in the time/temperature datafiles and set up new datafiles containing the heat flux values.

The equation used was that for the heat flow rate to a channel -

$$\begin{aligned} \dot{q} &= \dot{m} C_P \Delta\theta \\ &= \dot{V} \rho C_P \Delta\theta \end{aligned} \quad (8)$$

where

\dot{V} = volume flow rate of water

ρ = density of water

C_P = specific heat capacity of water

$\Delta\theta$ = water temperature difference

$$q'' = \dot{q} / A \quad (9)$$

where A is the area of the panel

\dot{V} for each panel was calculated from the \dot{V}_{tot} for the furnace and the flow resistance factor for the panel (see Appendix III).

ρ and C_P are known for the mean water temperature.

$\Delta\theta$ was derived from the time temperature datafile adding the calibration factor.

APPENDIX III.

Determination Of Flow Resistance Factors.

The general flow equation for a channel is used -

$$\dot{V} = \frac{\Delta P}{R_T} \quad (10)$$

where \dot{V} = volume flow rate

ΔP = pressure drop

R_T = total resistance to flow

The panels are connected in parallel between the inlet bezel ring and outlet bezel ring, with the inlet flow (which is known) being divided into twelve components. As pressure losses in the bezels are very small compared to those in the panels, the pressure drop across each panel can be considered equal and hence the flowrate in each panel depends upon it's resistance to flow. This resistance may vary with flowrate, but the relative resistances of the twelve panels will be constant and therefore the proportion of the total inlet flow in each panel will not vary. To calculate these factors, steady state values of the total flowrate and pressure drop are used -

$$\begin{aligned} \Delta P &= 120 \text{ kPa} \\ \dot{V} &= 0.05 \text{ m}^3 \text{ s}^{-1} \\ \text{i.e. } R_T &= 2.4 \times 10^6 \text{ kg m}^{-4} \text{ s}^{-1} \end{aligned}$$

The flow resistance of a channel is due to frictional or momentum losses which vary according to the flow regime. Assuming surface friction to be minimal, the major resistance component is that due to changes of flow direction, such as the 90 degree and 180 degree bends in the panel's internal baffle system (see figure 3). These can be quantified relative to each other by using S factors, the sum of which are directly related to the flow resistance.

$$R = K \sum S \quad (11)$$

The mean S factors for 90 and 180 degree bends are 1.0 and 2.0 respectively, and the totals for each panel type including inlet and outlet fittings are given below -

Type O = 43

Type P = 41

Type R = 40

Type S = 35

Type T = 28

Sustituting these values into the equation for resistances in parallel gives -

$$\frac{1}{2.4 \times 10^6} = \frac{1}{41K} + \frac{1}{40K} + \frac{1}{35K} + \frac{1}{40K} + \frac{1}{35K} + \frac{1}{28K} \dots \text{etc.}$$

which becomes -

$$\frac{K}{2.4 \times 10^6} = \frac{1}{41} + \frac{5}{40} + \frac{3}{35} + \frac{2}{28} + \frac{1}{43}$$

$$K = 791493$$

The resistance of each panel can now be calculated using equation (11) and the volume flowrates using equation (10). The individual flowrates for all the panels in the furnace add up to the bezel inlet water flowrate of 0.05 m s^{-3} , and hence the fraction of the total can be determined for each panel. These values are used as factors in calculating the actual flowrates in the panels, based on the measured water feed flowrates.

0.	5.	10.	15.	20.	25.	30.	35.	40.	45.	50.	55.	60.
80.	90.	95.	100.	105.	110.	115.	120.	125.	130.	140.	145.	150.
160.	175.	185.	190.	195.	200.	205.	210.	215.	220.	230.	235.	240.
4.0	10.3	4.0	0.0	9.5	7.3	4.1	0.0	10.7	9.8	5.0	4.3	4.8
3.8	9.1	4.0	0.0	8.2	3.7	1.8	0.0	4.5	13.8	4.8	4.5	6.3
13.8	21.9	5.0	0.0	12.5	12.8	8.6	0.0	14.8	30.2	9.9	6.3	6.2
12.8	12.8	13.1	0.0	11.9	12.9	12.8	0.0	11.2	12.0	6.7	6.2	6.2
4.9	9.4	4.1	0.0	8.8	6.3	2.9	0.0	8.7	10.5	4.9	5.9	7.0
7.0	12.8	5.3	0.0	10.3	7.6	4.0	0.0	8.7	10.5	6.9	7.0	7.0
7.3	13.0	5.5	0.0	10.7	7.7	3.9	0.0	8.2	11.3	8.2	6.9	7.1
8.7	13.3	5.9	0.0	10.6	7.7	4.4	0.0	8.2	11.1	8.2	7.1	7.1
10.0	13.9	6.7	0.0	10.8	8.1	5.0	0.0	8.2	11.0	8.0	8.0	8.0
9.5	12.3	5.5	0.0	10.4	7.8	4.0	0.0	8.5	13.4	7.7	7.9	7.9
10.2	19.1	7.6	0.0	11.2	8.0	4.5	0.0	9.3	16.4	9.7	7.4	7.4
8.2	14.6	7.0	0.0	10.5	7.4	4.1	0.0	8.5	12.5	13.7	8.4	8.4
6.5	10.5	5.6	0.0	8.9	5.4	2.8	0.0	6.2	8.7	8.1	7.1	7.1
5.0	9.0	4.7	0.0	8.1	4.5	2.2	0.0	5.2	7.3	5.9	6.1	6.1
5.7	7.2	4.3	0.0	7.7	3.6	2.0	0.0	5.0	5.5	3.2	5.4	5.4
1.4	4.4	3.4	0.0	6.7	2.2	1.2	0.0	3.2	3.3	0.0	4.3	4.3
5.8	6.1	3.5	0.0	8.3	4.3	2.6	0.0	2.3	4.4	3.5	5.5	5.5
3.6	5.7	3.7	0.0	7.8	3.5	1.9	0.0	2.2	3.7	1.4	5.1	5.1
2.5	4.6	3.0	0.0	6.6	2.0	1.1	0.0	1.3	4.1	0.9	4.5	4.5
3.1	5.3	3.7	0.0	7.0	2.6	1.9	0.0	1.6	3.7	2.3	5.1	5.1
3.0	5.0	3.3	0.0	6.2	2.0	1.4	0.0	1.5	3.5	1.7	4.8	4.8
9.5	10.2	4.1	0.0	8.5	5.0	2.5	0.0	3.9	10.0	12.2	6.7	6.7
13.5	18.2	5.0	0.0	9.0	4.7	2.7	0.0	6.8	12.0	7.7	7.7	7.7
12.6	16.7	6.0	0.0	11.8	6.2	4.4	0.0	11.4	22.1	7.1	8.8	8.8
8.4	12.2	6.6	0.0	13.6	8.7	3.8	0.0	15.0	20.6	6.7	7.9	7.9
9.2	12.2	6.9	0.0	11.7	6.9	3.5	0.0	9.7	13.5	5.6	10.6	10.6
8.8	11.7	6.4	0.0	11.6	6.0	3.7	0.0	8.8	12.4	5.4	10.5	10.5
10.2	11.4	6.6	0.0	11.6	6.3	3.9	0.0	9.2	13.9	5.9	11.5	11.5
9.9	12.5	7.0	0.0	13.7	6.6	3.7	0.0	9.7	13.5	5.9	10.7	10.7
10.0	13.8	8.0	0.0	12.4	7.2	3.4	0.0	9.4	13.4	6.0	10.1	10.1
10.9	14.1	8.8	0.0	12.6	7.7	4.5	0.0	10.0	12.4	6.3	10.3	10.3
9.7	12.8	8.1	0.0	11.6	6.8	3.3	0.0	8.2	11.4	5.2	9.2	9.2
7.9	11.7	7.3	0.0	11.3	6.5	3.2	0.0	7.7	10.2	4.7	8.4	8.4
6.7	9.3	6.0	0.0	9.6	5.0	2.4	0.0	6.6	7.6	3.2	7.2	7.2
3.3	4.6	3.6	0.0	6.8	2.0	1.2	0.0	3.7	3.1	0.2	4.8	4.8
0.0	0.0	0.0	0.0	0.0	0.0	0.0	0.0	0.0	0.0	0.0	0.0	0.0
1.0	1.0	1.0	1.0	1.0	1.0	1.0	1.0	1.0	1.0	1.0	1.0	1.0

APPENDIX IV (part 1) Example Of Time/Temperature Data

0.	5.	10.	15.	25.	30.	35.	40.	45.	50.	55.	70.
80.	90.	95.	100.	105.	110.	115.	120.	125.	130.	140.	145.
150.	160.	175.	185.	190.	195.	200.	205.	210.	215.	220.	230.
89.	109.	53.	0.	147.	249.	163.	0.	105.	109.	96.	41.
62.	87.	49.	0.	123.	192.	108.	0.	109.	102.	77.	36.
59.	75.	49.	0.	104.	115.	60.	0.	51.	137.	74.	37.
160.	192.	62.	0.	160.	302.	199.	0.	145.	288.	121.	55.
150.	109.	169.	0.	172.	304.	285.	0.	112.	121.	91.	54.
71.	77.	50.	0.	112.	168.	82.	0.	89.	107.	75.	51.
92.	109.	64.	0.	171.	195.	105.	0.	89.	107.	93.	61.
95.	110.	60.	0.	137.	197.	103.	0.	85.	114.	105.	60.
109.	113.	74.	0.	135.	197.	113.	0.	85.	112.	105.	62.
122.	119.	84.	0.	138.	205.	125.	0.	85.	111.	103.	71.
117.	104.	63.	0.	133.	199.	105.	0.	87.	133.	100.	70.
128.	172.	89.	0.	148.	210.	119.	0.	98.	166.	122.	67.
107.	129.	91.	0.	138.	197.	110.	0.	90.	129.	160.	77.
89.	99.	79.	0.	116.	155.	83.	0.	68.	92.	107.	64.
71.	76.	59.	0.	193.	136.	70.	0.	59.	80.	86.	54.
60.	60.	84.	0.	100.	116.	66.	0.	57.	63.	61.	48.
34.	32.	42.	0.	87.	87.	49.	0.	40.	42.	30.	37.
76.	48.	43.	0.	108.	131.	78.	0.	71.	52.	64.	48.
59.	49.	44.	0.	102.	114.	64.	0.	30.	46.	44.	45.
46.	34.	37.	0.	85.	83.	47.	0.	22.	49.	39.	29.
54.	41.	46.	0.	91.	95.	64.	0.	25.	46.	52.	45.
57.	37.	30.	0.	79.	81.	52.	0.	23.	43.	46.	41.
139.	94.	82.	0.	111.	144.	75.	0.	46.	104.	144.	59.
152.	161.	63.	0.	116.	138.	79.	0.	73.	122.	102.	68.
150.	137.	74.	0.	153.	169.	115.	0.	116.	217.	96.	80.
107.	108.	94.	0.	177.	221.	102.	0.	145.	203.	92.	71.
116.	105.	88.	0.	152.	183.	96.	0.	100.	136.	82.	97.
111.	109.	61.	0.	151.	165.	100.	0.	91.	126.	80.	96.
136.	94.	81.	0.	151.	171.	104.	0.	95.	140.	85.	106.
127.	101.	89.	0.	152.	177.	100.	0.	100.	136.	85.	98.
134.	119.	101.	0.	151.	190.	94.	0.	97.	135.	86.	93.
122.	108.	101.	0.	154.	200.	117.	0.	103.	126.	88.	94.
117.	119.	104.	0.	151.	191.	92.	0.	86.	117.	78.	84.
102.	100.	93.	0.	127.	175.	90.	0.	81.	105.	74.	76.
90.	77.	75.	0.	121.	144.	73.	0.	71.	81.	60.	64.
45.	74.	43.	0.	137.	83.	48.	0.	44.	39.	32.	41.
0.0	0.0	0.0	0.0	0.0	0.0	0.0	0.0	0.0	0.0	0.0	0.0
20.	30.	40.	20.	20.	20.	20.	20.	20.	20.	20.	20.

APPENDIX IV (part 2) Data Converted To Heat Fluxes

```

DIMENSION YA(39), YB(39), YC(39), YD(39), YE(39), YF(39)
DIMENSION YG(39), YH(39), YI(39), YJ(39), YK(39), YL(39)
READ(2,10) (XA(I), I=1,12)
READ(2,10) (XB(I), I=1,12)
READ(2,10) (XC(I), I=1,12)
READ(2,10) (XD(I), I=1,12)
10 FORMAT (12F5.0)
XA(37)=0.0
XA(38)=5.0
XA(39)=5.0
DO 25 I=1,39
  READ(2,20) YA(I), YB(I), YC(I), YD(I), YE(I), YF(I), YG(I),
  1 YH(I), YI(I), YJ(I), YK(I), YL(I)
20 FORMAT (12F5.0)
25 CONTINUE
CALL PLOTS(0.0,1)
CALL PLOT(0.0,2.0,-3)
CALL AXIS(0.0,0.0,0.0, TIME (MINS), -11,46.0,0.0,0.0,5.0)
CALL AXIS(0.0,0.0,0.0, HEAT FLUX (W/M2), 16,30.0,0.0,20.0)
WRITE(6,30)
30 FORMAT (//, INPUT 12 VALUES CORRESPONDING TO PANELS 1 TO 12, *
  1 READ(5,* ) 11,12,13,14,15,16,17,18,19,110,111,112
  IF (11.EQ.0) GO TO 40
  CALL LINE(XA,YA,36,1,1)
  40 IF (12.EQ.0) GO TO 50
  CALL LINE(XA,YB,36,1,2)
  50 IF (13.EQ.0) GO TO 60
  CALL LINE(XA,YC,36,1,3)
  60 IF (14.EQ.0) GO TO 70
  CALL LINE(XA,YD,36,1,4)
  70 IF (15.EQ.0) GO TO 80
  CALL LINE(XA,YE,36,1,5)
  80 IF (16.EQ.0) GO TO 90
  CALL LINE(XA,YF,36,1,6)
  90 IF (17.EQ.0) GO TO 100
  CALL LINE(XA,YG,36,1,7)
  100 IF (18.EQ.0) GO TO 110
  CALL LINE(XA,YH,36,1,8)
  110 IF (19.EQ.0) GO TO 120
  CALL LINE(XA,YI,36,1,9)
  120 IF (110.EQ.0) GO TO 130
  CALL LINE(XA,YJ,36,1,10)
  130 IF (111.EQ.0) GO TO 140
  CALL LINE(XA,YK,36,1,11)
  140 IF (112.EQ.0) GO TO 150
  CALL LINE(XA,YL,36,1,12)
  150 CALL PLOT(10.0,0.0,999)
  CALL EXIT
  END

```

FILE: GPLOT4 FILEDEF 4 *** VM/SP AT SHEFFIELD CITY POLYTECHNIC (CMS GEN 02SLP87) ***

FILEDEF 1 DISK GPLOT4 PLOT A (REC'D F LRECL 133 BLOCK 133)
FILEDEF 2 DISK GPLOT4 DATA

APPENDIX IV (part 4) File Definition

APPENDIX V.

The Calculation Of View Factors For An Electric Arc Furnace.

By approximating the geometry of an arc furnace to cylinders and a truncated cone (see figure 5.) all of the view factors can be calculated using just three equations. Two of these are the basic rules for view factors in an enclosure and the third is the equation for the view factor from one disc to another parallel disc.

$$\sum_{n=1}^{n=x} F_{1-n} = 1 \quad (15)$$

where F_{1-n} = view factor from surface 1 to surface n

x = number of surfaces in enclosure

$$F_{1-2} A_1 = F_{2-1} A_2 \quad (16)$$

where F_{1-2} = view factor from surface 1 to surface 2

A_1 = area of surface 1

F_{2-1} = view factor from surface 2 to surface 1

A_2 = area of surface 2

$$F_{1-2} = \frac{1}{2} \left(\frac{B^2}{a^2} \right) \left[X - \sqrt{X^2 - 4 \frac{B^2}{a^2} C^2} \right] \quad (17)$$

where F_{1-2} = view factor from disc 1 to disc 2

$$B = b/a$$

$$C = c/a$$

$$X = \left(1 + \frac{B^2}{a^2} + \frac{C^2}{a^2} \right)$$

a = distance between the two discs

b = radius of disc 1

c = radius of disc 2

To demonstrate the calculation, actual dimensions taken from Stocksbridge's "B" furnace are used -

- i) furnace inside diameter = 5.6 m
- ii) hearth floor diameter = 3.6 m
- iii) height of water cooled sidewall = 1.25 m
- iv) height of lower sidewall = 0.5 m
- v) depth of hearth (B to F) = 1.0 m

The calculation consists of a series of steps -

1) Firstly consider the volume bounded by R,P and A:

- a) $F_{R-A} = 0.642$ (from equation 17)
- b) $F_{R-R} = 0$ (a planar surface cannot view itself)
- c) $F_{R-P} = 0.358$ (from equation 15)
- d) $F_{P-R} = 0.401$ (from equation 16)
- e) $F_{P-A} = F_{P-R}$ (by symmetry)
- f) $F_{P-P} = 0.198$ (from equation 15)

2) Next consider the volume bounded by A,W and B:

- a) $F_{B-A} = 0.837$ (from equation 17)
- b) $F_{B-B} = 0$ (planar surface)

- c) $F_{B-W} = 0.163$ (from equation 15)
- d) $F_{W-B} = 0.456$ (from equation 16)
- e) $F_{W-A} = F_{W-B}$ (by symmetry)
- f) $F_{W-W} = 0.088$ (from equation 15)

3) Now consider the volume bounded by R,P,W and B:

- a) $F_{R-B} = 0.541$ (from equation 17)
- b) $F_{R-W} = 0.101$ (from equation 15)
- c) $F_{B-R} = 0.541$ (from equation 16 or 17)
- d) $F_{B-P} = 0.296$ (from equation 15)
- e) $F_{W-R} = 0.283$ (from equation 16)
- f) $F_{P-B} = 0.332$ (from equation 16)
- g) $F_{W-P} = 0.173$ (from equation 15)
- h) $F_{P-W} = 0.069$ (from equation 15)

4) To determine the additional factors for an empty furnace, firstly the volume bounded by B,H and F must be considered:

- a) $F_{F-B} = 0.837$ (from equation 17)
- b) $F_{F-F} = 0$ (planar surface)
- c) $F_{F-H} = 0.163$ (from equation 15)
- d) $F_{B-F} = 0.346$ (from equation 16)
- e) $F_{H-F} = 0.081$ (from equation 16)
- f) $F_{B-H} = 0.654$ (from equation 15)
- g) $F_{H-B} = 0.788$ (from equation 16)
- h) $F_{H-H} = 0.131$ (from equation 15)

5) Then consider the volume bounded by A,W,H and F:

- a) $F_{F-A} = 0.711$ (from equation 17)
- b) $F_{F-W} = 0.126$ (from equation 15)
- c) $F_{W-F} = 0.146$ (from equation 16)

d) $F_{A-F} = 0.294$ (from equation 16)

e) $F_{A-H} = 0.543$ (from equation 15)

f) $F_{H-A} = 0.654$ (from equation 16)

g) $F_{H-W} = 0.134$ (from equation 15)

h) $F_{W-H} = 0.311$ (from equation 16)

6) Finally consider the empty furnace volume bounded by R,P,W,H and F:

a) $F_{R-F} = 0.189$ (from equation 17)

b) $F_{F-R} = 0.457$ (from equation 16)

c) $F_{R-H} = 0.352$ (from equation 15)

d) $F_{H-R} = 0.424$ (from equation 16)

e) $F_{H-P} = 0.230$ (from equation 15)

f) $F_{F-P} = 0.254$ (from equation 15)

g) $F_{P-H} = 0.214$ (from equation 16)

h) $F_{P-F} = 0.118$ (from equation 16 or 15)

The results are summarised in Tables A5.1 and A5.2.

TABLE A5.1

View Factors Between Surfaces In An EAF With A Molten Bath.

(F₁₋₂ where surfaces are as defined in Figure 5.)

SURFACE 1	SURFACE 2			
	R	P	W	B
R	0.000	0.358	0.101	0.541
P	0.401	0.198	0.069	0.332
W	0.283	0.173	0.088	0.456
B	0.541	0.296	0.163	0.000

TABLE A5.2

View Factors Between Surfaces In An Empty EAF.

(F₁₋₂ where surfaces are as defined in Figure 5.)

	S U R F A C E 2				
	R	P	W	H	F
SURFACE 1					
R	0.000	0.358	0.101	0.352	0.189
P	0.401	0.198	0.069	0.214	0.118
W	0.283	0.173	0.088	0.311	0.146
H	0.424	0.230	0.134	0.131	0.081
F	0.457	0.254	0.126	0.163	0.000

```

DIMENSION CSAB(19),CMET(19),CGAS(19),E(19),TM(19)
READ(7,200) CSAB,CMET,CGAS,E,TM
LP=0
200 FORMAT (10F5.2/19F4.0/10F5.3/7F5.3/19F3.1/10F6.0/9F6.0)
5 LP=LP+1
WRITE(6,10)
10 FORMAT(' IS THE LAYER TWO PHASE (1) OR THREE PHASE (2)?')
READ(5,*) IN1
IF (IN1.EQ.1) CALL TUPH(P,CSLAG,CMET,CGAS,E,TM)
IF (IN1.EQ.2) CALL TREPH(P,CSLAG,CMET,CGAS,E,TM)
WRITE(6,20)
20 FORMAT(' DO YOU WISH TO CALCULATE THE CONDUCTIVITY OF?
1 * ANOTHER LAYER? (YES=1,NO=2)')
READ(5,*) IN2
IF (IN2.EQ.1) GO TO 5
STOP
END

SUBROUTINE TUPH(LP,CSLAG,CMET,CGAS,E,TM)
DIMENSION CSAB(19),CMET(19),CGAS(19),PSIMP(19),CEUCC(19)
DIMENSION CRUSS(19),CRUSSR(19),CLODEB(19),E(19),TM(19)
4 WRITE(6,5)
5 FORMAT(' WHICH PHASES ARE PRESENT? (ENTER CONTINUOUS PHASE,
1 * FIRST)?? METAL=1,SLAG=2,GAS=3.')
READ(5,*) I1,I2
WRITE(6,10)
10 FORMAT(' DO YOU REQUIRE TABULAR OUTPUT? (YES=1,NO=0)')
READ(5,*) I3
WRITE(6,20)
20 FORMAT(' DO YOU REQUIRE GRAPHICAL OUTPUT? (YES=1,NO=0)')
READ(5,*) I4
IF (I4.EQ.1) CALL PLOTA(SF,L,LP,I5,I6,I7,I8,I9,I10,I13,I14,I15)
60 WRITE(6,70)
70 FORMAT(' ANY ONE OF THE FOLLOWING VARIATIONS MAY BE INTRODUCED-')
1 * CROSS-SECTIONAL VOLUME FRACTION OF DISPERSER FROM 0 TO 0.9 (1)
2 * PORE DIAMETER (WHERE APPLICABLE) FROM 0.5 TO 5 MM (2)
3 * NON-SPHERICAL PORES (3)
4 * CHANGE OF CONTINUOUS PHASE (4)
5 * NONE (5)
READ(5,*) I11
IF (I11.GT.2) GO TO 110
PSF=1.0
A=0.9
IF (I11.EQ.2) GO TO 90
WRITE(6,80)
80 FORMAT(' ENTER PORE DIAMETER IN METRES (0.0 IF NOT APPLICABLE).')
READ(5,*) D
DO GO J=1,10
PC=(J-1)*0.1
PL=PC
IF (I11.EQ.1) CALL PLOTB(SF,L,I10)
CALL CALC (I1,I2,CSLAG,CMET,CGAS,PC,PL,A,D,E,PSF,TM,
CFUSS,CRUSS,CSIMP,CRUSSR,CLODEB)
1 IF (I3.EQ.1) CALL TABLE (CEUCC,CRUSS,CSIMP,CRUSSR,CLODEB,TM,CSLAG,

```

**APPENDIX VI Thermal Conductivity Calculation
FORTRAN Program (page 1)**

```

1 CMET,CGAS,I1,I2,PSF,A,D,PC,PL)
IF (CA,ER.1) CALL PLOT (CEUCC,CRUSS,CSIMP,CRUSS,CLOEB,I5,TH,
1 I6,I7,I8,I9,SE,I13,I14,I15,CGAS,CMET,CSLAG)
85 CONTINUE
GO TO 910
90 WRITE(6,100)
100 FORMAT(' ENTER VALUE FOR CROSS-SECTIONAL POROSITY.')
PL=PC
DO 105 K=1,10
D=K*.0005
IF (I4,ER.1) CALL PLOT (SF,L,I10)
CALL CALC (I1,I2,CSLAG,CMET,CGAS,PC,PL,A,D,E,PSF,TH,
1 CEUCC,CRUSS,CSIMP,CRUSS,CLOEB)
IF (I3,ER.1) CALL TABLE (CEUCC,CRUSS,CSIMP,CRUSS,CLOEB,TH)CSLAG,
1 CMET,CGAS,I1,I2,PSF,A,D,PC,PL)
IF (I4,ER.1) CALL PLOT (CEUCC,CRUSS,CSIMP,CRUSS,CLOEB,I5,TH,
1 I6,I7,I8,I9,SE,I13,I14,I15,CGAS,CMET,CSLAG)
105 CONTINUE
GO TO 910
110 IF (I2,NE.3) GO TO 141
WRITE(6,120)
120 FORMAT(' YOU WILL BE REQUESTED VALUES FOR LOEB PORE SHAPE FACTOR',
1 ' RUSSELL COMBINED PORE FACTOR, LONGITUDINAL PORE SIZE, AND',
3 ' TO TERMINATE, ENTER ALL 3.0.')
130 IF (I2,NE.3) GO TO 141
WRITE(6,140)
140 FORMAT(' ENTER PSF,CFE,V,PC AND PL.')
READ(5,*) PSF,A,D,PC,TH
IF (PC,ER.2.) GO TO 910
GO TO 150
141 WRITE(6,142)
142 FORMAT (' ENTER VOLUME FRACTION OF DISPERSE. (2.0 TO TERMINATE)')
READ(5,*) PC
IF (PC,ED.2.) GO TO 910
IF (I1,PS.4) GO TO 150
WRITE(6,145)
145 FORMAT(' DO YOU WISH TO REVERSE CONTINUITY OF THE METAL/SLAP ?')
1 * (YES=1,NO=0)
READ(5,*) I12
IF (I12,ER.1) CALL SUBP (I1,I2)
150 CONTINUE
IF (I4,ER.1) CALL PLOT (SF,L,I10)
CALL CALC (I1,I2,CSLAG,CMET,CGAS,PC,PL,A,D,E,PSF,TH,
1 CEUCC,CRUSS,CSIMP,CRUSS,CLOEB)
IF (I3,ER.1) CALL TABLE (CEUCC,CRUSS,CSIMP,CRUSS,CLOEB,TH)CSLAG,
1 CMET,CGAS,I1,I2,PSF,A,D,PC,PL)
IF (I4,ER.1) CALL PLOT (CEUCC,CRUSS,CSIMP,CRUSS,CLOEB,I5,TH,
1 I6,I7,I8,I9,SE,I13,I14,I15,CGAS,CMET,CSLAG)
100 IF (I1,GT.2) GO TO 130
910 IF (I4,EQ.0) GO TO 990
CALL SUBP(0,0,0,0,0,0,0)
990 RETURN
END

```

**APPENDIX VI Thermal Conductivity Calculation
FORTRAN Program (page 2)**

```

SUBROUTINE COMP (C1,C2,PC,PCUCC,CRUSS)
DIMENSION CRUCC(19),CRUSS(19),C1(19),C2(19)
DO 10 I=1,17
RAT=C1(I)/C2(I)
R=(1-RAT)/(2*RAT+1)
CRUCC(I)=C1(I)*(1+2*PC*Q)/(1-PC*Q)
PCE=PC**0.66667
CRUSS(I)=C1(I)*(PCE+(RAT*(1-PCE)))/(PCE-PC+(RAT*(1-PCE+PC)))
10 CONTINUE
RETURN
END

SUBROUTINE FORD (C1,C2,PC,PL,A,D,E,PSF,CRUSR,CLOER,TH,CSIMP)
DIMENSION CRUSR(19),CLOER(19),C1(19),C2(19),E(19),TH(19),CSIMP(19)
SRC=5.6697E-8
DO 10 I=1,17
CSIMP(I)=C1(I)*(1-PC)
CR=4*SRC*A*(TH(I)+273.15)**3*D
C2R=C2(I)+CR
RAT=C1(I)/C2R
PE=PC**0.66667
CRUSR(I)=C1(I)*(PE+RAT*(1-PE))/(PE-PC+RAT*(1-PE+PC))
B=PL*C1(I)/(4*SRC*E(I)*PSF*D*(TH(I)+273.15)**3)
CLOER(I)=C1(I)*((1-PC)+PC/(B+(1-PL)))
10 CONTINUE
RETURN
END

SUBROUTINE SROP (J1,J2)
J3=J1
J1=J2
J2=J3
RETURN
END

SUBROUTINE PLOTA (SF,L,LP,YS,16,17,18,19,110,113,114,115)
WRITE(6,50)
30 FORMAT (' WHICH SCALE WILL BE REQUIRED ?' /
1 ' 0 - 50, ENTER 4.0' / ' 0 - 12.5, ENTER 1.0' / ' 0 - 2.5, ENTER 0.2' )
READ(5,*) SF
L=0
CALL PLOTS (0,0,LP)
CALL PLOT (15.0,5.0,-3)
CALL AXIS (0.0,0.0,' THERMAL CONDUCTIVITY (W/MK)',27,12.5,90.0,0.0,
1 SF)
CALL AXIS (0.0,0.0,' TEMPERATURE (100C)',-18,16.0,0.0,0.0,1.0)
WRITE(6,40)
40 FORMAT (' ENTER WHICH THEORIES YOU REQUIRE PLOTTING, USING A (1) /
1 FOR A PLOT AND A (0) FOR NO PLOT.' /
2 ' THE THEORIES ARE EUCKEN,RUSSELL,SIMPLE,RUSSELL(RAD),LOER.')

```

**APPENDIX VI Thermal Conductivity Calculation
 FORTRAN Program (page 3)**

```

READ(5,*) I5,I6,I7,I8,I9
WRITE(6,*)
45 FORMAT(7) ENTER WHICH OF THE THREE PHASES YOU REQUIRE PLOTTING',
1,7 FOR COMPARISON -?' GOS,METAL,SLAG (AS ABOVE)')
READ(5,*) I13,I14,I15
WRITE(6,50)
50 FORMAT(7) DO YOU REQUIRE ALL CURVES ON A SINGLE PLOT (1) OR A'/
1,7 SEPERATE GRAPH FOR EACH SET OF VALUES (0) ?')
RETURN
END

SUBROUTINE PLOTB (SF,L,I10)
IF (I10.EQ.1) GO TO 220
L=L+1
IF (L.EQ.1) GO TO 220
CALL PLOT (30.0,0.0,-3)
CALL AXIS (0.0,0.0,0.0,THERMAL CONDUCTIVITY (W/MK)',27,12-5,90.0,0.0,0.0,
SF)
1 CALL AXIS (0.0,0.0,0.0,TEMPERATURE (100C)',-18,16.0,0.0,0.0,1.0)
220 CONTINUE
RETURN
END

SUBROUTINE PLOTG (CEUCC,CRUSS,CSIMP,CRUSS,CLOEB,I5,IM,
I3,I7,I8,I9,SF,I13,I14,I15,CGRAS,CMET,CSLAG)
DIMENSION CEUCC(19),CRUSS(19),CSIMP(19),CRUSS(19),CLOEB(19),TM(19)
CEUCC(19)=0.0
CRUSS(19)=0.0
CSIMP(19)=0.0
CRUSS(19)=0.0
CLOEB(19)=0.0
CGRAS(19)=0.0
CMET(19)=0.0
CSLAG(19)=0.0
CEUCC(19)=SF
CMET(19)=SF
CSLAG(19)=SF
CEUCC(19)=SF
CRUSS(19)=SF
CSIMP(19)=SF
CRUSS(19)=SF
CLOEB(19)=SF
IF (I15.EQ.0) GO TO 200
CALL LINE(TM,CGRAS,I7,I1,1,6)
200 IF (I14.EQ.0) GO TO 210
CALL LINE(TM,CMET,I7,I1,1,7)
210 IF (I15.EQ.0) GO TO 279
CALL LINE(TM,CSLAG,I7,I1,1,8)
279 IF (I15.EQ.0) GO TO 280
CALL LINE(TM,CEUCC,I7,I1,1,1)
280 IF (I16.EQ.0) GO TO 290

```

**APPENDIX VI Thermal Conductivity Calculation
FORTRAN Program (page 4)**

```

CALL LINE(TM,CRUSS,17,1,1,2)
290 IF (17.EQ.0) GO TO 300
CALL LINE(TM,CSIMP,17,1,1,3)
300 IF (18.EQ.0) GO TO 310
CALL LINE(TM,CRUSR,17,1,1,4)
310 IF (19.EQ.0) GO TO 320
CALL LINE(TM,CLOEB,17,1,1,5)
320 CONTINUE
RETURN
END

SUBROUTINE TABLE (CEUCC,CRUSS,CSIMP,CRUSS,CLOEB,TM,CSLAG,
1 CMET,CGAS,I1,I2,PSF,A,D,PC,PL)
DIMENSION CEUCC(19),CRUSS(19),CSIMP(19),CRUSR(19),CLOEB(19)
DIMENSION CSLAG(19),TM(19),CMET(19),CGAS(19)
WRITE(6,250) I1,I2
250 FORMAT(' CONT. PHASE=',I2,' DISP. PHASE=',I2/)
IF (I2.EQ.3) GO TO 259
WRITE(6,251) PC
251 FORMAT(' PC=',F3.1)
259 CONTINUE
WRITE(6,260) PSF,A,D,PC,PL
260 FORMAT('/' PSF=',F3.1,' CPF=',F3.1,' D=',F6.4/
1 ' PC=',F3.1,' PL=',F3.1/)
265 CONTINUE
WRITE(6,270) (TM(I),CSLAG(I),CMET(I),CGAS(I),CEUCC(I),CRUSS(I),
1 CSIMP(I),CRUSR(I),CLOEB(I),I=1,17)
270 FORMAT(/' TEMP CSLAG CMET CGAS CEUCC CRUSS CSIMP',
1 ' CRUSR CLOEB'/
2 ' (C)',2X,' (M/MC)'/17(' ',F6.0,F6.3,F5.1,F8.4,5F8.3/))
RETURN
END

SUBROUTINE CALC (I1,I2,CSLAG,CMET,CGAS,PC,PL,A,D,E,PSF,TM,
1 CEUCC,CRUSS,CSIMP,CRUSR,CLOEB)
DIMENSION CEUCC(19),CRUSS(19),CSIMP(19),CRUSR(19),CLOEB(19)
DIMENSION CSLAG(19),TM(19),CMET(19),CGAS(19),E(19)
IF (I2.EQ.3) GO TO 230
IF (I2.EQ.2) GO TO 230
CALL COMP (CSLAG,CMET,PC,CEUCC,CRUSS)
230 CALL COMP (CMET,CSLAG,PC,CEUCC,CRUSS)
GO TO 260
240 IF (I1.EQ.1) GO TO 250
CALL COMP (CSLAG,CGAS,PC,CEUCC,CRUSS)
CALL FORO (CSLAG,CGAS,PC,PL,A,D,E,PSF,CRUSR,CLOEB,TM,CSIMP)
GO TO 260
250 CALL COMP (CMET,CGAS,PC,CEUCC,CRUSS)
CALL FORO (CMET,CGAS,PC,PL,A,D,E,PSF,CRUSR,CLOEB,TM,CSIMP)
260 CONTINUE
RETURN
END

```

**APPENDIX VI Thermal Conductivity Calculation
FORTRAN Program (page 5)**

```

SUBROUTINE TREP(PLP,CSLAG,CMET,CGRAS,E,FM)
DIMENSION CMLAG(19),CMET(19),CGRAS(19),CEURU(19),CEURD(19)
DIMENSION CEUSI(19),CEURR(19),CEULO(19),E(19),FM(19)
DIMENSION CRUEU(19),CRURU(19),CRUSI(19),CRURR(19),CRULD(19)
4 WRITE(6,5)
5 FORMAT (' ENTER CONTINUOUS AND DISPERSE PHASE OF SOLID ?' /
1 ' METAL=1,SLAG=2.')
READ(5,*) I1,I2
WRITE(6,10)
10 FORMAT (' DO YOU REQUIRE TABULAR OUTPUT ? (YES=1,NO=0)')
READ(5,*) I3
WRITE(6,20)
20 FORMAT (' DO YOU REQUIRE GRAPHICAL OUTPUT ? (YES=1,NO=0)')
READ(5,*) I4
IF (I4.EQ.1) CALL PLOTAB(SF,I,L,LP,I5,I6,I7,I8,I9,I10,I13,I14,I15,
17,I18,I19,I20,I21)
60 WRITE(6,70)
70 FORMAT(' ANY ONE OF THE FOLLOWING VARIATIONS MAY BE INTRODUCED-'//
1 ' CROSS-SECTIONAL POROSITY FROM 0 TO 0.9 (1)'/
2 ' PORE DIAMETER FROM 0.5 TO 5 MM (2)'/
3 ' METAL/SLAG RATIO OF SOLID FROM 0.25 TO 4 (3)'/
4 ' NON-SPHERICAL PORES (4)'/
5 ' CHANGE OF CONTINUOUS PHASE (5)'/
6 ' NONE (6)')
READ(5,*) I11
IF (I11.EQ.3) GO TO 110
SF=1.0
A=0.9
IF (I11.EQ.1) GO TO 90
WRITE(6,80)
80 FORMAT(' ENTER PORE DIAMETER IN METRES AND METAL/SLAG RATIO')
READ(5,*) D,RAT
D0=D5 J=1,10
PC=(J-1)*0.1
PL=PC
VNET=(1-PC)*RAT/(RAT+1)
VSLAB=1-PC-VNET
IF (I4.EQ.1) CALL PLOTB(SF,I,I10)
CALL CALCS(I,I2,CSLAG,CMET,CGRAS,PC,PL,A,D,E,PSF,FM,
1 CEURU,CEURD,CEUSI,CEURR,CEULO,USLAG,
2 CRUED,CRURD,CRUSI,CRURR,CRULD,VNET)
IF (I2.EQ.1) CALL TABLE3(CEURU,CEURD,CEUSI,CEURR,CEULO,
1 CRUEU,CRURU,CRUSI,CRURR,CRULD,I1,I2,FM,
2 PSF,A,D,PC,PI,VNET,VSLAG,CGRAS,CMET,CSLAG)
IF (I4.EQ.1) CALL PLOTCS(CEURU,CEURD,CEUSI,CEURR,CEULO,
1 CRUEU,CRURU,CRUSI,CRURR,CRULD,I5,FM,I17,I18,I19,I20,I21,
2 I6,I7,I8,I9,SF,I13,I14,I15,CGRAS,CMET,CSLAG)
85 CONTINUE
90 TO 910
90 IF(I11.EQ.2) GO TO 106
WRITE(6,100)
100 FORMAT(' ENTER VALUES FOR CROSS-SECTIONAL POROSITY, METAL VOLUME'/
1 ' FRACTION AND SLAG VOLUME FRACTION.')

```

**APPENDIX VI Thermal Conductivity Calculation
FORTRAN Program (page 6)**

```

READ(5,*) %C,VMET,VSLAG
PL=PC
DO 105 K=1,30
D=K*0.0005
IF (I4.EQ.1) CALL PLOTR (SF,L,I10)
CALL CALC3 (I1,I2,CSLAG,CMET,CGAS,PC,PL,A,D,E,PSF,TM,
1 CEUEU,CEURU,CEUSI,CEURR,CEULO,VSLAG,
2 CRUEU,CRURU,CRUSI,CRURR,CRULO,VMET)
IF (I3.EQ.1) CALL TABLE3 (CEUEU,CEURU,CEUSI,CEURR,CEULO,
1 CRUEU,CRURU,CRUSI,CRURR,CRULO,I1,I2,TM,
2 PSF,A,D,PC,PL,VMET,VSLAG,CGAS,CMET,CSLAG)
IF (I4.EQ.1) CALL PLOT3 (CEUEU,CEURU,CEUSI,CEURR,CEULO,
1 CRUEU,CRURU,CRUSI,CRURR,CRULO,I5,TM,I17,I18,I19,I20,I21,
2 I6,I7,I8,I9,SF,I13,I14,I15,CGAS,CMET,CSLAG)
105 CONTINUE
GO TO 910
106 WRITE(6,107)
107 FORMAT(' ENTER VALUES FOR CROSS-SECTIONAL POROSITY AND PORE SIZE')
READ(5,*) PC,D
PL=PC
DO 108 JL=1,10
RAT=0.125*2**JL
VMET=(1-PC)*RAT/(RAT+1)
VSLAG=1-PC-VMET
IF (I4.EQ.1) CALL PLOTR (SF,L,I10)
CALL CALC3 (I1,I2,CSLAG,CMET,CGAS,PC,PL,A,D,E,PSF,TM,
1 CEUEU,CEURU,CEUSI,CEURR,CEULO,VSLAG,
2 CRUEU,CRURU,CRUSI,CRURR,CRULO,VMET)
IF (I3.EQ.1) CALL TABLE3 (CEUEU,CEURU,CEUSI,CEURR,CEULO,
1 CRUEU,CRURU,CRUSI,CRURR,CRULO,I1,I2,TM,
2 PSF,A,D,PC,PL,VMET,VSLAG,CGAS,CMET,CSLAG)
IF (I4.EQ.1) CALL PLOT3 (CEUEU,CEURU,CEUSI,CEURR,CEULO,
1 CRUEU,CRURU,CRUSI,CRURR,CRULO,I5,TM,I17,I18,I19,I20,I21,
2 I6,I7,I8,I9,SF,I13,I14,I15,CGAS,CMET,CSLAG)
108 CONTINUE
GO TO 910
110 WRITE(6,120)
120 FORMAT(' YOU WILL BE REQUESTED VALUES FOR LOEB PORE SHAPE FACTOR'/
1 ' RUSSELL COMBINED PORE FACTOR, LONGITUDINAL PORE SIZE,'/
2 ' CROSS-SECTIONAL AND LONGITUDINAL POROSITY, AND'/
3 ' VOLUME FRACTIONS OF METAL AND SLAG')
150 WRITE(6,140)
140 FORMAT(' ENTER PSF,CPE,D,PC,PL,VMET,VSLAG')
READ(5,*) PSF,A,D,PC,PL,VMET,VSLAG
IF (I11.NE.5) GO TO 150
WRITE(6,146)
146 FORMAT(' DO YOU WISH TO REVERSE CONTINUITY OF THE METAL/SLAG ?'/
1 ' (YES=1,NO=0)')
READ(5,*) I12
IF (I12.EQ.1) CALL SWOP (I1,I2)
150 CONTINUE
IF (I4.EQ.1) CALL PLOTR (SF,L,I10)
CALL CALC3 (I1,I2,CSLAG,CMET,CGAS,PC,PL,A,D,E,PSF,TM,
1 CEUEU,CEURU,CEUSI,CEURR,CEULO,VSLAG,
2 CRUEU,CRURU,CRUSI,CRURR,CRULO,VMET)

```

**APPENDIX VI Thermal Conductivity Calculation
FORTRAN Program (page 7)**

```

IF (I3.EQ.1) CALL TABLES (CEUO,CEURU,CEURR,CEUR,CEUL0,CEUL1,CEUL2,CEUL3,CEUL4,CEUL5,CEUL6,CEUL7,CEUL8,CEUL9,CEUL10,CEUL11,CEUL12,CEUL13,CEUL14,CEUL15,CEUL16,CEUL17,CEUL18,CEUL19,CEUL20,CEUL21,CEUL22,CEUL23,CEUL24,CEUL25,CEUL26,CEUL27,CEUL28,CEUL29,CEUL30,CEUL31,CEUL32,CEUL33,CEUL34,CEUL35,CEUL36,CEUL37,CEUL38,CEUL39,CEUL40,CEUL41,CEUL42,CEUL43,CEUL44,CEUL45,CEUL46,CEUL47,CEUL48,CEUL49,CEUL50,CEUL51,CEUL52,CEUL53,CEUL54,CEUL55,CEUL56,CEUL57,CEUL58,CEUL59,CEUL60,CEUL61,CEUL62,CEUL63,CEUL64,CEUL65,CEUL66,CEUL67,CEUL68,CEUL69,CEUL70,CEUL71,CEUL72,CEUL73,CEUL74,CEUL75,CEUL76,CEUL77,CEUL78,CEUL79,CEUL80,CEUL81,CEUL82,CEUL83,CEUL84,CEUL85,CEUL86,CEUL87,CEUL88,CEUL89,CEUL90,CEUL91,CEUL92,CEUL93,CEUL94,CEUL95,CEUL96,CEUL97,CEUL98,CEUL99,CEUL100)
1 CRUO,CRURU,CRURR,CRUR,CRUL0,CRUL1,CRUL2,CRUL3,CRUL4,CRUL5,CRUL6,CRUL7,CRUL8,CRUL9,CRUL10,CRUL11,CRUL12,CRUL13,CRUL14,CRUL15,CRUL16,CRUL17,CRUL18,CRUL19,CRUL20,CRUL21,CRUL22,CRUL23,CRUL24,CRUL25,CRUL26,CRUL27,CRUL28,CRUL29,CRUL30,CRUL31,CRUL32,CRUL33,CRUL34,CRUL35,CRUL36,CRUL37,CRUL38,CRUL39,CRUL40,CRUL41,CRUL42,CRUL43,CRUL44,CRUL45,CRUL46,CRUL47,CRUL48,CRUL49,CRUL50,CRUL51,CRUL52,CRUL53,CRUL54,CRUL55,CRUL56,CRUL57,CRUL58,CRUL59,CRUL60,CRUL61,CRUL62,CRUL63,CRUL64,CRUL65,CRUL66,CRUL67,CRUL68,CRUL69,CRUL70,CRUL71,CRUL72,CRUL73,CRUL74,CRUL75,CRUL76,CRUL77,CRUL78,CRUL79,CRUL80,CRUL81,CRUL82,CRUL83,CRUL84,CRUL85,CRUL86,CRUL87,CRUL88,CRUL89,CRUL90,CRUL91,CRUL92,CRUL93,CRUL94,CRUL95,CRUL96,CRUL97,CRUL98,CRUL99,CRUL100)
2 CRUO,CRURU,CRURR,CRUR,CRUL0,CRUL1,CRUL2,CRUL3,CRUL4,CRUL5,CRUL6,CRUL7,CRUL8,CRUL9,CRUL10,CRUL11,CRUL12,CRUL13,CRUL14,CRUL15,CRUL16,CRUL17,CRUL18,CRUL19,CRUL20,CRUL21,CRUL22,CRUL23,CRUL24,CRUL25,CRUL26,CRUL27,CRUL28,CRUL29,CRUL30,CRUL31,CRUL32,CRUL33,CRUL34,CRUL35,CRUL36,CRUL37,CRUL38,CRUL39,CRUL40,CRUL41,CRUL42,CRUL43,CRUL44,CRUL45,CRUL46,CRUL47,CRUL48,CRUL49,CRUL50,CRUL51,CRUL52,CRUL53,CRUL54,CRUL55,CRUL56,CRUL57,CRUL58,CRUL59,CRUL60,CRUL61,CRUL62,CRUL63,CRUL64,CRUL65,CRUL66,CRUL67,CRUL68,CRUL69,CRUL70,CRUL71,CRUL72,CRUL73,CRUL74,CRUL75,CRUL76,CRUL77,CRUL78,CRUL79,CRUL80,CRUL81,CRUL82,CRUL83,CRUL84,CRUL85,CRUL86,CRUL87,CRUL88,CRUL89,CRUL90,CRUL91,CRUL92,CRUL93,CRUL94,CRUL95,CRUL96,CRUL97,CRUL98,CRUL99,CRUL100)
330 WRITE(6,330)
330 FORMAT(' DO YOU WISH TO RE-RUN THIS OPTION? (1=YES,0=NO)')
READ(5,*) I16
IF (I16.EQ.1) GO TO 130
910 CALL PLOT(10.0,0.0,999)
990 RETURN
END

SUBROUTINE PLOT03 (SF,I,LP,I5,I6,I7,I8,I9,I10,I11,I12,I13,I14,I15,
1 I17,I18,I19,I20,I21)
WRITE(6,30)
30 FORMAT (' WHICH SCALE WILL BE REQUIRED ?')
1 0 - 50,ENTER 4.0// 0 - 12.5,ENTER 1.0// 0 - 2.5,ENTER 0.2//
READ(5,*) SF
L=0
CALL PLOTS (0,0,LP)
CALL PLOT (15.0,5.0,-3)
CALL AXIS (0.0,0.0,'THERMAL CONDUCTIVITY (W/MK)',27,12.5,90.0,0.0,
1 SF)
CALL AXIS (0.0,0.0,'TEMPERATURE (100C)',-18,16.0,0.0,0.0,1.0)
WRITE(6,40)
40 FORMAT (' ENTER WHICH THEORIES YOU REQUIRE PLOTTING, USING A (1)//
1 1 FOR A SLOTT AND A (0) FOR NO PLOT.')
2 1 THE THEORIES ARE -> ,GX, EUCKEN/EUCKEN//
3 25X, EUCKEN/RUSSELL/25X, EUCKEN/SIMPLE//
4 25X, EUCKEN/RUSSELL(RADIATION)/25X, EUCKEN/LOER//
5 25X, RUSSELL/EUCKEN/25X, RUSSELL/RUSSELL//
6 25X, RUSSELL/SIMPLE/25X, RUSSELL/RUSSELL(RAD)//
7 25X, RUSSELL/LOER//
READ(5,*) I5,I6,I7,I8,I9,I10,I11,I12,I13,I14,I15
WRITE(6,45)
45 FORMAT(' ENTER WHICH OF THE THREE PHASES YOU REQUIRE PLOTTING,
1 1 FOR COMPARISON -// GAS,METAL,SLAG (AS ABOVE)')
READ(5,*) I13,I14,I15
WRITE(6,50)
50 FORMAT(' DO YOU REQUIRE ALL CURVES ON A SINGLE PLOT (1) OR A//
1 1 SEPARATE GRAPH FOR EACH SET OF VALUES (0) ?')
READ(5,*) I10
RETURN
END

SUBROUTINE PLOT04 (CEUO,CEURU,CEURR,CEUR,CEUL0,CEUL1,CEUL2,CEUL3,CEUL4,CEUL5,CEUL6,CEUL7,CEUL8,CEUL9,CEUL10,CEUL11,CEUL12,CEUL13,CEUL14,CEUL15,CEUL16,CEUL17,CEUL18,CEUL19,CEUL20,CEUL21,CEUL22,CEUL23,CEUL24,CEUL25,CEUL26,CEUL27,CEUL28,CEUL29,CEUL30,CEUL31,CEUL32,CEUL33,CEUL34,CEUL35,CEUL36,CEUL37,CEUL38,CEUL39,CEUL40,CEUL41,CEUL42,CEUL43,CEUL44,CEUL45,CEUL46,CEUL47,CEUL48,CEUL49,CEUL50,CEUL51,CEUL52,CEUL53,CEUL54,CEUL55,CEUL56,CEUL57,CEUL58,CEUL59,CEUL60,CEUL61,CEUL62,CEUL63,CEUL64,CEUL65,CEUL66,CEUL67,CEUL68,CEUL69,CEUL70,CEUL71,CEUL72,CEUL73,CEUL74,CEUL75,CEUL76,CEUL77,CEUL78,CEUL79,CEUL80,CEUL81,CEUL82,CEUL83,CEUL84,CEUL85,CEUL86,CEUL87,CEUL88,CEUL89,CEUL90,CEUL91,CEUL92,CEUL93,CEUL94,CEUL95,CEUL96,CEUL97,CEUL98,CEUL99,CEUL100)
1 CRUO,CRURU,CRURR,CRUR,CRUL0,CRUL1,CRUL2,CRUL3,CRUL4,CRUL5,CRUL6,CRUL7,CRUL8,CRUL9,CRUL10,CRUL11,CRUL12,CRUL13,CRUL14,CRUL15,CRUL16,CRUL17,CRUL18,CRUL19,CRUL20,CRUL21,CRUL22,CRUL23,CRUL24,CRUL25,CRUL26,CRUL27,CRUL28,CRUL29,CRUL30,CRUL31,CRUL32,CRUL33,CRUL34,CRUL35,CRUL36,CRUL37,CRUL38,CRUL39,CRUL40,CRUL41,CRUL42,CRUL43,CRUL44,CRUL45,CRUL46,CRUL47,CRUL48,CRUL49,CRUL50,CRUL51,CRUL52,CRUL53,CRUL54,CRUL55,CRUL56,CRUL57,CRUL58,CRUL59,CRUL60,CRUL61,CRUL62,CRUL63,CRUL64,CRUL65,CRUL66,CRUL67,CRUL68,CRUL69,CRUL70,CRUL71,CRUL72,CRUL73,CRUL74,CRUL75,CRUL76,CRUL77,CRUL78,CRUL79,CRUL80,CRUL81,CRUL82,CRUL83,CRUL84,CRUL85,CRUL86,CRUL87,CRUL88,CRUL89,CRUL90,CRUL91,CRUL92,CRUL93,CRUL94,CRUL95,CRUL96,CRUL97,CRUL98,CRUL99,CRUL100)
2 CRUO,CRURU,CRURR,CRUR,CRUL0,CRUL1,CRUL2,CRUL3,CRUL4,CRUL5,CRUL6,CRUL7,CRUL8,CRUL9,CRUL10,CRUL11,CRUL12,CRUL13,CRUL14,CRUL15,CRUL16,CRUL17,CRUL18,CRUL19,CRUL20,CRUL21,CRUL22,CRUL23,CRUL24,CRUL25,CRUL26,CRUL27,CRUL28,CRUL29,CRUL30,CRUL31,CRUL32,CRUL33,CRUL34,CRUL35,CRUL36,CRUL37,CRUL38,CRUL39,CRUL40,CRUL41,CRUL42,CRUL43,CRUL44,CRUL45,CRUL46,CRUL47,CRUL48,CRUL49,CRUL50,CRUL51,CRUL52,CRUL53,CRUL54,CRUL55,CRUL56,CRUL57,CRUL58,CRUL59,CRUL60,CRUL61,CRUL62,CRUL63,CRUL64,CRUL65,CRUL66,CRUL67,CRUL68,CRUL69,CRUL70,CRUL71,CRUL72,CRUL73,CRUL74,CRUL75,CRUL76,CRUL77,CRUL78,CRUL79,CRUL80,CRUL81,CRUL82,CRUL83,CRUL84,CRUL85,CRUL86,CRUL87,CRUL88,CRUL89,CRUL90,CRUL91,CRUL92,CRUL93,CRUL94,CRUL95,CRUL96,CRUL97,CRUL98,CRUL99,CRUL100)
DIMENSION CGAS(19),CMET(19),CSLAG(19)

```

APPENDIX VI Thermal Conductivity Calculation
 FORTRAN Program (page 8)

```

DIMENSION CRUEU(19),CRURU(19),CRUSI(19),CRURR(19),CRULO(19)
CEUEU(18)=0.0
CEURU(18)=0.0
CRUSI(18)=0.0
CEURR(18)=0.0
CEULO(18)=0.0
CRUEU(18)=0.0
CRURU(18)=0.0
CRUSI(18)=0.0
CRURR(18)=0.0
CRULO(18)=0.0
CGAS(18)=0.0
CNET(18)=0.0
CSLAG(18)=0.0
CGAS(19)=SF
CNET(19)=SF
CSLAG(19)=SF
CEURU(19)=SF
CEURR(19)=SF
CEUSI(19)=SF
CEURR(19)=SF
CEULO(19)=SF
CRURU(19)=SF
CRURR(19)=SF
CRUSI(19)=SF
CRURR(19)=SF
CRULO(19)=SF
IF (I13.EQ.0) GO TO 200
CALL LINE(TM,CGAS,17,1,1,4)
200 IF (I14.EQ.0) GO TO 210
CALL LINE(TM,CNET,17,1,1,7)
210 IF (I15.EQ.0) GO TO 279
CALL LINE(TM,CSLAG,17,1,1,8)
279 IF (I16.EQ.0) GO TO 290
CALL LINE(TM,CEUEU,17,1,1,1)
280 IF (I16.EQ.0) GO TO 290
CALL LINE(TM,CEURU,17,1,1,2)
290 IF (I17.EQ.0) GO TO 300
CALL LINE(TM,CEUSI,17,1,1,3)
300 IF (I18.EQ.0) GO TO 310
CALL LINE(TM,CEURR,17,1,1,4)
310 IF (I19.EQ.0) GO TO 320
CALL LINE(TM,CEULO,17,1,1,5)
320 IF (I17.EQ.0) GO TO 330
CALL LINE(TM,CRUEU,17,1,1,9)
330 IF (I18.EQ.0) GO TO 340
CALL LINE(TM,CRURU,17,1,1,10)
340 IF (I19.EQ.0) GO TO 350
CALL LINE(TM,CRUSI,17,1,1,11)
350 IF (I20.EQ.0) GO TO 360
CALL LINE(TM,CRURR,17,1,1,12)
360 IF (I21.EQ.0) GO TO 370
CALL LINE(TM,CRULO,17,1,1,0)
370 CONTINUE
379 RETURN
    
```

**APPENDIX VI Thermal Conductivity Calculation
FORTRAN Program (page 9)**

END

```

SUBROUTINE TORLEZ (CEUEU, CEURU, CEUSI, CEURR, CEULO,
1 CRUFU, CRURU, CRUSI, CRURR, CRULO, I1, I2, TM,
2 PSF, A, D, PC, PL, VMET, VSLAG, CGAS, CMET, CSLAG)
DIMENSION CEUEU(19), CEURU(19), CEUSI(19), CEURR(19), CEULO(19), TM(19)
DIMENSION CGAS(19), CMET(19), CSLAG(19)
DIMENSION CRUEU(19), CRURU(19), CRUSI(19), CRURR(19), CRULO(19)
WRITE(6, 250) I1, I2
250 FORMAT( ' CONT. PHASE= ', I1, ' DISP. PHASE= ', I2 /)
WRITE(6, 260) PSF, A, D, PC, PL, VMET, VSLAG
260 FORMAT( / ' PSF= ', F3.1, ' D= ', F6.4 /
1 ' PC= ', F3.1, ' PL= ', F3.1, ' VMET= ', F5.3, ' VSLAG= ', F5.3 / /)
WRITE(6, 270) (TM(I), CSLAG(I), CMET(I), CGAS(I), CEUEU(I), CEURU(I),
1 CEUSI(I), CEURR(I), CEULO(I), CRUEU(I), CRURU(I),
2 CRUSI(I), CRURR(I), CRULO(I)), I=1, 17)
270 FORMAT( / ' TEMP CSLAG CMET CGAS EUEU EURU EUSI EURR EULO ',
1 ' RUEU RURU RUSI RURR RULO', / ' (C)', 3BX, ' (W/MC)', / /)
RETURN
END

```

```

SUBROUTINE CALC3 (I1, I2, CSLAG, CMET, CGAS, PC, PL, A, D, E, PSF, TM,
1 CEUEU, CEURU, CEUSI, CEURR, CEULO, VSLAG,
2 CRUFU, CRURU, CRUSI, CRURR, CRULO, VMET)
DIMENSION CSLAG(19), CMET(19), CGAS(19), CEUEU(19), CEURU(19)
DIMENSION CEUSI(19), CEURR(19), CEULO(19), E(19), TM(19)
DIMENSION CRUEU(19), CRURU(19), CRUSI(19), CRURR(19), CRULO(19)
DIMENSION CEUC(19), CRUSS(19)
IF (I1.EQ.1) VU/SP=(VSLAG+VMET)
IF (I1.EQ.2) VU/SP=(VMET/(VSLAG+VMET))
IF (I1.EQ.3) CALL COMP(CMET, CSLAG, VU/SP, CEUC, CRUSS)
CALL COMP(CEUC, CGAS, PC, CRUFU, CEURU)
CALL COMP(CRUSS, CGAS, PC, CRUFU, CRURU)
CALL COMP(CEUC, CGAS, PC, PL, A, D, E, PSF, CEURR, CEULO, TM, CEUSI)
CALL COMP(CRUSS, CGAS, PC, PL, A, D, E, PSF, CRURR, CRULO, TM, CRUST)
RETURN
END

```

APPENDIX VI Thermal Conductivity Calculation
FORTTRAN Program (page 10)

FILE: R005 DATA A *** UM/SP AT SHEFFIELD CITY POLYTECHNIC (CMS GEN 02DFC86) ***

1.39	1.41	1.43	1.45	1.46	1.48	1.50	1.52	1.54	1.56
1.58	1.59	1.61	1.62	1.65	1.67	1.69	0.00	0.50	
45.	41.	43.	40.	37.	35.	33.	31.	30.	29.
39.	37.	35.	33.	31.	30.	29.	29.	30.	31.
33.	35.	37.	0.	2.					
.025	.030	.037	.042	.048	.054	.059	.064	.068	.073
.072	.082	.087	.092	.097	.101	.103	.100	.100	
.9	.9	.9	.9	.9	.9	.9	.9	.9	.9
0.	100.	200.	300.	400.	500.	600.	700.	800.	900.
1000.	1100.	1200.	1300.	1400.	1500.	1600.	0.	100.	

APPENDIX VI Thermal Conductivity Calculation Data File

FILE: M005 1 DISK M005A PLOT A (RECFM F LRECL 128 BLOCK 128)
FILE: M005 2 DISK M005B PLOT A (RECFM F LRECL 128 BLOCK 128)
FILE: M005 3 DISK M005C PLOT A (RECFM F LRECL 128 BLOCK 128)
FILE: M005 4 DISK M005D PLOT A (RECFM F LRECL 128 BLOCK 128)
FILE: M005 7 DISK M005E DATA

APPENDIX VI Thermal Conductivity Calculation
File Definition

APPENDIX VII.

The Calculation Of Convective Heat Transfer

Coefficients.

102

Using the equation and data below ;

$$Nu = 0.023 Pr^{0.4} Re^{0.8}$$

$$h = k/x \cdot 0.023 Pr^{0.4} Re^{0.8}$$

where

h = convective heat transfer coefficient

k = thermal conductivity of water

at 35 C = 0.618 W/mK

x = characteristic dimension of channel = 0.1 m

Pr = Prandlt No. for water at 35 C = 4.89

$$Re = \text{Reynolds No.} = \frac{v x}{\nu}$$

v = mean velocity of water

ν = kinematic viscosity of water

at 35 C = $7.284 \times 10^{-7} \text{ m}^2/\text{s}$

The mean velocities of water in the various panels can be determined from the flow equations developed in Appendix III, and from these the Reynolds numbers and hence the heat transfer coefficients can be found. The results are tabulated below -

Sample	v	Re	h
B5-06	0.481 m/s	66035	1924 W/K
B10-06	0.421 m/s	57798	1730 W/K
B3-07	0.457 m/s	62740	1847 W/K
B5-07	0.457 m/s	62740	1847 W/K
B5-08	0.433 m/s	59445	1769 W/K

APPENDIX VIII.

Case Study : Potential Savings From Heat Loss Minimisation In Electric Arc Furnaces By Sidewall Slag Layer Control.

1. Introduction.

The work to which this case study is appended has investigated the formation and structure of the slag layers formed on water cooled sidewalls, and the physical properties of these layers that influence heat losses. A model was proposed for calculating the heat loss over a wide range of structural conditions but for a specific instant in the melting cycle. This study will expand that model to give an indication of total heat losses over the whole melting cycle, and use the results for various possible sidewall slag structures to identify potential cost savings.

Instantaneous steady state heat losses will be calculated for a number of slag layer structures based on those observed in the furnace, and a shielding factor, similar to Bowman's refractory factor (reference 11 in main text), will be used to calculate the total heat loss during the melting cycle. These results will be converted into approximate costs for comparison, and then critically appraised.

2. Slag Layer Structures.

A wide range of slag layer thicknesses and structures were observed, but their stability was very dependant on the conditions in the furnace, especially the power and exposure of the arcs. For some of the slag layers used in this study, the possible methods of producing and maintaining such layers are discussed. However, there are certain factors which are universal and they will be addressed first.

The thickness of a layer is limited by the intensity of the radiation from the arc and it's flame, and this can be reduced without altering the arc power by the use of a foamy slag. Hence the comparison between thick and thin layers could be considered as an assessment of the effect of using foaming slags, which are produced by the injection of carbon powder. Foaming slags will also tend to produce more porous slag structures on the sidewall. The effect of the arc depends on it's distance from the sidewall, and hence thickness control could be achieved by altering furnace design to increase or reduce that dimension. More important is the directional nature of the arc and arc flame, which currently results in thinner layers at the hot spots. Again, a change in furnace design could help to increase the slag layer thickness. This could be by mechanical rotation of the electrodes to eliminate the hot spots, or use of inwardly inclined electrodes or controlled electrode tip geometry. Alternatively, electrical parameters could be

changed, possibly phase rotation to reduce the hot spot effect or ultimately the use of direct current. Many of these proposals and developments have been studied in the light of, amongst other advantages, reducing heat losses, but in this study the perspective is slightly redefined as the ability to maintain a thicker slag layer.

Slag Layer A.

A 250 mm thick layer of slag with metal ($k = 2 \text{ W/mK}$), having a hot face metal layer of 5 mm, similar to those observed at the panel number 8 position. The hot face temperature will be 1500 C. This layer could possibly be artificially produced at the start of the campaign by deliberately pulsing the arc to full power to create excessive slag splash yet allowing it to solidify on the panel, repeating the exercise on the clear metal bath for a short period. Maintaining such a layer would only be possible by one of the methods of containing the arc heat described above.

Slag Layer B.

A 50 mm thick layer of slag with metal ($k = 2 \text{ W/mK}$), similar to those observed in the panel number 11/12 position. Such a layer could be produced by spraying a slurry of slag powder onto a slag-catcher system of wire mesh attached to the panel face prior to start-up, and maintaining the layer would be as for A. The mesh matrix would provide sufficient strength to resist fracture and

shedding due to shock loading, but would be susceptible to high temperature oxidation.

Slag Layer C.

A 50 mm layer of porous slag ($k = 1 \text{ W/mK}$), similar to some of those observed, and as could be produced and maintained with a foamy slag practice.

Slag Layer D.

A 5 mm solid slag layer ($k = 1.5 \text{ W/mK}$), such as might be produced without slag-catchers at a hot spot position.

Slag Layer E.

No slag layer. This situation occurs when an existing layer is shed from the panel, and is not steady state. Simple radiation calculations indicate that the heat flux from the arc will instantaneously increase by 5 %, and that from the bath and refractories by 100 %, due to the low temperature face being exposed. If the rate of slag splashing is very low, the face of the panel will be rapidly heated until it stabilises at a temperature of, from observations, at least 1000 C at the hot spot position.

Slag Layer F.

A 20 mm slag and metal layer ($k = 2 \text{ W/mK}$), similar to those frequently observed in this work.

Slag Layer G.

A 20 mm porous slag layer ($k = 1 \text{ W/mK}$), again similar to many observed layers.

3. Heat Flux Calculation.

The linear steady state heat flux from the hot face of the layer to the water cooling has been calculated for each layer using appropriate temperature, thickness and thermal conductivity values. The details are given in tables A8.1 and A8.2 for cold water and hot water cooling respectively, where the mean temperature of a hot water cooling system has been taken as 150 C. The heat transfer coefficient for both systems has been taken as $1800 \text{ W/m}^2 \text{ K}$, as the thermal resistance for turbulent flow conditions is insignificant, even if the actual value at the higher water temperature is an order of magnitude smaller.

The range of heat flux values obtained relate closely to those actually measured on the furnace, and demonstrate how the heat losses can be as little as 2 % of the worst case value.

4. Total Heat Loss Calculation.

The calculation of total heat loss for a melting cycle is based on an 80 tonne capacity furnace with twelve sidewall panels, each having an area of 1 m^2 . Scrap shielding factors have been used to determine an effective time of exposure, which is then multiplied by the steady state heat flux to give an amount of heat which is then converted to an equivalent cost based on an electricity price of 5 pence per Kwh.

The shielding factors are based on a three hour cycle

time with a two basket charging practice, and are detailed below;

a) Hot spot position -

0 - 20 mins	0
20 - 50 mins	linear from 0 to 0.667
50 - 65 mins	0
65 - 105 mins	linear from 0 to 1
105 - 180 mins	1

b) Cold spot position -

0 - 115 mins	0
115 - 135 mins	linear from 0 to 1
135 - 180 mins	1

c) Other positions -

0 - 35 mins	0
35 - 50 mins	linear from 0 to 0.667
50 - 90 mins	0
90 - 120 mins	linear from 0 to 1
120 - 180 mins	1

d) All positions for a furnace without hot spots -

0 - 29 mins	0
29 - 50 mins	linear from 0 to 0.667
50 - 84 mins	0
84 - 120 mins	linear from 0 to 1
120 - 180 mins	1

To account for the shedding of slag layers, it is assumed that the panels are bare for a fixed percentage of the exposure time, which would be dependant on the

cohesive strength of the slag structure.

For a furnace with hot spots, two situations of slag cover have been included, a best case with thick porous layers and a worst case with thinner higher conductivity layers. All types of layers have been included for the furnace without hot spots, and the final set of calculations has assumed no shedding of the layers to give the minimum costs attainable.

Details of the calculations and the results are given in Tables A8.3 to A8.6.

5. Discussion.

Generally, the results indicate that the reported heat loss value of 20 kWh/t, which is the difference between refractory wall and water cooled wall, correlates closer to the worst case of slag cover. This suggests that the cost savings highlighted in this study could be attained in the right circumstances, and are therefore of genuine value to EAF operators.

Considering firstly the conventional furnace with hot spots, it can be seen that, by achieving the best case of sidewall slag cover, heat losses can be reduced by as much as 60% or the equivalent of 90 pence/tonne.

The relative effect of layer shedding is obviously greater for the best case situation, where improving the rate from 15% to 5% reduces the heat loss by over 40%. Even for the worst case the saving is significant, being

approximately equal to 40 pence/tonne.

Use of hot water cooling has a lesser effect than both the above, but for a furnace with a high level of heat loss the saving of up to 21 pence/tonne would probably justify the investment required to convert from a cold system. Even the minimum saving of 6 p/t could pay back an outlay of several thousand pounds over 1000 heats.

Considering a furnace without hot spots, contrived by one of the means suggested in the introduction, the effect of the slag layer thickness and structure is made clearer.

Assuming that the normal layer is a 20 mm mixed slag and metal, i.e. type F, then by increasing the thickness to 50 mm a saving of 50 p/t is possible. Alternatively, maintaining a 20 mm layer with high porosity offers a similar saving of over 40 p/t.

The effect of layer shedding and hot water cooling is similar to that seen in the conventional furnace, with layer shedding being more important for low heat loss situations and hot water cooling showing greater benefits for high heat loss situations.

The preferred method of achieving a low heat loss is to increase the thickness of the layer, as low metal, high porosity layers are more likely to be shed.

Promoting thicker layer formation requires development work in the following areas -

- a) furnace design
- b) slag catcher design and construction
- c) improving the shielding effect of the slag
- d) the effect of melting practice

Producing layers with sufficient metal content to give strength and reduce the frequency of shedding may require deliberate arcing at high power onto a slag free metal bath, either at the start of a campaign or for a short period in each melt cycle. Alternatively, design improvements in the slag catchers could increase the adherence of the layer.

6. Conclusion.

The potential heat savings for furnace designers and operators to aim for are in the region of 1500 kWh per melt, or 20 kWh/t, which could result in financial savings in excess of 100 pence/tonne.

SLAG LAYER

	A	B	C	D	E	F	G
theta 1	1500	1200	1200	1200	1000	1200	1200
theta 2	35	35	35	35	35	35	35
convective HTC	1800	1800	1800	1800	1800	1800	1800
t steel	0.025	0.025	0.025	0.025	0.025	0.025	0.025
k steel	20	20	20	20	20	20	20
t air	0	0	0	0	0	0	0
k air	0.04	0.04	0.04	0.04	0.04	0.04	0.04
t slag1	0.245	0.05	0.05	0.005	0	0.02	0.02
k slag1	2	2	1	1.5	1	2	1
t slag2	0.005	0	0	0	0	0	0
k slag2	30	1	1	1	1	1	1
t slag3	0	0	0	0	0	0	0
k slag3	1	1	1	1	1	1	1
t slag4	0	0	0	0	0	0	0
k slag4	1	1	1	1	1	1	1
t slag5	0	0	0	0	0	0	0
k slag5	1	1	1	1	1	1	1
t slag6	0	0	0	0	0	0	0
k slag6	1	1	1	1	1	1	1
omega1	0.000555	0.000555	0.000555	0.000555	0.000555	0.000555	0.000555
omega2	0.00125	0.00125	0.00125	0.00125	0.00125	0.00125	0.00125
omega3	0	0	0	0	0	0	0
omega4	0.1225	0.025	0.05	0.003333	0	0.01	0.02
omega5	0.000166	0	0	0	0	0	0
omega6	0	0	0	0	0	0	0
omega7	0	0	0	0	0	0	0
omega8	0	0	0	0	0	0	0
omega9	0	0	0	0	0	0	0
sum omega	0.124472	0.026805	0.051805	0.005138	0.001805	0.011805	0.021805
delta theta	1465	1165	1165	1165	965	1165	1165
heat flux	11770	43401	22488	226703	534462	98662	53427
W/m2							
kW/m2	11.8	43.5	22.5	226.7	534.5	98.7	53.4

Table A8.1 Heat Flux Calculation For Slag Layers A To G With Cold Water Cooling.

SLAG LAYER

	A	B	C	D	E	F	G
theta 1	1500	1200	1200	1200	1000	1200	1200
theta 2	150	150	150	150	150	150	150
convective HTC	1800	1800	1800	1800	1800	1800	1800
t steel	0.025	0.025	0.025	0.025	0.025	0.025	0.025
k steel	20	20	20	20	20	20	20
t air	0	0	0	0	0	0	0
k air	0.04	0.04	0.04	0.04	0.04	0.04	0.04
t slag1	0.245	0.05	0.05	0.005	0	0.02	0.02
k slag1	2	2	1	1.5	1	2	1
t slag2	0.005	0	0	0	0	0	0
k slag2	30	1	1	1	1	1	1
t slag3	0	0	0	0	0	0	0
k slag3	1	1	1	1	1	1	1
t slag4	0	0	0	0	0	0	0
k slag4	1	1	1	1	1	1	1
t slag5	0	0	0	0	0	0	0
k slag5	1	1	1	1	1	1	1
t slag6	0	0	0	0	0	0	0
k slag6	1	1	1	1	1	1	1
omega1	0.000555	0.000555	0.000555	0.000555	0.000555	0.000555	0.000555
omega2	0.00125	0.00125	0.00125	0.00125	0.00125	0.00125	0.00125
omega3	0	0	0	0	0	0	0
omega4	0.1225	0.025	0.05	0.003333	0	0.01	0.02
omega5	0.000166	0	0	0	0	0	0
omega6	0	0	0	0	0	0	0
omega7	0	0	0	0	0	0	0
omega8	0	0	0	0	0	0	0
omega9	0	0	0	0	0	0	0
sum omega	0.124472	0.026805	0.051805	0.005138	0.001805	0.011805	0.021805
delta theta	1350	1050	1050	1050	850	1050	1050
heat flux	10846	39171	20268	204324	470769	88941	48153
W/m2	10.8	39.2	20.3	204.3	470.8	88.9	48.2
kW/m2							

Table A8.2 Heat Flux Calculation For Slag Layers A To G With Hot Water Cooling.

FURNACE WITH HOT SPOTS - COLD COOLING - WORST CASE - 5% BARE PANELS														
SCENARIO 1	FURNACE POSITION	SLAG LAYER	NO. OF PANELS	HEAT FLUX	HEAT EXPOSURE TIME	HEAT LOSS	LESS 5%	+ 5% BARE	TOTAL HEAT	COST PER MELT	Kwh PER TONNE	COST PER TONNE	Kwh PER TONNE	
	HOT SPOT	D	3	226.7	105	4284630	4070399	505103	4575501					
	INTER	F	6	98.7	80	2642560	2700432	769680	3470112					
	COLD SPOT	B	3	43.5	55	430650	409118	264578	673695		Kwh	£	£	
				Kw/m2	mins	KJ	KJ	KJ	KJ	2422	8719308	121.10	30.3	1.51
FURNACE WITH HOT SPOTS - COLD COOLING - WORST CASE - 15% BARE PANELS														
SCENARIO 2	FURNACE POSITION	SLAG LAYER	NO. OF PANELS	HEAT FLUX	HEAT EXPOSURE TIME	HEAT LOSS	LESS 15%	+ 15% BARE	TOTAL HEAT	COST PER MELT	Kwh PER TONNE	COST PER TONNE	Kwh PER TONNE	
	HOT SPOT	D	3	226.7	105	4284630	3641936	1515308	5157243					
	INTER	F	6	98.7	80	2842560	2416176	2309040	4725216					
	COLD SPOT	B	3	43.5	55	430650	366053	793733	1159785		Kwh	£	£	
				Kw/m2	mins	KJ	KJ	KJ	KJ	3067	11042244	153.36	38.3	1.92
FURNACE WITH HOT SPOTS - HOT COOLING - WORST CASE - 5% BARE PANELS														
SCENARIO 3	FURNACE POSITION	SLAG LAYER	NO. OF PANELS	HEAT FLUX	HEAT EXPOSURE TIME	HEAT LOSS	LESS 5%	+ 5% BARE	TOTAL HEAT	COST PER MELT	Kwh PER TONNE	COST PER TONNE	Kwh PER TONNE	
	HOT SPOT	D	3	204.3	105	3861270	3688207	444906	4113113					
	INTER	F	6	88.9	80	2560320	2432304	677952	3110256					
	COLD SPOT	B	3	39.2	55	388080	368676	233046	601722		Kwh	£	£	
				Kw/m2	mins	KJ	KJ	KJ	KJ	2174	7825090.	108.68	27.2	1.36
FURNACE WITH HOT SPOTS - HOT COOLING - WORST CASE - 15% BARE PANELS														
SCENARIO 4	FURNACE POSITION	SLAG LAYER	NO. OF PANELS	HEAT FLUX	HEAT EXPOSURE TIME	HEAT LOSS	LESS 15%	+ 15% BARE	TOTAL HEAT	COST PER MELT	Kwh PER TONNE	COST PER TONNE	Kwh PER TONNE	
	HOT SPOT	D	3	204.3	105	3861270	3282080	1334718	4616798					
	INTER	F	6	88.9	80	2560320	2176272	2038856	4210128					
	COLD SPOT	B	3	39.2	55	388080	329868	699138	1029000		Kwh	£	£	
				Kw/m2	mins	KJ	KJ	KJ	KJ	2738	9855931.	136.89	34.2	1.71

Table A8.3 Heat Loss Calculation For Worst Case Slag Cover.

FURNACE WITH HOT SPOTS - COLD COOLING - BEST CASE - 5% BARE PANELS													
SCENARIO 5	FURNACE POSITION	SLAG LAYER	NO. OF PANELS	HEAT FLUX	HEAT EXPOSURE TIME	HEAT LOSS	LESS 5%	+ 5% BARE	TOTAL HEAT	COST PER MELT	Kwh PER TONNE	COST PER TONNE	Kwh PER TONNE
	HOT SPOT	G	3	53.4	105	1009260	958797	505103	1463900				
	INTER	C	6	22.5	80	648000	615600	769680	1385280				
	COLD SPOT	A	3	11.8	55	116820	110979	264578	375557		Kwh	£	£
				Kw/m2	mins	KJ	KJ	KJ	KJ	896	44.79	11.2	0.56
FURNACE WITH HOT SPOTS - COLD COOLING - BEST CASE - 15% BARE PANELS													
SCENARIO 6	FURNACE POSITION	SLAG LAYER	NO. OF PANELS	HEAT FLUX	HEAT EXPOSURE TIME	HEAT LOSS	LESS 15%	+ 15% BARE	TOTAL HEAT	COST PER MELT	Kwh PER TONNE	COST PER TONNE	Kwh PER TONNE
	HOT SPOT	G	3	53.4	105	1009260	857871	1515308	2373179				
	INTER	C	6	22.5	80	648000	550800	2309040	2859840				
	COLD SPOT	A	3	11.8	55	116820	99297	793733	893030		Kwh	£	£
				Kw/m2	mins	KJ	KJ	KJ	KJ	1702	85.08	21.3	1.06
FURNACE WITH HOT SPOTS - HOT COOLING - BEST CASE - 5% BARE PANELS													
SCENARIO 7	FURNACE POSITION	SLAG LAYER	NO. OF PANELS	HEAT FLUX	HEAT EXPOSURE TIME	HEAT LOSS	LESS 5%	+ 5% BARE	TOTAL HEAT	COST PER MELT	Kwh PER TONNE	COST PER TONNE	Kwh PER TONNE
	HOT SPOT	G	3	48.2	105	910980	865431	444906	1310337				
	INTER	C	6	20.3	80	584640	555408	677952	1233360				
	COLD SPOT	A	3	10.8	55	106920	101574	233046	334620		Kwh	£	£
				Kw/m2	mins	KJ	KJ	KJ	KJ	800	39.98	10.0	0.50
FURNACE WITH HOT SPOTS - HOT COOLING - BEST CASE - 15% BARE PANELS													
SCENARIO 8	FURNACE POSITION	SLAG LAYER	NO. OF PANELS	HEAT FLUX	HEAT EXPOSURE TIME	HEAT LOSS	LESS 15%	+ 15% BARE	TOTAL HEAT	COST PER MELT	Kwh PER TONNE	COST PER TONNE	Kwh PER TONNE
	HOT SPOT	G	3	48.2	105	910980	774333	1334718	2109051				
	INTER	C	6	20.3	80	584640	496944	2033856	2530800				
	COLD SPOT	A	3	10.8	55	106920	90882	699138	790020		Kwh	£	£
				Kw/m2	mins	KJ	KJ	KJ	KJ	1508	75.41	18.9	0.94

Table A8.4 Heat Loss Calculation For Best Case Slag Cover.

FURNACE WITHOUT HOT SPOTS - COLD COOLING - 5% BARE PANELS

SLAG LAYER	NO. OF PANELS	HEAT FLUX	HEAT EXPOSURE TIME	HEAT LOSS	LESS 5%	+ 5% BARE	TOTAL HEAT	COST PER MELT	Kwh PER TONNE	COST PER TONNE	
A	12	11.8	85	722160	686052	1635570	2321622	645	32.24	8.1	0.40
B	12	43.5	85	2662200	2529090	1635570	4164660	1157	57.84	14.5	0.72
C	12	22.5	85	1377000	1308150	1635570	2943720	818	40.89	10.2	0.51
D	12	226.7	85	13874040	13180338	1635570	14815908	4116	205.78	51.4	2.57
F	12	98.7	85	6040440	5738418	1635570	7373988	2048	102.42	25.6	1.28
G	12	53.4	85	3268080	3104676	1635570	4740246	1317	65.84	16.5	0.82
		Kw/m2	mins	KJ	KJ	KJ	KJ		£	Kwh	£

FURNACE WITHOUT HOT SPOTS - COLD COOLING - 15% BARE PANELS

SLAG LAYER	NO. OF PANELS	HEAT FLUX	HEAT EXPOSURE TIME	HEAT LOSS	LESS 15%	+ 15% BARE	TOTAL HEAT	COST PER MELT	Kwh PER TONNE	COST PER TONNE	
A	12	11.8	85	722160	613836	4906710	5520546	1533	76.67	19.2	0.96
B	12	43.5	85	2662200	2262870	4906710	7169580	1992	99.58	24.9	1.24
C	12	22.5	85	1377000	1170450	4906710	6077160	1688	84.41	21.1	1.06
D	12	226.7	85	13874040	11792934	4906710	16699644	4639	231.94	58.0	2.90
F	12	98.7	85	6040440	5134374	4906710	10041084	2789	139.46	34.9	1.74
G	12	53.4	85	3268080	2777868	4906710	7684578	2135	106.73	26.7	1.33
		Kw/m2	mins	KJ	KJ	KJ	KJ		£	Kwh	£

Table A8.5 Heat Loss Calculation For Furnace Without Hot Spots And With Cold Water Cooling.

FURNACE WITHOUT HOT SPOTS - HOT COOLING - 5% BARE PANELS											
SLAG LAYER	NO. OF PANELS	HEAT EXPOSURE FLUX	HEAT LOSS	LESS 5%	+ 5% BARE	TOTAL HEAT	COST PER MELT	Kwh PER TONNE	COST PER TONNE	£	£
A	12	10.8	660960	627912	1440648	2068560	575	7.2	28.73	7.2	0.56
B	12	39.2	2399040	2279088	1440648	3719736	1033	12.9	51.66	12.9	0.65
C	12	20.3	1242360	1180242	1440648	2620890	728	9.1	36.40	9.1	0.46
D	12	204.3	12503160	11878002	1440648	13318650	3700	46.2	184.98	46.2	2.31
F	12	88.9	5440680	5168646	1440648	6609294	1836	22.9	91.80	22.9	1.15
G	12	48.2	2949840	2802348	1440648	4242996	1179	14.7	58.93	14.7	0.74
		Kw/m2	KJ	KJ	KJ	KJ	Kwh	£	£	£	£
FURNACE WITHOUT HOT SPOTS - HOT COOLING - 15% BARE PANELS											
SLAG LAYER	NO. OF PANELS	HEAT EXPOSURE FLUX	HEAT LOSS	LESS 15%	+ 15% BARE	TOTAL HEAT	COST PER MELT	Kwh PER TONNE	COST PER TONNE	£	£
A	12	10.8	660960	561816	4321944	4883760	1357	17.0	67.83	17.0	0.85
B	12	39.2	2399040	2039184	4321944	6361128	1767	22.1	88.35	22.1	1.10
C	12	20.3	1242360	1056006	4321944	5377950	1494	18.7	74.69	18.7	0.93
D	12	204.3	12503160	10627686	4321944	14949630	4153	51.9	207.63	51.9	2.60
F	12	88.9	5440680	4624578	4321944	8946522	2485	31.1	124.26	31.1	1.55
G	12	48.2	2949840	2507364	4321944	6829308	1897	23.7	94.85	23.7	1.19
		Kw/m2	KJ	KJ	KJ	KJ	Kwh	£	£	£	£
FURNACE WITHOUT HOT SPOTS - HOT COOLING - NO BARE PANELS											
SLAG LAYER	NO. OF PANELS	HEAT EXPOSURE FLUX	HEAT LOSS	COST PER MELT	Kwh PER TONNE	COST PER TONNE	£	£	£	£	£
A	12	10.8	660960	184	9.18	2.3	0.11	0.11	0.11	0.11	0.11
B	12	39.2	2399040	666	33.32	8.3	0.42	0.42	0.42	0.42	0.42
C	12	20.3	1242360	345	17.26	4.3	0.22	0.22	0.22	0.22	0.22
D	12	204.3	12503160	3473	173.66	43.4	2.17	2.17	2.17	2.17	2.17
F	12	88.9	5440680	1511	75.57	18.9	0.94	0.94	0.94	0.94	0.94
G	12	48.2	2949840	819	40.97	10.2	0.51	0.51	0.51	0.51	0.51
		Kw/m2	KJ	Kwh	£	£	£	£	£	£	£

Table A8.6 Heat Loss Calculation For Furnace Without Hot Spots And With Hot Water Cooling.

APPENDIX IX.

Safety Requirements For Use Of Water Cooled Panels.

- 1) Distance from bottom of panel to the melt surface must not be too small (400mm is a typical minimum).
- 2) For tilting furnaces, this must be greater in the area of the taphole and there should be a safety hole above the taphole to indicate level of molten steel should it approach the panel.
- 3) The panels should be substantial enough to withstand small arc-backs without leaking. Should a leak into the furnace occur, safety measures as for any water leakage (e.g. electrode cooling) must be taken.
- 4) The panels should be positioned as far set back from the lower sidewall as possible so that any major leaks will tend to run outside of the furnace hearth.
- 5) Cooling water flow and temperature measurement is essential.
- 6) An emergency water supply should be available in case of water pump failure.
- 7) Safety pressure release valves should be provided on each panel.